Bio-inspired optical systems
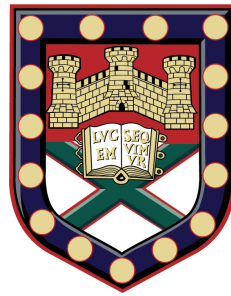
Alfred John Lethbridge

School of Physics

University of Exeter

A thesis submitted for the degree of

Doctor of Philosophy

September 2013

Bio-inspired optical systems

Submitted by Alfred John Lethbridge to the University of Exeter as a thesis for
the degree of Doctor of Philosophy in Physics
September 2013

I certify that all material in this thesis which is not my own work has been identified and that no material has previously been submitted and approved for the award of a degree by this or any other University.

Alfred John Lethbridge
2013

They say that stars that shine twice as bright live half as long.

This thesis is for Michael 'Monsieur' Daddow and Jed McQueen Jones, you guys shone so very bright indeed.

You are both sorely missed.

Acknowledgements

This thesis, for me, epitomises group efforts, cooperation and collaboration. Therefore, there are many people who I need to acknowledge, mostly just for keeping me going through the last four years. I could not have achieved this without you.

Firstly I would like to thank my supervisor, Prof. Pete Vukusic. It was your enthusiasm in teaching lectures and in undergraduate labs that inspired me to take on a PhD. Since then your enthusiasm has not waned and you always seem to say just the right thing to spur me on when my spirits were low. More than this though I am eternally grateful for your endless patience with me, I'm sure I can't have been the easiest student to manage and yet you never gave up on me. I think we can both take comfort in the fact that your hair was already grey before I started!

I would like to thank my mentor, Gyaneshwar Prasad Srivistava (GP). Thank you for being so willing to help and always smiling and relaxed. I would like to thank Prof. J. Roy Sambles F.R.S. as head of the research group and as someone who many look up to. Your worldly wisdom has inspired many an academic to be the best they can be. Also I cannot describe the honour of being coauthor with the president elect of the Instute of Physics. Prof. Bill Barnes also deserves considerable thanks from me for always reminding me that I know more than I think. I would often ask you a question, then you would turn around and say "what do you think the answer is?", after which I would answer my own question for you to respond "well there we are". I would also like to thank Euan Hendry and Alistair Hibbins for teaching the most important lesson of all, you are never too old to have fun!

During my PhD I have experienced first hand that collaborations are fruitful for all as no one person knows everything. Here I would like to thank those people. From Georgia Tech I thank Ken Sandhage, for his down-to-earth approach to science and, of course, for a great night out in Boston. Craig Cameron for being such a strong driving force on our project and for not

Her cheeky little smile never fails to cheer me up! I would like to thank with my whole heart my mother. You always always always believed in me and often let me know! Thank you so much for everything you have done for me over the last 26 years. I would also like to thank my father for always being supportive, I'm sure I don't have to tell you that I would never have got through the last year without you. Thanks also for keeping my feet on the ground. I owe you both so much and will love you always. You guys are the best!

To the person I wish to spend the rest of my life with, Laura. You helped keep me sane in the lead up to my viva and kept encouraging me no matter what. You have made me so happy I can't begin to describe and my times with you have been the best I've ever had. You make me the person I want to be. For this, I owe you the world and endless love. Thank you.

And then there's Chris Holmes.....

Abstract

This thesis presents an investigation into some of the structural colours that are produced in nature. There are many animals and plants that produce structural colour, with a particularly high structural colour diversity in insects. Of the species that exhibit structural colours, three species are the subjects for investigation of this thesis. Those comprise a group of beetles from South-East Asia, *Torynorrhina flammea*, a butterfly, *Parides sesostris* and a fruit, *Margaritaria nobilis*, both from South American rainforests. The structures that produce the vivid colours of these species were analysed using electron microscopy. This information aided the design and creation of three inorganic, synthetic replicas of the natural structures.

The fruit of *Margaritaria nobilis* was structurally analysed, yielding the discovery of a novel multilayer fibre. These fibres were cylindrical in design and were found to be layered together producing the epidermis of the fruit. The multilayer structure produced a vivid blue colour appearance, which is believed to offer a selective advantage because the colour deceives birds into thinking that the fruit contains, nutritious flesh. This selective advantage earns *M. nobilis* the label of mimetic fruit.

The structure found within the *M. nobilis* fruit epidermis inspired the synthesis of a structure which comprises single cylindrical multilayer fibres. The synthetic fibres were manufactured from elastic materials which allow the structure to be deformed under strain and, therefore, a change in colour can be observed. As the structure was stretched, this made the layers get thinner and, therefore, the colour of the fibre blue-shifted. The fibre was able to be stretched to over twice it's original length which yields a shift in peak reflected wavelength of over 200 nm.

Four beetles from the *Torynorrhina flammea* species were investigated with the aim of replicating the nanostructures responsible for their colour appearance. The initial interest in the beetles came from their strikingly vivid colour appearances. The structure responsible for the vivid colours in all four of the subspecies is a mulitlayer with high structural order and over

100 laminae. Both of these attributes contribute to the saturation of the colours exhibited. The multilayer was found to be intersected by an array of rods, the long axis of which is orthoganol to the surface. The rods are believed to be the cause of an interesting diffraction phenomenon exhibited by the beetles. Using imaging scatterometry, the structure was found to diffract the colour produced by the multilayers into an annulus around a specularly reflected white spot.

This inspired the synthesis of a multilayer permeated with an array of holes with the aim of replicating a system that could reproduce the annular pattern of colour reflection. The initial synthesised system comprised a quarter-wave stack with a perfectly ordered hexagonal array of holes permeating the surface orthogonally. The sample displayed the scattering characteristics of a hexagonal array, and the reflection spectra of the multilayer stack. When disordered hexagonal arrays were milled into the structure with a focussed ion beam, the scattering pattern started to show more of the green colour from the multilayer and less of the ordered scattering pattern. The highly disordered, synthesised structure displayed no hexagonal scattering pattern, but instead it showed a highly scattered bluish-green colouration. One sample was created by directly mapping out the array of holes using an image of the original array from one of the beetle samples. This sample was expected the same annular diffraction pattern as the beetles, however, the sample instead exhibited the same scattering pattern as the highly disordered array.

Some structurally coloured systems in nature have more than one light scattering structure, all of which contribute to the overall colour of the system. For complicated systems such as this, it is necessary to devise a technique to characterise the individual scattering structures separately. One such species that displays a complex, multicomponent system is *Parides sesostris*. The male of the species displays bright green patches on the dorsal side of the forewings which are made up of thousands of green wing scales. These green scales contain a 3D gyroid poly-crystal at centre with a membrane layer surrounding the underside of each scale and a scattering structure on top. Using focussed ion beam milling techniques allowed the individual characterisation of each of these structures. The gyroid poly-crystal was found to reflect not green but blue wavelengths. This led to the discovery by another group[1] that the scales contain at least one type of fluorophore. The removal of the membrane structure and some of the gyroid poly-crystal from the base of the scale resulted in the change of the

overall scale structure from green to cyan. This suggests that the membrane maybe a significant source of fluorescence. Computational modelling, witout fluorescence, suggests that the addition of the membrane layer to the gyroid does not shift the band-gap wavelengths, however, the overall reflection intensity does increase.

The scattering structure on the top side of each scale is comprised a bi-grating which sits on top of the 3D gyroid structure. The long periodicity of the bi-grating protrudes above the surface, resulting in the very top layer of the scale to be a mono-grating. This whole structure decreases the angular-dependence of the colour by efficiently scattering the incident light into the gyroid and also scattering the reflected light from the gyroid, resulting in a double-scattering. FIB-milling was used to isolate the scattering part of the structure. Analysis of this component of the structure revealed that it was not a source of the green colour itself, however, it did show the characteristic scattering pattern of a mono-grating. The small periodicity of the bi-grating did not produce a scattering pattern since the periodicity is too small to produce optical diffraction at normal incidence.

To characterise the effect of the fluorophores, the whole scale structure was photo-bleached using ultra-violet radiation for two months with the aim of destroying the fluorophores contained within the structure. The expected result occurred which was the blue-shifting of the peak reflected wavelengths. However, it could not be confirmed whether or not the photo-bleaching reduced the physical size of the light scattering structures which would, in theory, result in a blue-shift of the peak reflected wavelengths.

The male *P. sesostris* green wing scales were also the subject for investigation for trying to make inorganic replicas of the gyroid-polycrystal. A surface sol-gel coating process was utilised to coat the green wing scales with titania. This coating process was performed using a few different methods. Half of the samples were coated with TiO_2 and the other half with tin-doped TiO_2. Half of each of these samples had their surfaces dendritically amplified before the coating processes and the other half were left untreated. The samples were coated with 25 surface sol-gel (SSG) cycles of each treatment at a time. After each 25 cycle treatment the samples were optically characterised. The total number of cycles applied to the samples at the end was 150. The addition of layers of titania resulted in a general red-shift that was higher for the tin-doped titania samples than for the titania samples. Another general trend found was that the samples that had their surfaces

dendritically amplified, produced a lower red-shift in peak wavelength. this was contrary to the hypothesis that the amplification process was supposed to aid the SSG coating process and, therefore, increase the red-shift in peak wavlength.

The unamplified, tin-doped titania coated samples exhibited the highest red-shift in peak reflected wavelengths and were, therefore, chosen for pyrolysis. This process essentially heated the coated scale structures until the organic chitin material vapourised. This left a gyroid structure that comprised of only inorganic tin-doped titania. The pyrolysis process also caused some shrinkage to the structure therefore a blue-shift from the coated samples to the pyrolised samples was observed. Another observation made was that the more cycles of SSG coating that each sample underwent meant a reduction in the amount of structural shrinkage. This meant that the replicas that were produced with a higher number of SSG cycles, had a higher peak reflected wavelength. The parameters involved in producing the inorganic replicas mean that the structures could be tuned to specific colours.

Contents

Contents

Contents

List of Figures

List of Figures

List of Figures

Chapter 1

Thesis overview

The field of photonics and photonic crystals is expanding rapidly. As our understanding of these systems expands, the number of applications that have been realised also expands. One of the huge advancements in the field is the realisation that these devices maybe used in optical computing [2, 3, 4, 5, 6], therefore there is a growing demand to produce and optimise such devices. Creating a photonic crystal for a particular regime of the electromagnetic spectrum requires the crystal to have a periodicity that is comparable to the desired wavelengths. Therefore, when creating optical photonic crystals, one needs to produce a structure with nano-scale dimensions. This can be a challenging task. This thesis explores some of the structutally coloured species in nature and the synthetic structures they inspired.

1.1   Thesis outline

This thesis includes eight chapters, comprising this overview, two background chapters, an experimental methods chapter and four experimental chapters describing, in detail, the research undertaken. The first background chapter presented gives an insight into structural colour in nature that has been reported in the literature. The second background chapter is a general summary of the physics of electromagnetic radiation and how this interacts with matter, describing the fundamental mechanisms behind structural colour. The experimental methods chapter gives a description of all the techniques employed to gain better understanding in this field, as well as a description of the numerical methods used to strengthen the understanding taken from the experimental results. The four experimental chapters describe the investigations into three sample species, both faunal and floral, that exhibit structural colour. The first three experimental chapters also showcase methods used to synthesise the structures found either by simply copying the natural structures or by using those structures as direct

templates for inorganic materials. The last chapter shows an up-to-date method of deconvoluting the hierarchical components of a complicated structure found in nature by removing individual components.

In chapter 2 many reports of structural colour in nature have been described, giving examples of progress in the field to date. Simple multilayer structures are reported that show high levels of iridescence, followed by more complicated structures that exhibit bright, angle-independent colours. A collection of faunal and floral species are investigated that include butterflies, beetles and some plants. A review into some biologically-inspired, synthetic structures is also reported for a comparison to the techniques shown later in this thesis.

The physics behind structural colour is presented in chapter 3. The physics shown describes how electromagnetic radiation (e.g light) interacts with matter (e.g. the structures found in the specimens reported here). A simple look at how light interacts at an interface between two optical materials is described, followed by a more detailed look at structures that exhibit a periodic variation in refractive index. Equations and theory that govern these interactions are also presented.

Chapter 4 contains all the experimental techniques used to produce the data collected for the purposes of the studies presented here. A brief explanation into how one collects reflection and transmission spectra of electromagnetic radiation from natural and synthetic structures is given. Then the principles of optical microscopy are explained and also detailed accounts of how simple microscopes were modified to examine the optical properties of microspopic structures and small areas of larger structures. An explanation of imaging scatterometry is then given, a relatively new technique that allows qualitative analysis of the characteristics of reflected light, specifically the radial patterns exhibited by the structures in question.

Numerical methods are also presented such as the computational modelling used to provide theoretical data which could then be compared to the experimental data. A simple approach is shown that can accurately describe simple multilayer systems which involves calculating the coefficients of reflection and transmission at each optical interface. A more complicated method is presented which gives an approximation to structures that have variations in up to three spatial dimensions. The latter method involves calculating the electric fields from thousands of small sections of the structure and combining them. From this one can then extract information such as the reflection and transmission of the structured system being modelled.

In chapter 5, the first of the experimental chapters, a detailed analysis of the colour and structure of the fruits of *Margaritaria nobilis* is presented. Angle-resolved reflection spectra are taken showing the iridescent nature of the fruit. Electron microscopy techniques are utilised to study the nano-scale structure embedded in the fruit's epi-

dermal layer. The effects of dehydrating and rehydrating the fruit are investigated, showing how the introduction of water either increases the dimensions of the embedded photonic crystal, or increases the rerfractive indices of the materials already present.

The investigation into the fruits of *M. nobilis* inspired a synthetic system to be created. This system is a simplified, mimetic version of the photonic crystal found in the fruit. The synthetic crystal is simply a multilayer 'rolled up' into a cylinder. This system was also optically and structurally characterised, and compared to the natural system.

Chapter 6 details the investigation into the species of beetle known as *Torynorrhina flammea*. There are three adult subspecies investigated, and also the juvenile form of one of those. The beetles were investigated due to the high Q-factor of the wavelengths that are reflected, resulting in a pure and vivid looking colour. The beetles exhibit an interesting and unfamiliar diffraction pattern. This peculiarity inspired the creation of another synthetic system to see if the origin of the diffraction could be ascertained. Computational modelling is used to strengthen the arguments made.

A new method of structural interrogation is presented in chapter 7. The green wing scales of *Parides sesostris* are structurally and optically analysed to provide a basic picture of how the scale produces the green colour. Then, using FIB-milling techniques, the scale was deconstructed allowing a deconvoluted approach to identifying the role of each of the colour producing components. This highly detailed study heavily utilised the imaging scatterometry techniques as shown in chapter 4 to show the colour and spatial characteristics of the reflected radiation from a single scale, and whole wing sections alike.

Parides sesostris is also the specimen under investigation in chapter 8. In this chapter the triply periodic, bicontinuous gyroid found in the green wing scales is used as a bio-template for an inorganic replica. The motivation for this biomimicry was simple; photonic crystals tuned for the optical regime have to be nano-scale structures, therefore manufacture is much more difficult than it is for larger wavelength regimes, such as microwave radiation. A surface sol-gel (SSG) technique was used to coat the chitinous gyroid with inorganic titanium dioxide (TiO_2). The resulting coated gyroids were then pyrolised to remove the chitin, leaving only an inorganic replica of the gyroid structure. Variances in the structures were tested, such as variations in the refractive indices of the coated materials and also variations in how many SSG cycles were used, resulting in varying coating thickness. The latter variation also affected the amount of shrinkage occurring during the firing. All of these structures were investigated optically using micro-spectrophotometry and a reflection probe to measure the peak wavelength of whole scales. Computational models were created, simulating the original chitinous gyroid, the chitinous gyroid coated with TiO_2 and the fired TiO_2 only samples to

support the experimental evidence.

The final chapter presents a brief summary of the conclusions drawn from this work, and als offers prosepcts for continued research.

Chapter 2

Structural colour in nature

"We will now discuss in a little more detail the struggle for existence."
- Charles Darwin

For millions of years plants and animals have been fighting for survival, in a bold effort to pass on a genetic legacy to the next generation. This has made our planet a battleground for all species to compete and survive long enough to reproduce [7]. After hundreds of millions of years of competing in a continually changing environment we find ourselves amongst a diverse array of species in all shapes, sizes and colours [8]. The term '*survival of the fittest*' can lead one to think of the strongest, fastest or more intelligent species as the most prevalent, however, as Charles Darwin himself noted, it is the species that is the most adaptable to change, which stands the greatest chance of preserving its genetic legacy. For this reason the colour and patterns exhibited by a species can play as important a role as the strength, speed and intelligence of the individual in evolutionary terms. For instance in the dense rainforests, a brightly coloured display can help potential mates find each other [9]. Other functions may include camouflage [1, 8, 10, 11, 12, 13, 14, 15, 16, 17, 18, 19, 20], thermal regulation [21, 22, 23], sexual communication [8, 9, 19, 24, 25, 26, 27] and UV protection from the Sun [28] [18]. Competition therefore requires some species to display intense, optimized colour appearances [1, 10, 14, 29, 30, 31, 32, 33, 34, 35, 36, 37, 38]. More often than not, the colours displayed by a particular species (floral or faunal) are accredited to chemical, or pigmentary colour. Pigments produce the colours we perceive due to the preferential absorption of particular wavelengths of the illumination source (in nature, this is usually the Sun) and the scattering of the rest. It is the non-absorbed, scattered colours that we perceive as the colour of that species. Clear examples of this are plants, they are largely green because the chlorophyll contained in plant leaves absorb red and blue wavelengths from the Sun, and scatter the green wavelengths which our

eyes detect [18, 39]. The conventional elastic scattering of the perceived colours means that pigmentary colour is angle independent and very diffuse [18]. The brightest, purest colours in nature, however, are attributed to what is known as structural colour [40]. Structural colour arises from interactions of light with the structure/arrangement of materials with different refractive indices on a nano-scale [41]. It is because nature has had so long to diversify and optimise such displays that we, as scientists, have turned to nature for inspiration and ideas so we can apply that knowledge into creating our own devices for a myriad of purposes [42]. These include anti-couterfeiting [43], sensing applications [31, 33, 44, 45, 46, 47] and anti-reflective coatings [48, 49, 50]. One such purpose is the future prospect of optical computing [51, 52]. Optical computation will require highly optimised, efficient photonic crystals which can manipulate light within an optical integrated circuit for the purpose of computational processing [53]. As discussed before, nature has had millions of years to produce optimised and efficient photonic crystals. Hence, it is quite important we look to nature for inspiration.

2.1 Photonic crystals in nature

A photonic crystal is a structure that has a periodic variation of refractive index in one, two or three dimensions. It is this periodicity that gives rise to to the colours of the brightest surfaces in nature. Nature cannot, produce structures with perfect structural order, but in some occasions nature has come quite close. Nevertheless, in some instances it can be beneficial for a species to exhibit structures with quasi or disordered structures as this will reduce the angle-dependence that many structurally coloured systems exhibit. In this section a few examples of the investigations into ordered and disordered photonic crystals in nature are presented.

2.1.1 1D photonic crystals in nature

2.1.1.1 Multilayers

A multilayer system is one of simplest types of photonic crystals. It comprises a simple arrangement of lamina with a periodicity in just one dimension. This results in a system that has a very directional response to incident illumination. It is because the periodicity is only in one direction that the colour can change dramatically when viewed from different angles.

As shown by Yoshioka and Kinoshita (2007) [21], a one dimensional photonic crystal was found to be the structure responsible for the colouring of *Chrysiridia ripheus*, more commonly known as the Madagascan sunset moth. Their study concentrated on the reddish-purple region present on the ventral side of the hindwing. TEM micrographs

of the structure responsible for the colour confirm that a 1D photonic crystal is present in the form of an 11 layer multilayer. The multilayer comprises 6 layers of cuticle (refractive index assumed to be n=1.55) separated by five layers of air. The thicknesses of the cuticle layers and air spacing are found to be 170 ± 20 nm and 130 ± 30 nm, respectively. Whilst the structure is essentially a multilayer, the overall colour produced is a little more complicated as the scales embedded with the multilayers are very curved in nature, resulting in some interesting optical effects. The arrangement of the highly curved scales produces grooves between rows of scales. These grooves cause multiple reflections of light from one scale to the next row. When viewing the scales normally, the top part of the scale appears purplish-red, whereas the curved regions within the groove appear to be yellow. The purplish-red colour seems fairly consistent when changing polarisation, however, the yellow region changes dramatically when the polarisation conditions are changed.

Nixon et al. (2013) [10] found a multilayer in *Matronoides cyaneipennis* male damselflies with some unusual optical properties (figure 2.1). The hindwings show a blue colouration on the dorsal side and a green colour on the ventral side. The colours shown on each side are found to originate from a membrane found on the wings in the form of small 'windows' that fill in the areas between the wing veins as shown in figures 2.1(b) and 2.1(c).

TEM images (figure 2.2) show that the colours exhibited can be attributed to two very similar multilayer systems, each comprising 5 layers. The two multilayers are found on either side of the hindwing membrane. The layer thicknesses of each multilayer are almost identical except for the second layer from the surface in each sytstem. This second layer is slightly larger on the ventral side of the wing than it is on the dorsal side, and it is this small difference that produces the green colour instead of blue.

The thick central layer that separates the two multilayers is expected to contain melanin which absorbs the transmitted light through each multilayer so that it does not diminish the structural colour of the opposing side.

Computational Fresnel-based modelling of this system (figure 2.2(c)) reveals that varying the second layer from the surface on each side gives the greatest change in peak wavelength of the entire system. This leads the authors to theorise that this system is highly optimised, because two different colours are produced with the minimum possible change in the system.

The iridescent colouration of *Chyrsochroa raja* was studied by Noyes et al. [54]. This beetle was found to exhibit a green colouration with a red stripe running down the side of each elytra (figure 2.3). The aim of the investigation was to create a way to determine the refractive index of the beetle cuticle. The method developed in the investigation used an already established method for taking reflection spectra
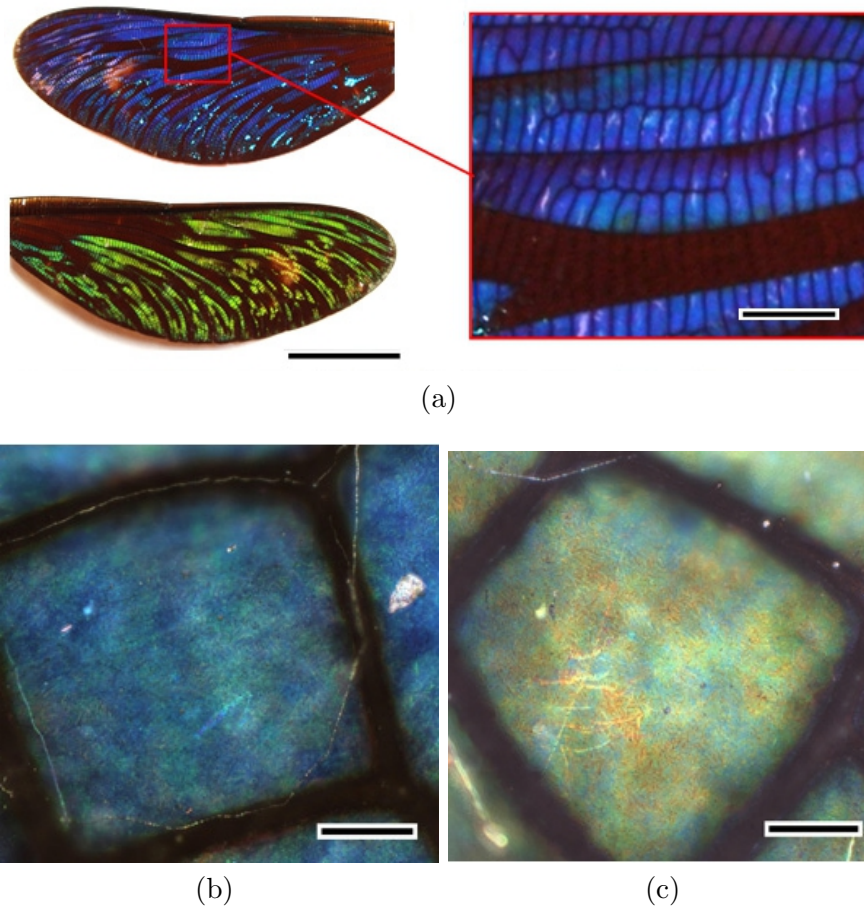
Figure 2.1: (a) Optical micrographs of the dorsal (blue side) and ventral (green side) of the male *M. cyaneipennis* hindwing. The zoomed region shows the arrangement of veins on the blue dorsal side. (b) Optical micrograph of a single 'window' of the blue dorsal side of the wing. (c) Optical micrograph showing a window of the green ventral side of the hindwing. Colour variation can be seen in both sides of the wing, indicating a level of noise in the dimensions key to colour production. Scale bars: (a) 10 mm and zoomed region 2 mm, (b) 100 μm and (c) 200 μm. Images courtesy of M. Nixon [10].

from the beetle elytra at different angles and polarisations, this data was then used in conjunction with the TEM cross-section (figures 2.4(a) and 2.4(b)) structural analysis to create a Fresnel-based multilayer computational model. The structures of both multilayers were found to comprise a range of layers between 8 and 22. The green layers comprised electron opaque layers with a range of thicknesses from 50 to 60 nm and electron transluscent layers with a range of thicknesses from 65 to 92 nm. The red layers comprised electron opaque layers with a range of thicknesses from 52 to 92 nm and electron transluscent layers from 72 to 111 nm. The resulting modelling data was
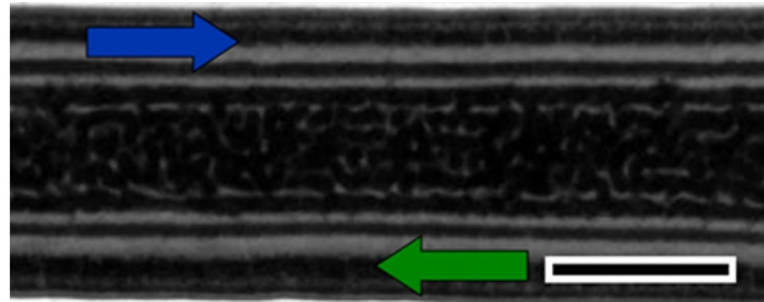
(a)
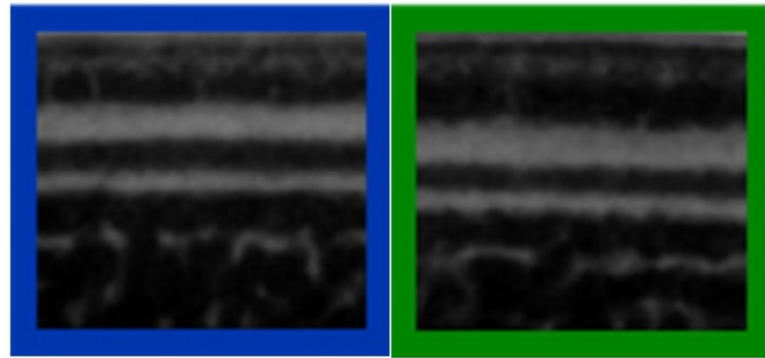
(b)
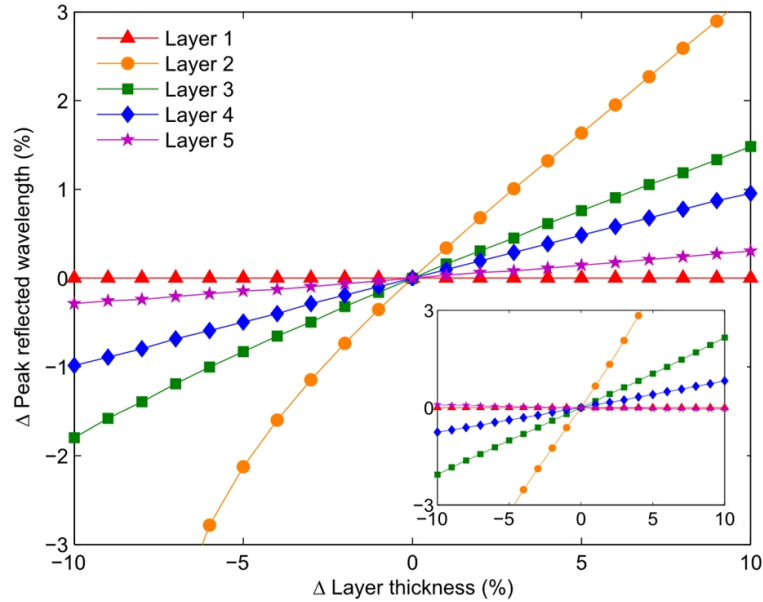
(c)

Figure 2.2: (a) A TEM cross-section of the wing showing the multilayers either side of the wing membrane. (b) Cross-section TEMs of the blue dorsal and green ventral sides of the wing membrane. Structural interrogation revealed the second layer from the surface on each side showed the biggest difference in dimension. (c) Computer modelling showed the second layer to be the most sensitive to variation, with respect to colour production. Scale bar: (a) 1 μm. Images and computational modelling, courtesy of M. Nixon [10].
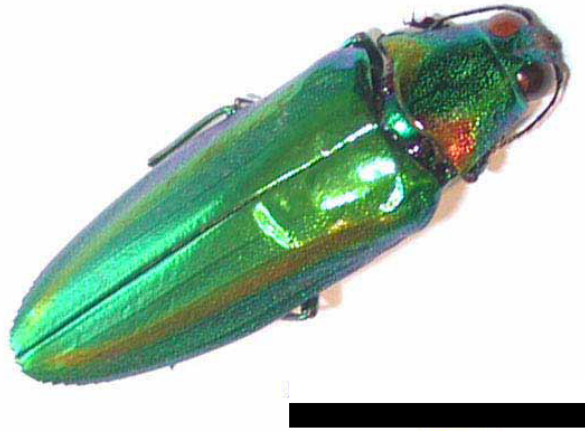
Figure 2.3: (a) Optical photograph of the beetle *C. raja*. The beetle displays an iridescent green colour appearance with a thin red stripe running down the side of each of the elytra. Scale bars: (a) 20 mm. Images courtesy of J. Noyes [54].

then fitted to the experimental data (figures 2.4(c) and 2.4(d)) to establish the complex refractive indices, which were found to be $n = 1.68 + 0.03i$ and $1.55 + 0.14i$ for the electron translucent and electron opaque layers in the TEM, respectively.

Periodic multilayers have been shown to be responsible for the particular colours of beetles such as the two multilayers previously described in *C. raja*, however, non-periodic multilayers can be used to reflect more broadband colours. Instead of having a regularly periodic multilayer that reflects a small band of wavelengths, a multilayer with a steadily increasing or decreasing layer thickness with distance from the surface will reflect many different wavelengths. The range of wavelengths will depend on the range of thicknesses involved. Such a system has been called a 'chirped' multilayer and, due to the broadband nature of reflection, can be used to produce mirror-like gold or silver coloured multilayers. Parker et al. [55] showed an investigation into a gold beetle, *Aspidomorpha tecta*, which exhibits such a specular, gold colouration.

Reflection spectroscopy of the gold elytra of *A. tecta* reveals a broadband response, reflecting above 60% of incident light between approximately 500 nm and 1400 nm. The structure responsible for the colour appearance was found, via TEM cross-sections, to be a chirped multilayer that has a decreasing layer thickness with distance from the surface as shown in figure 2.5.

It has ben shown how simple structures that have a periodic variation of refractive index in just one dimension produce bright, iridescent colour appearances on butterflies, damselflies and beetles. Although the geometry of the systems shown here are very

(a)

(b)

(c)

(d)
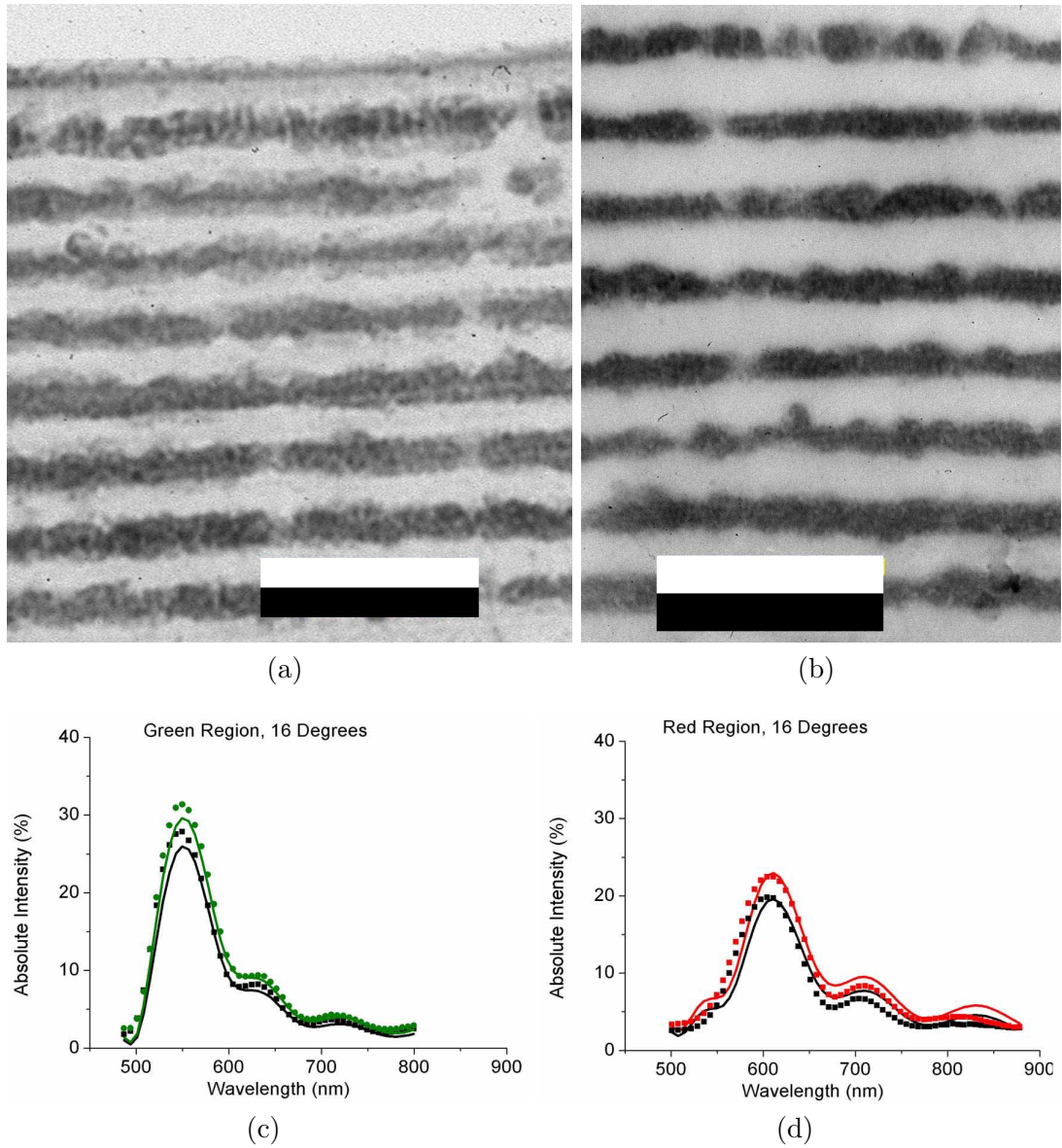
Figure 2.4: (a) and (b) show TEM cross-section images of the green and red areas of the *C. raja* elytra, respectively. (c) and (d) show the reflection spectra of the green and red areas as compared with the Fresnel-based computational modelling. The points in each graph represent the experimental data and the solid lines are the theoretical modelling. The black data points and solid lines in each graph represent TM polarised incident illumination and the TE polarisations are represented by the green data in (c) and the red data in (d). This comparison shows good agreement, demonstrating the accuracy of the refractive index found. Scale bars: (a) and (b) 500 nm. Images and spectra courtesy of J. Noyes [54].

(a)   (b)

(c)   (d)
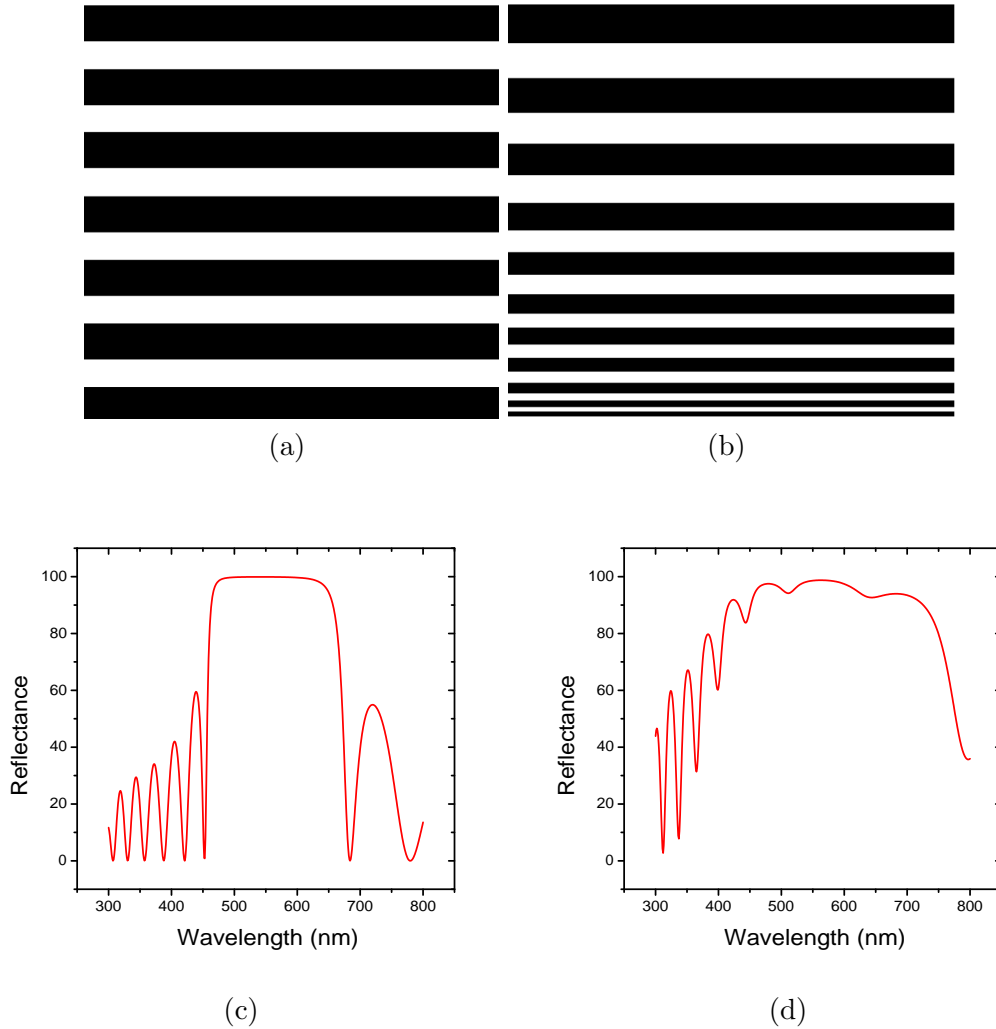
Figure 2.5:   (a) A regular multilayer, showing a fixed periodicity from the top of the structure to the bottom. (b) A chirped multilayer exhibiting a decrease in periodicity from the top to the bottom. (c) and (d) show the theoretical reflectance spectra of the two structures, respectively. The regular multilayer, in this case a quarter-wave stack (see chapter 3), will reflect a narrow band of wavelengths because all the layers in the system have the same optical path length. However, due to the varying layer thickness of the chirped multilayer, the different optical path lengths mean that a broadband array of wavelengths will be reflected, giving the system a gold or silver mirror-like reflection. The refractive indices used for thhis theoretical investigation are 1.38 and 2.42 for the black and white layers, respectively.

similar, small variations in the geometric dimensions and refractive indices can cause strikingly different colour appearances.

2.1.1.2   Diffraction gratings

Other than photonic crystals, a monograting also exihibits a periodicity in one direction. Unlike a multilayer, however, a diffraction grating has a periodicity in the plane of the surface of the structure as opposed to parallel to the surface normal. This mechanism scatters incident light by specific angles depending on the angle and wavelength of incident light as described in chapter 3. There are a few examples of diffraction gratings in nature, many of which are combined with other light scattering structures.

A few of the examples presented here are perhaps the oldest specimens ever to exhibit structural colour. The Burgess Shale were thought to exist about 500 million years ago (about the time of the Cambrian explosion) [37]. Parker (1998) reported that *Wiwaxia corrugata*, *Canadia spinosa* and *Marella splendens* from the Burgess Shale exhibited diffraction gratings from the hard, external, protective surfaces. This discovery then leads to the conclusion that these animals would have displayed iridescence. The surface scales of *W. corruggata*, for example, display areas of grooves with a constant periodicity of 900 nm. In the areas that exhibit natural diffraction gratings, the orientation, periodicity and approximate depth are consistent for all three Burgess Shale species mentioned. Also the evidence suggests that all the grooved areas, of the three different species, appear on the external surfaces which is strong evidence that the purpose of these grooves is in fact for structural colour. Parker also reports that manufactured replicas of the diffraction grating structures of the animals mentioned above produce efficient reflection of all optical wavelengths when immersed in sea water and illuminated by a collimated beam of white light. Therefore, these structures appear silver when stationary and with flashes of colour when the system is in motion under diffuse, white light.

Hinton et al. [56] studied the Phalacrid beetles and their diffraction gratings. *Litolibrus obesus* was shown to exhibit a diffraction grating on it's elytra with a periodicity between 1.0 and 1.1 μm. The authors also found that many different Phalacrid beetles exhibit diffraction gratings. A suggested evolutionary advantage of these diffraction gratings is to serve as a warning colour.

It has been shown that some species in nature display hybrid structures comprising of two or more light scattering mechanisms. Vukusic et al. [9] reported a multilayer that is periodically 'broken' to form diffracting ridges. These spatially discrete multilayers were reported to be present in two butterflies, *Morpho rhetenor* and *Morpho didius* (figure 2.6).

<div align="center">(a)   (b)</div>
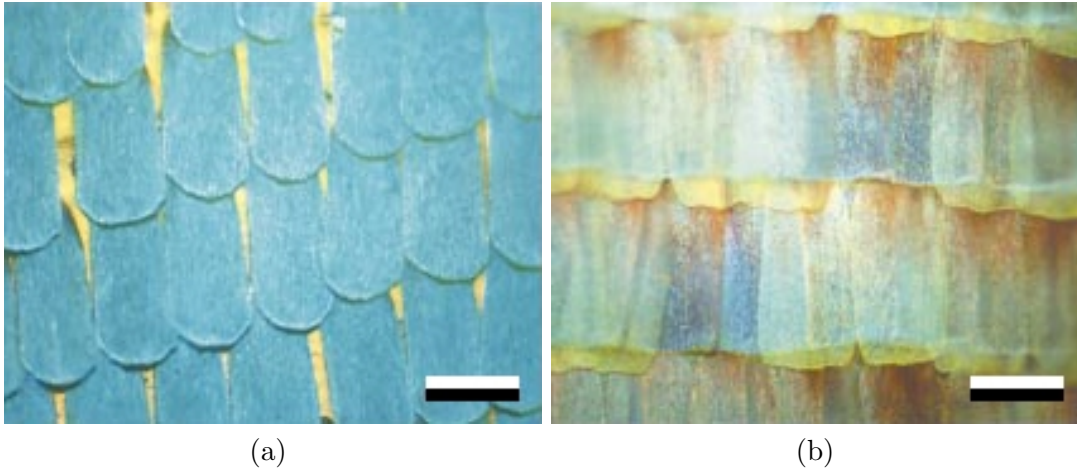
Figure 2.6: (a) Optical micrograph of the blue scales on the *M. rhetenor* wing. (b) Optical micrograph of the blue scales of the *M. didius* wing. Scale bars: (a) and (b) 100 μm. Images courtesy of P. Vukusic [9].

Structural analysis via TEM imaging (figure 2.7) reveals that both *Morpho* species studied here exhibit an intricate multilayer/diffracting ridge structure. Both structures comprise rows of ridges and grooves which provide a diffracting character to the scales, then within each ridge there are branches, providing a tree-like appearence to the scattering structures. The branches of the trees are the fine structure that provide the iridescent blue colour to the scales, through wave interference of the light reflecting from the top and bottom interfaces of the branch layers.

Optical spectra and microscopy show that the scales have an iridescent blue quality, but the iridescence, or rather angle-dependence of the colour is slightly surpressed due to the diffracting ridges on the scale. To quantify the light scattering properties of the wing, 488 nm light was made normally incident on the top side of the scales, then the scattered light was collected 360° around the scale in the plane created by the surface normal and the direction of the ridge periodicity (figure 2.8). These results show that there are two lobes of reflection at approximately 30° either side of the normal for the *M. rhetenor* scales and a very diffuse scattering character for the *M. didius* scales. The difference in the scattering response can be attributed to the alternating branches on either side of the ridges in the *M. rhetenor* scales as seen in the TEM cross-sections (figure 2.7). This geometry makes an effective angled layering of the tree branches. This effective off normal angling of the branches reflects the light off normal accordingly. The diffuse scattering of the *M. didius* scales is due to the glass cover scales having a diffractive character in transmission. The glass scales scatter incident light as well

(a)   (b)
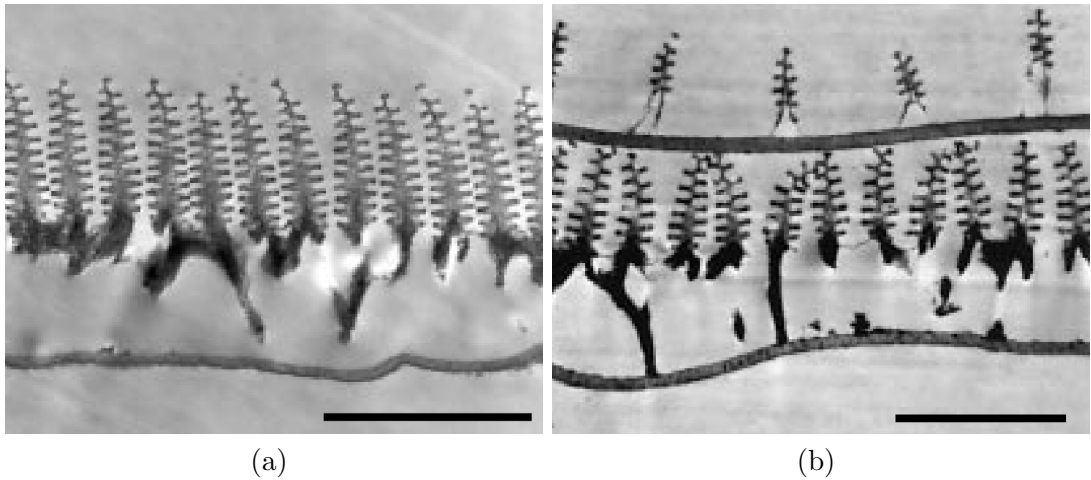
Figure 2.7: (a) A TEM cross-section through a blue scale of *M. rhetenor*, showing the tree-like nature of the photonic structure. (b) A TEM cross-section through a blue *M. didius* ground scale sitting below the glass scales. The same tree-like stuctures are observed on both layers but the glass scales create ridges with a much higher periodicity. Scale bars: (a) 3 μm and (b) 2 μm. TEM images courtesy of P. Vukusic [9].

as reflected light from the ground scales underneath. This makes the blue colouration of the wing less angle-dependent. Using equation 3.26 it was found that the angles of diffraction when in transmission for the *M. didius* glass scales (shown in figure 2.8(b)) were caused by a diffraction grating with a periodicity matching the spacings between the uppermost set of 'trees' in figure 2.7(b).

Another butterfly from the Morphidae family, *Morpho menelaus* was investigated by Berthier et al. [57]. This butterfly also exhibits spatially discrete multilayers as previously described, also exhibiting a brilliant iridescent blue colour appearance. Hemispherical reflectance spectroscopy was performed on the dorsal side of the wings using an integrating sphere (as described in chapter 4). The results confirm that there is a shift in the wavelengths of the reflection band when the angle of incidence is altered, an expected result for a thin film based system.

TEM and SEM imaging reveal that the tree-like multilayers in this species comprise 6-12 layers or branches which are responsible for the blue iridescnct colour appearance. The diffracting ridges formed by the apex of each tree are approximately 600 nm apart. This creates a greater angular spread of the reflected colours.

It has been shown here what roles diffracting structures can have in nature. It has been reported that diffracting structures can provide iridescent, structural colouration and also how a diffracting structure can work in synergy with other light scattering structures with the function of decreasing angle-dependence of colour, thereby reflecting
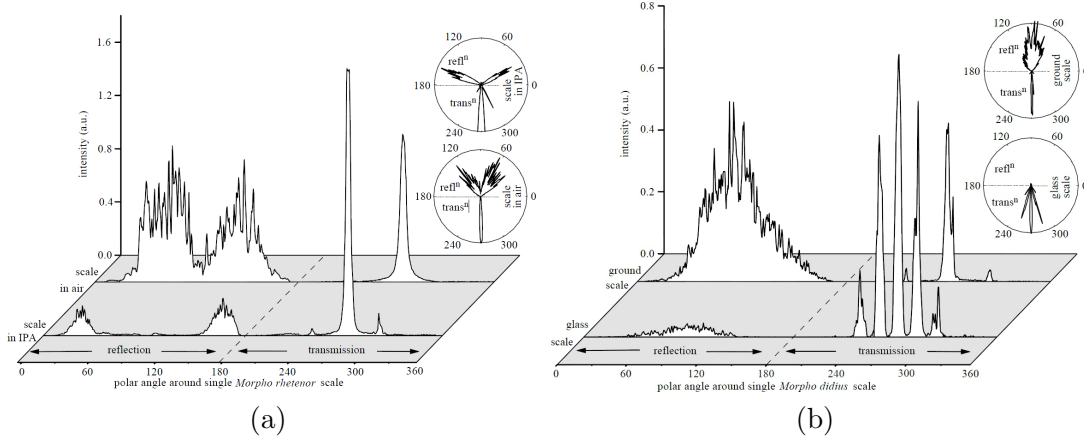
Figure 2.8: (a) A 360° scan of reflected and transmitted intensities of 488 nm radiation, normally incident upon the scales of *M. rhetenor* in both air and immersed in IPA. The IPA immersion was for he purpose of gathering more data on the structure for fitting purposes. (b) 360° scans of reflected and transmitted intensities of 488 nm radiation, normally incident upon both the ground scales and the glass scales of *M. didius*. The insets show the same data in a polar plot form to aid visualising how the system works. All data courtesy of P. Vukusic [9].

the desired wavelengths over a larger angle range for increased visibility.

2.2   2D photonic crystals in nature

Trzeciak et al. [58] reported a 2D photonic crystal fibre to be responsible for the iridescent hairs on the polychaete worm *Pherusa*. The worm displays iridescence in the setae found at the base of the specimen. The iridescent colouration of the setae was found to vary along the fibre from the root to the tip (figure 2.10). The colour starts off as red and blue-shifts proportionally with increasing distance from the root. At the tip the setae display a green colour appearance. There are also differences in colour when the setae are rotated around the longitudinal axis (figure 2.9). The origin of the colour difference is due to two things, as the setae is rotated, different planes within the structure are observed and, therefore, different colours will be displayed. The second possible reason is that there could be many domains of the photonic crystal within the setae which would allow the observer to see different colours produced at the same orientation.

From the reflection spectra in figure 2.10 an interesting feature is observed, the peak reflected wavelength decreases with length from the root to the tip opf the setae. Another interesting feature is that there is also a decrease in full width half maximum

| (a) | (b) | (c) |
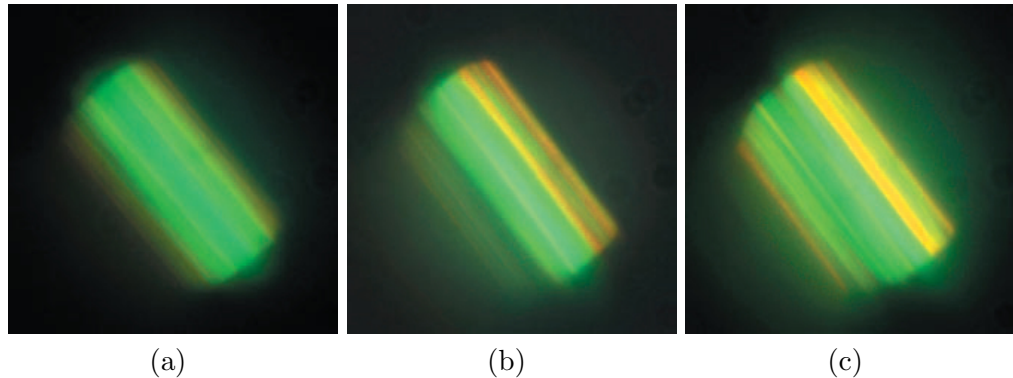
Figure 2.9: (a) - (c) Optical micrographs of a setae of *Pherusa*. The three images show the variation in colour as the fibre is rotated around the longitudinal axis. Images courtesy of T. Trzeciak [58]

(FWHM) of the reflection peaks from root to tip as well.

The packing fraction of the hollow tubular fibrils was found to be $\phi = 0.47 \pm 0.06$, a value that would require the refractive index of the surrounding material to be approximately $n = 1.6$ to fulfil the requirement of making the size of the band gaps as large as possible for maximum reflection, and they also found in the literature that similar structures had a value of refractive index very close to that figure. This led the authors to conclude that the iridescent colour appearence of the setae is very optimised via natural selection.

Structural analysis was performed using TEM cross-sections of the setae (figure 2.11). Within each setae there are many hollow channels which run parallel to the longitudinal axis. The channels have a close packed, hexagonal arrangement. Polycrystalline domains can be seen across the plane of the cross-section. It is this structure which is responsible for the iridescent colour appearance in the setae.

Another 2D photonic crystal in nature was found by Yoshioka et al. [59] who made an investigation into the structure responsible for iridescence found in the blue and yellow feathers of peacocks. Both the blue and yellow feathers show an angle-dependent colouration as the peak reflected wavelength decreases with angle from the normal of the flat edge of the feather barbules. They also found that, when illuminated normally with monochromatic laser light, that the reflection from a small illuminated area (several μm) is relatively specular, but if a beam spot that covers the entire width of a the barbule is used then the angular range of reflection increases dramatically.

The SEM structural investigation of the blue and yellow feathers reveal a macroscopic curvature of the barbules. TEM analysis reveals a 2D photonic crystal to be

(a)   (b)
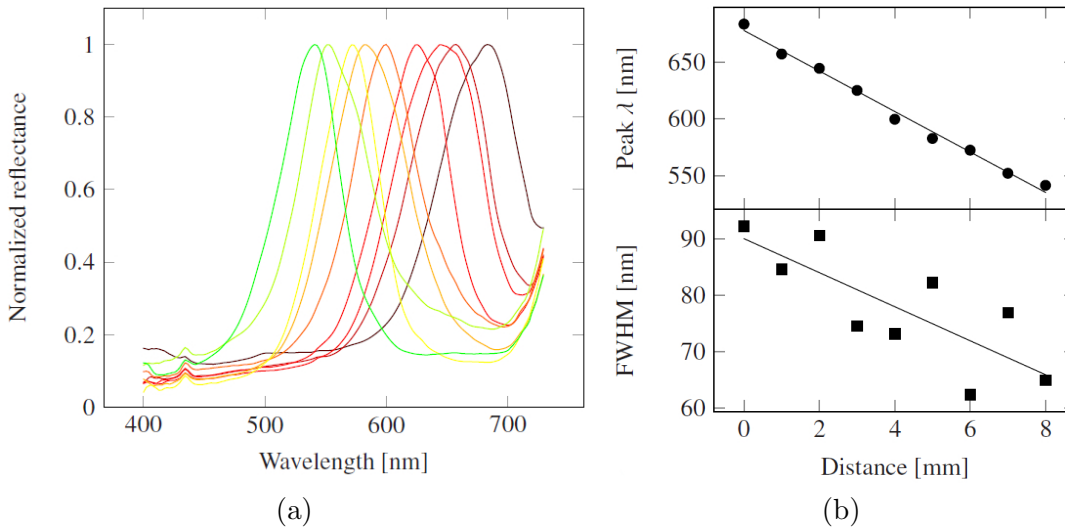
Figure 2.10: (a) Reflection spectra as a function of wavelength for different points along the length of the setae. (b) Peak reflected wavelength and FWHM of the reflection band at different points along the length of a setae. There is a clear decrease in both values as spectra are collected from the root of the setae to the tip. Data courtesy of T. Trzeciak [58]

present which displays a square array of nano rods across the width of the barbule. Longitudinal cross-sections reveal the structure is homogenous in the third dimension, down the length of the barbule. The 2D photonic crystal combined with the macroscopic curvature of the barbules leads to the conclusion that the two work together to produce brilliantly coloured, less angle-dependent blue and yellow feathers

Kientz et al. [60] found a 2D photonic crystal that is produced, not by one organism, but by a collection of many bacteria. The arrangement of the bacteria, *Cellulophaga lytica* as a group produced a quasi-ordered hexagonal array of rods. A glitter-like green colouration was observed on pure *C. lytica* colonies with a red and blue colours found at the outer edges of each colony. However, at a different illumination angle the peripheral colours changed from red and blue to green, and the green central areas became blue, an obvious indicator of structural colour. Unpublished data from Kientz et al. reveals that the structure responsible for the iridescent nature was found to be attributed to the geometry of the way the bacteria sit together. The bacteria are elongated 'cigar-like' cells which stack together to form a quasi-ordered hexagonal array. The periodicity of the array causes the discrete diffracted modes that are reported to reflect from the amalgam structure.

As with 1D photonic crystals, such as multilayers, 2D photonic crystals also display

(a)

(b)

(c)

(d)
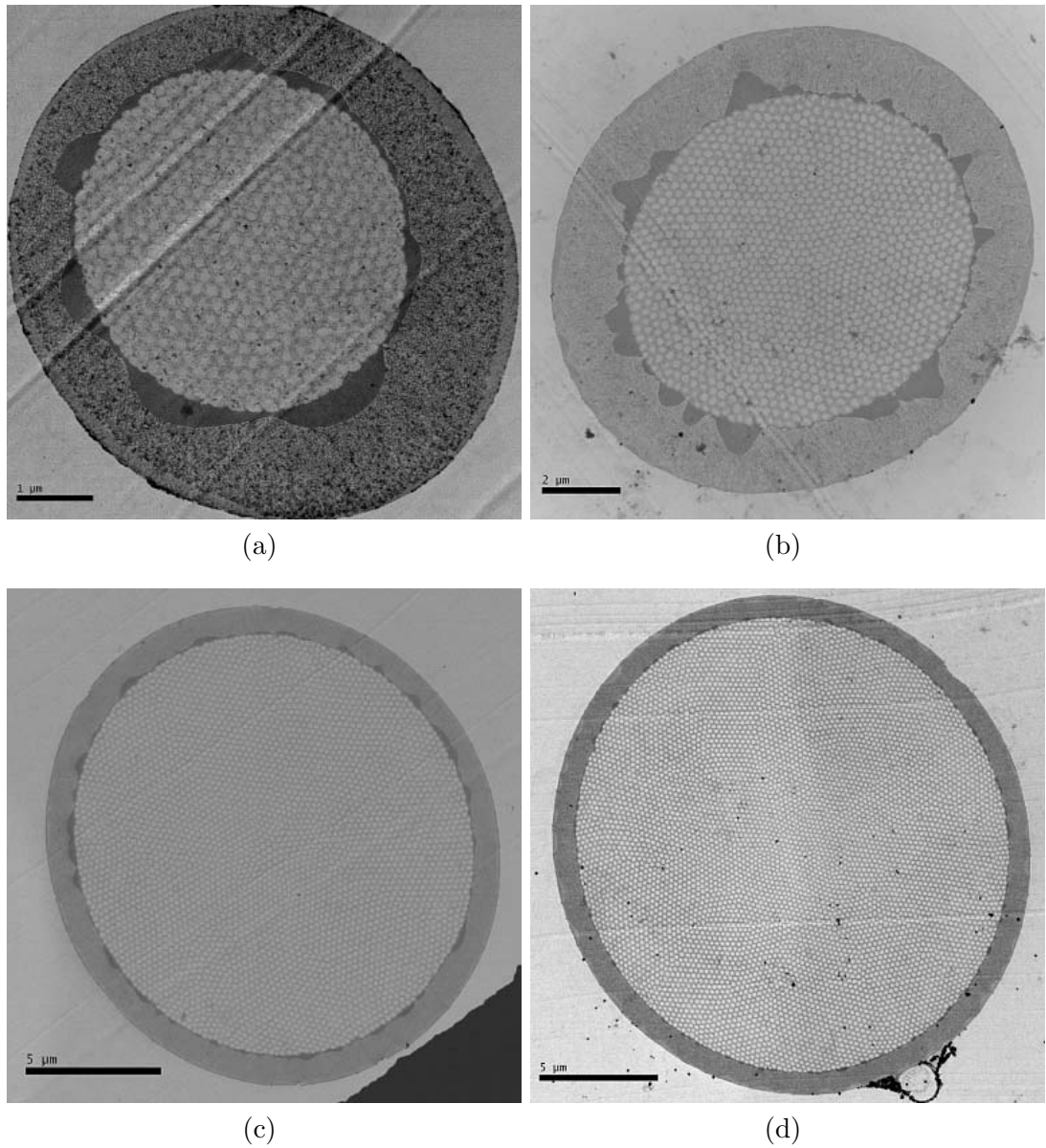
Figure 2.11: (a) - (d) TEM cross-sections at different points along the length of the scale, showing how the geometry of the 2D photonic crystal varies. Scale bars: (a) 1 μm, (b) 2 μm, (c) and (d) 5 μm. TEM micrographs courtesy of T. Trzeciak [58]

iridescent structural colours. The major difference is that there is a periodicity of a 2D crystal in any direction within a plane as opposed to the 1D case where there is only a periodicity in one dimension. This means that, within the plane of periodicity, there is a higher array of angles that will reflect a particular wavelength within the band-gap. This is especially useful with long thin structures such as feather barbules and setae where the structure can be viewed from more angles, unlike butterfly scales which are generally only viewed from the top side.

2.3 3D photonic crystals found in nature

Morris reported that *Callophrys rubi*, commonly known as the Green Hairstreak butterfly, produced an iridescent green colour appearance resulting from a 3D photonic crystal [61]. Morris reports a 3D photonic crystal to be responsible for the green colouration exhibited by *C. rubi*. It is suggested that the crystal has a cubic nature and strengthens this theory using theoretical data, showing a good agreement in peak wavelength of the structure. Electron microscopy is used to confirm that the cubic photonic crystal is poly-crystalline in nature with domain sizes on the order of microns. The advantage of differently oriented crystal grains is theorised to suppress iridescence even under diffusely illuminated conditions, giving the overall structure a uniform colour appearance.

Four different butterflies (including the previously mentioned *C. rubi* butterfly), all incorporating 3D photonic crystals in their scale structures were compared by Poladian et al. (2009) [62]. The four species were *Parides sesostris*, *T. imperialis*, *C. rubi* and *M. gryneus*. A TEM investigation of the corresponding colour producing structures reveals that all three butterflies exhibit photonic crystals with periodicities in all 3 spatial dimensions. The structures are topologically similar and they also share very similar dimensions. The differences between the four structures are the thickness of the 3D photonic section, the domain size of single crystals and also accompanying structures such as the ridges found on the top side of *P. sesostris* and *T. imperialis*. Poladian concluded that iridescence suppression in butterflies can be achieved in multiple ways. Poladian adds that the ridge structure of *P. sesostris* could act as a collimating structure that guides high incident angle light into the photonic crystal at normal incidence. It is stated that it could also be used to produce a higher randomisation of light which is incident at any angle, thereby suppressing iridescence, a completely contrary method to the first method suggested.

Pouya et al. (2012) [63] also reported an investigation into the colour production of the butterfly *P. sesostris*, also the subject of investigation for chapters 7 and 8 of this thesis. It was found in earlier work by Michielsen et al. [22] and Vukusic et al.

(a)   (b)
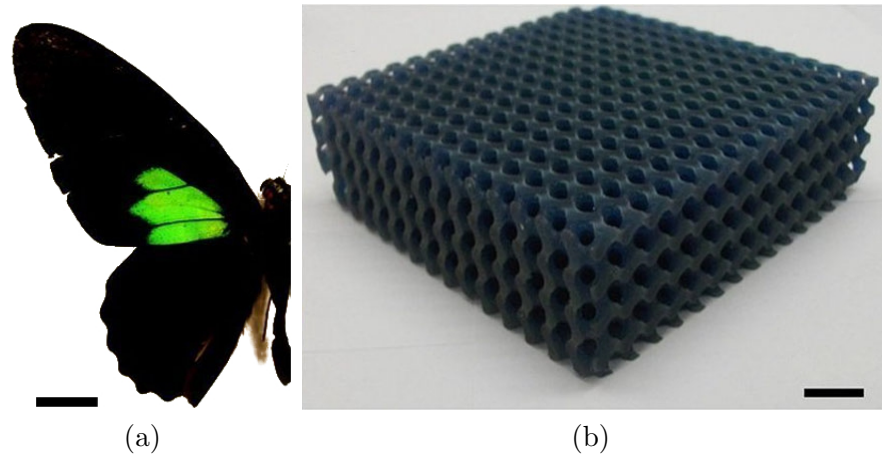
Figure 2.12: (a) Photograph of the butterfly *P. sesostris* showing the green wing patches which contain a nano-scale gyroid poly-crystal. (b) A millimetre scale model of the gyroid found in *P. sesostris* for interrogation with microwave radiation. Scale bar: (a) 10 mm. Images courtesy of C. Pouya [63].

[64] that a gyroid poly-crystal lies in the centre of all the green wing scales. In order to characterise the gyroid structure in detail, the structure was synthesised on the millimetre scale using 3D rapid prototyping techniques. The millimetre scale replica had a lattice constant of 7 mm and was fabricated from a polymer with a similar refractive index as the natural, optical scale crystal. The larger scale of the crystal meant that, in order to get the same dispersion plot as the natural structure, the illuminating wavelengths also had to be scaled up. Microwave radiation was chosen as the appropriate regime for this investigation as this structure, in theory, should have the same characteristics in the microwave regime, as the natural gyroid would in the optical regime.

The results indicated that the gyroid structure of *P. sesostris* exhibits an optimised optical character. An investigation into varying the filling fraction (figure 2.13) revealed that the band-gap width is at a maximum for the filling fraction found in the natural gyroid crystal (40%). This result indicates that the process of natural selection has led to an optimised design since a large band-gap promotes the angle-independent nature of the scales.

Wilts et al. [1] recently reported about the pigment, present in the green wing scales of *P. sesostris*. The pigment was analysed by immersing the scales with index matching fluid to remove the structural colour appearance. Using this method it was them simple to analyse the pigment using transmission spectra, which revealed a maximum in optical absorption at approximately 395 nm. The pigments function was reported to act as a
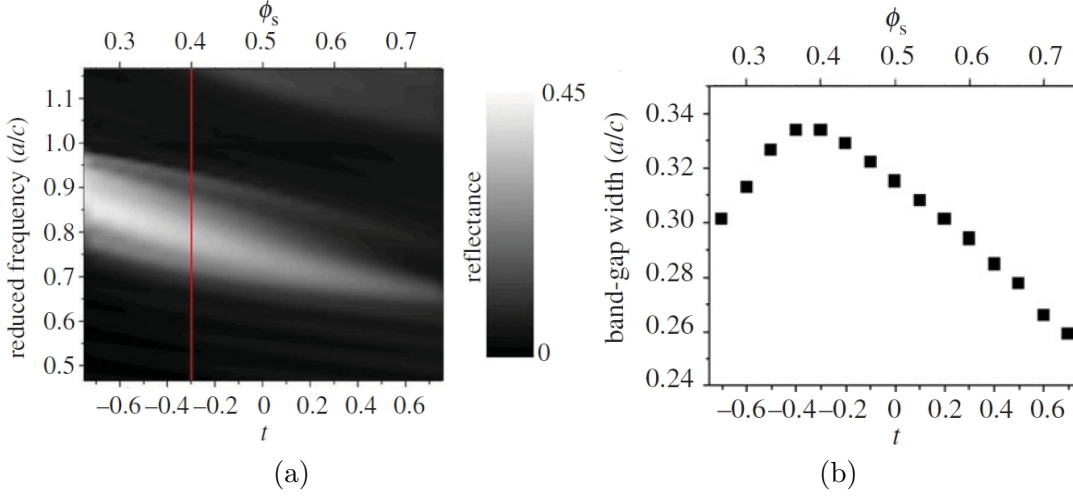
Figure 2.13: (a) Reflectivity as a function of filling fraction (x-axis) and reduced frequency (y-axis), where a is the lattice constant of the structure and c is the speed of light in a vacuum. The value t is a variable in the equation of the gyroid surface that determines the filling fraction of the solid material, shown here as ϕ_s. This graph shows how the normal incidence reflection spectra changes with an increasing filling fraction of the solid material in the gyroid. The red line shows the result for a 40% filling fraction, which happens to be the value that produces the widest band-gap. It is also the value of filling fraction that the *P. sesostris* butterfly exhibits in the gyroid part of the wing scales. (b) A graph showing band-gap width as a function of filling fraction. The peak in width can be seen to occur for the filling fraction value of approximately 40%. This value is the value of filling fraction for the natural, optical gyroid found in the green wing scales of *P. sesostris*. Data courtesy of C. Pouya [65].

long-pass filter, suppressing the blue and UV wavelengths from the reflection spectra, leaving a narrow range of green wavelengths to be reflected.

Pouya et al. (2011) [65] also discovered the origin of two different coloured bands on the elytra of the weevil *Eupholus magnificus*. They reported that the yellow and blue coloured bands exhibit very angle independent colours (figure 2.14).

Normal incidence reflection spectra from single yellow and blue scales are shown in figure 2.15. These spectra show that the yellow scales have a relatively saturated colour with a reflectance maximum at approximately 600nm. The blue scales, however, exhibit a much less saturated, more broadband peak at approximately 420 nm in wavelength. This result indicates that two different scattering mechanisms are at play.

SEM micrographs (figure 2.16) reveal that the angle independent colours are produced in two different ways. The yellow colouration seems to be a pointillistic colour mixing effect due to differently orientated,highly periodic photonic crystals. The blue

(a)

(b)   (c)
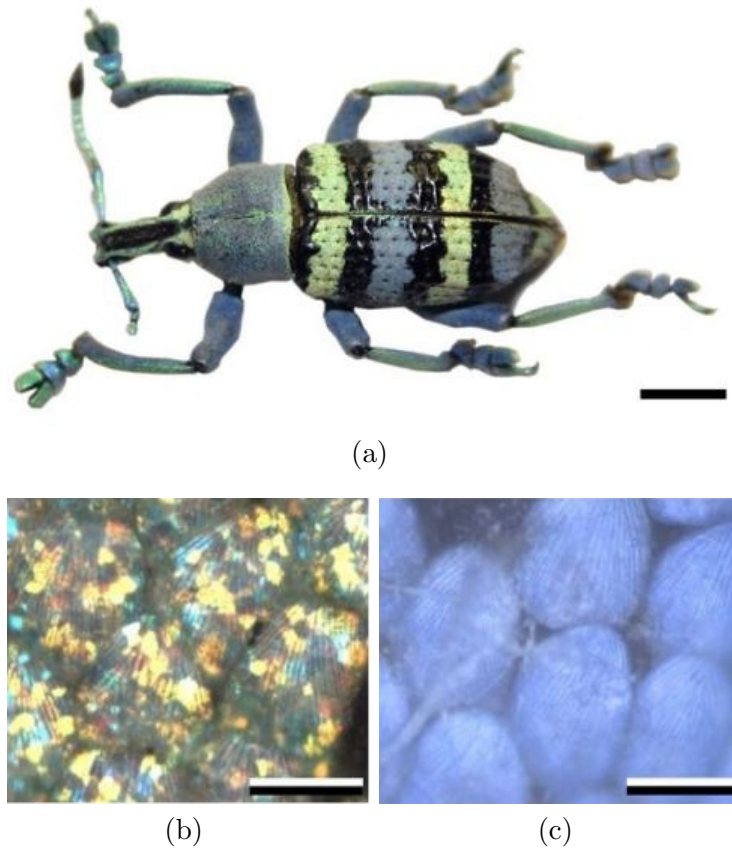
Figure 2.14: (a) Photograph of the weevil *E. magnificus.* The regions of interest that were reported are the yellow and blue, angle-independent stripes on the weevil's elytra. (b) An optical micrograph of the yellow scales, revealing that the yellow colour is the result of pointillistic mixing of several different colours. (b) An optical micrograph showing the blue scales, which have a homogenous colour. Scale bars: (a) 4mm, (b) & (c) 50 μm. Images courtesy of C. Pouya [65].

scales, however, appear to comprise a quasi-ordered photonic crystal that exhibits very little order and no clear crystal grain boundaries. The lack of long range periodicity means that the structure will reflect light much more diffusely.

Fast Fourier transforms (FFTs) (figure 2.17) of the structures found in the SEMs show that the yellow scales exhibit a highly ordered structure, reported to be inverse opal in nature. The blue scales, however, give the response of, not a completely disordered structure, but that of a close range, quasi-ordered crystal. This is attributed to the fact that a completely disordered system would show no features in an FFT image (see chapter 4, figure 4.12 for more information on FFTs), but a structure with close range order will show a circle-like feature as can be seen in figure 2.17(b). The circular
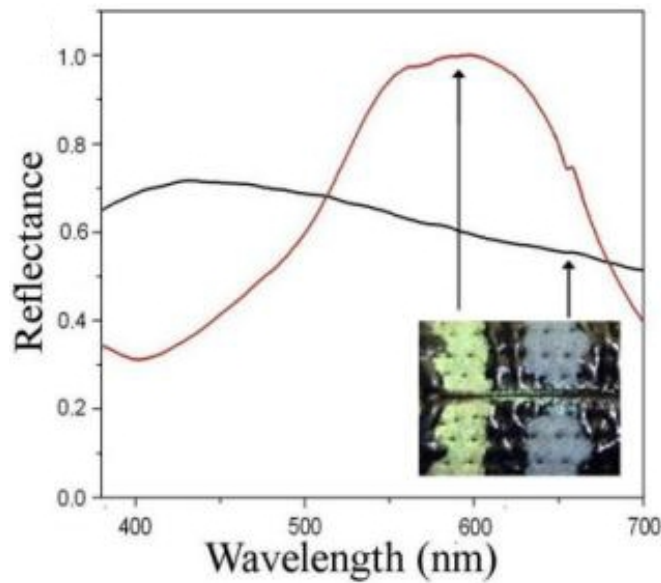
(a)

Figure 2.15:   Reflection spectra from the yellow and blue scales of the weevil *E. magnificus*. The yellow scales show a more saturated colour, an indication of high structural order of the photonic crystal. The blue scales appear to exhibit a far more broadband, less saturated colour, hinting at a lower level of order. Data courtesy of C. Pouya [65].
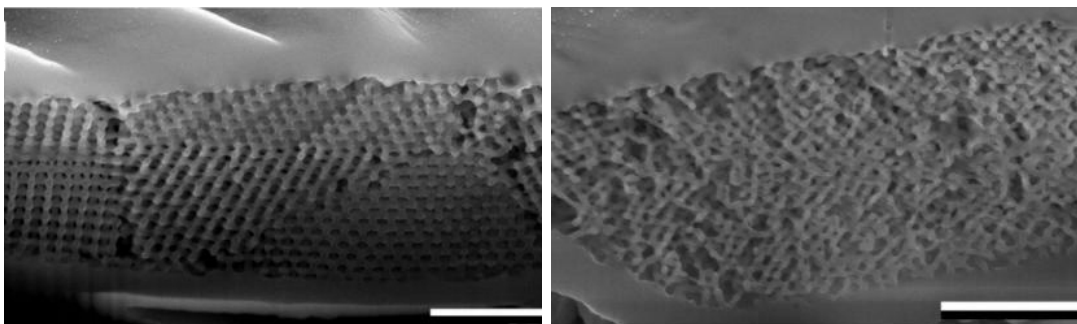
(a)   (b)

Figure 2.16:   (a) and (b) SEM micrographs of cross-sections through the yellow and blue scales of *E. magnificus*, respectively. The yellow scales exhibit differently oriented photonic crystals with high order, whilst the blue scales exhibit a quasi-ordered system. SEM images courtesy of C. Pouya [65].
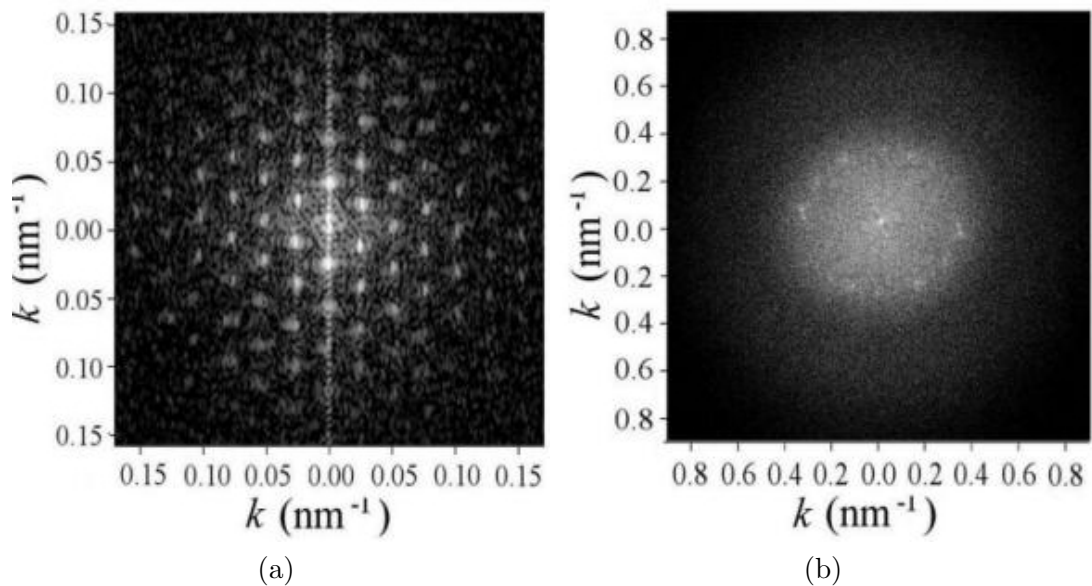
Figure 2.17: (a) A fast Fourier transform of an SEM cross-section through the yellow scales of *E. magnificus* (figure2.16(a)). The discrete features with a hexagonal pattern indicate the presence of a highly ordered structure. (b) An FFT of an SEM cross-section through one of the blue scales (figure 2.16(b)). The circular pattern with no directionality indicates the presence of a quasi-ordered photonic crystal structure. Data courtesy of C. Pouya [65].

feature also indicates that there is no preferred direction of reflection, hence giving rise to the angle independent nature of reflection.

E. magnificus shows examples of both ordered and quasi-ordered structures that produce evolutionary advantageous colour appearances. Quasi-order refers to a system that is not completely ordered, but is also not completely disordered, therefore retaining some colourful properties. If we go a step further we also find that completely disordered systems can produce an optical appearance which also offers a selective advantage. Examples of such structures are shown in the next section.

2.4 Disordered structures in nature

It has been shown that some non-periodic structures in nature scatter light so efficiently that they produce brilliant whiteness. Luke et al. [29] reported the naturally achieved ultra-whiteness of three beetles, *Cyphochilus*, *Lepidiota stigma* and *Calothyrza margaritifera* (figure 2.18). The whiteness obtained in the *Cyphochilus* beetle [35] is a characteristic of a system that is only 5 μm thick, an order of magnitude less than

the synthesised structures found in white paper. The structure responsible for the natural brilliant whiteness is embedded in scales that cover the head, body and legs of the *Cyphochilus* beetle. The broadband scattering structure comprises an envelope containing a mesh of interconnecting cuticular filaments that have a diameters of approximately 250 nm (figure 2.18(e)). This aperiodic array of filaments with low absorption gives the beetle the property of multi-wavelength scattering, which is required for brilliant whiteness without the aid of fluorescenct whitening. Standard white paper generally makes use of fluorescent whitening materials to make a sheet of paper look whiter than it actually is. This fluorescence effect in paper can be seen in figure 2.19 as an absorption dip below 400 nm and an emission peak at approximately 430 nm.

So the question was raised, how does this aperiodic structure produce a more efficient scattering structure than the scattering structures found in white paper coatings? The result found by Luke et al. [29] was that the structure found in the beetle is highly optimised for three individual parameters; filament thickness, spacing and volume filling fraction. The scattering filaments have a mean diameter of 244 ± 51 nm. The typical spacing between filaments was found to be 580 ± 120 nm. The mean filling fraction was found to be $68 \pm 7\%$. Optical spectroscopy confirmed observations of the broadband scattering structures, the spectrum taken showed a flat, broadband reflectance for the optical regime. Measurements of the beetles absolute reflection values give a response only 10 % less than that of typical white 80 gsm paper, but for a thickness of less than a tenth of the synthetic system. This result shows that there is a great level of optimisation for these structures, a level that we are still aspiring to achieve for the pupose of maximising whiteness and also cutting down on material costs.

Luke et al. also found a white producing structure on the wings of the male Japanese cabbage white butterfly, *Pieris rapae crucivora* [66] pictured in figure 2.20. The female cabbage white exhibits strong reflection for all optical wavelengths and also UV wavelengths, the male however has a strong absorption associated with the UV part of the spectrum and carries the same strong reflectance as the female over the optical regime. Due to the sexual dichroism, it is theorised that this difference is associated with a sexual communication selective advantage. The UV absorption was found to be due to an array of pterin beads which act as absorption centres for the UV light. Not only is that the case but the pterin beads are theorised to also act as scattering centres for optical wavelengths as a significant reduction in reflectance is observed after removal of the pterin bead array (SEMs show the varying level of pterin bead removal in figure 2.21). The effect of both the UV absorbing and optical scattering functions are evident from the data shown in figure 2.22 as a dip in reflection is observed for wavelengths below 450 nm for the samples that have not had the pterin beads removed. As more beads are removed (SEMs in figure 2.21) the blue wavelengths are reflected more and

(a)

(b)   (c)   (d)

(e)   (f)   (g)
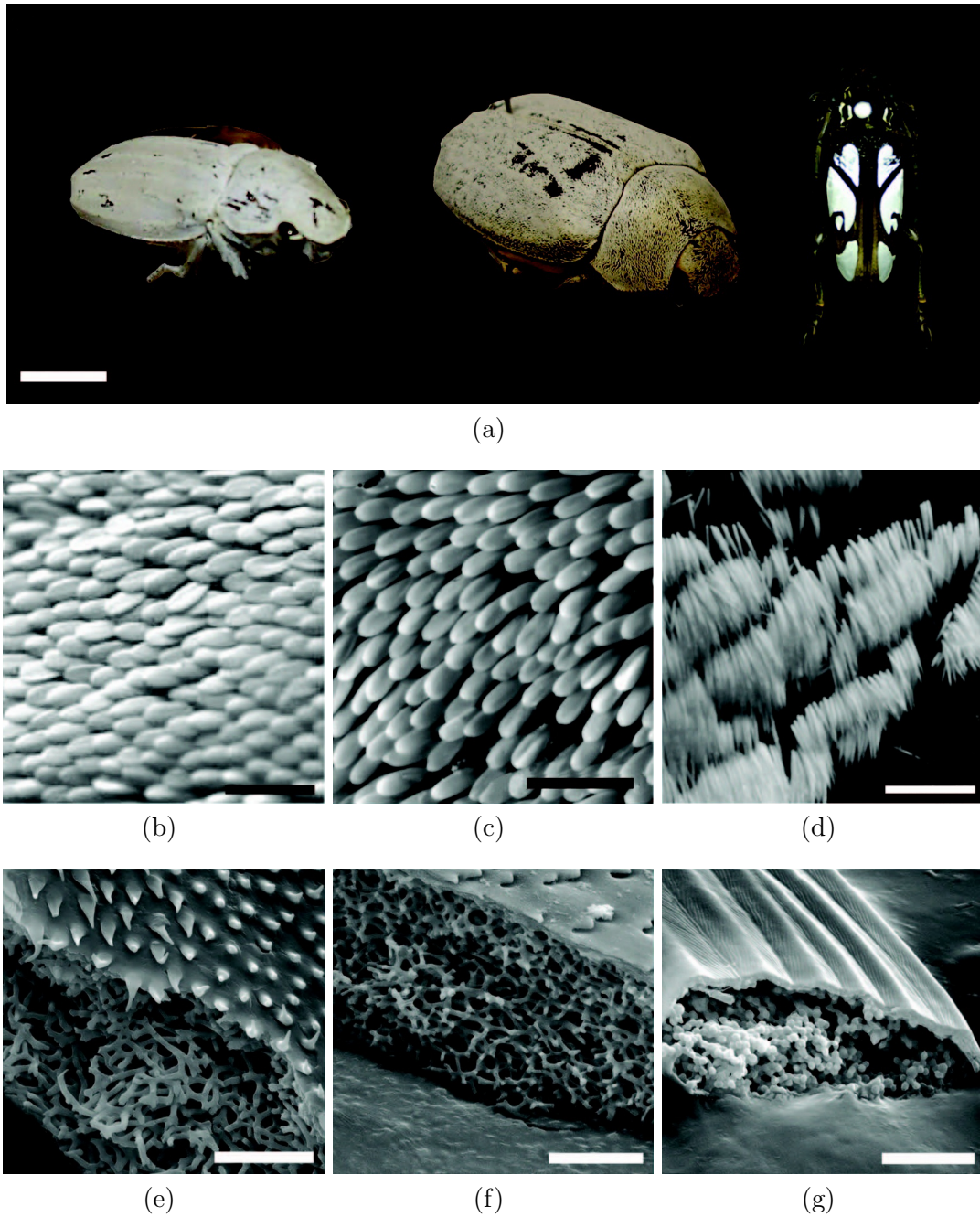
Figure 2.18: Scale bars: (a) Photographs of three ultra-white beetles named *Cyphochilus*, *L. stigma* and *C. margaritifera*. (b-d) Optical micrographs of ultra-white scales of the three beetles shown in (a), respectively. (e-h) SEM cross-sections of the disordered stuctures embedded within the scales shown in (b-d), respectively. (a) 1 cm, (b-d) 500 μm, (e) 3 μm, (f) 5 μm and (g) 4 μm. All images courtesy of S. Luke [29]
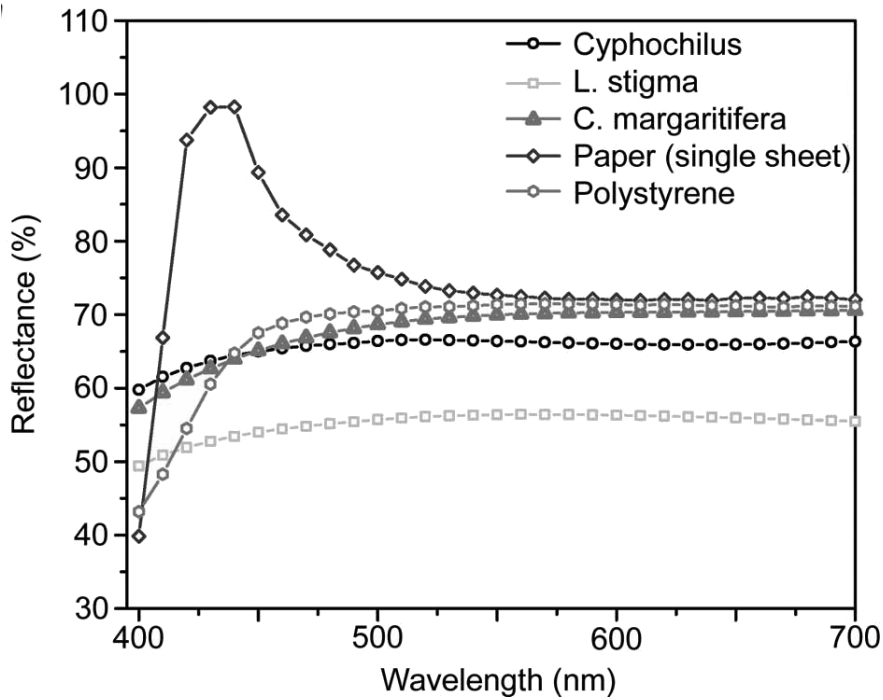
Figure 2.19: A graph showing the total reflected light as a percentage of the incident light from the elytra of the three ultra-white beetles as a function of wavelength. These levels of reflectance are comparable to the spectra obtained from standard 80 gsm white paper and also polystyrene. Data courtesy of S. Luke [29]

reflection at higher wavelengths decreases making the overall spectra more broadband in character.

Vigneron et al. reported a structurally coloured white system contained within filamentary hairs on the edelweiss plant, *Leontopodium nivale alpinum* [67]. Reflection spectroscopy of the white edelweiss bracts show a fairly constant 60% reflectance over most of the optical regime. There is a large dip in reflectance, however, for wavelengths under 400 nm. This is reportedly because the plant absorbs this part of the spectrum, as transmission measurements do not show high levels of UV light either. The whiteness appears to originate from filamentary hairs that are about 10 μm in diameter. Upon each hair there are sub-micron fibres that have a diameter of 180 nm. These fibres lie parallel to each other and run down the length of the filaments. Arranged in this way they produce a diffraction grating structure which is theorised to protect the plant from harmful UV rays. This is achieved due to the grating allowing UV radiation to be guided parallel to the surface of the filaments and easier coupling to guided modes using the grating of sufficiently small pitch. An industrial application to anti-ultraviolet solutions

Figure 2.20: .Optical micrograph of the male *P. rapae* butterfly showing a overall white appearance. Image courtesy of S. Luke [66].

is suggested. The edelwiess plant is one of few reported systems in floral species that exhibits a structural colouration. In the next section a few more examples of a few of the known structurally coloured floral systems is presented.

2.5 Structural colours in the Plant Kingdom

Whilst iridescence in insects is very common, in the plant kingdom examples are quite rare [28]. Generally in the plant kingdom, plants are quite commonly green due to the chlorophyll content of the leaves [18, 68, 69]. The chlorophyll absorbs blue and red light and scatters the rest, which is largely the wavelengths of light associated with the colour green. The green colour is fairly angle independent due to the pigment's isotropic scattering of the non-absorbed wavelengths. However, a few cases in the literature report some plants, especially plants with blue appearances, exhibit a structural colouration [18, 45, 68, 70, 71, 72]. A sample of those reports are described briefly here.

Graham et al. [28] reported on the structural colours of two neotrpical ferns and hypothesised the possible function. Within the leaves of *Danaea nodosa* they found, using TEM imaging, a multilayer comprising 18-30 layers of alternating electron-translucent and electron-opaque layers of thincknesses d=84 $\pm$ 3 nm and d=49 $\pm$ 10 nm, respectively. This multilayer was found on the abaxial side of the adaxial epidermal cell wall.
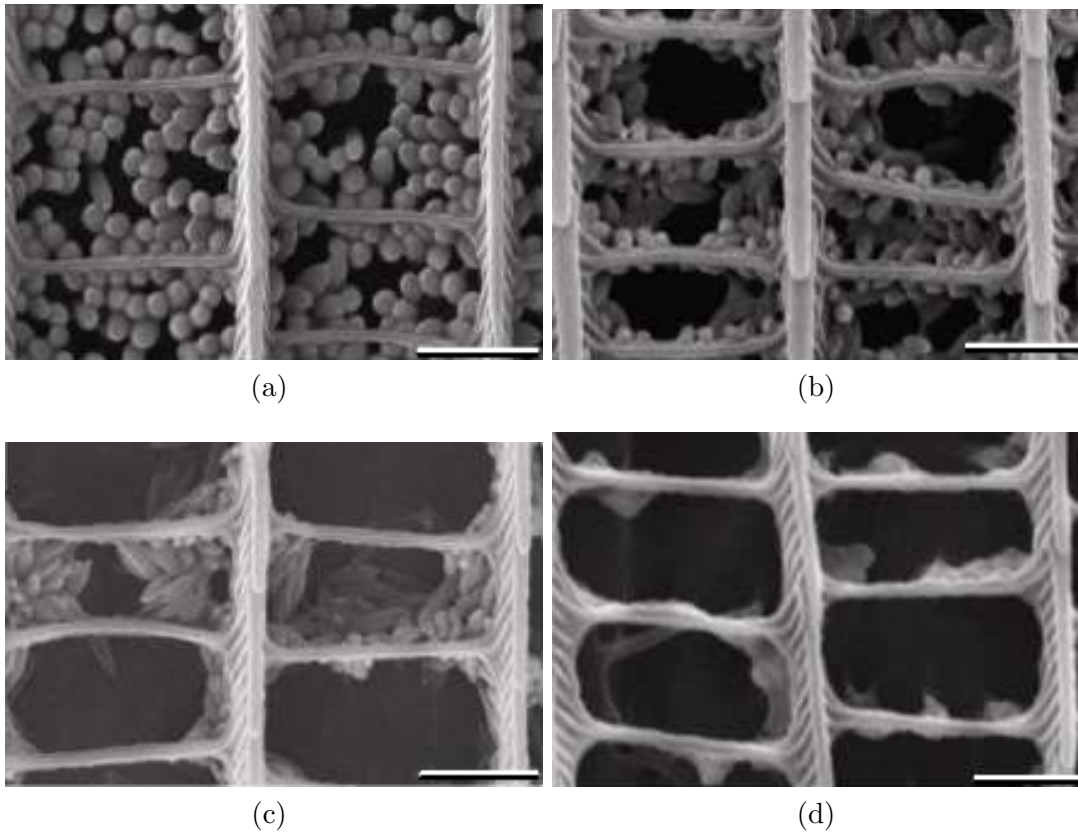
Figure 2.21: SEM images of a section of the male *P. rapae* wing scales both (a) untreated and also after (b) 10 seconds, (c) 30 seconds and (d) 60 seconds of NH_4OH immersion. Near complete removal of pterin beads is observed after only a minute of immersion. Scale bars: (a-d) 1 μm. SEM images courtesy of S. Luke [66].

The multilayer system was found to have a reflectance peak at 480 nm, in addition to the 550 nm reflection peak due to the chlorophyll. In the same paper they also reported the structural colour system in the leaves of *Trichomanes elegans*. The alternating layer thicknesses were found to be 91 nm for the electron opaque layers and 86 nm for the electron transluscent layers. This thin film system was reported to add a 530 nm reflection 'shoulder' to the standard 550 nm reflection peak of chlorophyll. The selective advantage of these plants is suggested to be linked to the shaded habitat that these plants naturally grow in.

Thomas et al. [68] made an investigation into tropical understory plants that have a four layer optical interference system in the top layer of the plant leaves. The plant investigated in the report was *Selaginella willdenowii*, a type of fern. TEM cross-sections through the leaves reveal a four layer thin film interference system dimensions
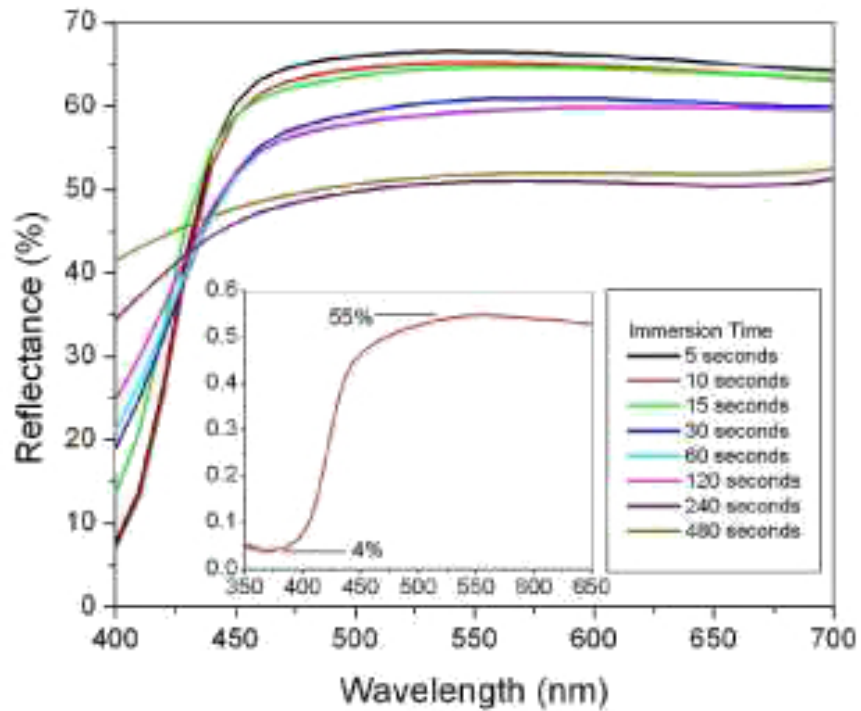
Figure 2.22: Reflectance spectra of the male *P. rapae* dorsal wings both untreated and also after increasing times of NH_4OH immersion, a process which removes the pterin beads from the scale structure. A decrease in optical reflectivity is observed as more pterin beads are removed and an increase in UV reflectance is observed, indicating decreasing absorption of these frequencies. Data courtesy of S. Luke [66].

of alternating thicknesses of 66 nm and 55 nm. This system exhibits a peak in specular reflection at 430 nm for an angle of incidence of 16°. These ferns are usually found in the dark, shaded understory of the rain forests, it was theorised that the blue-light reflecting multilayer protected the plant from flashes of sunlight produced by trees in the canopy swaying in the wind. The short, intense exposure to direct sunlight could cause photoinhibition, which is reported to be the hindrance of the photosynthesis process due the chlorophyll being inundated with sunlight. They also report that the blue-light reflectivity could protect the leaves from damage due to the intense flashes of sunlight in an otherwise shaded environment.

Iridescent colours in floral species can have functions other than protection from the sun and warding off herbivores, Vignolini et al. describe a fruit which displays an intense blue structural colour with the theorised selective advantage of attracting seed dispersing birds [73]. The *Pollia* fruit grows naturally over much of the African

tropical region where it is likely to be collected by birds either for their mating displays or because the fruit mimics nutritious blue berries that are found in the same region. Optical micrographs of the *Polia* fruit show that there are many cells that reflect mainly blue wavelengths, but some cells reflect green or even red. From a distance the fruits have a pointillistic colour mixing effect due to the resolution of our eyes, so we only see blue. The fruit displays, what appears to be a multilayer with a helicoidal arrangement causing the fruit to exhibit optical activity. This means that the fruit has an amount of circular polarisation selectivity. Whether or not the optical activity has a selective advantage or not is undetermined.

The fruit of *Margaritaria nobilis* is a very simliar sample to the *Polia* fruit. Both are located in hot climates in the southern hemisphere, and both species are theorised to exhibit their blue colouration for the selective advantage of attracting birds as seed dispersing vectors. A highly detailed investigation of *M. nobilis* is presented in chapter 5. A synthetic system inspired by the fruit is also presented.

2.6   Conclusion

Whilst not the most common form of colour production in nature, structural colour appears to play a significant role or function in many natural systems. These roles include iridescence, diffraction, ultra-brightness, polarisation and anti-reflection. It also appears that the process of natural selection has produced some wonderfully optimised light scattering structures, a result of hundreds of millions of years of competition to survive. Many different species in nature are shown to exhibit structural colour appearances and their selective advantages are discussed. Such creatures include many butterflies, beetles, birds, and a few floral examples also exist. It has been shown that a myriad of photonic structures for different functions exist, adding to the diversity of natural colour displays. A few examples of the more common functions include camouflage, sexual communication, protection from intense sunlight and seed dispersal. Many of the designs will have relevant physical applications in technology, industry and aesthetics. Some of these examples include, angle-independent, vivid colourations, optical computing and anti-reflective coatings. It is, therefore, important to keep extracting photonic design ideas from nature, a process which has the ability to propagate the fields of optics and electromagnetics. Taking such ideas from nature and producing synthetic designs to further our scientific toolbox is known as biomimicry.

Chapter 3

Theory

3.1 Introduction

To fully understand how natural systems produce bright and interesting structural colours, one must first have a good understanding of the laws of electromagnetism. The physics underlying the optical qualities of photonic crystals are largely governed by Maxwell's equations of electromagnetism (we will discuss these in more detail later), as we are dealing with the way in which light and matter interact [74, 75].

As electromagnetic radiation impinges on an interface between two different materials, a fraction of the incident radiation is reflected and the rest, assuming a lossless system, is transmitted. If there are multiple interfaces at play, then multiple reflections can occur. Each photon exhibits a phase, which is dependent on the length of the path travelled by that photon. The reflected rays will then interfere with each other either constructively or deconstructively, depending on the phase relations between the photons. If the electormagnetic waves of a particular wavelength constructively interfere, then those waves are reflected. However, if the radiation destructively interferes then the radiation is generally transmitted. The phase difference between photons will depend on the dimensions of the structure, the wavelength of the incident radiation and also the angle of incidence as this will have an effect on the optical path difference (the physical distance the photon travels multiplied by the refractive index). This is the basis of how structural colours are produced and from these simple concepts, a wide range of interesting optical phenomena arise, some of which will be discussed in this chapter.

3.2 Reflection and refraction at optical interfaces

Consider a ray of light incident on a perfectly flat and smooth interface between two materials that differ only by how fast light travels through them (fig 3.1). The ratio of the speed of light in a vacuum to the speed of light in the material is known as the refractive index, which shall be denoted in this thesis by the symbol: n. The two materials in question have refractive indices of n_1 and n_2. The light ray will partially reflect from and partially transmit through the interface between the materials depending on their refractive indices and the angle of incidence, θ_i, defined as the angle between the incoming beam and the surface normal). In this case, a flat interface, the reflected light ray will be reflected at the same angle as the incident beam but with the opposite sign ($\theta_r = -\theta_i$) and this is known as specific angular reflection or specular reflection. The transmitted beam, however, is refracted towards the normal for the case $n_2 > n_1$ and away from the normal for the opposite case, $n_2 > n_1$. The angles in either case can be calculated from Snell's law

$$n_i \sin(\theta_i) = n_t \sin(\theta_t) \tag{3.1}$$

When analysing theoretical models of the systems found in nature it is useful, if not mandatory, to work out the electric fields in the system. The amplitudes of the reflected and transmitted fields are dependent on, not only the refractive indices and the angle of incident radiation, but also the polarisation of the electric field of the incident light. The polarisations are usually defined by their orientation to the plane of incidence. Light with an electric field vector that is parallel to the plane of incidence is known as transverse magnetic (TM) polarisation and denoted by the symbol $\parallel$. When the electric field vector is perpendicular to the plane of incidence, the light is said to be of transverse electric (TE) polarisation and denoted by the symbol $\perp$. Fresnel's reflection and transmission coefficients are used to work out the electric field amplitudes for both transmission and reflection for both polarisations (TE and TM) which are normalised to the amplitude of the incident radiations electric field amplitude.

Fresnel equations:

$$r_\parallel = \frac{\tan(\theta_i - \theta_t)}{\tan(\theta_i + \theta_t)} \quad , \quad r_\perp = \frac{\sin(\theta_t - \theta_i)}{\sin(\theta_t + \theta_i)} \tag{3.2}$$

$$t_\parallel = \frac{2\sin(\theta_t)\cos(\theta_i)}{\sin(\theta_t + \theta_i)\cos(\theta_t - \theta_i)} \quad , \quad t_\perp = \frac{2\sin(\theta_t)\cos(\theta_i)}{\sin(\theta_t + \theta_i)} \tag{3.3}$$
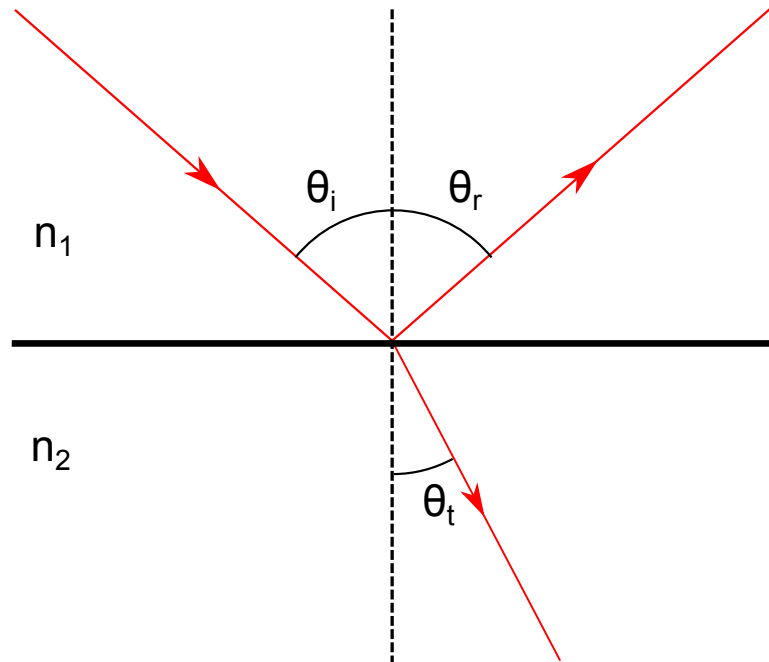
Figure 3.1: Reflection from and transmission through an optical interface with $n_2 > n_1$. From Snell's law (equation 3.1 it can be deduced that light impinging from the media with a low refractive index will refract towards the surface normal and in the opposite case ($n_1 > n_2$) the light will refract away from the normal. At a certain angle, known as the critical angle (θ_c) the light will be refracted at an angle of 90°, at and above θ_c, therefore, all light is reflected.

The intensity of reflected light, $R_{\parallel,\perp}$ is simply the square of the amplitude coefficient,$r_{\parallel,\perp}$ and the intensity for transmitted light is, $T_{\parallel,\perp} = (n_2/n_1)t_{\parallel,\perp}^2$.

These equations work for the specific cases of TE and TM polarisations. A more general case for linearly polarised light would include the angle of polarisation, ψ, with respect to the plane of incidence. The equation for reflected intensity then becomes

$$R = R_{\parallel} \cdot \cos^2 \psi + R_{\perp} \cdot \sin^2 \psi \tag{3.4}$$

From equation 3.2 it can be seen that for a certain angle of incidence the reflected electric field amplitude coefficient is 0 for TM polarisation, whereas the reflected amplitude for TE polarisation continuously increases with angle of incidence. The angle at which $r_{\parallel} = 0$ can be determined from equation 3.1. This angle is known as the Brewster angle (θ_B) and is defined by

$$\theta_B = \tan^{-1}\left(\frac{n_2}{n_1}\right) \tag{3.5}$$
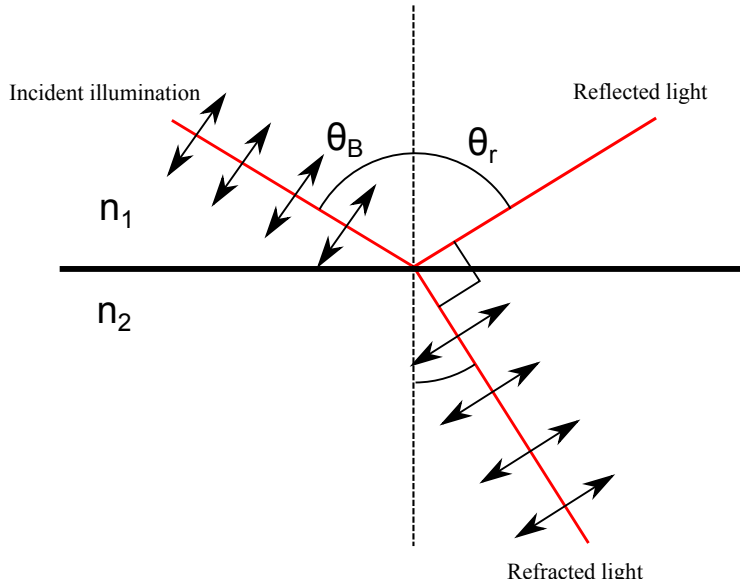
Figure 3.2: Schematic showing the physical origin of the Brewster angle. TM polarised light impinging on the interface from the side of the low refractive index media will oscillate dipoles orthogonally from the direction of transmitted light. Dipoles cannot emit radiation in the same direction as the oscillating **E** field as this would contradict the orthogonal relationship between the wave vector, **k**, and the electic field, **E**.

The physical interpretation of this phenomenon can be explained by the realisation that the reflected radiation does not simply 'bounce' off the interface but rather the radiation is absorbed and re-emitted by dipoles in the material (fig 3.2). The dipoles will oscillate in the same direction as the refracted electric vector. Therefore, the angle at which the reflected E-field amplitude equals zero is the value of θ_i that produces an angle of 90 degrees between the predicted specular reflection and the transmitted light. This is because a dipole cannot radiate energy in the direction of its own oscillation as the resultant reflected electric field would be oscillating in the same direction as its propagation which is a forbidden state [76]. Therefore, in the case where the Brewster angle condition is met, the reflected light will be completely TE polarised, which is why the Brewster angle is also known as the polarisation angle.

Another interesting phenomenon that arises from Snell's law is the angle of total internal reflection. At this angle no light is transmitted. We know from Snell's law that when light transmits through an interface with an incident medium that has a lower refractive index than the exit medium, light is refracted toward the interface normal. The converse case is also true, when light transmits from an incident medium with a higher refractive index the light is bent away from the interface normal. At a certain incident angle, the transmitted light will be 90 degrees from the normal and
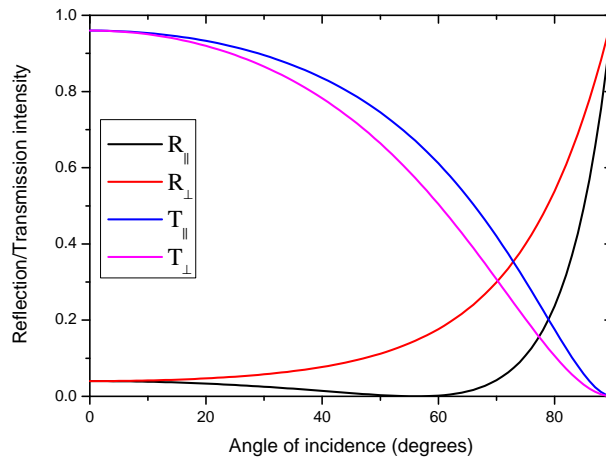
Figure 3.3: Normalised intensity of reflected and transmitted light for both TE and TM polarisations for an optical interface where $n_2 > n_1$. In this system the refractive indices are $n_1 = 1$ and $n_2 = 1.5$. This results in a Brewster angle (θ_B) of 56.31°.

hence parallel to the interface. Therefore, at this angle and above, no light will be transmitted, only reflected. Using Snell's law, the angle of incidence above which no light is reflected (the critical angle, θ_c) becomes

$$\theta_c = \sin^{-1}\left(\frac{n_2}{n1}\right) \tag{3.6}$$

3.3   Thin film interference

Structural colours rely on the reflected waves from different interfaces to either constructively or destructively interfere. For interference to occur there needs to be a mechanism for creating a path difference between rays and, therefore, a phase difference. One of the simplest systems in which such interference can be achieved is a thin film, where the thickness of the film is comparable to the wavelength of the incident light. A thin film system comprises three sections of different materials with refractive indices n_1, n_2 and n_3. Figure 3.4 shows such a system and all the possible reflections and transmissions for light to take. The notations r_{ij} and t_{ij} denote that the light has reflected or transmitted respectively from an interface with incident medium denoted i and a medium on the other side of the interface denoted j, for light propagating the other way, the converse is true, giving r_{ji} and t_{ji}. The phase differences required for interference are determined by the optical path length (OPL) each light ray takes. The

37
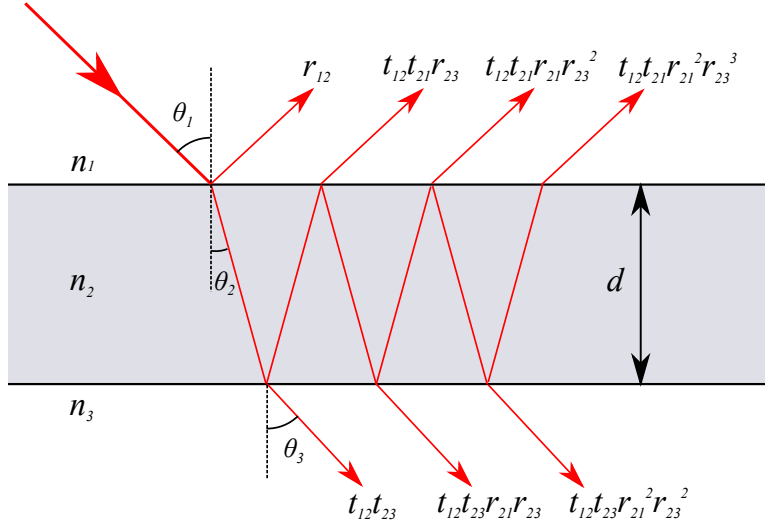
Figure 3.4: Schematic of the possible paths light can take when impinging onto a thin film. At the first interface the light can either reflect (r_{12}) or transmit (t_{12}) as discussed previously. The transmitted light will then hit the second interface where, once again, it will reflect (r_{23}) or transmit (t_{23}). The light can undergo multiple reflections within the thin film before finally transmitting back through the original interface (t_{21}) or into the third medium (t_{23}). The rays from different reflection/transmission combinations then recombine either in medium 1 or 3 and, due to the optical path difference, they will interfere, either constructively or destructively. The fractions of light that reflects and transmits at each interface are polarisation dependent and are calculated using equations 3.2 and 3.3.

path difference between the two rays denoted r_{12} and $t_{12}t_{21}r_{23}$ works out to be

$$OPL = 2n_2 d cos\theta_2 \tag{3.7}$$

The phase difference, $\Delta\phi$ can then be expressed as:

$$\Delta\phi = k \times OPL \pm \pi, \tag{3.8}$$

where k is the wavenumber in the material and the π term is included to account for the 180° phase shift incurred by reflections from a low to high refractive index interface [77]. If we set δ to be:

$$\delta = \frac{2\pi}{\lambda} n_2 d cos\theta_2, \tag{3.9}$$

then a derivation for the reflection intensity R for a system with more than one interface can be derived by firstly considering considering the reflection coefficient for such a

system, as shown below:

$$r = r_{12} + t_{12}r_{23}t_{21}e^{-2\delta} + t_{12}r_{23}^2r_{21}t_{21}e^{-4\delta} + t_{12}r_{23}^3r_{21}^2t_{21}e^{-6\delta} + ... \tag{3.10}$$

This expression can be represented as an infinite series, then using the property of such a series that $\Sigma_{j=0}^{\infty}(r)^j = \frac{1}{1-r}$ to produce the equation:

$$r = \frac{t_{12} + r_{23}t_{21}e^{-i2\delta}}{1 - r_{23}r_{12}e^{-i2\delta}} \tag{3.11}$$

By rearranging the equation and by using the Fresnel equations the coefficient for reflection amplitude becomes:

$$r = \frac{r_{12} + r_{23}e^{-i2\delta}}{1 + r_{23}r_{12}e^{-i2\delta}} \tag{3.12}$$

Using the equation for refelction intensity, $R = r^*r$, the reflection intensity for a thin film then becomes:

$$R = \frac{r_{12}^2 + r_{23}^2 + 2r_{12}r_{23}cos(2\delta)}{1 + r_{23}^2r_{12}^2 + 2r_{12}r_{23}cos(2\delta)} \tag{3.13}$$

Using a similar treatment (not shown here), the expression for the transmission amplitude coefficient can be derived, resulting in equation 3.14:

$$t = \frac{t_{12}t_{23}e^{-i\delta}}{1 + r_{12}r_{23}e^{-i2\delta}} \tag{3.14}$$

From this equation, the transmission intensity can be calculated using:

$$T = Re\frac{k_zN}{k_{z1}}tt^* \tag{3.15}$$

Using the equations for R and T one can now calculate the optical properties of a system with more than one optical interface.

3.4 Dispersion

The dispersion relation is defined by the relationship between energy and momentum of a system. In electromagnetism it is defined by the effect of a given material on the phase velocity of electromagnetic radiation. For a vacuum the linear dispersion relation is defined by

$$\omega(k) = ck, \tag{3.16}$$

where ω is the angular frequency, c is the speed of light in a vacuum, k is the wavenumber. For a bulk material, the linear dispersion has to be scaled to account for the shift in phase velocity, the scaling factor is simply the refractive index n which is equivalent to the square root of the permittivity ε. This then gives

$$\omega(k) = \frac{ck}{\sqrt{\varepsilon}}, \tag{3.17}$$

where ε is the permittivity of the material. For many materials the permittivity of a material is wavelength dependent, in which case the equation becomes more complicated.

3.5   Photonic crystals

In solid state physics we learn that a crystal lattice of atoms or molecules can allow an electron of appropriate wavelength to propagate through the crystal without scattering, as if it were a gas allowed to move freely [78]. The wavelength at which this phenomena occurs is dependent on the dimensions of the crystal lattice. Knowledge of this phenomena allows us to design electronic devices comprising crystals tailored to manipulate the flow of electrons in a desirable manner [78]. As electromagnetic radiation also propagates as a wave, an analogy can be made [79][80][81]. Optical photons have much bigger wavelengths than electrons and therfore a much bigger crystal lattice is required. Instead of using atomic crystal lattices to manipulate the flow, we need to employ a lattice with periodicities comparable to the wavelength of light, 350 - 800 nm. A photonic crystal is any macroscopic structure that has a periodic value of permittivity as a function of distance, $\varepsilon(\vec{r})$, that therefore allows photons of appropriate wavelengths to travel freely, and other wavelengths to be forbidden from propagation. A photonic crystal can comprise periodicties in one, two or three spatial dimensions (figure 3.5), and those are dubbed 1D, 2D or 3D photonic crystals, respectively.

The Maxwell equations (Gauss's law for electric fields, Gauss's law for magnetic fields, Faraday's law and the Ampere-Maxwell law) can be expressed in the following way;

$$\oint_S \vec{E} \cdot \widehat{n} da = \frac{Q_{\text{enc}}}{\varepsilon_0} \quad , \quad \vec{\nabla} \cdot \vec{E} = \frac{\rho}{\varepsilon_0} \tag{3.18}$$

$$\oint \vec{B} \cdot \widehat{n} da = 0 \quad , \quad \vec{\nabla} \cdot \vec{B} = 0 \tag{3.19}$$

$$\oint_C \vec{E} \cdot d\vec{l} = - \int_S \frac{\partial \vec{B}}{\partial t} \cdot \widehat{n} da \quad , \quad \vec{\nabla} \times \vec{E} = -\frac{\partial \vec{B}}{\partial t} \tag{3.20}$$
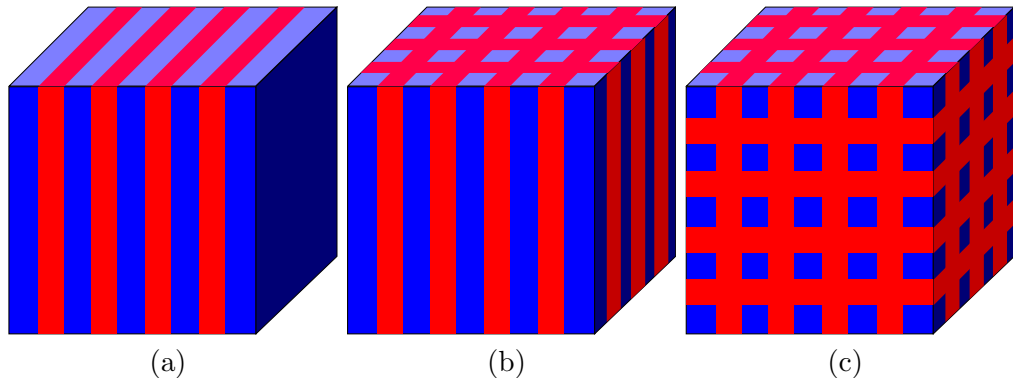
Figure 3.5: (a), (b) and (c) show schematics of simple 1D, 2D and 3D photonic crystals, respectively. The periodic red and blue colours represent the periodic arrangement of materials with different refractive indicies.

$$\oint_C \vec{B} \cdot d\vec{l} = \mu_0 \left(I_{\text{enc}} + \varepsilon_0 \frac{d}{dt} \int_S \vec{E} \cdot \hat{n} da \right) \quad , \quad \vec{\nabla} \times \vec{B} = \mu_0 \left(\vec{J} + \varepsilon_0 \frac{\partial \vec{E}}{\partial t} \right) \qquad (3.21)$$

If we take the differential forms of equations 3.20 and 3.21 and we can substitute $\vec{B} = \mu \vec{H}$ and $\vec{D} = \varepsilon_0 \varepsilon(\vec{r}) \vec{E}$. Now we have the two equations in terms of electric and magnetic fields

$$\vec{\nabla} \times \vec{E}(\vec{r}, t) + \mu_0 \frac{\partial \vec{H}(\vec{r}, t)}{\partial t} = 0 \quad , \quad \vec{\nabla} \times \vec{H}(\vec{r}, t) - \varepsilon_0 \varepsilon(\vec{r}) \frac{\partial \vec{E}(\vec{r}, t)}{\partial t} \qquad (3.22)$$

where

$$\vec{H}(\vec{r}, t) = \vec{H}(\vec{r}) e^{-i\omega t} \quad , \quad \vec{E}(\vec{r}, t) = \vec{E}(\vec{r}) e^{-i\omega t} \qquad (3.23)$$

substituting these into equation 3.21 and taking the curl followed by substituting the first equation in 3.22 to eliminate the electric fields gives

$$\vec{\nabla} \times \left(\frac{1}{\varepsilon(\vec{r})} \vec{\nabla} \times \vec{H}(\vec{r}) \right) = \left(\frac{\omega}{c} \right)^2 \vec{H}(\vec{r}) \qquad (3.24)$$

This is the master equation and can be used to find the harmonic modes, $\vec{H}(\vec{r})$, and their corresponding frequencies for a given structure, $\varepsilon(\vec{r})$.

3.5.1 One dimensional photonic crystals

The simplest case of a photonic crystal is one that has a periodicity of refractive index in only in one dimension, referred to as a dielectric stack or, more commonly, the multilayer (a multilayer schematic is shown in figure 3.6). However, the simple cases in science often make it easier to understand the more complicated concepts, as is the case here. Phenomena such as the photonic band-gap can be explained by multilayers alone. A dielectric stack, works in much the same way as a thin film, but due to not being limited to one layer, effects that were subtle in the multilayer now produce much brighter, purer (monochromatic) colour. The increase in brightness can be attributed to there being more layers and, therefore, more interfaces for each photon to reflect from. The monochromacity can be attributed to the repeated dimensions favourably interacting most strongly with the wavelengths comparable to the dimension multiplied by the refractive index. This effect can be seen quite clearly in figure 3.7, as the layer number increases, the width of the reflected band decreases and the intensity increases. A quarter-wave stack is a special case of multilayer that comprises two alternating layers with refractive indices n_1 and n_2 and thicknesses d_1 and d_2, where $n_1 d_1 = n_2 d_2$. This system can also be called be referred to in some texts as an ideal multilayer [82], however, as the term 'ideal' is ambiguous, I will be using the term 'quarter-wave stack'. In such a system, both layers will reflect the same wavelengths most strongly and therefore will have a highly monochromatic colour appearance.

In order to understand the physical origin of the photonic band-gap, it helps to observe the dispersion relation of bulk materials and multilayers (3.8). For a bulk material the dispersion relation, assuming constant refractive index, is linear. At the Brillouin zone boundary, there is only one solution to equation. However, when a periodicity in just one dimension is introduced, two solutions of the frequency are required to satisfy the equation. As can be seen in figures 3.8(e) and 3.8(f), there is no frequency which satisfies the equation within the material inbetween the two Brillouin zone edge frequencies. This gap in frequency (shown in yellow), is known as the photonic band-gap. In other words no frequency within this band is able to exist within the photonic crystal.

Figures 3.9 and 3.10 show how the electric field propagates through the multilayers with a low dielectric contrast and a high dielectric contrast, respectively. The plotted electric fields show how the waves propagate through the crystal at the frequencies which correspond to the solutions of the Brillouin zone edge. In each case the high frequency band edge is called the air band as the electric fields have anti-nodes within the low dielectric material. The low frequency band edge is known as the dielectric band as the electric fields have anti-nodes within the high dielectric material. These two

Figure 3.6: Schematic of a multilayer stack. The multiple layers in the stack provide more possibilites of reflection and therefore the reflected colours are more intense than reflections from a system with fewer layers.

modes have to have a $\frac{\pi}{2}$ phase difference between them (shown in figures 3.9 and 3.10) because the two solutions have to be orthoganol, as is the condition for standing wave solutions. The phase difference of the two solutions cause energy to be concentrated in the two different materials meaning the two solutions have different energy, hence the band-gap.

3.5.2 Two dimensional photonic crystals

Now we have looked at the simple 1D photonic crystals, we can take what we have learned and apply the physics to a slightly more complicated system, a 2D photonic crystal (figure 3.5(b)). A 2D photonic crystal has a periodicity in two spatial dimensions and is completely homogeneous in the third dimension. The addition of the second dimension of periodicity has many advantages over a simple 1D dielectric stack. For instance, the range of angles can be increased for a particular colour to be relflected. A 2D photonic crystal of the type shown in chapter 2 in *Pherusa* sp. could be used as a photonic crystal fibre, which would guide modes down a central core defect within a 2D regular array of rods.

Figure 3.7: Reflectance as a function of wavelength for a multilayer system with varying layer numbers. The two materials used to create this multilayer had refractive indices of $n_1 = 2.42$ and $n_2 = 1.38$. The thicknesses of the two layers are $d_1 = 57nm$ and $d_2 = 99nm$. An increase in the intensity and the Q-factor of reflected wavelengths can be observed for higher layer numbers. Another property which can be observed is that as the layer number goes up, the reflection intensity within the band-gap wavelengths converge to 100%.

3.5.3 Three dimensional photonic crystals

3D photonic crystals form the most complex sub group of photonic crystals. They have a periodicity in three different directions and can be far easier to design a crystal that achieves a complete photonic band gap for a given frequency range. This is due to the fact that the periodicity is in all three spatial dimensions and, therefore, the angular range over which the band-gap wavelengths are reflected is dramatically increased.

3D photonic crystals in nature are usually made from minimal surfaces of which there are several distinct types, known as Schwarz surfaces [83].
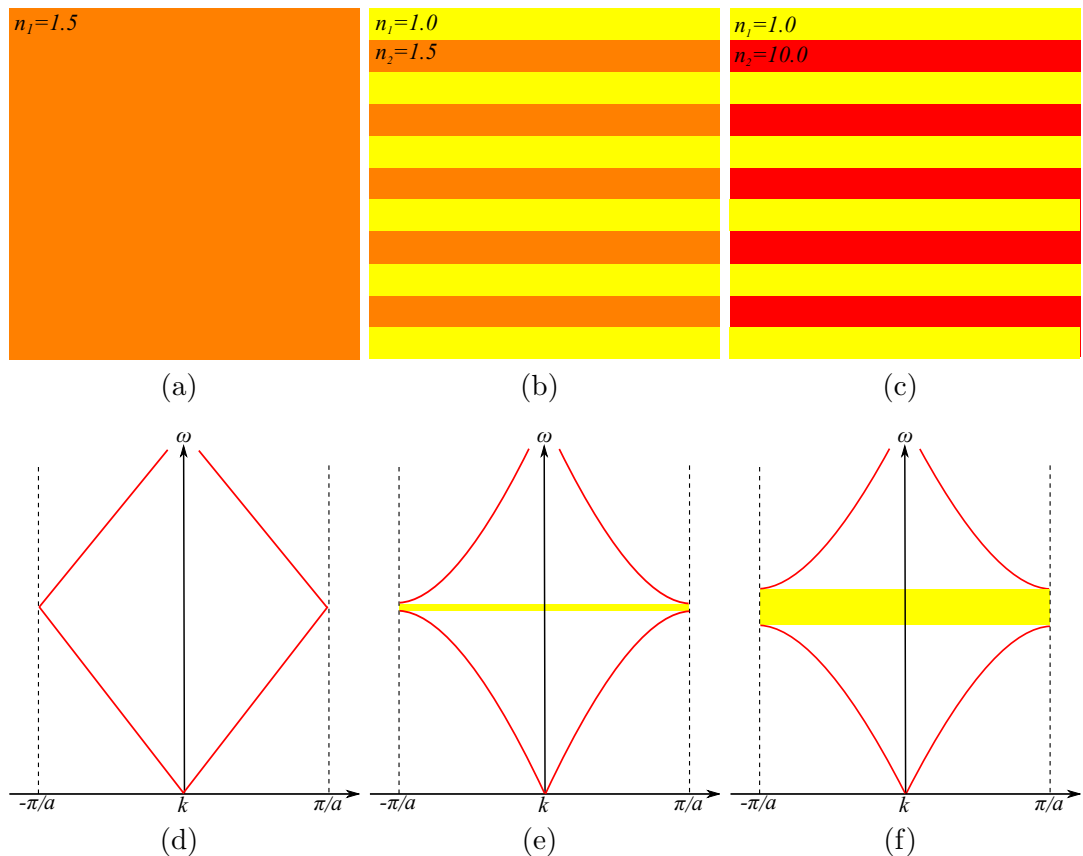
Figure 3.8:   Structural schematics of (a) bulk material, (b) a low dielectric contrast multilayer and (c) a high dielectric contrast multilayer. The first Brillouin zone dispersion diagrams associated with bulk material and the two different multilayers are shown in (d-f), respectively. The dispersion plot shown in (d) demonstrates the linear relationship between frequency and momentum in a bulk medium, given by equation 3.17. The plot shown in (b) shows the dispersion relation for a multilayer with a periodicity of 250 nm and refractive indices $n_1 = 1.0$ and $n_2 = 1.5$. The emergence of a band-gap (here shown as a yellow band) is observed. This represents the physical phenomenon which forbids the frequencies within the band-gap to propagate through the structure and hence, that light is reflected from the system. (c) The same structure as shown in (b) but with $n_2 = 10.0$, showing the effect of a higher dielectric contrast on the size of the band-gap.
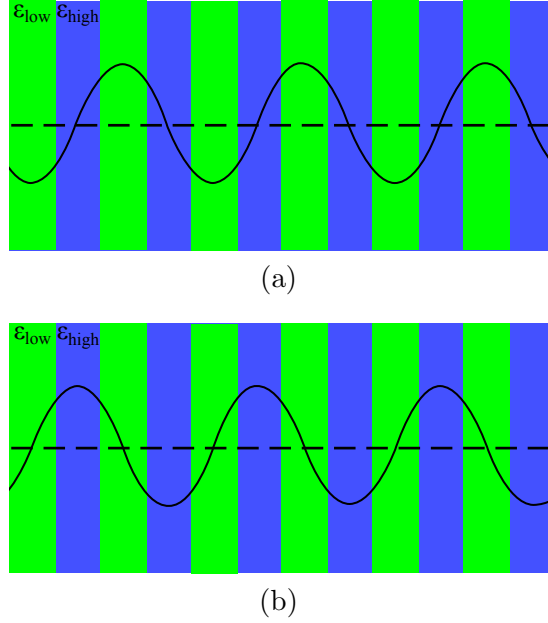
Figure 3.9: The electric field profile of a standing wave set up within a low dielectric contrast multilayer system. (a) and (b) show the profiles for the high frequency band edge (air band) and the low frequency band edge (dielectric band), respectively. An approximately sinusoidal standing wave can be seen at both band edges. The anti-nodes of the standing wave occur in the low permittivity material for the air band and the in high permittivity material for the dielectric band.

3.5.4 The Scalability of Maxwells equations

As with solid state physics, which has a fundamental length scale set by the Bohr radius [75], there is no fundamental length scale with photonic crystals. Simply put, assuming no dispersion of refractive indices, a larger structure will react in the same way as a smaller structure, only with larger wavelengths. The dielectric function $\varepsilon(\mathbf{r})$ is just a measure of how fast light travels with respect to distance r. Therefore imagine the system illustrated in figure 3.11 with a dielectric function $\varepsilon'(\vec{r}) = \varepsilon(\vec{r})/s^2$, where s is the physical scaling factor, and rearrange to give $\varepsilon(\vec{r}) = s^2\varepsilon'(\vec{r})$, now substituting this into the master equation (eq'n 3.24) gives:

$$\vec{\nabla} \times \left(\frac{1}{\varepsilon'(\vec{r})} \nabla \times \mathbf{H}(\mathbf{r}) \right) = \left(\frac{s\omega}{c} \right)^2 \mathbf{H}(\mathbf{r}) \tag{3.25}$$

Here it can be seen that if we double the dielectric constant, then we just have to quarter the frequency to get the same result. Utilising this interesting property of Maxwell's equations allows us to realise that we do not have to create difficult to manufacture optical systems to interrogate the properties of a particular photonic

(a)

(b)
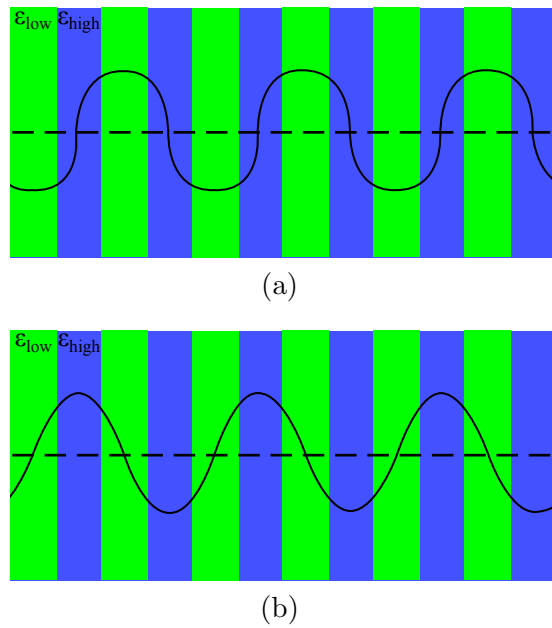
Figure 3.10: The electric field profile of a standing wave set up within a high dielectric contrast multilayer system. (a) and (b) show the profiles for the high frequency band edge (air band) and the low frequency band edge (dielectric band), respectively. The minimal energy band is the dielectric band therefore the higher energy bands perturb towards this state but the phase relation of the two solutions hass to be $\frac{\pi}{2}$ radians out of phase, hence why the air band anti-nodes are forced to be located in the low permittivity material. This contradiction forces the sinusoidal wave to become perturbed so that as much energy as possible lies in the high permittivity material.
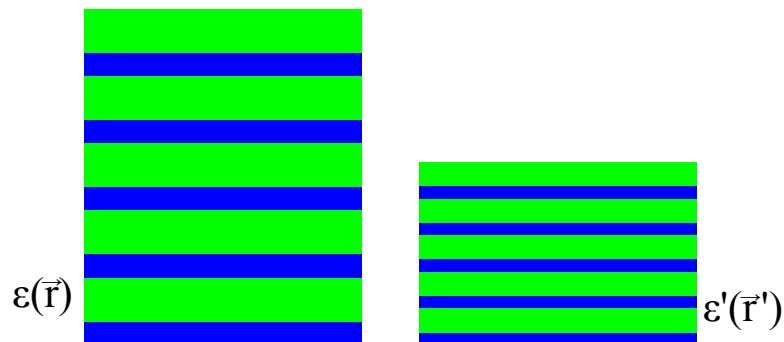
Figure 3.11: Two dielectric stacks where the left stack has been scaled by $1/s$ to produce the right stack.

47

Figure 3.12: Schematic of a dielectric stack with a defect layer. A simple multilayer with alternating A and B layers with the addition of a defect, which manifests itself here as the central B layer with twice the thickness as normal.

crystal, we can simply make larger, easier to manufacture, millimetre-scale crystals and interrogate them using radiation with the appropriate smaller frequencies, such as microwaves.

3.5.5 Defects in photonic crystals

Imagine a simple dielectric stack such as that shown in figure 3.6 comprising two alternating layers A and B. Now if we take a layer near the middle and double its thickness, the system is no longer perfectly periodic as we have introduced a 'defect' layer into the system as illustrated in figure 3.12. The defect layer acts to confine the band-gap wavelengths of the surrounding dielectric stacks, as these are the wavelengths that are disallowed to propagate through the stacks. This effectively 'traps' the band-gap wavelengths within the defect layer. This sort of system can be used as a waveguide which will guide the disallowed modes through the defect. Naturally, a defect waveguide of this type can also be produced in 2D [84] and 3D [85] photonic crystals. Such waveguides can be designed to have incredibly high Q-factors.

3.6 Diffraction

"No one has ever been able to define the difference between interference and diffraction satisfactorily. It is just a question of usage, and there is no specific, important physical difference between them."
- Richard P. Feynman.

It can be quite difficult to discern the differences between scattering and diffraction. In a basic sense diffraction is the result of multiple, evenly spaced, scattering objects acting in synergy to produce a final interference pattern [77]. To understand diffraction one must treat the array of scattering objects as an array of point sources of electromagnetic waves. The wavefronts combine in such a way that an effective wavefront can be said to emanate from the structure at a specific, geometry dependent, angle. The angle of such a wavefront can be calculated if the geometry and illumination conditions are known, using the following equation:

$$d(\sin\theta_m - \sin\theta_i) = m\lambda, \tag{3.26}$$

where d is the separation between scattering objects, θ is the angle of incidence and m is the mode index. From the grating equation it can be seen that no diffracted modes can exist in either reflection or transmission for wavelengths above the pitch of the grating, when illuminated normally. This makes sense when you think about how light interacts with an object. Optical microscopes cannot image objects smaller than the wavelength of light as the features are too small to scatter the illuminating wavelengths, this limit is defined by the Rayleigh criterion [77]. Therefore if the grating pitch is smaller than the illuminating wavelengths, the light won't scatter from the grating but instead the light will interact with the grating as if it were an effective homogenous slab. A more complicated form of the grating equation (eqn 3.27) includes not just the angle from the normal, θ, but also the angle about the normal axis, ϕ.

$$k_x = k_0 sin\theta_m cos\phi_m = k_0 sin\theta_i cos\phi_i + mk_g \tag{3.27}$$

where k_x is the x-component of the in-plane momentum within the system. Rearranging and substituting $k_g = \frac{2\pi}{\lambda_g}$ gives:

$$\lambda_g = \frac{m\lambda}{sin\theta_m cos\phi_m - sin\theta_i cos\phi_i} \tag{3.28}$$

From this equation, the pitch in real space, λ_g, can be calculated if the angles are known for the incident light and the diffracted modes. This equation provides the general case of diffraction for a mono-grating which can be illuminated from any polar

angle.

3.7   Conclusion

In this chapter, a brief overview of the underlying physics of structural colour have been shown. The physics of the reflections and refractions at a single interface between two optically different materials was discussed. This was shown to be the starting point for any structurally coloured system, most of which include many such optical interfaces. The physical origin of the photonic band-gap has been discussed for periodic, multilayer systems. The implications of this physics for more complicated structures was also discussed here. Polarisation effects were discussed to some extent as were the effects of changing the optical characteristics of the constituent materials and also the geometry. Defects in otherwise periodic systems were shown to confine certain wavelengths of light to certain areas of a structure, which is known as a defect waveguide.

Chapter 4

Materials and techniques

When characterising or designing optical systems, one needs to formulate an understanding of how a structure manipulates the light reflecting from it or passing through it. Therefore it is important to quantify these characteristics by using optical spectroscopy. As well as optical characterisation it also important to analyse the structures responsible for the optical responses given by the samples. Due to the structure's dimensions being comparable to the wavelength of light, it is necessary to use electron microscopy to capture and analyse the fine detail. Optical microscopy, however, can be utilised for the purpose of observing colour changes in samples, and also for looking at the larger scale structures involved. Optical microscopes can also be modified for the purpose of optical characterisation. In this chapter, the different methods and equipment for performing such optical and structural characterisations are described.

4.1   Optical characterisation

4.1.1   Bidirectional reflectance distribution function

Before performing optical characterisations on natural samples, it is good practice to first understand the variables involved. In order to measure the reflectance from a sample, the first variables that need to be considered are the illumination conditions. These are the angles of incident light (θ_i and ϕ_i) and, of course, the wavelength (λ). Another variable of incident light that is not so obvious is the solid angle of light that is incident (ω_i). Unless the light is collimated then it is usually focussed down, creating a cone of light. The solid angle of the cone, defines the variation in incident angles, which will cause a variation in reflection response. The character of reflected light will not only be dependent on the incident light conditions, but also the conditions of where the reflected light is collected with respected to the illuminated area on the sample.
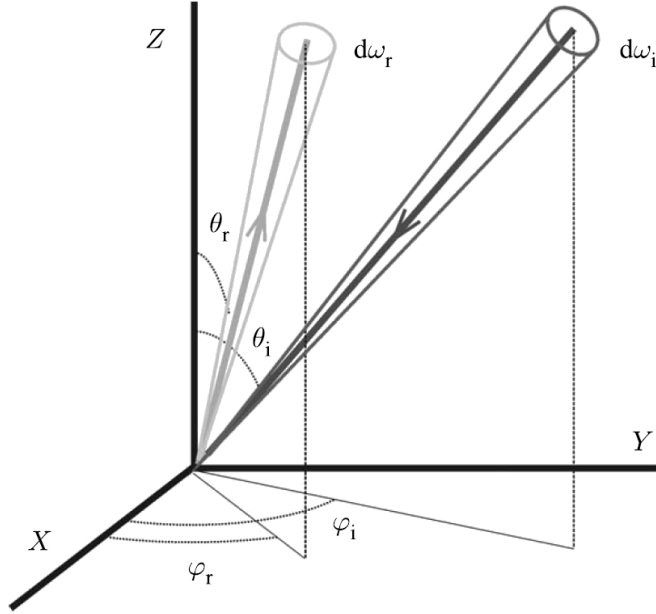
Figure 4.1: The bidirectional reflectance distribution function gives the reflected light as a fraction of the intensity of reflected light in a given direction and over a small solid angle and the intensity of the incident light within a small solid angle. Image courtesy of Vukusic et al. [87].

These variables include the angles of reflection (θ_r and ϕ_r) and the solid angle of the collection area (ω_r). These variables (shown diagramatically in figure 4.1) all come together in the equation that shows the reflectance for a given wavelength as a ratio of the reflected intensity and the incident intensity:

$$R_\lambda(\theta_i, \phi_i, \theta_r, \phi_r) = \frac{I_r(\theta_r, \phi_r)d\omega_r}{I_i(\theta_i, \phi_i)cos\theta_i d\omega_i}. \tag{4.1}$$

This equation is known as the bidirectional reflectance distribution function (BRDF) [13, 86, 87]. Once a firm understanding of all the variables involved with the BRDF has been achieved, then it becomes easier to choose what kind of experimental setup is needed to investigate certain variables. For instance, if the specific-angular (specular) reflection is of concern, then it should be clear that the angle of incidence from the normal, θ_i, should be equal to the angle of collected light, θ_r, and $\omega_r = \omega_i + 180°$, ensuring that both the beam and collection probe are in the same plane.
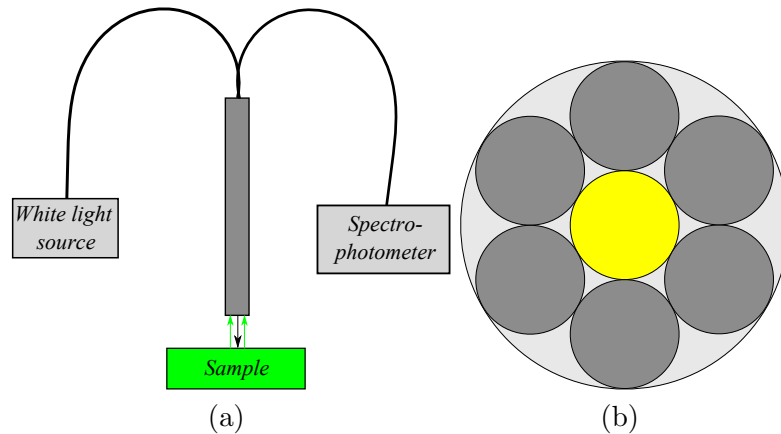
Figure 4.2: (a) Schematic of the experimental setup for taking simple reflection measurements. The black arrow indicates the incident, white light, the green arrows represent the reflected, green light characteristic of the green, demonstration sample (b) View of the end of the fibre at the sample end. Light is guided down the central fibre from a white light source to the sample. Reflected light is then collected by the six outer fibres and guided to the spectrophotometer. This system allows quick, easy to obtain, near-normal incidence reflection spectroscopy.

4.1.2 Spectrophotometry

Spectrophotometry is an important tool when analysing structural colours in nature, as it is important to know which wavelengths of light are being reflected and transmitted from structures of certain sizes and geometries. Knowing this allows one to fully understand the system, and, therefore, allows one to design and tune synthetic systems. Simple reflection spectroscopy, for macroscopic areas, was performed using an Ocean Optics Premium 600 μm reflection probe (figure 4.2). This probe utilises a bundle of 7 optical fibres, the central one of which is used to illuminate the sample by guiding light from an Ocean Optics HPX high powered Xenon light source. The other six optical fibres are used to collect reflected light from the sample which is guided to an Ocean Optics HR2000+ high resolution spectrophotometer. Spectra Suite can then be employed to create digital copies of the data. The advantage of using the reflection probe is how quickly data can be taken, as mounting a sample can be as easy as simply placing it on a flat surface, for example, an optical bench or even just a desk. The disadvantages of using this system are, only macroscopic measurements can be made as the smallest beam spot achievable is 1 mm in diameter and the system also shares the same pitfall as a lot of optical systems because it is impossible to make true normal incidence measurements.
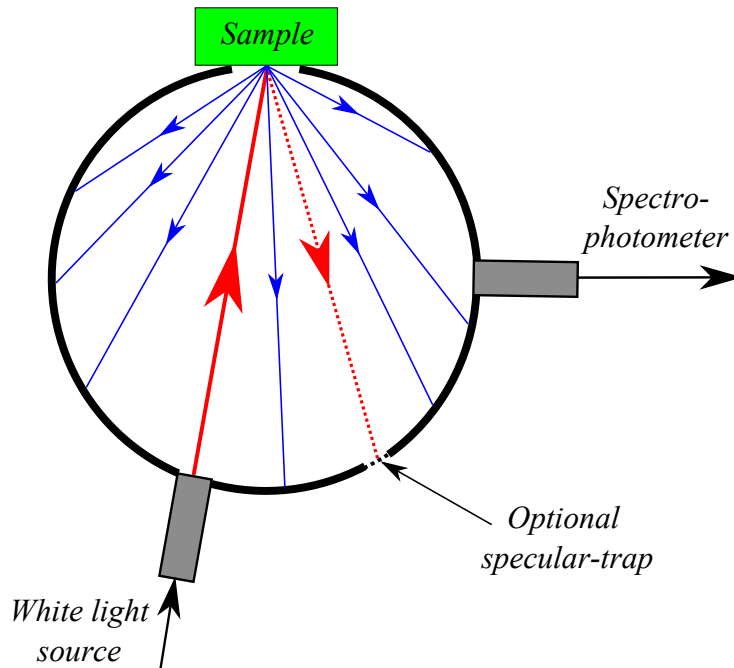
Figure 4.3: Schematic of the Integrating Sphere. The large red arrow shows the incident white light ray, the dashed red arrow shows the direction of specular reflection, leading to an optional 'specular-trap', a function that has not been used in this thesis. The blue arrows indicate the diffuse reflection from the sample. Each reflected ray reflects multiple times from the white interior wall of the integrating sphere. The multiple reflections lead to a uniform spectra at all positions on the white inner wall of the sphere including where the exit port is which takes the angle-independent spectra to a spectrophotometer.

4.1.3 The integrating sphere

In some cases of optical interrogation, it is useful to quantify all the reflected light (scattered and specular) of a system. This is extremely difficult to achieve using optical fibres and lenses, however, a very simple solution can be employed. This is achievable using a device called an integrating sphere (figure 4.3), which is a hollow sphere with a white inner coating. The coating, produces uniformly scattered light in all directions. The result of which, is a uniform spectrum being reflected from all points of the white inner wall. The sphere has three holes in it, one for incident illumination, one for collection of light and one optional hole that can be added to remove the specular comnponent of the reflected light. The collected light is guided through an optical fibre to an Ocean Optics HR2000+ high resolution spectrophotometer.
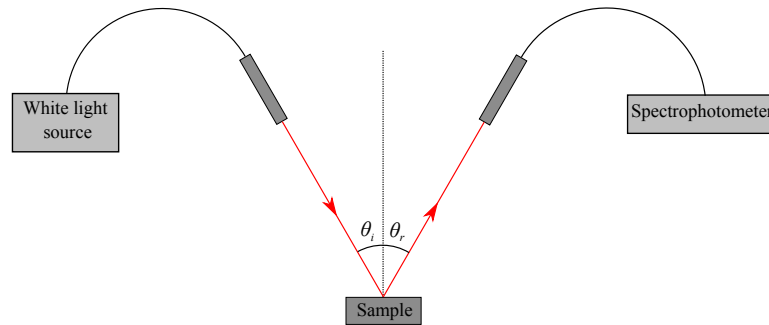
Figure 4.4: Schematic showing the experimental setup for performing angle-resolved optical microscopy. The angles θ_i and θ_r are defined by the angle from the surface normal of the incident and reflected light rays. In this setup $\theta_i = \theta_r$ at all times, ensuring that only the specularly reflected light is being collected for analysis.

4.1.4 Angle-resolved spectrophotometry

A major indication of a system exhibiting structural colour, as opposed to pigmentation, is iridescence. If the colour of the sample changes with viewing angle then you are most likely looking at a structurally coloured system. Therefore, it is of paramount importance to be able to quantify the change of colour as the viewing conditions, i.e. angle of incidence, change.

The solution employed for this thesis, is a simple $\theta/2\theta$ setup (figue 4.4), where θ is defined as the angle between the sample's surface normal, and the angle of incidence of light. The system comprises two arms that rotate around a common axis. Attached to each arm is an optical fibre, one for illuminating the sample, and the other for collecting the reflected rays. The angle of each arm from the sample's surface normal is always equal and opposite. Therefore, the detecting arm always collects specularly reflected light. This of course limits the collection range of angles, that is because the illuminating and detecting arms cannot occupy the same space, therefore normal incidence reflection cannot be analysed. If set up well, however, it should be possible to attain light at a grazing angle (light incident at $90°$ from the normal). In practice, this can be quite difficult but it is certainly not impossible.

4.1.5 Microspectrophotometry

When a very specific area of a sample needs to be characterised optically, it is sometimes necessary to use a modified microscope. This makes it possible to spectrally analyse samples or regions of interest that are only microns across. This process is called microspectrophotometry (MSP). Microspectrophotometry can be performed on single butterfly scales or even just small sections of a larger sample such as a beetle's elytron.
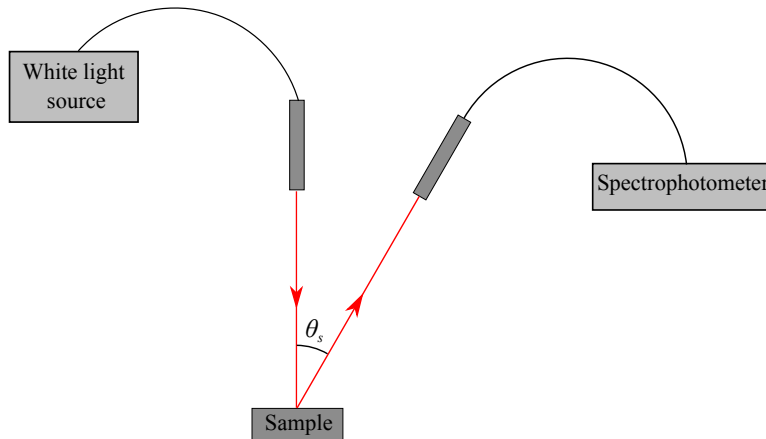
Figure 4.5: Schematic showing the experimental setup for performing spectrophotometry as a function of scattered angle. For this particular function, the angle of incidence is always zero and the light collecting arm moves from near 0° upto 90°.

For the work performed in this thesis MSP was achieved by using a Zeiss Ortholux stereomicroscope with a 20x Olympus 0.46 NA objective. Light was collected from the microscope and transmitted through an optical fibre to an Avantes USB 2048-2 spectrometer with Avasoft 7.5 (Avantes, Eerbeck), NL. The reference signal was taken using either an aluminium mirror, where possible, or a white reflectance standard (Spectralon, Labsphere, North Sutton, NH, USA).

When performing MSP it is a good idea to record the beam spot size, or rather, the area being illuminated, for reflectance spectroscopy. A small beam spot size is good for recording the reflection response of very small areas of the sample, for example, an area that has been FIB milled in order to remove a part of the photonic structure. However, some samples exhibit some variation around the sample and in order to average out this effect, a large beam spot is sometimes required. To calibrate the beam spot size, an image needs to be taken of the beam spot hitting a micro-ruler, at exactly the same magnification.

The beam spot size itself can be controlled to an extent by using a combination of different fibres and objective lens magnifications. A general rule is that the beam spot size will be roughly the size of the fibre divided by the magnification setting. For example, a 400 μm fibre combined with a 20x magnification objective lens should theoretically result in a beam spot size of 20 μm. A calibration is necessary to confirm the theory. Another item to consider when changing the magnification of the objective lens for spectrophotometry purposes is that the cone of light being produced by the objective lens will be different for different lenses. The 5x lens, for instance, will focus
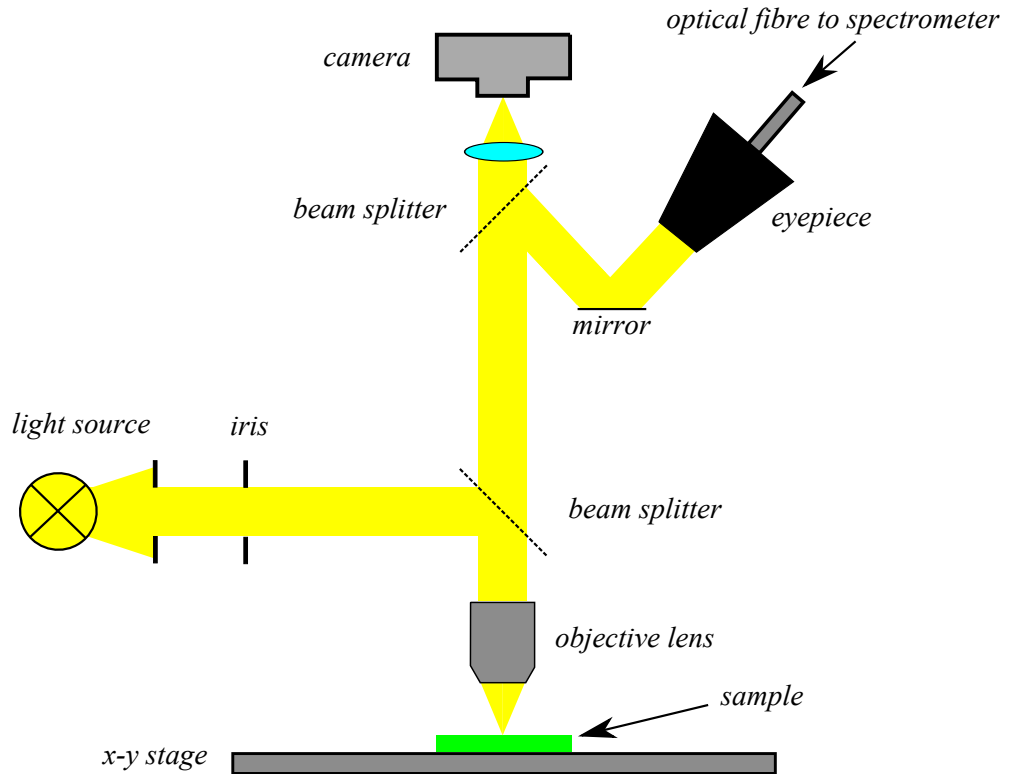
Figure 4.6: Schematic showing the experimental setup for performing microspectrophotometry. A standard stereo-microscope is at the heart of this equipment with one major modification, the left eyepiece has been replaced by an optical fibre.

the light down in a thin cone that will only illuminate the sample at near normal incidence. The 100x lens, however, will have a much higher numerical aperture and will, therefore, illuminate the sample from much higher angles from the surface normal. This change in illumination conditions undoubtedly results in a change in spectra and the colour of the sample. This effect can be seen in figure 4.7.

4.1.6 Imaging scatterometry

4.1.6.1 Primary beam imaging scatterometry

In order to analyse the scattering patterns of natural samples an imaging scatterometer was employed. The idea and design for an imaging scatterometer was devised and realised by the Stavenga group, Groningen University, The Netherlands [13]. Imaging scatterometry was performed on needle-mounted single butterfly scales [1], small pieces of fruit epidermis (Lethbridge et al. unpublished work) and sections of beetle elytra [65]. This process utilizes an elliptical mirror (denoted M, in figure 4.8.) with a small
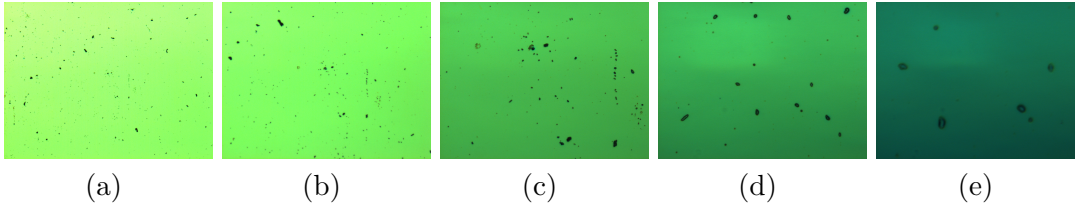
Figure 4.7: (a-e) Optical micrographs of a multilayer system demonstrating the effect on the colour of a sample when using different objective lenses. It can be seen that as the magnification is increased the colour blue-shifts as a higher solid angle of light collection is used. This particular effect arises because the reflection peak of a multilayer blue-shifts as the angles of illumination are increased.

hole in the centre. The sample is placed at the primary focal point of the mirror (F_2), then normally incident, narrow beam illumination from the primary light source, S_1, is focussed directly onto the surface of the sample, via the small hole in the mirror. The elliptical mirror captures the whole reflected hemisphere of scattered light which is then focussed down to the far focal point, F_2, which coincides with the back focal plane of a camera lens, L_6. This lens then collimates the beam. The collimated light is then focussed by an imaging lens, L_7, onto a charge coupled device (CCD), C_2.

Once the images are collected a MATLAB [88] routine is then utilized to correct the radial distortion caused by the collimating and imaging lenses and also to add an angular scale to the image [13].

4.1.6.2 Secondary beam imaging scatterometry

The secondary light beam is used for imaging the hemisphere of specular reflection. This system utilises the secondary light source, S_2, in the imaging scatterometer experimental setup. This light source is focussed down to a point where a diaphragm, D_5, is placed that has an equivalent distance to the elliptical mirror as the secondary focal point of the mirror, F_2. The illumination then hits the beam splitter, H, and is directed towards the mirror. The beam fills the whole mirror and is therefore focussed onto the sample placed at the primary focal of the elliptical mirror. The reflected light then hits the mirror and is focussed down to the CCD in the same way described for the primary beam function.

Filters can be placed between the lenses labelled L_4 and L_5 to ensure that only certain wavelengths of light are captured in the images. It is because the images will then show a small, almost monochromatic, wavelength range that this technique can be used to de-convolve the data by showing the scattering effects at just one wavelength. This can make it easier to see where diffracted modes of a certain wavelength are, or
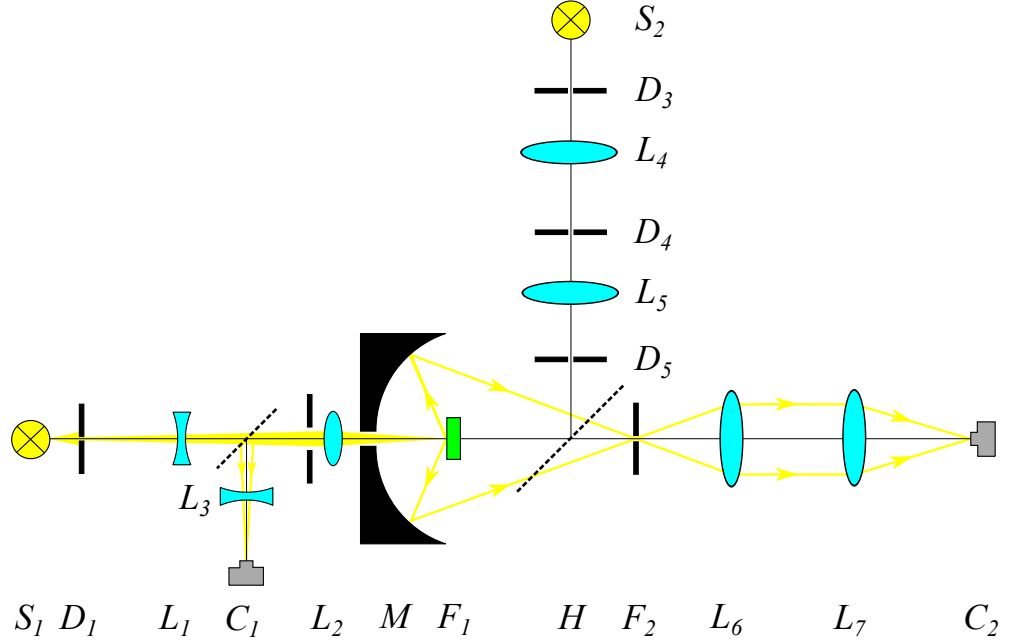
Figure 4.8: Schematic showing the experimental setup for the Imaging Scatterometer primary beam function. The sample is placed at one of the focal points of an elliptical mirror, where it is illuminated with normally incident light. The specially designed elliptical mirror captures the scattered light which is then reflected through the second focal point, to optics which guide the light to a CCD.

even for plasmon imaging [89], however this technique is not described in this thesis.

4.1.6.3 Dark-field secondary beam imaging scatterometry

The imaging scatterometer experimental setup can also be used in dark-field mode, so that the only illumination is high angle and the light captured by the CCD is light that has been scattered without any specular reflection. As shown in figure 4.10, dark field imaging scatterometry (DFIS) is achieved by blocking out the low angle illumination $(0° - 75°)$ of the secondary beam between lenses L_4 and L_5, therefore, leaving only high angle $(75° - 90°)$ incident illumination. The collected image only shows the lower angle portion $(0° - 75°)$ thereby only showing scattered light. This is achieved by placing an aperture between F_2 and L_6 which is used to block all high angle reflected light.

4.1.6.4 Micro-imaging scatterometry

Micro imaging scatterometry (MIS) was performed using an Olympus microscope with the addition of a Bertrand lens. The addition of this lens means that the system images the back focal plane of the objective lens rather than the sample, thereby showing
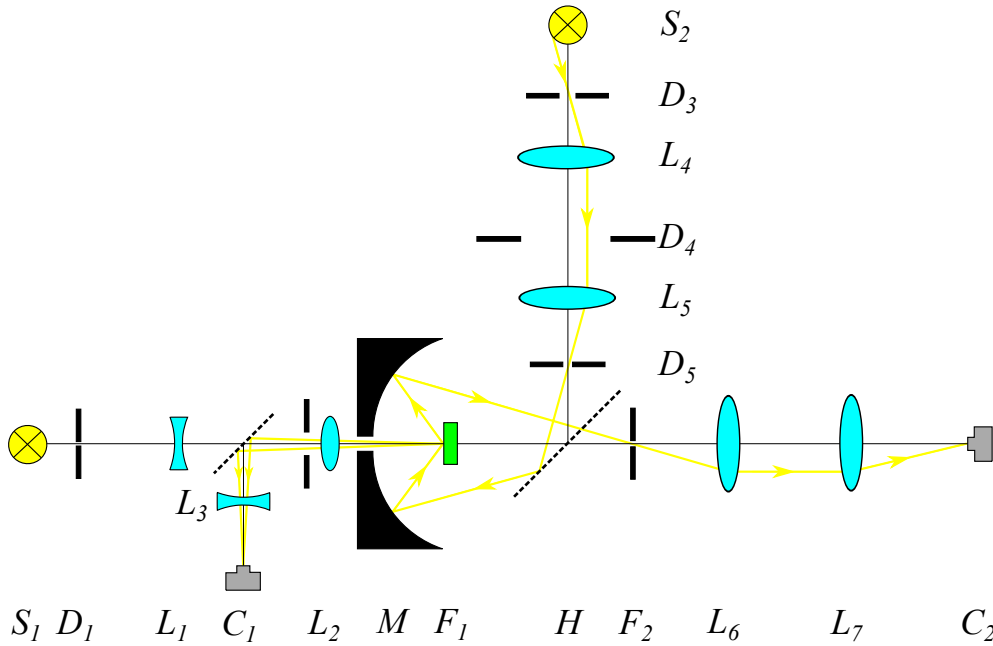
Figure 4.9: Schematic showing the experimental setup for the Imaging Scatterometer secondary beam function. The sample is placed at the primary focal point, F_1, of an eliptical mirror. The secondary light source, S_2 illuminates the whole mirror, this light is then focussed down onto the sample, from every possible angle in the reflection hemisphere. This light then reflects from the sample, according to the optics of the sample, and is recaptured by the mirror. The re-reflected light is then focussed down to the F_2 and then is focussed to the CCD.

the direction of the propagating light as a function of radial distance, much like the imaging scatterometer. This effectively means that there is now a microscope within the microscope. The advantage here is that one can probe a much smaller spot size, the lower limit lying at approximately 2 μm.

4.2 Structural characterisation

4.2.1 Optical microscopy

Optical microscopy was performed primarily using a Carl Zeiss Axioskop 2 polarising microscope. The microscope allows the capture of both reflection and transmission images. Other functions include polarisation of both incident and collected light and also the choice between bright field and dark field illumination. The lenses in operation on this device are: (5x, 10x, 20x, 50x and 100x) and these lenses have dark field capabilities. Another quite useful function of the microscope is the z-stack function.
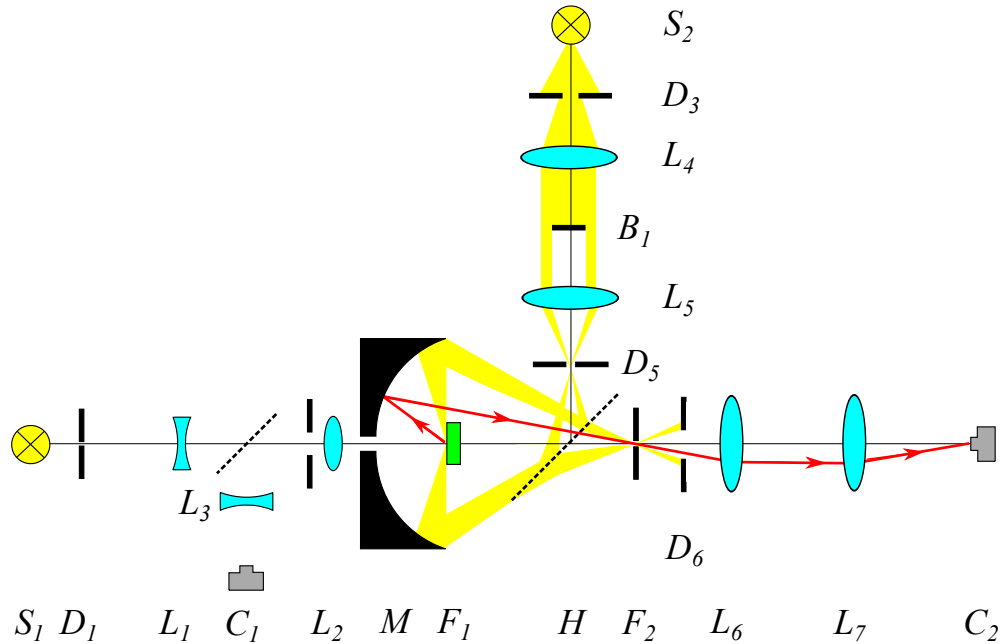
Figure 4.10: Schematic showing the experimental setup for the dark-field imaging scatterometer. This is achieved simply by placing a light blocker at the point labelled B_1 and a diaphragm to block the specular reflection at the point labelled D_6. The red line in the schematic shows a possible path for the scattered light to take.

This is employed when individual samples are too curved to image the whole subject in focus, a problem that usually occurs with the high magnitude lenses, due to a small working distance. The z-stack function allows the capture of many images with different stage heights, thereby having each feature in focus in at least one of the images in the array. The Axiovision software [90] is then used to combine all the focussed sections together, resulting in a single focussed image at a high magnification that would otherwise not be possible. In this thesis, the sample preparation for using this microscope usually involved scraping butterfly scales onto a microscope slide, or cutting small sections (2 mm x 2 mm) of beetle elytra or fruit epidermis.

4.2.2 Scanning electron microscopy

4.2.2.1 Imaging

Some samples, especially naturally occurring samples, can be too brittle for the TEM preparation process. This can result in fracturing or defects in the morphology of the samples such as shrinkage. Also the preparation stage can be quite time consuming (1-2 weeks), therefore, the use of a scanning electron microscope SEM can be an ad-
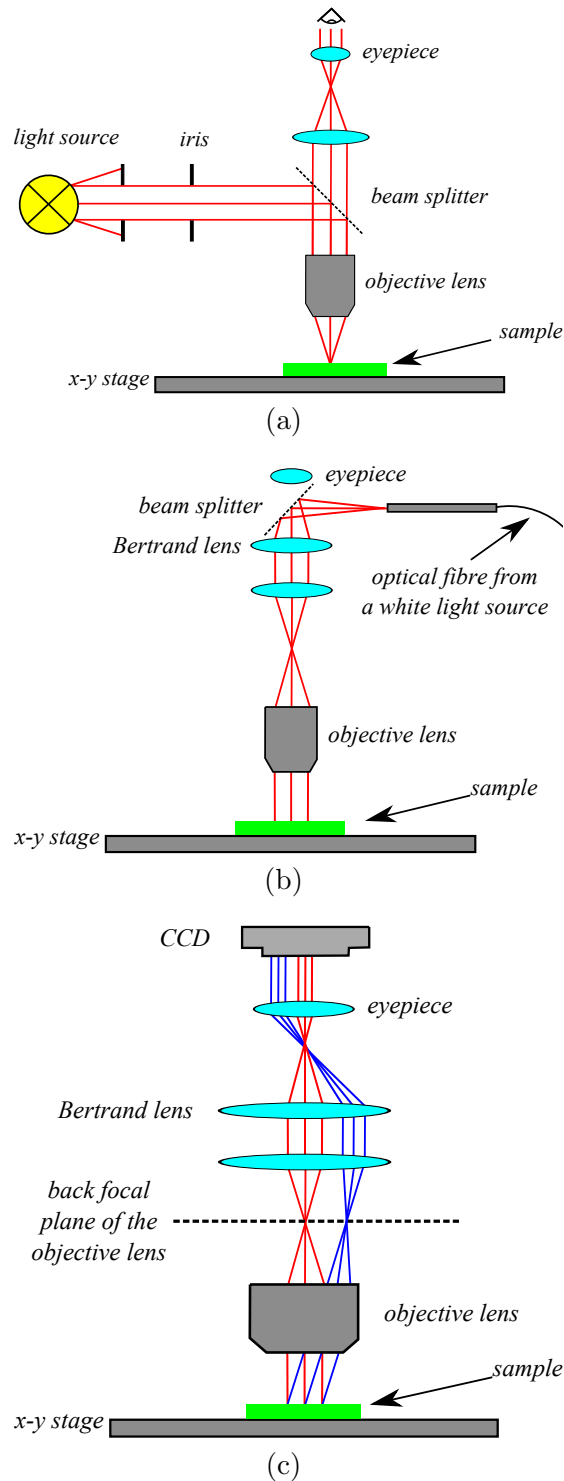
Figure 4.11: (a) A ray diagram showing how a normal microscope in bright-field mode works. Light is focussed onto the sample plane, which is then imaged by a CCD or the human eye. (b) A ray diagram showing how collimated light can be used to illuminate a sample. (c) A ray diagram of reflected light from the sample, showing that the objective lens design means that light rays that are scattered in the same direction will be focussed to the same point on the back focal plane of the lens. This focal plane is then imaged, utilising the addition of the Bertrand lens.

vantageous method of obtaining nanometre-scale images. The typical sizes of samples were 2-3 mm across sections of elytra or wing-section. Due to the nature of the electron beam, non-conductive samples were initially fixed onto an aluminium stub via conductive carbon or copper tape. The samples were then sputtered with approximately 3 nm of gold-palladium to ensure that the sample did not charge, which would otherwise have led to a significant decrease in image quality. The sputter coater used was a Cressington 208 HR. The SEM instrument employed was an FEI Nova 600 dual-beam system. The typical voltage and current of the beam was 10 kV and 0.13 nA respectively. This ensured a good middle ground of clear images, without destroying the sample. The magnification factor was limited to 60,000x which is an appropriate figure for probing optical nano-structures.

4.2.2.2 Focussed ion beam milling

In order to produce a clean cross-section for the SEM imaging of a natural structure, one can simply snap or freeze-fracture a sample. However, this approach is unreliable and often does not give a reasonably sized region of interest. To overcome the problem, a much more reliable method is needed. Focussed ion beam (FIB) milling is a solution to this problem. FIB milling offers the opportunity to gain a smooth, clean cross-section that makes the imaging process much easier. The FIB milling process works by bombarding the structure with a beam of argon ions. These ablate away parts of the structure to a high resolution so that a clean cross-section on the nano-scale can be obtained. When FIB milling different materials, different protocols are expected to be used. For instance, if a softer polymer material is used then generally speaking lower beam currents are required.

4.2.3 Transmission electron microscopy

Transmission electron microscopy (TEM) was performed on natural samples using a JEOL 100S TEM instrument. TEM micrographs were taken after a preparation process was performed to ensure the samples were hardened and subsequently cut into thin 80 nm slices to ensure good quality images. The preparation process starts by fixing samples in 3% glutaraldehyde at 21°C for 2 hours to ensure cross-linking of cellular structures into a matrix, thereby preserving all the features of the sample and also to ensure that minimal alterations to the morphologies of the sample during the remainder of the process, including exposure to the electron beam for imaging. This stage was followed by rinsing in sodium cacodylate buffer for 1-2 hours. Samples were then fixed in 1% osmic acid in buffer for 1 hour, followed by block staining in 2% aqueous uranyl acetate for 1 hour. Before embedding in resin, the sample needed to be com-

pletely dehydrated, therefore, rinsing in a series of ethanol baths ending with 100% ethanol was required. Subsequently the samples were then embedded in Spurr resin [91] and microtomed to produce thin samples for imaging. Post-microtomed samples were stained in lead citrate to increase the contrast of the images [92].

4.2.4 Fast Fourier transform analysis

As previously described, most structural colour systems possess a periodicity in refractive index, whereas some systems, possess complete disorder, usually white structure such as the scales of the *Cyphochilus* beetle [29]. Sometimes, however, a structure can have a periodicity that exhibits a limited amount of disorder. The amount of order to the periodicity can be quantified in a few different ways. Perhaps one of the clearest ways to achieve this is by applying a Fourier transform to a TEM or SEM image of the structure. Applying a discrete Fourier transform (DFT) to an image transforms the image from a real-space image into a frequency-space image. Therefore, if there is a well ordered periodicity present in the TEM, like a multilayer, the Fourier transform image will show sharp periodic features that correspond to the size and direction of the periodicity. This technique transforms the original spatial image (electron micrographs etc.) by decomposition into the sine and cosine components of the overall image function [93]. The DFT is a complex computation which requires N^2 calculations, where N is the problem size. The shear number of calculations requires a lot of computer power. Nevertheless, a fast Fourier transform (FFT) is a way of calculating the DFT but by using only $Nlog_2N$ calculations instead. This reduces the number of computational tasks by orders of magnitude [94]. The fast fourier transforms in this thesis were produced using a MATLAB code [88]. This code utilised the in-built MATLAB FFT function. First the input image had to be a perfect square as measured in number of pixels. The code also requires an input of the scale which in this case was measured in pixels per nanometre. The output of such a process is a graph that has x and y axes measured in inverse distance with units: nm^{-1}. The patterns shown in the FFT images in figure 4.12 not only give an idea of the periodic structures found in the corresponding jpeg images, but they also represent the diffraction pattern associated with each image, assuming the black and white areas depicted two different refractive indices and each image is illuminated with a collimated, coherent light source such as a laser.

4.3 Numerical simulation methods

Generally in science, an observation is made and then that observation is explained, either correctly or not, and then the explanation has to be tested. Usually this requires
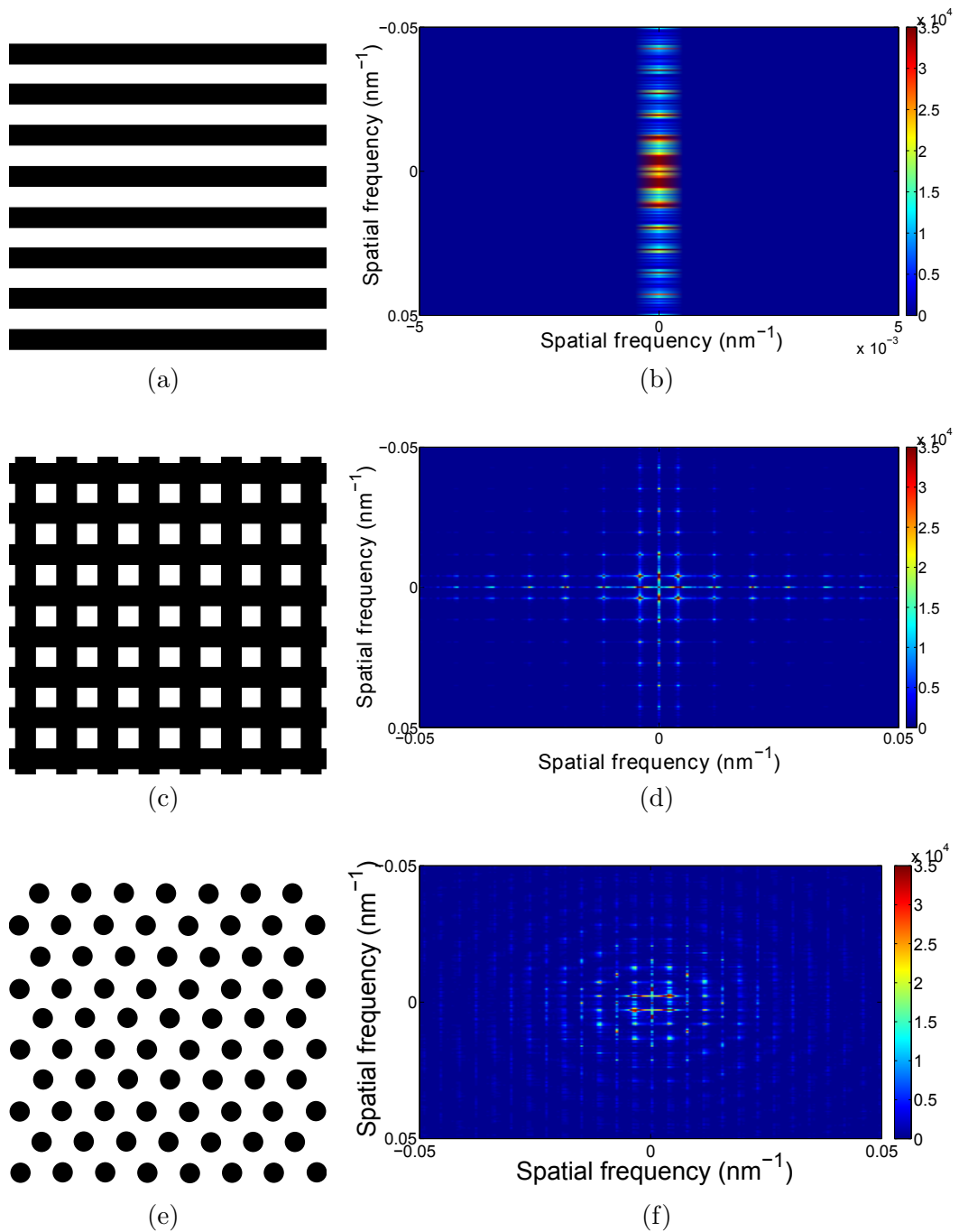
Figure 4.12: (a), (c) and (e) show schematics of three possihble structures. Each structure has a periodicity of 250 nm. (b), (d) and (f) reveal the corresponding FFT images to the schematics shown. The FFT shown in (b) indicates the presence of a structure that is only periodic in one direction only. The FFT in (d) shows a strong periodicity in two directions and a weaker periodicity in diagonal directions as there is a longer diagonal periodicity present. (f) The inverse structure of a hexagonal pattern is also hexagonal but the pattern is rotated by 90°.

some sort of prediction to be made based on the theory, and then a subsequent experiment performed to test the prediction. Present day computing specifications allow us to perform experiments without actually leaving the desk. Of course, when I say perform I really mean simulate. Nowadays an observation can be made, an explanation is attempted, and then exactly the same system can be simulated to see if the same result is found. To gain the same result, current computational software requires us to fully understand the system, hence this is an ideal way of testing such hypotheses and our own understanding of the physics involved. Computational modelling can be as simple as using a calculator and known values such as the wavelength of light and the pitch of a diffraction grating to work out the angles of diffraction using the grating equation (equation 3.26). This result would then be compared to experiment for validity. However, when looking at more complicated systems such as working out the reflection spectra from multilayers or 3D photonic crystals, more demanding simulations need to be made. The research performed in this thesis required 3 different systems to be used, TFCalc [95], HFSS [96] and MEEP [97].

4.3.1 Multilayer modelling using TFCalc

The simplest system used was a Fresnel-based software package called TFCalc [95]. TFCalc uses the equations for the electric field amplitude at optical interfaces given earlier in this thesis (equations 3.2 and 3.3). This software can only be used for 1D photonic crystal systems and was developed for designing band pass filters, long pass filters etc. For this thesis, computational modelling of simple multilayer systems were produced largely by using TFCalc software. To create a model using this user friendly software, all one has to do is enter the simple parameters, refractive indices and dimensions, of each layer of the the system you desire to analyse. The software then outputs results for reflection, transmission and absorption. The results for each can be for different wavelengths, angles of incidence and polarisations.

4.3.2 Finite element method computational modelling

The more complicated 3D systems demanded more complicated, processor heavy computations to be made. One such program utilized to do this is HFSS, Ansoft Ltd. HFSS (high frequency structured surfaces) is a program that relies on a modelling technique known as the finite element method (FEM). FEM modelling basically means that the structure or structures graphically input into the simulator are broken down into a number of tetrahedral-shaped elements. Maxwells equations are then solved for each tetrahedron at the boundaries, using the boundary conditions of the surrounding tetrahedra to accurately calculate the fields. HFSS was a piece of software designed

primarily to aid design of electronic components such as radio frequency antennas, integrated circuitry and printed circuit board design. However, considering that the fundamental equations utilised in this software are Maxwells equations that we now know do not exhibit a limited length scale, the software works just as well in the optical regime. Many photonic crystals in nature can be on the order of hundreds of unit cells in any given direction. Modelling an entire crystal, however, can be very expensive in terms of processing time and power. This can actually be quite a wasteful method considering a periodic structure can be reduced down to a single element, the unit cell, which is repeated over and over again to build up the entire crystal. The same treatment can be applied to computational modelling, only one unit cell needs to be analysed and therefore the time and processing costs can be reduced quite significantly whilst not sacrificing accuracy.

For this thesis two distinct HFSS methods were applied, incident plane wave modelling and Floquet port modelling. In both cases the structures are split into tetrahedra and master/slave boundaries are applied. Incident plane wave modelling works by sending a plane wave towards the model at a specified angle and frequency. As the wave passes through the stucture the fields are then calculated. From the fields the reflection and transmission coefficients can be calculated. The reflected and transmitted waves are then integrated over their respective hemispheres. The values of transmittance and reflection are then output from the system. As the waves pass through the top and bottom boundaries of the air boxes, there is a probability for reflections to occur. These reflections from the air box are not part of the real-life systems, therefore, a perfectly matched layer (PML) is required. A perfectly matched layer provides an effective refractive index matching structure, thereby reducing significantly the amount of undesired reflection.

Computational modelling using the Floquet port method differs significantly from the incident wave method. The incident waves are now a set of Floquet modes, the number of which is user defined. These modes are calculated based on the structure before the simulations start running. The polarisation of each mode can also be defined, allowing the user to individually analyse each diffracted mode for each polarisation. In this case no PMLs are required.

4.3.3 Finite difference time domain modelling with MEEP software

As previously described, HFSS can be used for most 3D structures, with the exception of large structures that cannot be broken down into a primitive unit cell. In this case, the large structure would require larger specification computers than are currently available to the research team. However, one can employ a different method of computational
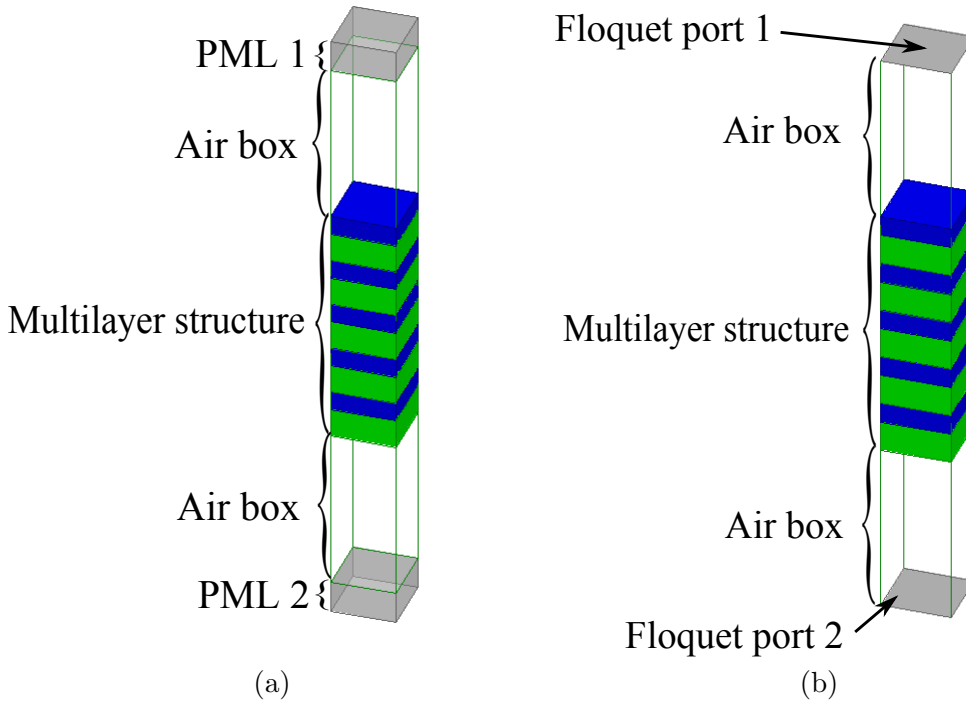
Figure 4.13: (a) A computational model of a multilayer structure in HFSS. The multilayer is surrounded by a sufficiently large air box. On either side of the air boxes there are PMLs which stop unwanted reflections from the top and bottom of the air box. (b) The same model as in (a) but using a different modelling technique within HFSS. Instead of setting up an incident plane wave and PMLs, Floquet ports are added to the top and bottom of the air box. From the combination of these two ports, diffracted modes can be analysed in both reflection and transmission. In both (a) and (b), master/slave boundaries are applied to the x and y boundaries of the entire model, this effectively repeats the structure infinitely in both of these dimensions.

modelling, such as finite difference time domain (FDTD) modelling. This essentially means that instead of simulating the electromagnetic response in the frequency domain, as HFSS does, the simulations are performed in the time domain. An advantage of this method is that slide-shows can be produced that show the propagation of an electromagnetic wave, as a function of time.

The software that was utilised for this thesis was MEEP, a Linux based software packaged developed at MIT, Massachusetts, USA. It should be noted that all MEEP computations in this thesis were peformed by Mathias Kolle of Harvard University, Massachusetts, USA.

4.4 Conclusion

This chapter has presented many different ways in which one can optically analyse structures shown in nature. The abundance of methods here does not signify the options available, but rather the options required as some samples will work betterl for some experiments and not so well for others. When trying to get a sense of the role of each variable within the BRDF for a given structure, it is necessary to do several experiments to confirm the understanding and sometimes to overcomec logistical difficulties.

Structural analysis is paramount to gaining a full understanding of naturally occurring photonic systems. The first stage of analysis is always optical microscopy, as visualising the larger scale structures first helps the understanding of how the nano-scale structures fit into the over all geometry. Simple reflection and transmission microscopy can be utilised show where the structurally coloured photonic crystals are located and how they fit together.

To structurally probe the nano-scale structures, however, electron microscopy is required. This can be performed in reflection via SEM imaging or, for more detail, in transmission via TEM imaging. The combination of the two methods provides a more complete picture of the geometry of the structures.

It is very beneficial to theoretically model responses from given structures using more than one technique as the results output by a computer model are rarely a realistic version of the experimental techniques on the first try. Therefore, it is always reccomended that back up techniques are utilised and, therefore, the results confirmed for reliability. The purpose of theoretical modelling is to confirm our understanding of the experimental results and to enable us to fine tune optical repsonses with the aim of producing optimised, synthetic systems.

Chapter 5

A detailed study of *Margaritaria nobilis* and stretch-tuneable polymer replicas

5.1   Introduction

This chapter is a two-part investigation into the colour and structure of the mimetic fruit of *Margaritaria nobilis* and also the synthetic, tunable fibres inspired by the photonic crystal found in the fruit. *M. nobilis* shows a brilliant, greenish-blue colour appearance and is native to the rainforests of Central and South America. Both the colour and structure are investigated in detail, the findings of which inspired the synthetic system. The structure of the synthetic system is analagous to a simplified version of the structure found in the fruit, but which is fabricated with stretchable materials. The elasticity of the fibres can be utilised to mechanically tune the colour produced, a property which was also investigated in detail. Computational calculations were performed to confirm the experimental findings. The advantages of both the natural and synthetic systems are discussed.

Evolution teaches us that, in general, the brighter and more visible a fruit is coloured, then the more likely it is to be spotted by birds and other seed dispersing vectors [70, 71, 98, 99, 100, 101]. The seed disperser will then consume the fruit and disperse the seeds elsewhere, away from the parent plant thereby reducing sibling competition and increasing geographic dispersal [102]. The origins of such colours are usually pigments in the epidermal layer of the fruit which promote preferential absorption of scattered light, such as the bright red nature of strawberries and tomatoes which contain anthocyanin [69, 103], a red reflecting pigment. Quite rarely in

5. A detailed study of *Margaritaria nobilis* and stretch-tuneable polymer replicas

(a)   (b)
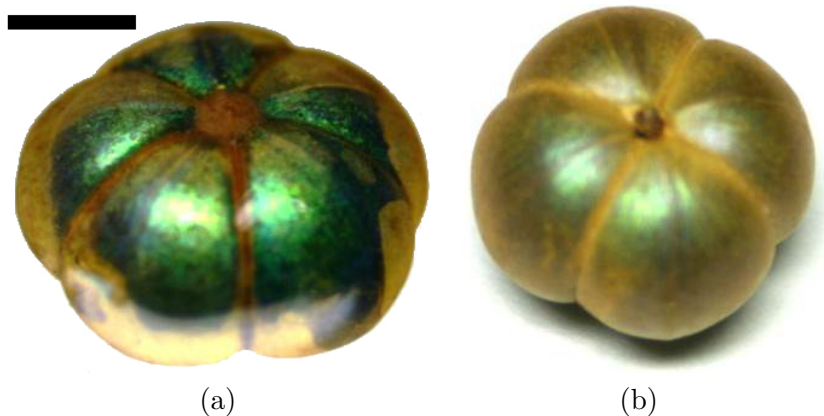
Figure 5.1: Photographs of the mimetic fruit *Margaritaria nobilis*. (a) The hydrated and (b) the dehydrated fruit. A significant reduction in colour saturation can be seen when the fruit is dried. Scale bar: 5 mm.

floral systems, however, some fruits and plants exhibit a bright colour appearance that is due to the sub-micron structure embedded within the epidermis, rather than any constituent pigments [18, 28, 45, 64, 68, 71, 72, 73]. In nature, it is often surprising to observe some of the techniques that have been optimised over many millions of years through natural selection. It is for this reason that so many scientists are looking to nature for novel designs, hence why the field of biomicry is flourishing [42, 45, 48, 49, 50, 52, 104, 105, 106, 107].

The subject of this investigation is a fruit named *Margaritaria nobilis*. This fruit exhibits iridescence in the form of a vivid greenish-blue colour (figure 5.1(a)). The dehydrated fruit, however, only exhibits the greenish-blue colour at normal incidence and a broadband, duller colour at high angles (figure 5.1(b)). Interestingly, when the dull, dehydrated fruit is placed into water to soak for at least 15 minutes, the original vivid colours return. This suggests that the dehydrated system either exhibits shrinkage, pushing the peak reflected wavelengths down into the UV, or the structure itself collapses with the result of degraded optical performance. These reversible hydration/dehydration optical effects have also been investigated in other natural systems including the pupa of the butterfly *Euploaea core* [8, 17].

Margaritaria nobilis, commonly known as "Bastard Hogberry", originates from tropical, and seasonal deciduous forests exclusively in Central and South America [98]. The tree bears fruits from the start of February in the wet season. The fruits grow on the tree inside a green exocarp which opens after the fruit spontaneously falls to the forest floor. The exposed fruit exhibits a bright blue iridescence which fades with increasing time exposed to the air [98]. During the exposure of the vivid blue colour,

the fruit is far more visible to birds, which act as seed dispersers.

It is reported that *M. nobilis* is a mimetic fruit. This means that instead of applying an energy cost into producing a sweet fleshy pulp (as incentive for seed dispersers), *M. nobilis* exhibits a bright colouration similar to that of fleshy, nutritious fruits, thereby tricking the birds into eating them and, therefore, dispersing the seeds inside [98].

The samples used in this research came from a reserve in Brazil called Revista Brasileira de Botânica [98] and also from Paula J. Ruddel, Jodrell Laboratory, Royal Botanic Gardens, Kew, UK [108].

5.2   Optical characterisation

Optical micrographs in reflection (figure 5.2(a)) of the epidermis of the *M. nobilis* fruit reveal the greenish-blue colouration, therefore, one can say that the structure responsible for the colour is embedded within the skin of the fruit. Transmission optical micrographs have an orange colour appearance which represents the wavelengths that are able to propagate through the photonic crystal present in the epidermis. If we look closer at the micrographs in figure 5.2 then we can start to see the micro-structure that exhibits the structural colour. Elongated cell-like building blocks are observed in a grain-like pattern. The criss-crossing of these grains, observed in the transmission image in figure 5.2(b), suggests several layers of these cells in different orientations, possibly offering mechanical strength to the epidermis, whilst not compromising optical performance.

The reflection and transmission spectra at near normal incidence are fairly, but not perfectly, complimentary in nature. Reflection and transmission spectra are complimentary when at any particular wavelength there is high reflection and low transmission and vice versa. A perfectly complimentary system occurs when a one or higher order dimensional systems is made of lossless materials so no absorption is present. In such a perfectly complimentary system, transmission plus reflection would equal unity for all wavelengths. It can be seen in figure 5.3(a) that the fruit epidermis is a non-perfect complimentary system. This result agrees with the colours seen in the optical micrographs. The greenish-blue appearance was confirmed from reflection spectra acquired using the integrating sphere (figure 5.3). This result shows a maximum in reflection for the dry fruit at approximately 510 nm. The spectra also shows a broadband 'tail' in reflection, confirming the broadband colour observed from the whole fruit (figure 5.1(b)).

Figure 5.3 shows the reflection spectrum obtained from the black seeds that lie under the integument of the fruit. This spectrum was acquired using an integrating sphere and therefore shows approximately 10% total reflection for the visible range. The

(a)   (b)
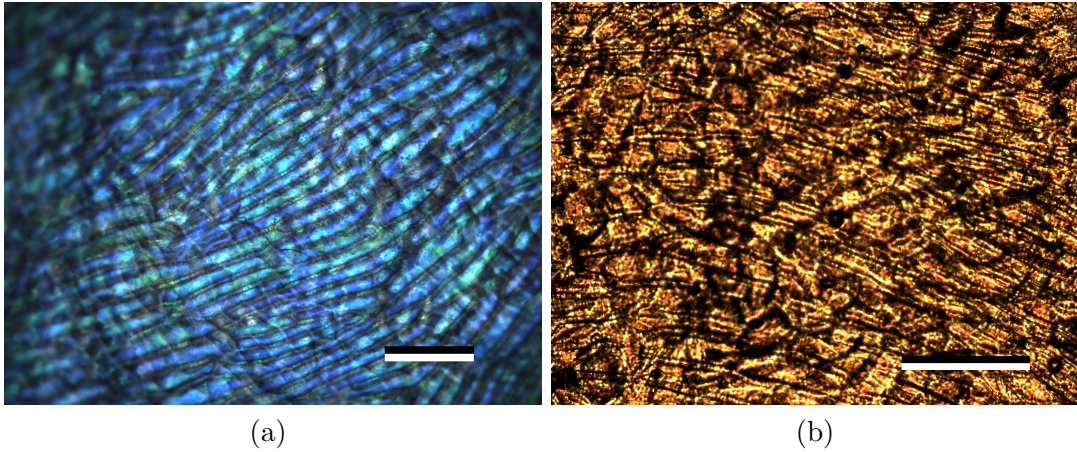
Figure 5.2:   Microscope images showing the colours produced by the epidermis of *Margaritaria nobilis*. (a) Reflection and (b) transmission from the cell-like structure making up the epidermis. The micron-scale structure of the epidermis is apparent in these micrographs. We see cell-like structures linked together to form a layer that covers the entire fruit. Scale bars: (a) 100 μm and (b) 200 μm.

(a)   (b)
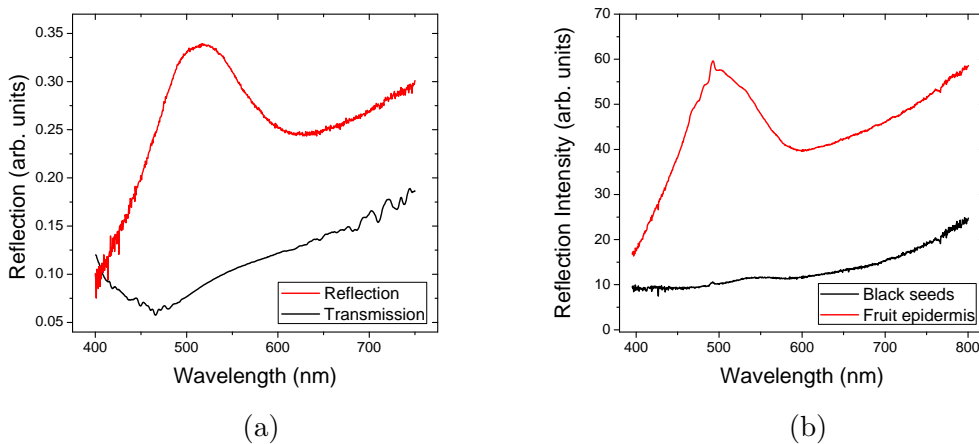
Figure 5.3: (a) Reflection and transmission spectra from the epidermis of the fruit of *M. nobilis*, showing the complimentary nature of the two spectra. (b) Optical characterisation perfomed on the epidermis and seeds from the fruit of *M. nobilis* using an integrating sphere. The spectrum of the black seeds that lie underneath the brightly coloured integument offer an optical advantage by absorbing the transmitted colours (figure 5.2(b)) to prevent undesired back-reflections. The system, therefore, retains the vivid saturation of colour.

high absorption of the seeds prevent the light that transmits through the integument from being back-reflected. This results in a more saturated, or less broadband, overall colour. This creates an advantage for the fruit as the colour is far more saturated, a property which will increase the fruit's conspicuousness against the background of the rain forest floor. This will increase the probability of a bird seeing the fruit and hence increase the probability of seed dispersal. This demonstrates further that the structure exhibited is not just for structural integrity but actually has a colour function, most likely to be seed dispersal via visibility to birds.

Angle-resolved reflection spectra from the epidermis of the *M. nobilis* fruit were taken (figure 5.4) with an angular resolution of 1°. The resulting graphs show the expected result for a multilayer system with a decrease in the peak reflected wavelength with angle. There appears to be a secondary reflection band entering the visible regime at higher angles. This band appears at an angle of incidence of approximately 60° for TM polarisation and 20° for TE polarisation. This disparity can be attributed to a Brewster angle effect that will only be observed for TM polarisation. A specific Brewster angle is the result of reflections from a flat surface of optically thick material. However, in this case the structure comprises more than one material and so multiple refractive indices have to be taken into account, therefore, it is referred to as a Brewster angle of an effective medium.

The optical changes that occurred when the fruit was hydrated/dehydrated were analysed using an integrating sphere (figure 5.5). The fruit was soaked in water for 15 minutes. The reflection spectrum was immediately taken on the freshly hydrated fruit and then again every minute for 32 minutes as the fruit dried at room temperature. A small red-shift in peak wavelength was observed for the freshly hydrated fruit, the peak wavelength then returns to the initial value as the fruit dries out. The peak wavelength only shifts by 15 nm and is only obvious when we look at a much smaller wavelength range, as shown in figure 5.5(b). This change in wavelength can be attributed one of two things, firstly the water swelling the dimensions of the nano-structure of the fruit so that the layers will produce resonance at a higher wavelength. Secondly, the introduction of water could also change the refractive index of the constituent materials, therefore changing the optical path length of the layers in the structure. The shift in peak reflected wavelength could also, of course, be attributed to both of the above effects.

Other than a red-shift in the peak reflected wavelength, the hydrated spectra show a much more prominent peak in reflection, when compared to the background reflection, a result which confirms the more saturated colouration observed from the hydrated sample. This effect may be attributed to a collapse of the structure as the fruit epidermis dries out, this would cause a decrease in optical performance as the order of

(a)

(b)
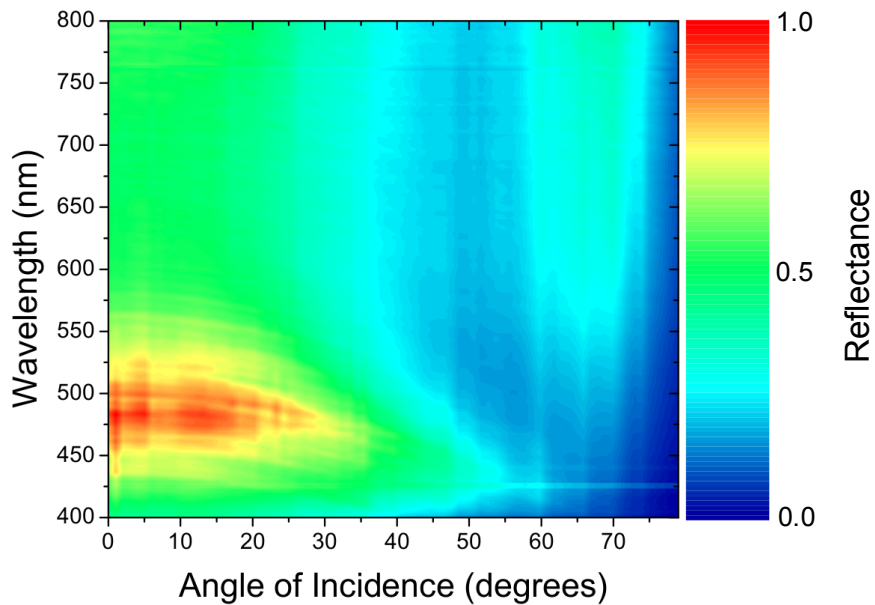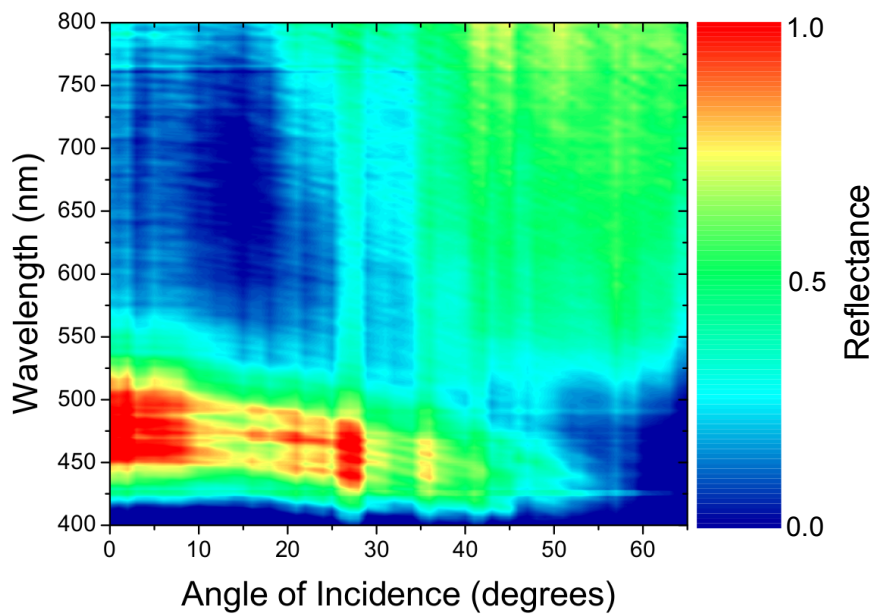
Figure 5.4: Angule resolved reflection spectra for (a) TM illumination and (b) TE illumination. A reflection band is seen in both polarisations around 510 nm which then decreases in wavelength with angle. A secondary mode is exhibited at non-normal angles for longer wavelengths. This mode appears at a higher angle for TM than for TE which appears to be an artefact of the Brewster angle.

(a)

(b)

(c)
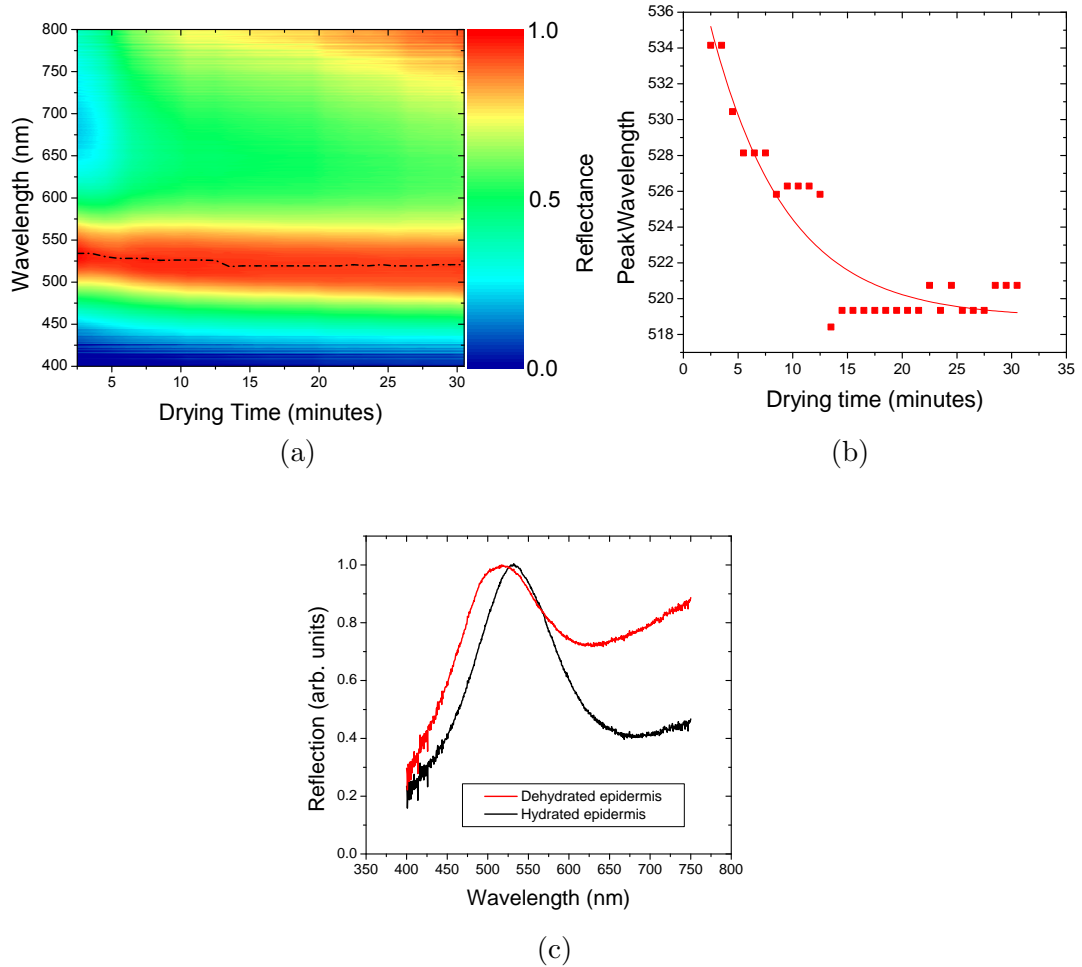
Figure 5.5: (a) The reflection spectra for the seed after being soaked in water for 15 minutes. The reflection spectrum was then retaken every minute afterwards whilst the fruit dried at room temperature, thereby logging the effect of dehydration. The black dotted line tracks the peak reflected wavelength. (b) A graph showing the relationship between the maximally reflected wavelegth and drying time. The addition of water, therefore, is either increasing the dimensions of the structure via swelling of the multilayer, or is increasing the refractive indices of the materials in the system. A combination of both swelling of the geometric dimensions and an increase in refractive index of the materials cannot be ignored either. The red line shows the line of best fit. (c) A comparison in spectra between hydrated and dehydrated epidermis. A higher saturation can be seen when the fruit is hydrated.

the structure would break down, therefore periodicity of the structure would decrease. This would cause the overall colour of the system to be more broadband in character.

Imaging scatterometry was performed only on the dehydrated *M. nobilis* fruit samples (figure 5.6) as it could not be guaranteed that the imaging scatterometry experimental apparatus would not be subject to water damage. The primary beam scatterograms reveal a largley specular reflection of blue light. The specular nature of reflection suggests that the colour is probably due to a planar system such as a multilayer with little diffraction or random scattering properties at visible wavelengths. The primary beam was also used to investigate the reflection pattern at a non-zero angle of incidence, which also showed the expected, specular reflection response of a blue-shift in the perceived colour.

Secondary beam scatterometry performed on the integument of the dehydrated *M. nobilis* fruit (figures 5.6(c) & 5.6(d)) revealed the blue-low angle of incidence response that can be observed macroscopically. The analysis also reveals the broadband, light brown to white response at high angles, also observed macroscopically. The green colour observed macroscopically, however, cannot be seen in the scatterograms. This result whilst not entirely intuitive, could be because of the curved nature of the fruit epidermis and the photonic structure embedded within, since we know that the peak reflected wavelength of the fruit decreases with angle. When the incident secondary beam is polarised, dark patches corresponding to Brewster angle reflections appear. This result indicates that the surface of the integument is fairly smooth in comparison to the size of the beam spot. The dark patch appears at approximately $60°$ in the polarised scatterogram (figure 5.6(d)) and we see a small dip in reflection at approximately $50°$ in the colour plot showing TM polarised reflection as a function of incident angle (figure 5.4(a)). The mean, effective refractive index calculated from these two Brewster angles is $n = 1.46$.

5.3 Structural characterisation

Analysis of the fruit integument using electron microscopy (figure 5.7) reveals that the structure consists of juxtaposed cylindrical multilayers with a high level of periodicity. Optical micrographs reveal the ordering of the cells' juxtaposed orientations shown earlier in figure 5.3(b). SEM cross-sections (figure 5.7) reveal that the structure comprises a mean of 4 layers of cylindrical multilayers across the entire thickness of the fruit's epidermis. Each cylinder has many layers of alternating materials, either wrapped or grown around a central core.

TEM images showing a cross-section of these layers can be seen in figures 5.8 and 5.9. These TEMs show a wood-grain style pattern. TEM analysis reveals that within
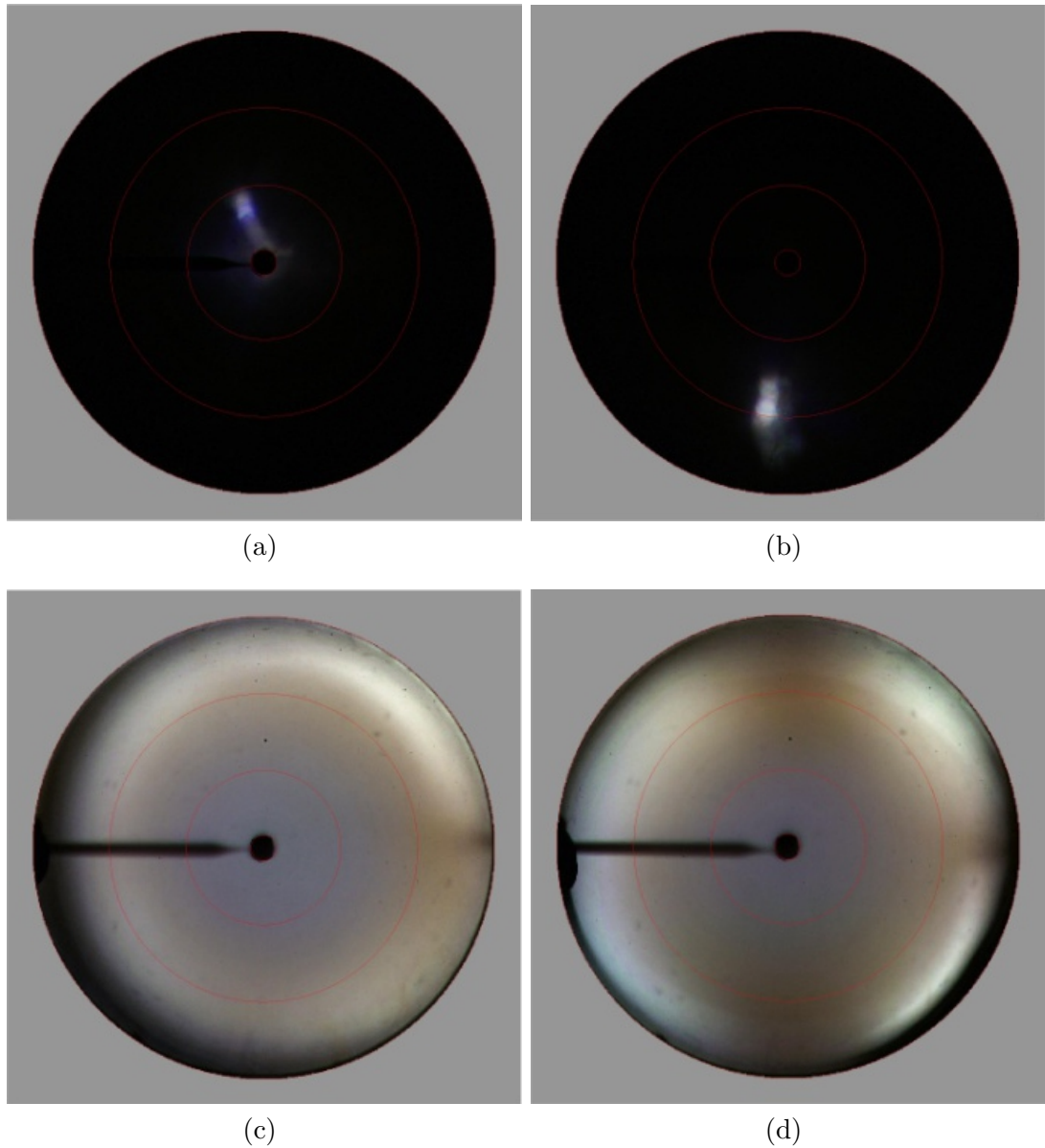
Figure 5.6: Imaging scatterograms of a small section (1 mm diameter) of the dehydrated integument of *M. nobilis*. (a) and (b) show primary beam imaging scatterometry at angles of incidence of 0° and 30° respectively. These two images reveal the largely specular nature of reflection from the fruit. (c) and (d) show secondary beam scatterometry for unpolarised and TM polarisation respectively. The unpolarised scatterogram shows a light blue colour for low angles of incidence and a much more broadband colour for high angles of incidence. In (d) dark patches occur which are representative of the Brewster angle exhibited by the effective medium of the fruit epidermis.
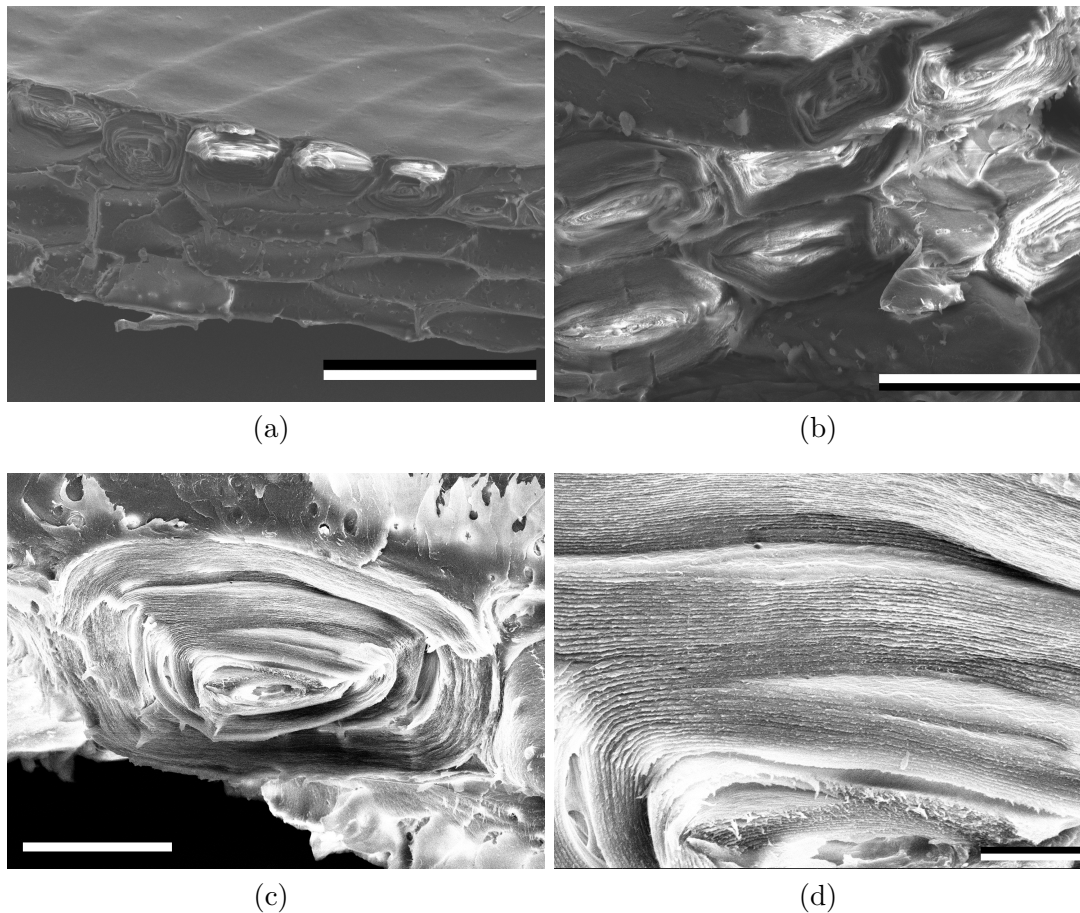
Figure 5.7: Scanning electron micrographs of the epidermis of *M. nobilis*. (a) A cross-section through the entire fruit epidermis showing the the thickness comprises about 4 layers of elongated cells that can be seen in the optical microscopy from above (figure 5.3(b)). (b) Cross-sections through the cells show that they are cylinders that look 'flattened' into almost square shapes. (c) and (d) show cross-sections through a single cell. These images show the layers producing the vivid greenish-blue colour appearance of the fruit. Scale bars: (a) 100 μm, (b) 40 μm, (c) 20 μm and (d) 5 μm.

each cell there is a nano-scaled multilayer with a mean pitch of 180 nm (standard deviation = 28.5 nm, n = 30) comprising alternating layers of 100 nm and 80 nm. The layers are assumed to be similar to, if not the same as, more and less hydrated cellulose with refractive indices of 1.45 and 1.33 respectively [72]. It should be noted that other authors in the field quote a different refractive index of plant cellulose, $n = 1.53$ [73, 109], a value which is higher than the refractive indices used for this investigation. From the TEMs it can also be seen that there are about four layers of cylindrical multilayers making up the thickness of the epidermis.

(a)   (b)

(c)   (d)
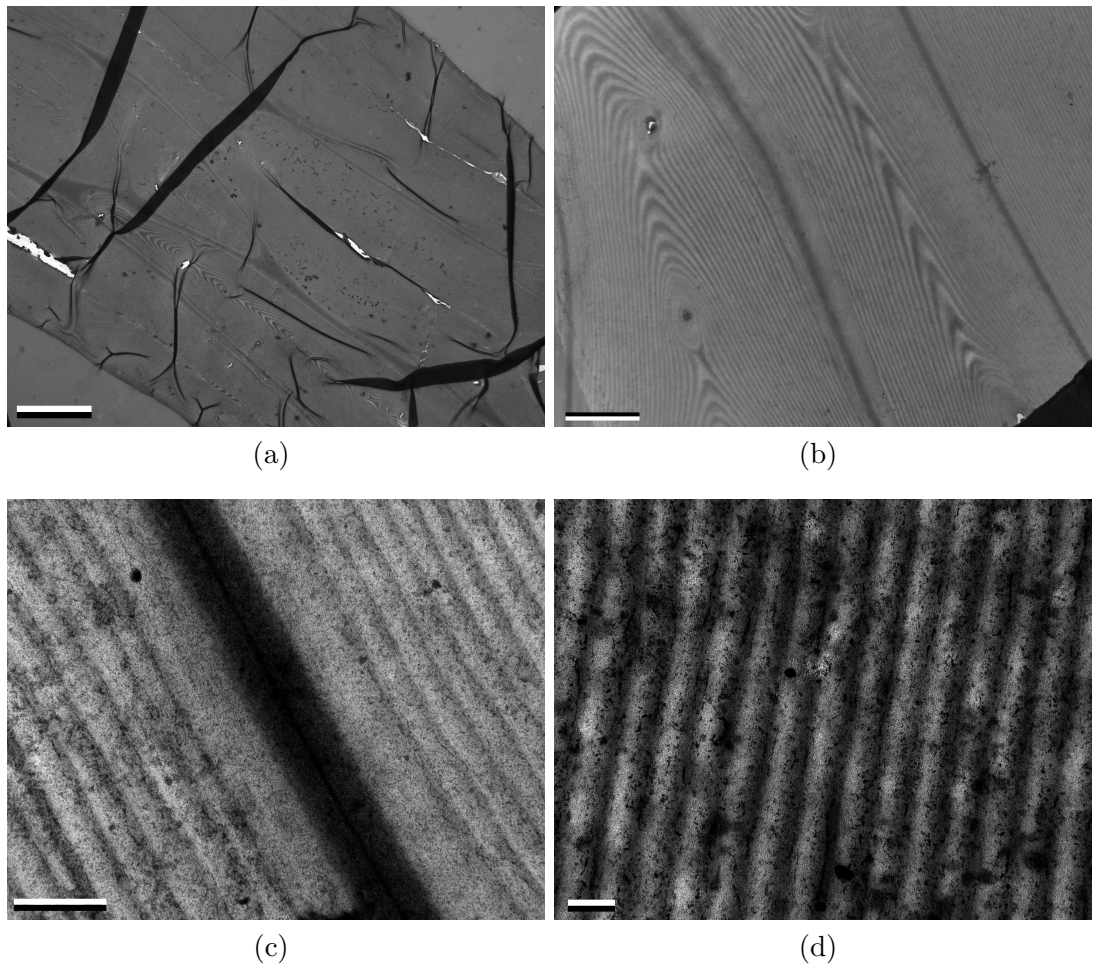
Figure 5.8: Transmission electron micrographs of the epidermis of *Margaritaria nobilis* (a) A cross-section through the entire fruit epidermis showing that the thickness comprises about 4 layers of elongated cells. (b) A cross-section through 2 of the cells showing the layers arranged in a very similar way as the grain pattern of a plank of wood. (c) shows a close-up of the boudary between two cells. (d) A close up of the layers, showing how well ordered the colour-producing multilayer is. Scale bars: (a) 10 μm, (b) 2 μm, (c) 500 nm and (d) 200 nm.

(a)

(b)

(c)

(d)
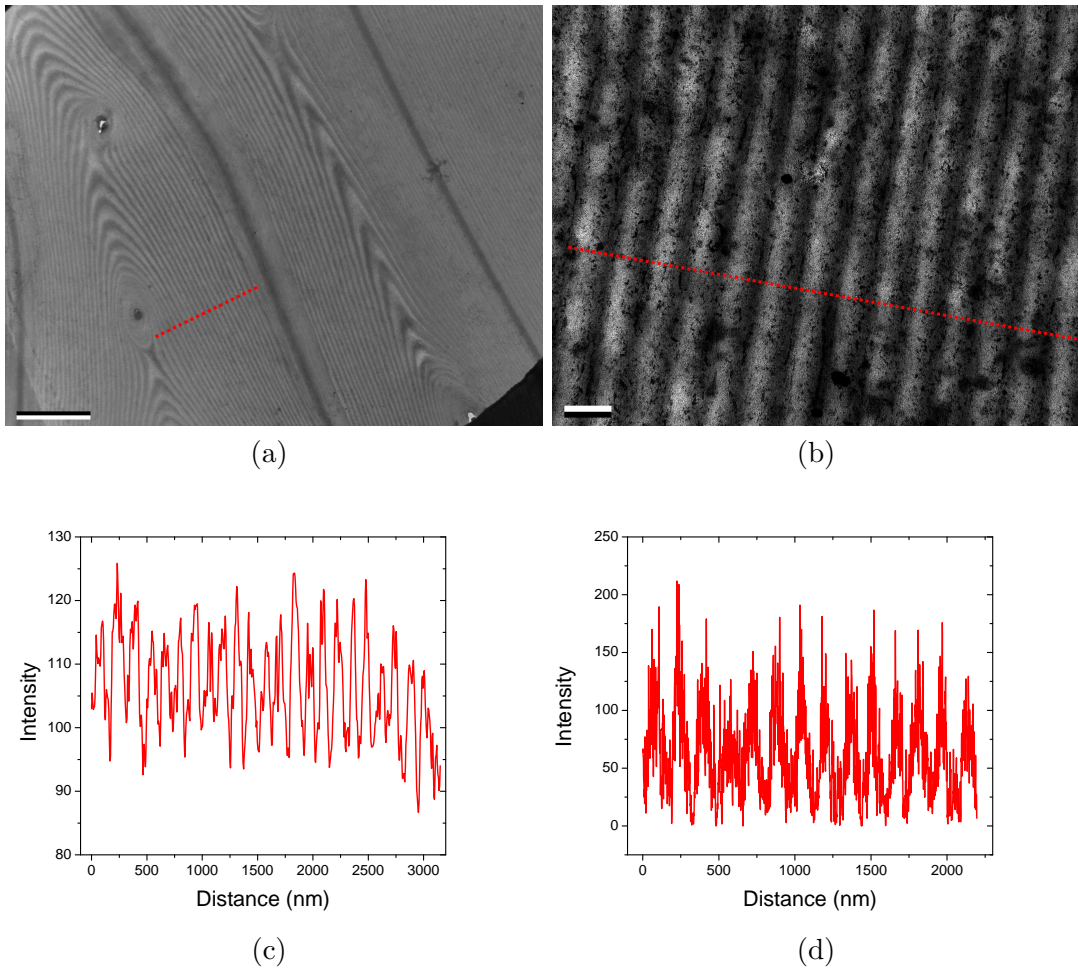
Figure 5.9: (a) and (b) TEMs of a cross-section through the *M. nobilis* fruit's multilayer. (c) and (d) show line plots of intensity, corresponding to the red dashed lines in (a) and (b), respectively. Using the line plots one can measure the periodicity of the structure. Doing this many times and taking a mean, ensures an accurate value, with a meaningful standard deviation. The calculated mean periodicity is 180 nm (standard deviation = 28.5 nm, n = 30). Scale bars: (a) 2 μm and (b) 200 nm.

The cylindrical geometry of the multilayer appears to be the cause of the broadband colour observed at high angles of incidence. This is because the juxtaposed cylinders produce an irregular multilayer due to the varying angle between the multilayer periodicity and the surface normal. This effect can be seen in figure 5.10. The red line in the graph shows a fairly regular cross-sectional profile of the red line in the seed cell illustration, through the centre of the cell. The blue line plot profile, however, shows an irregular periodicity as through a non-centred part of the cell cross-section. It is this irregularity which appears to be the cause of the broadband nature of the fruit's epidermis.

5.4   Synthesising the structure of *M. nobilis*

The remarkable structure exhibited by *M. nobilis* inspired the research group to replicate a synthetic version of the fruit's multilayer that is mechanically tuneable. The mechanical tunability was realised by fabricating the sample out of elastic materials that stretch when strain is applied, thereby decreasing the thickness of each layer, resulting in a blue-shift of the reflection band wavelengths [110]. This work was done with M. Kolle of Harvard University. The cylindrical design was simple to manufacture as an ingenious rolling technique was employed. For ease of replication, and to determine interesting optical effects of the cylindrical nature of the natural structure, single cylindrical multilayer fibres were fabricated.

5.4.1   Manufacturing the synthetic fibres

The first stage of creating the cylindrical multilayer was the creation of a bilayer, which could then be rolled into a cylinder. What we actually end up making is a trilayer where the first layer deposited onto the silcon wafer is a sacrificial, water-soluble layer that is used to lift the bilayer from the wafer before the rolling occurs. The ingredients of the three layers are: Poly(4- styrene sulfonic acid) for the sacrificial, water-soluble layer, polyisoprene-polystyrene triblock copolymer (PSPI) for the first layer of the required bilayer and polydimethylsiloxane (PDMS) for the second layer. The two bilayer materials were chosen for the relatively high refractive index contrast between them. The refractive indices (found using elipsometry performed by M. Kolle, Harvard University, USA) are $n_{PDMS} = 1.41 \pm 0.02$ and $n_{PSPI} = 1.54 \pm 0.02$. The layers were spin-coated onto a silicon wafer substrate. Poly(4- styrene sulfonic acid) at 18 wt % was reduced with water to a 5% solution and then spin-coated onto the wafer. Next a 4 % solution of PSPI in toluene was made and spin-coated on top of the sacrificial layer. The last layer to be spin-coated was a 4% solution of PDMS in

(a)

(b)
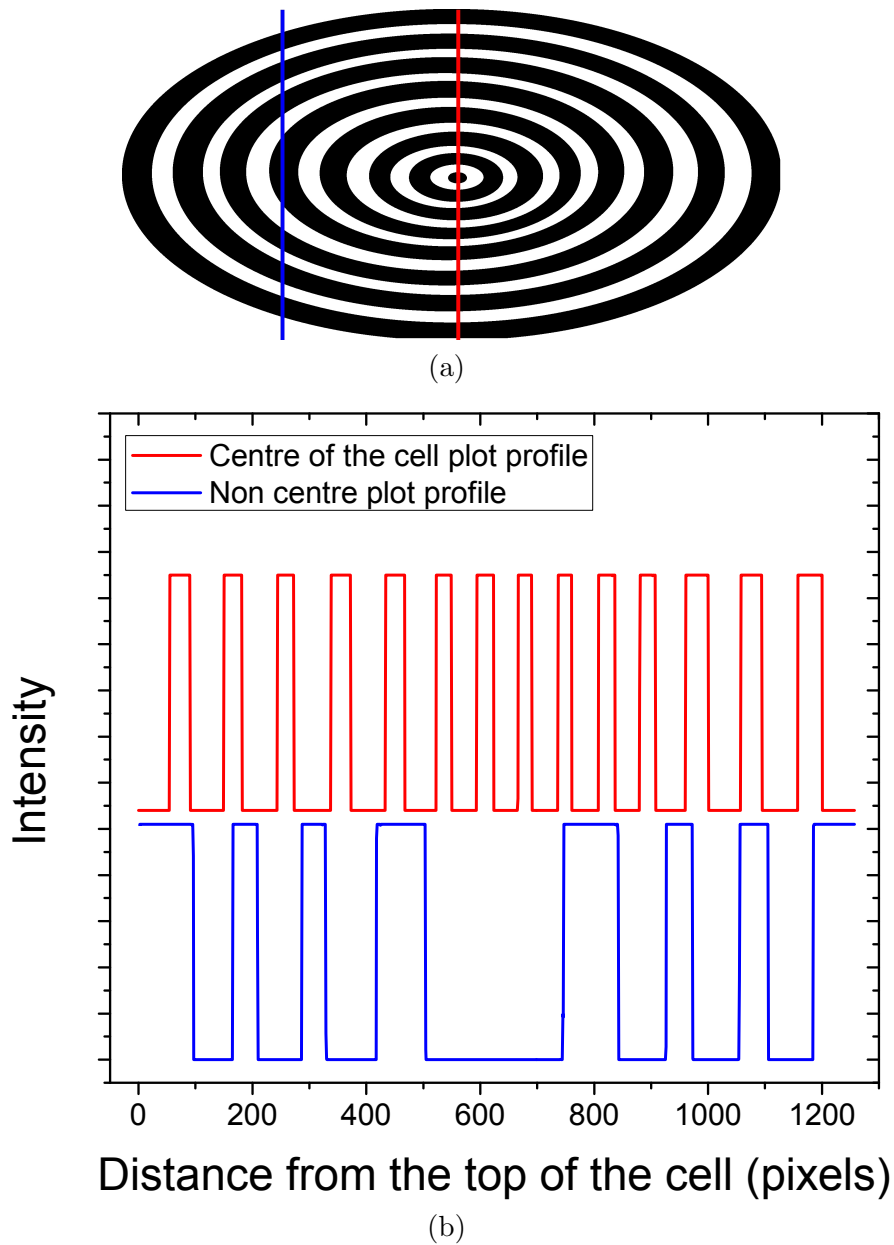
Figure 5.10: (a) A simplified schematic of a single cylindrical multilayer cell cross-section. (b) Plot profiles of two cross-sections through the schematic in (a). The red line cross-section shows a fairly regular periodicity, whilst the blue cross-section shows a far more irregular periodicity, high-lighting a possible reason for the dehydrated fruit's broadband colour appearance.
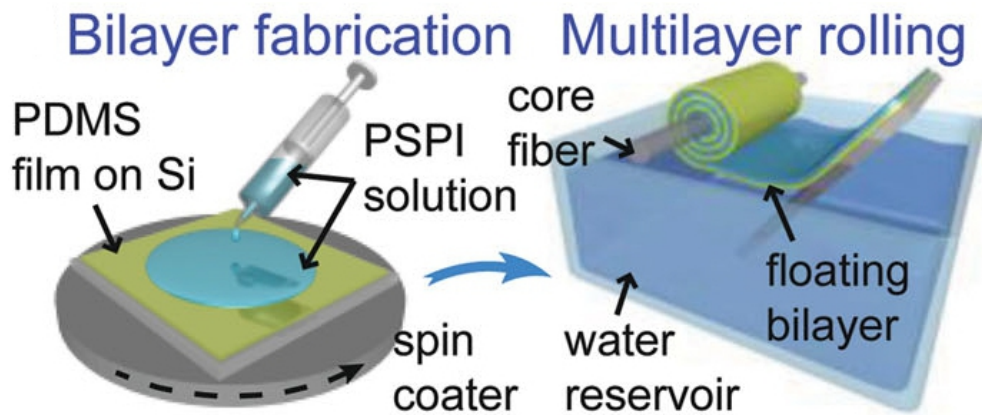
Figure 5.11: A schematic representing how the fibre was fabricated. Firstly a spin-coater was used to make a bilayer on a silcon wafer substrate. The next process was to float the bilayer on the surface of water, at which point a glass core of diameter 10-20 μm was stuck to the bilayer and then twisted allowing the bilayer to roll around the core, producing the concentric, cylindrical multilayer. Images courtesy of M. Kolle, Harvard University, USA.

heptane. A PDMS curing agent was added just before spin-coating to avoid hardening when in storage. The PDMS and PSPI solutions were made to a total of 150 grams to reduce the error in measurements. Once all three layers were spin-coated onto the substrate, the whole fabrication was left on a hot plate to cure for 1 hour.

Once the trilayer was completed, it was scored into 2 cm strips and mounted at an angle in an empty water bath which was then slowly filled up so that the sacrificial layer would dissolve allowing the bilayer to come off and float on the surface of the water. The bilayer was then attached to a glass fibre core with a diameter of 20 μm. The core was then rotated, allowing the strip of bilayer to wind around the core, producing a cylindrical multilayer comprising up to 200 layers. A schematic of this process is found in figure 5.11.

The cylindrical multilayer fibres were soaked in hydrofluoric acid to dissolve away the glass core, thereby allowing access to the stretchability of the polymer materials. One fibre, however, did not have the core dissolved, instead the core was snapped in one position to allow a stretching of that part of the fibre for the purpose of obtaining reflection spectra as a function of applied strain.

5.4.2 Structural characterisation of the synthetic fibres

The fibres were structurally characterised using a Zeiss Supra55VP scanning electron microscope instrument after sputter coating the samples with a 3-5 nm thick film

of platinum. Such structural analysis revealed a well ordered cylindrical multilayer has been achieved at room temperature manufacturing conditions (figure 5.12). The dimensions identified from the SEM micrographs are: $d_{core} = 14$ μm, $d_{PDMS} = 240$ nm and $d_{PSPI} = 100$ nm.

It can be seen in some of the SEM micrographs that where the core has snapped, the central layers have distorted producing a non-cylindrical core to the system (figure 5.12(b)). However, the outer layers still hold their ordered concentric multilayer characteristics.

5.4.3 Optical characterisation of the synthetic fibres

The three intial synthetic fibres exhibited three different lattice constants, thus providing three different colours as seen in figure 5.13. The three different colours exhibited are blue green and red, thus we know that we can easily make these fibres to reflect any part of the visible spectrum. The observed colour change when the fibres were stretched was a consistent blue shift for increasing strain. Figure 5.13 also shows the transmitted colours of the three fibres and, as expected with low loss materials, the colours are approximately the complimentary colours of the reflected spectra. Some of the images show an interference pattern manifesting as dark and light stripes running down the length of each fibre. This can be attributed to the curved nature of the fibre and the multiple reflections that occur as a result.

The stretch-tunable fibre sample that had a part of the glass core snapped was mounted into a device that clamped the fibre on both sides of the snapped part. The clamps were then pulled apart by 5 μm at a time, thus stretching the fibre. The fibre mount was then placed into an MSP system which recorded the spectra at different levels of strain. The main result observed in the strain-resolved spectra is that the fibres are able to stretch to over double their original length, providing a blue-shift in maximally reflected wavelength of over 200 nm. This change in colour can clearly be seen in figure 5.14(a). The unstretched fibre shows a green colour which, as stretching occurs, changes to blue, then to violet, purple, red, yellow and back to green. The fact that the colour goes through the spectrum and returns to green can be explained by higher order reflection modes being blue-shifted into the visible spectrum from the infra-red regime. The reflection spectra quantifying this result also reveal a third reflection band across the visible regime. Each one of the reflection bands blue-shifts with increasing strain, as can be seen clearly when the maximally reflected wavelength is plotted against strain (figure 5.14(c)). Reflection spectra as a function of applied strain were recorded 5 times on different parts of the fibre and the standard deviation of the maximally reflected wavelengths were recorded, these can be seen as error bars

(a)

(b)

(c)

(d)
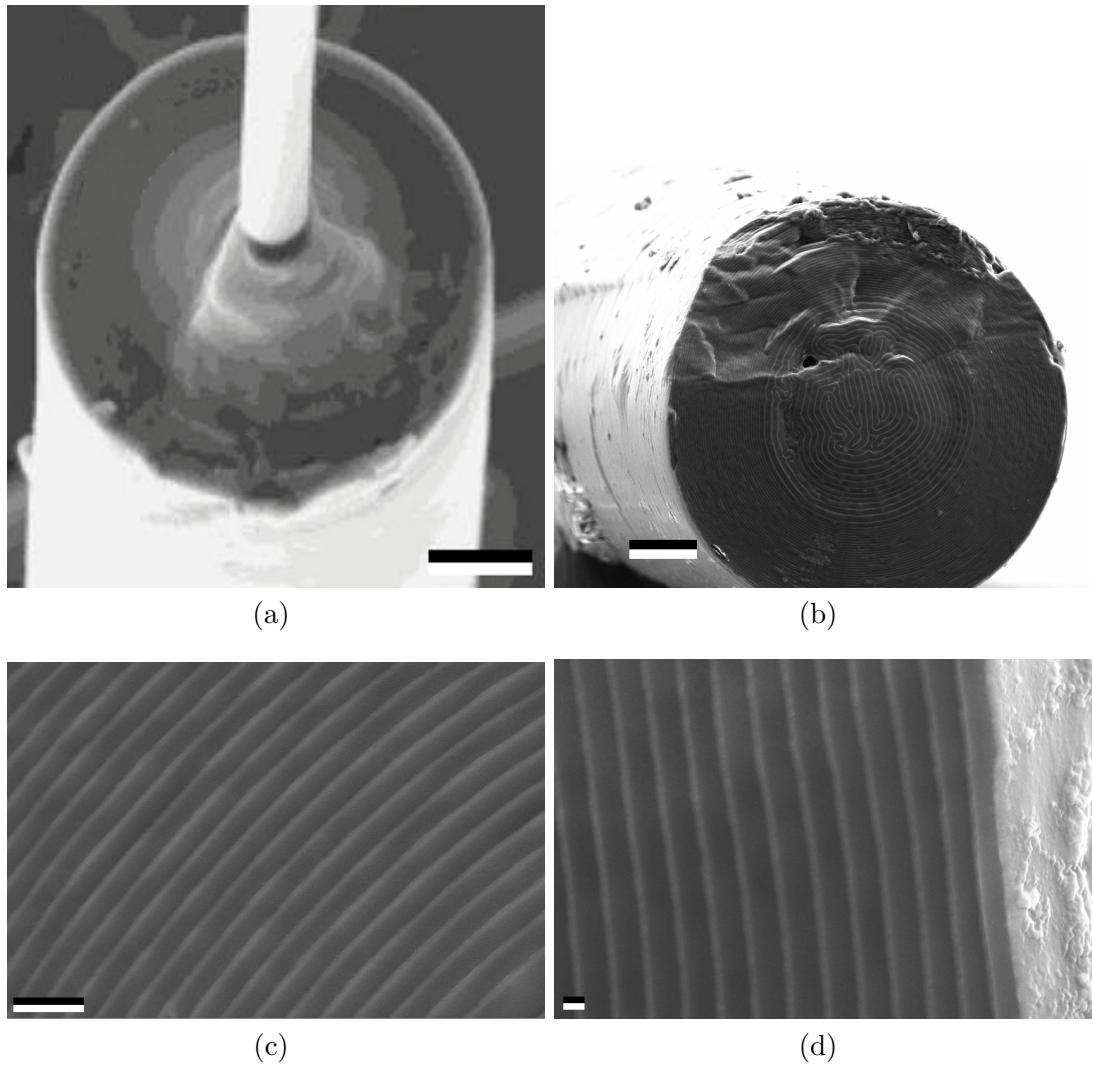
Figure 5.12: Scanning electron micrographs of the synthetic fibre system. (a) shows the glass fibre core surrounded by the cylindrical multilayer. (b) shows the centre of the fibre when the core is removed, the hole is filled in by the multilayer which has to distort its inner layers to fill the gap. (c) shows the highly ordered multilayer can be clearly seen on the micron scale. (d) A close-up of the multilayer near the edge of the fibre. Scale bars (a) 20 μm (b) 10 μm (c) 1 μm and (d) 200 nm. All SEMs taken by A. Lethbridge and M. Kolle
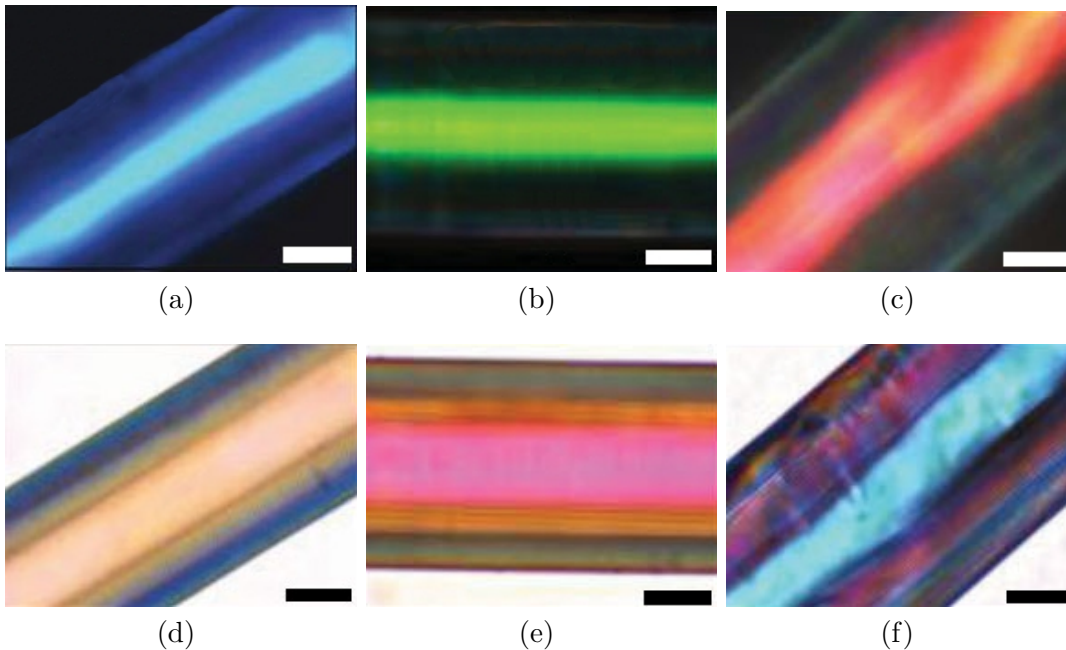
Figure 5.13: The *M. nobilis*-inspired synthetic fibres as photographed under a microscope. (a), (b) and (c) show reflection microscopy of three fibres with different multilayer dimensions. (d), (e) and (f) showing the corresponding transmission micrographs, showing the complimentary colours of the images above. Scale bars (a-f) 20 μm. Images courtesy of Mathias Kolle, Harvard University, USA [111]

in figure 5.14(c).

5.5 Computational modelling of the *M. nobilis* fruit epidermis and the synthetic fibre system

To confirm the understanding of the two systems, computational modelling was required to show that the optical effects are coming from the parts of the structure that we expect. For the natural sample, simple planar multilayer modelling was used to confirm the dimensions taken from TEM imaging. For the synthetic, cylindrical multilayer modelling, however, more complicated, finite difference time domain (FDTD) modelling was used so that the electric fields in the system could be analysed, allowing a more in-depth investigation into the cylindrical nature of the multilayers found in the fruit of *M. nobilis* and also in the fibres inspired by the fruit.
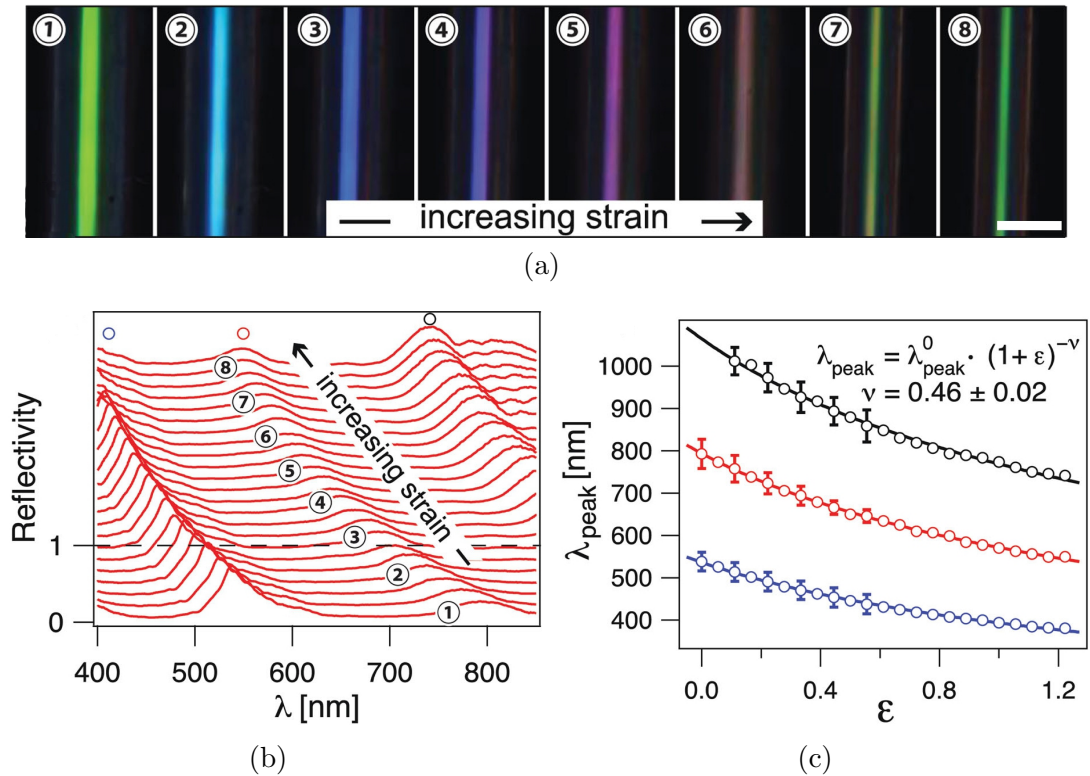
Figure 5.14: (a) Optical micrographs of the fibre under increasing strain from left to right. The expected decrease in wavelength with an increase in strain is clearly observed. (b) Optical spectra of the synthetic cylindrical multilayers. Three reflection bands can be observed in the optical regime. All three show a blue-shift in the maximally reflected wavelngths as the strain is increased. (c) A graph showing the change in wavelength for the three reflection bands exhibited in (b). The error bars in (c) correspond to the standard deviation of the position of the maximally reflected wavelengths recorded over five different stretch experiments. Images in (a) taken by A. Lethbridge and M. Kolle, data in (b) taken by A. Lethbridge and M. Kolle and the graph in (c) was prepared from the data in (b) by M. Kolle. Scale bar: 50 μm.

5.5.1 Multilayer modelling

Numerical characterisation of the simplified, planar version of the *M. nobilis* multilayer structure was performed by TFCalc. The model consisted of two alternating layers with dimensions of 100 nm and 80 nm. Theses dimensions were discovered after structural analysis was performed on TEM cross-sections through the epidermis of the *M. nobilis* fruit as shown in figure 5.9. During this analysis it was also discovered that there were approximately 200 layers through the entire epidermis, comprising 4 cells thick and each cell comprising approximately 50 layers. The two different layers were assigned refractive indices of 1.33 and 1.45 respectively. These refractive indices were taken from

the literature [72].

Results from the multilayer modelling reveal that a bandgap centred around 500 nm exists and is in agreement with experimental data from the fruit of *M. nobilis* (figure 5.4). This band gap reduces in wavelength as the angle of incidence is increased, a result that agrees with theory as well as the natural *M. nobilis* specimen. There is a Brewster angle present in the modelling for the TM polarisation, this Brewster angle can also be seen in the experimental reflection data of the fruit, shown in figure 5.4(a) and also the imaging scatterometry of the fruit shown in figure 5.6(d). A disagreement between simple, planar multilayer modelling and the optical interrogation of *M. nobilis* is the full-width half-maximum (FWHM) of the reflectance peak. Reflectivity measurements taken from the fruit's epidermis yield a much more broadband response than the measurements taken from the computational simulations. An obvious cause of this discrepancy is that the simplified model comprises a system of 200 layers with perfect order, whereas the natural *M. nobilis* system contains a degree of variation to its order and there is also the fact that the multilayers are ordered in cylinders so the layers that the electromagnetic radiation interacts with will vary through the structure, even at normal incidence. A high FWHM can be associated with a high level of order within the system which is why the natural system does not exhibit such a high FWHM as the model.

5.5.2 Cylindrical multilayer modelling

Cylindrical multilayer modelling of the system was performed by M. Kolle, the collaborator on this project, using the finite difference time domain (FDTD) method of modelling, utilizing MEEP by MIT [97].

The MEEP modelling has shown agreement with the experimental results and has also revealed that the cylindrical geometry has produced a lensing effect of the transmitted waves (figure 5.16(b)). This figure illustrates what happens when a plane wave impinges onto a multilayer fibre. We initially see the reflection spread out isotropically as the wave hits the curved, upper-surface of the fibre. A significant amount of light is transmitted and we see the *E*-fields converge to a focal point shortly after the waves pass through the fibre (figure 5.16(b)). This indicates that the circular structure of the fibre creates a lensing effect. The simulated reflection and transmission dispersion plots (figures 5.16(d) and 5.16(f)) show good agreement with the band-gap energies in the experimental results (figures 5.16(c) and 5.16(e)). The band-gaps shown in the experimental results, however, show less intense and broader peaks than the modelling. This result is expected as the SEMs of the synthetic fibres show that the system is not perfectly ordered (figure 5.12).
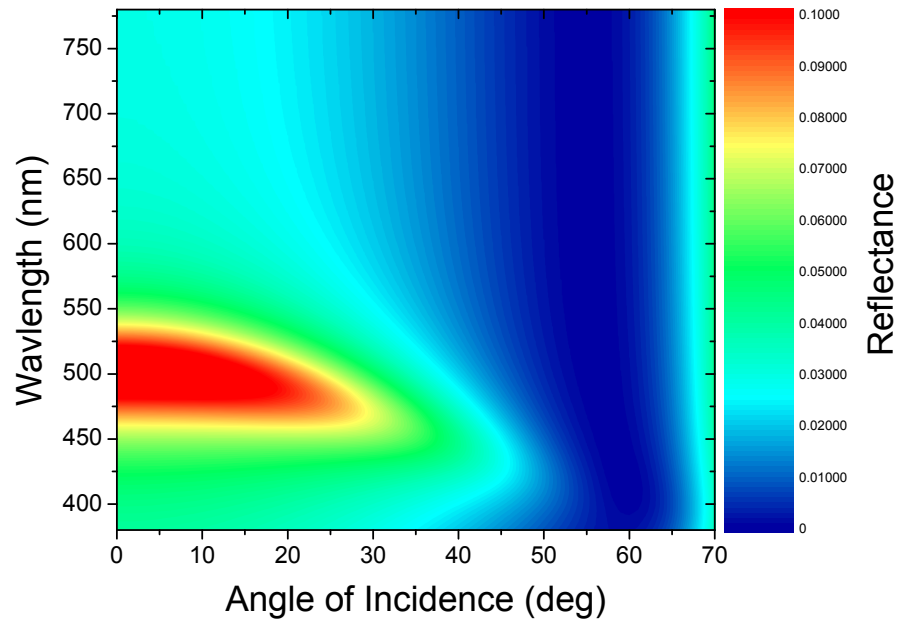
(a)
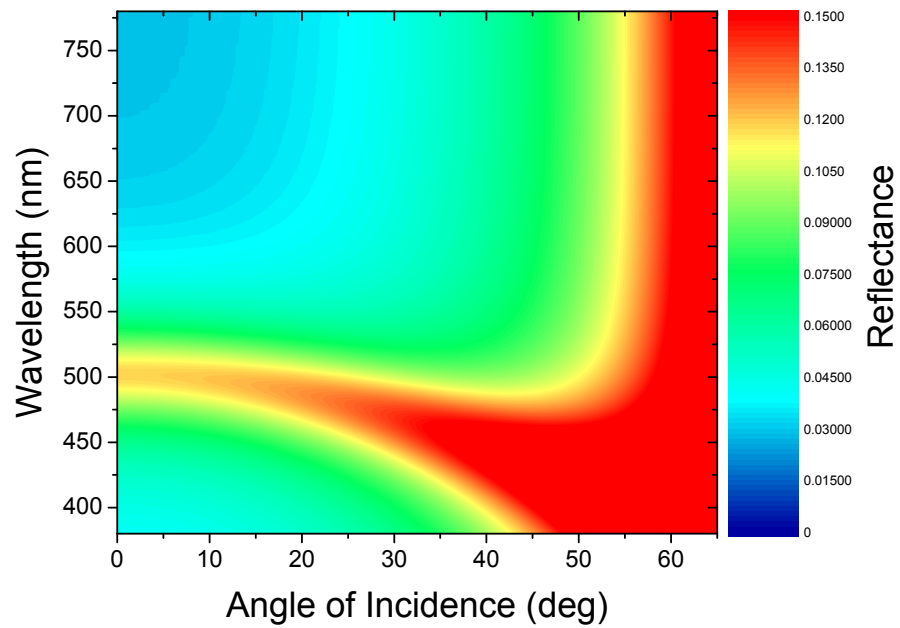
(b)

Figure 5.15: Simplified planar multilayer computational modelling of the structure found in *M. nobilis*. (a) TM polarisation modelling of the multilayer exhibiting a Brewster angle manifested as a dip in reflection. (b) TE polarisation modelling of the multilayer. Both polarisations show good agreement with the experimental data shown in figure 5.4

(a) (b)

(c) (d)

(e) (f)
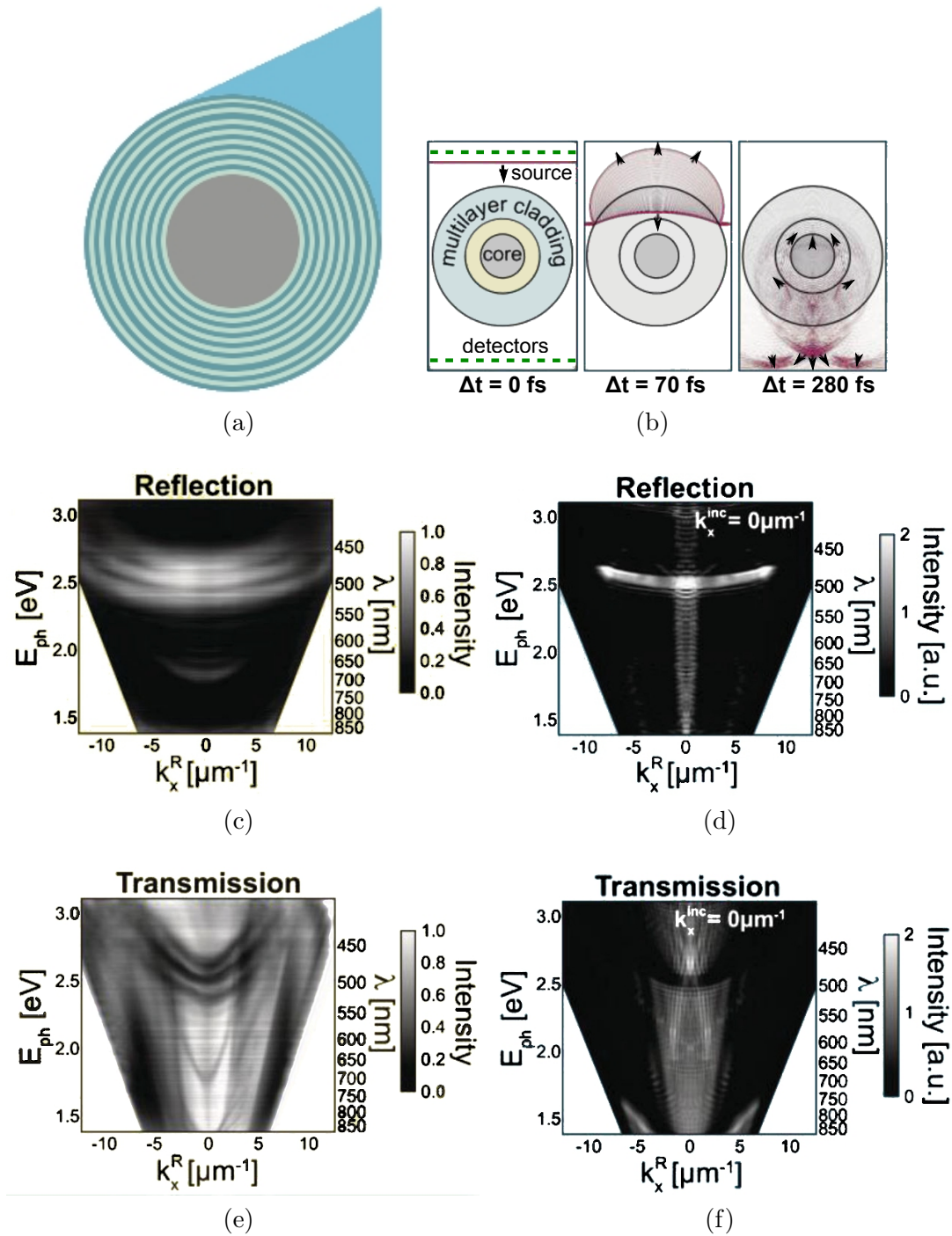
Figure 5.16: Simplified cylindrical multilayer computational modelling of the fibres inspired by the fruit of *M. nobilis.* (a) Simple schematic of the model used in the MEEP simulations. (b) The resulting electric field distribution of the electromagnetic waves impinging on, reflecting from and transmitting through a cross section of the fibre. The arrows indicate the direction of propagation (the wavevector) of the electromagnetic radiation. (c) Experimental and (d) simulated reflection band plots obtained from the cylindrical multilayer fibres. (e) Experimental and (f) simulated transmission band plots for the cylindrical multilayer fibres. Images and graphs courtesy of Mathias Kolle, Harvard University.

5.6 Conclusion

It has been shown using optical and structural analysis that *M. nobilis* exhibits structural colour. The reflected colour of the dehydrated fruit comprises a greenish-blue colour at normal incidence and a broadband colour at high angles. This optical response can be altered by soaking the fruit in water, the response then is a much more saturated colour, much like when the fruit first falls out of the tree. This change in response can be credited to water infiltrating the multilayer structure and changing the dimensions and/or the refractive indices of the system. It has also been discussed how the black seeds that lie under the epidermis absorb a large proportion of the transmitted light, thereby reducing back-reflections which would otherwise cause a diminished saturation in the resultant colour. This produces an evolutionary advantage as the fruit's colour is more striking and, therefore, more conspicuous. The increase in visibility will raise the probability of seed dispersal as more birds and other possible seed dispersing vectors will be more likely to see the fruit. Simple planar multilayer computational modelling using the parameters obtained from TEM analysis has yielded maxima in reflection which are consistent with the experimentally obtained reflection spectra at normal incidence. The species *Euploaea core* exhibits a gold like mirror appearance when hydrated. This has been explained by a high number of alternating layers (A and B) where the thickness of layer A remains constant and the thickness of layer B fluctuates, allowing a more broadband reflection [17]. Here we draw parallels as a similar effect is believed to arise in *M. nobilis* from the cylindrical nature of its multilayer geometry as the path light may take will be more convoluted than that of a planar, multilayer structure. This could possibly create an effective chirping of the multilayer causing a more broadband colour response.

The juxtaposed cylindrical multilayers may also offer another advantage. If the multilayer were planar and uniform across the entire skin of the fruit, then the skin might not be as strong as the configuration exhibited. The juxtaposed cylinders are believed to offer mechanical strength to the epidermis whilst not compromising on optical quality.

The greenish-blue iridescence of *M. nobilis*, when compared to the blue iridescence of the fruit from the *Polia* tree [73], reveals some interesting hypotheses about the evolutionary origins of the two fruits. The *Polia* tree comes from the African continent and the purpose of the colouration is suggested to be the same as that of *M. nobilis* where the colouration is used to attract the attention of birds who then eat it and disperse the seeds in their excrement. This is interesting because, unless a bird migrated from South America to Africa or vice versa, then the two species have developed, via evolution, the same method of seed dispersal completely independently.

5. A detailed study of *Margaritaria nobilis* and stretch-tuneable polymer replicas

The synthetic fibres produced showed high order in the SEMs of the cross section (figure 5.12). This result shows that this is a reliable, inexpensive method of manufacture. An advantage this manufacturing technique holds over the drawn fibre technique [112, 113, 114] is that by rolling, the fibre can be made at room temperature. One disadvantage of this system is the doubling-up of the layers towards the centre of the fibre if care is not taken to make sure the glass fibre is placed at the very end of the bilayer strip during the manufacturing process. Each fibre can be mechanically stretched to over twice its orginal length. Such a deformation yields a blue-shift in wavelength of over 200 nm towards the blue end of the spectrum. This compliance and colour shift together show that multilayer fibres made in this way could be utilised in industry for a myriad of purposes such as dynamically coloured clothes and high resolution stress testing. The manufacturing process can easily be scaled up to allow for longer fibres to be made. The circular nature of the fibre cross sections produces a lensing effect of transmitted light, hinting at other technological advantages. A lens that will change its focal length and transmission wavelengths when mechanical deformations are applied.

Chapter 6

Novel hybrid 3D photonic crystals inspired by the striking iridescence of *Torynorrhina flammea* beetles

6.1 Introduction

In this chapter a detailed study of four beetles from the *Torynorrhina flammea* sub-species is presented. An optical interrogation is performed on the beetles, followed by an analysis of the structures that produce the optical effects. The latter sections describe how the *T. flammea* beetles inspired the manufature of a synthetic analogue of the natural system The synthetic systems were then analysed optically and numerical calculations were performed to strengthen the general understanding of these systems.

Torynorrhina flammea beetles are found naturally in Thailand. Three known subspecies called; *T. f. violets*,*T. f. chicheryi* and *T. f. flammea* were used in this investigation. Both the adult and juvenile form of *T. f. flammea* were chosen for this investigation, totalling four specimens (fig. 6.1). The vivid colours displayed by the four beetles are the result of electromagnetic radiation reflecting from different interfaces in the structure, which then interfere to produce favourable reflection of particular wavelengths of light over others. The maximally reflected wavelength of such structures are dependent on the dimensional and material parameters of the system. Therefore, the difference in colour between the *T. flammea* subspecies can be attributed to slight variations of the dimensions of the structures embedded in the beetle elytra. This behaviour of photonic crystals is well known [75]. The *T. flammea* beetles were chosen

for investigation, largely because of the very saturated, or pure, colours they all exhibit. This was the motivation for a detailed analysis of the *T. flammea* species. Inspiration to produce the synthetic replicas was taken to improve the understanding of the optical performance of the structures.

6.2   Optical characterisation of the multilayer structures

The reflection spectra shown in figure 6.2 show the high purity of colour, manifested here as tall thin reflection peaks.

The four *T. flammea* beetles produce high quality factor (Q-factor) resonances at four different wavelengths. A quantitative analysis of the Q-factors obtained from reflection spectra of *T. f. violets*, *T. f. chicheryi*, *T. f. flammea* (juvenile) and *T. f. flammea* (adult) are shown in table 6.1. The Q-factors are not high when compared to synthetic sytems [84, 116, 117], however, for a natural system the peaks are very sharp, indicating highly saturated colours with high Q-factors. Optically speaking, the Q-factor is a measure of how monochrome a colour is. In this case it is calculated as a ratio of the resonant frequency to the bandwidth [75] (It can also be a ratio of the maximally resonant wavelength to FWHM of the band gap) and a high Q-factor indicates a pure, saturated colour. The high Q-factor responses can be accredited to a high level of order, a small dielectric contrast, a high number of lamina in the multilayer stack or a combination of the above. The TEM images of the beetle (figure 6.5) show that there is a high level of order for a natural system. The TEM also provides evidence for a high number of lamina, with over 100 layers, a number which has only previously been reported in very few systems [118].

A brief look at several different structurally coloured beetles, already reported in the literature [12, 54, 119, 120, 121] reveals the Q-factors of the reflectance peaks of seven different beetles, as shown in table 6.1. This table reveals a mean Q-factor of the *T. flammea* beetles to be 17.3 and for the seven previously reported beetles a mean Q-factor of 7.4. Speculation into the evolutionary advantage of the high Q-factor structures exhibited by the *T. flammea* beetles may reveal that they serve a communication purpose. Vivid, optical communication of this type has been reported elsewhere to help conspecifics find each other in dense, tropical jungles [18, 24, 92].

Each of the four beetles exhibit iridescence, namely the peak reflected wavelength blue-shifts as the angle of incident light is increased. This can be seen clearly in figure 6.3 which shows angle-resolved reflection spectra. Each graph shows the characteristic narrow reflection band.

The scatter plots in figure 6.4 show some peculiar features. There appears to be a broadband colour for normally incident light, followed by a dip in reflection for all

(a)　　　　　　　　　　　　　(b)

(c)　　　　　　　　　　　　　(d)
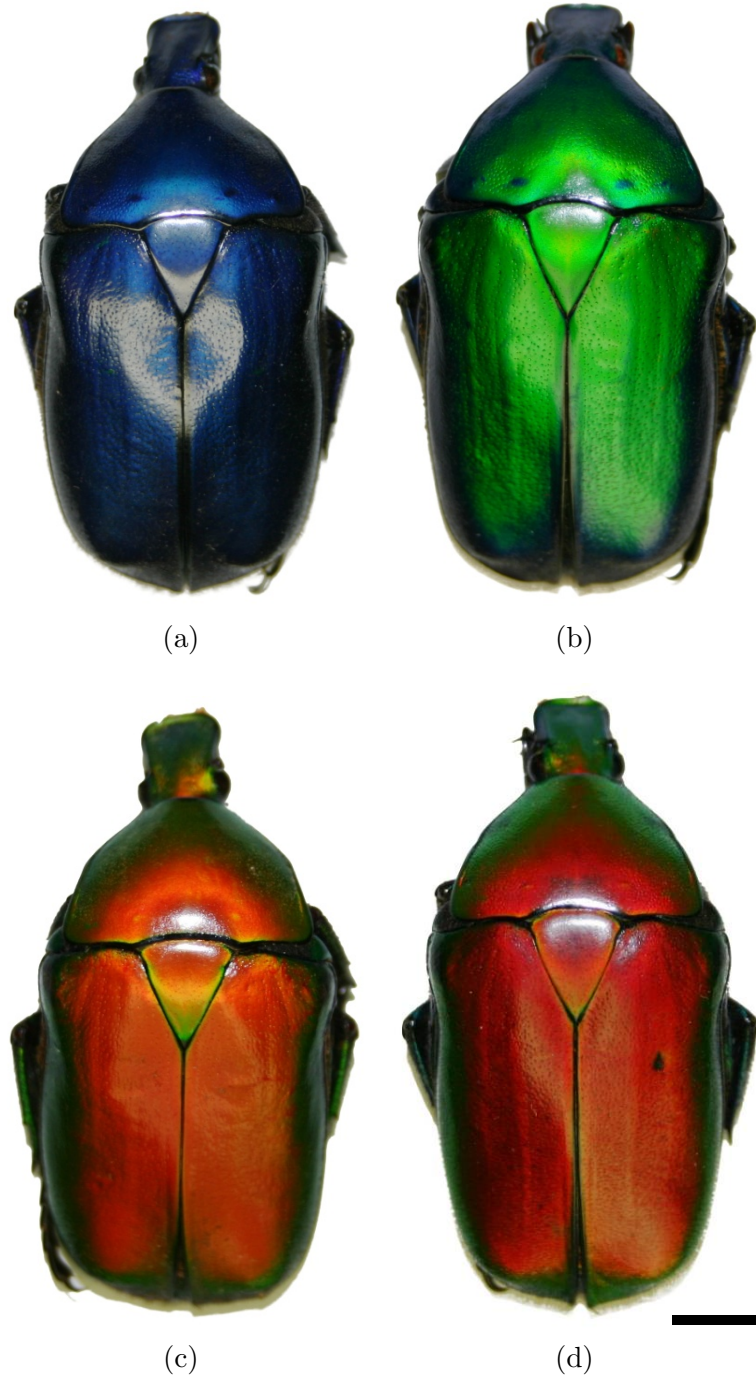
Figure 6.1: Four subspecies of *Torynorrhina flammea* beetles, (a) *T. f. violets*, (b) *T. f. chicheryi*, (c) *T. f. flammea* (juvenile) and (d) *T. f. flammea* (adult). Scale bar: 5 mm.

6. Novel hybrid 3D photonic crystals inspired by the striking iridescence of *Torynorrhina flammea* beetles

(a)   (b)
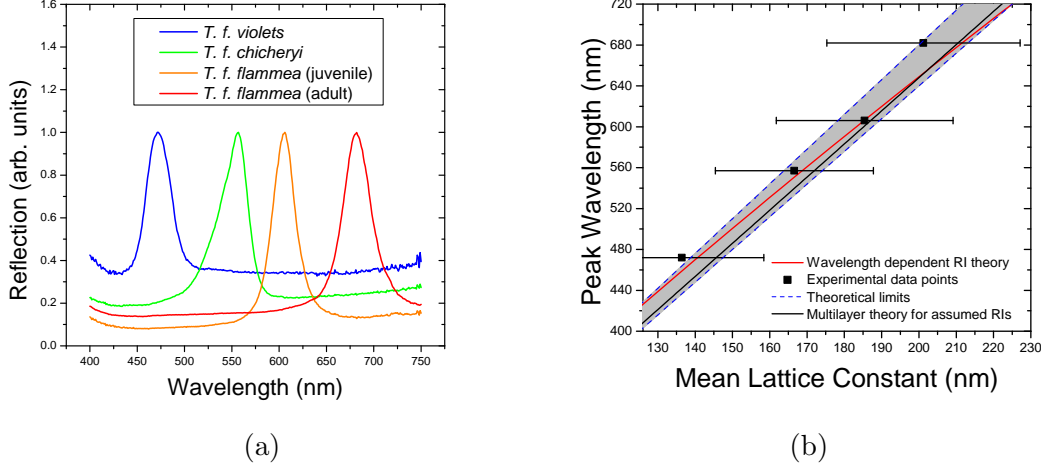
Figure 6.2: (a) Spectra obtained using MSP on small sections of the beetles' elytra. They show the high Q-factor nature of the reflection peaks. (b) A graph showing the relationship between the lattice constant of the four *T. flammea* beetles and their peak wavelength. The black line shows the theory for a wavelength-independent refractive index. The red line shows the theory for a wavelength-dependent refractive index. The range of refractive indices for the red line are $1.65 \geq n \geq 1.8$ for the high index regions and $1.55 \geq n \geq 1.6$ for the low index regions, these values are taken from the literature [115]. The grey area between the blue dotted lines shows the theoretical limits using the highest and lowest possible values of refractive index.

Table 6.1: *Q*-factors of the reflectance peaks from the *Torynorrhina flammea* beetles and seven structurally coloured beetles from the literature [12, 54, 119, 120, 121].

Species	*Q*-factors	Species	*Q*-factors
T. f. violets	16.5	*C. obscuripennis* [12]	5.4
T. f. chicheryi	11.4	*P. boucardi* [119]	9.6
T. f. flammea (juvenile)	21.6	*E. schoenherri* [120]	6.6
T. f. flammea (adult)	19.6	*P. monoliferus* [120]	7.3
		E. pulcher [120]	6.6
		C. raja [54]	8.9
		L. augusta [121]	7.1

wavelengths, and then an increase again around the reflection band area. This would seem to suggest a diffraction-like property of the system, with a specular white spot with first order diffracted modes either side, exhibiting the colour of the assumed multilayer. To gain a further understanding of the optical characteristics of the *T. flammea* beetles, the structure responsible for the colour appearance needed to be analysed as well.
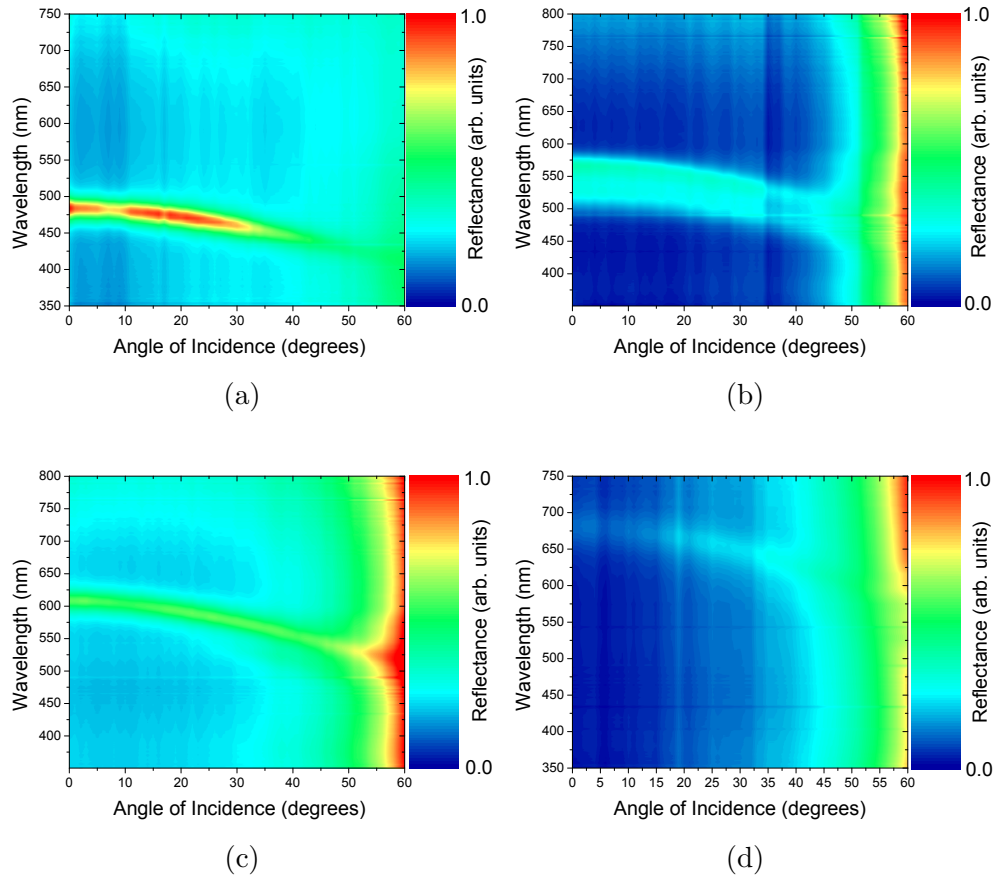
Figure 6.3: Specular reflection spectra as a function of incident angle for the four *Torynorrhina flammea* beetles. (a) *T. violets*, (b) *T. chicheryi*, (c) *T. flammea* (juvenile) and (d) *T. flammea* (adult).

6.3 Structural characterisation of the *T. flammea* beetles

TEM analysis reveals all four beetle structures to be fundamentally similar, with each structure comprising three main sections (figure 6.5). The section closest to the surface of the elytra comprises three large layers (dimensions shown in figure 6.7). The second section down is the multilayer structure responsible for the colour of the four beetles. This section comprises between 100 and 120 layers of alternating chitin and melanoprotein [118]. The third section of the structure comprises a multilayer but with the pitch increasing with the depth of structure. This section is assumed to have little or no effect on the overall colour of the system. In section 2, the multilayer, there is an array of rods permeating down through the structure perpendicularly to the elytral surface. The biological function of the rods is uncertain, but it does produce some
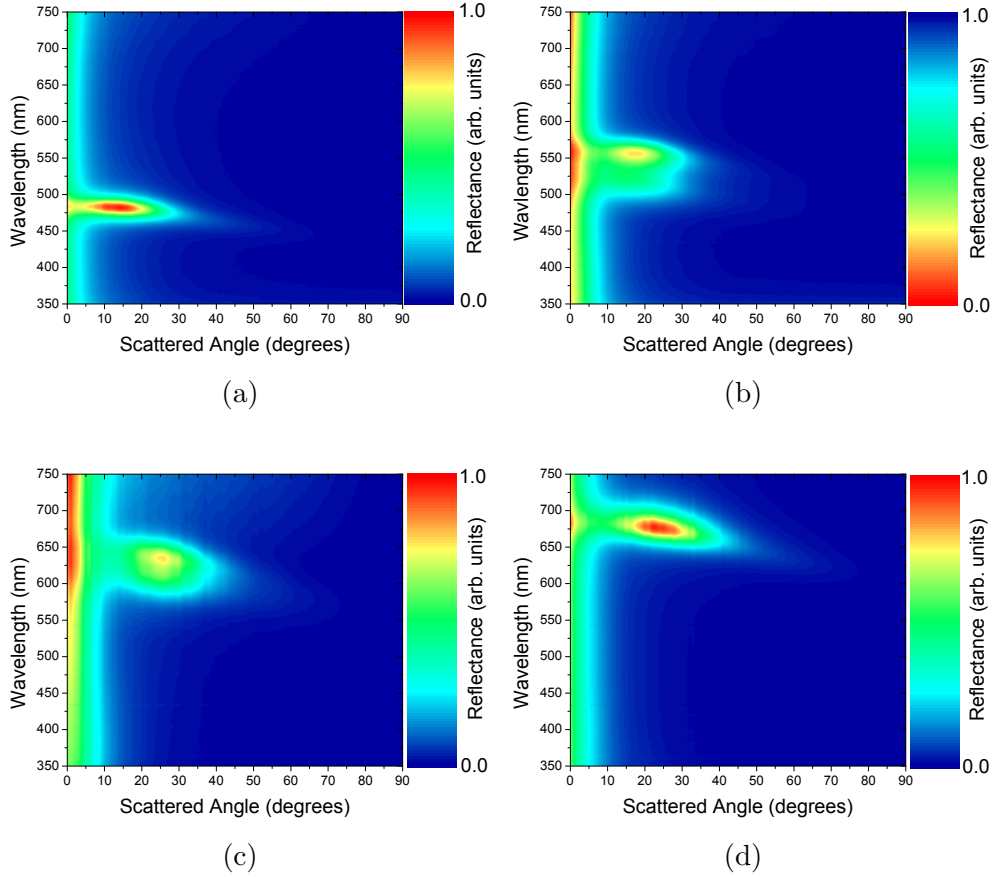
Figure 6.4: Reflection spectra as a function of scattered angle for normally incident illumination for the four *Torynorrhina flammea* beetles. (a) *T. violets*, (b) *T. chicheryi*, (c) *T. flammea* (juvenile) and (d) *T. flammea* (adult).

interesting optical effects. The rods are arranged in a close-range hexagonally-ordered fashion, when viewed normally to the surface. The rods are assumed to be a combination of both melanoprotein and chitin because of the contrasts shown in the TEM images. Due to the plane of periodicity of the hexagonal array being orthogonal to the periodicity of the multilayer, the structure exhibits periodicity in all three spatial dimensions, therefore one can say that this structure is a 3D hybrid photonic crystal. This type of structure is rarely seen in biological systems.

Each beetle has a characteristic peak wavelength as shown in figure 6.2(b) that is linear with respect to the lattice constants found in each beetle using TEM analysis. This result confirms the well-known theory that the Maxwell equations are scalable [75].
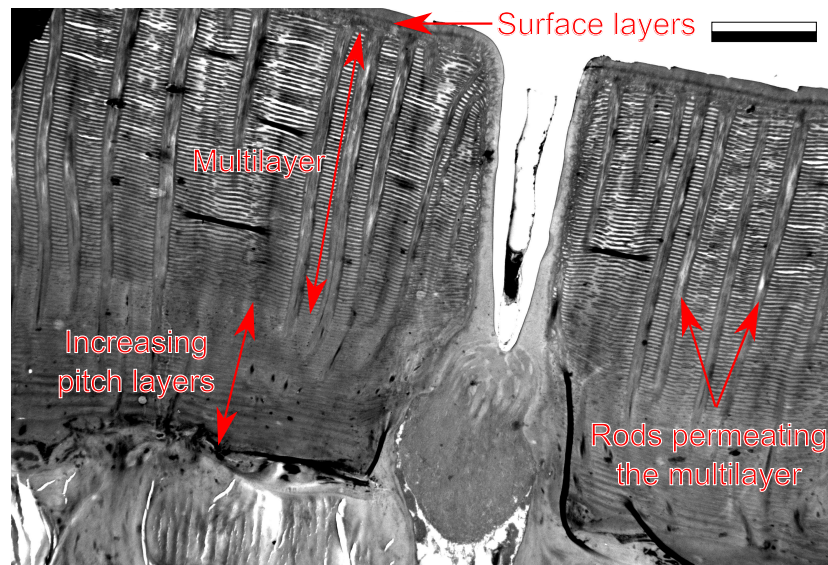
Figure 6.5: TEM of the photonic structure found embedded in the surface of each of the *Torynorrhina flammea* beetles. The structure can be broken down into four main parts. 1) The surface three layers, 2) the ordered multilayer comprising over 100 layers, 3) the array of rods permeating the multilayer and 4) the multilayer with an increasing pitch. Interestingly, a hair and it's root can also be seen at the centre of the image. Scale bar: 5 μm.

6.4 Diffraction from the close-range, quasi-ordered, 2D hexagonal array

Imaging scatterometry yields a diffraction pattern consistent with a 2D PhC with close-range hexagonal close-packed order and long-range disorder (figure 6.8). This is characterised by the apparent annulus of colour surrounding a central white zeroth order mode as seen in the scattering plots from figure 6.4. When we use micro-imaging scatterometry (figure 6.9), it can be seen that the annulus now becomes six intensity peaks in a hexagonal pattern around the zeroth order mode, revealing the disordered hexagonal nature of the array of rods. It is because of the hexagonal nature of the rods penetrating the multilayer, and the colour of the annulus (figure 6.8), that the evidence suggests that the system is scattering the colour produced by the multilayer into an annulus by the rods. Other systems have reported multilayers and diffraction gratings to work concurrently this way such as in *Morpho rhetenor* [11, 38] as discussed in the second chapter and also *Parides sesostris* which will be described in chapters 7 and 8. The secondary beam imaging scatterograms (figure 6.8) show the colours of each beetle blue-shifting as the angle of incidence increases. There are no features that
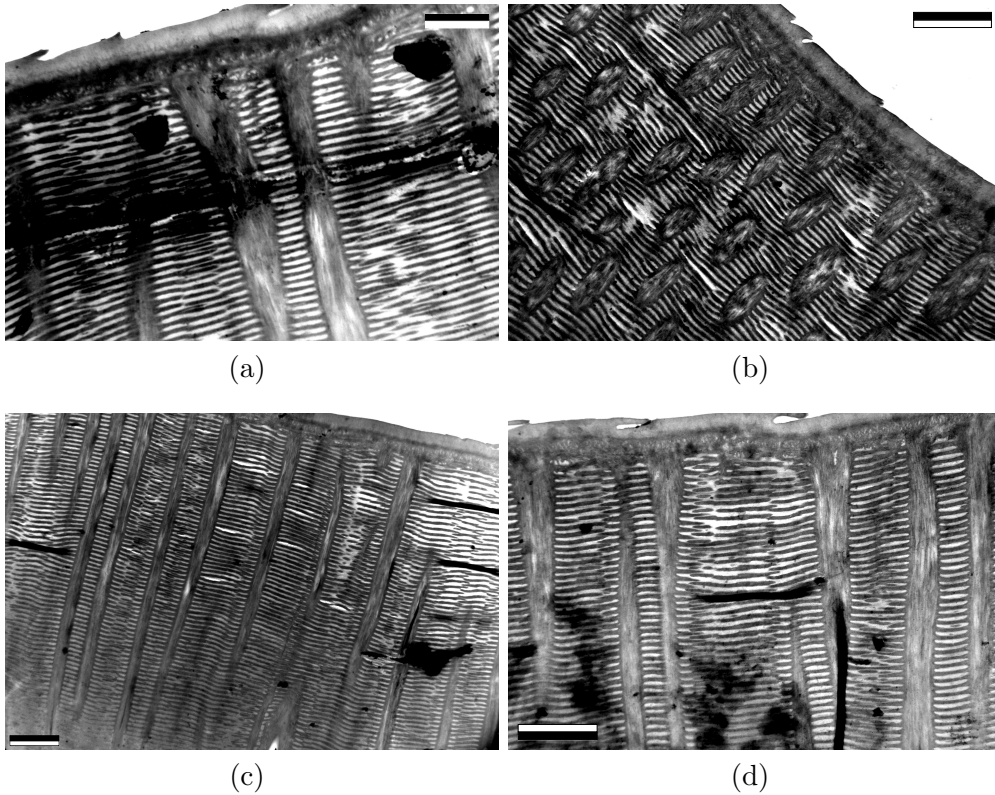
Figure 6.6: Transmission electron micrographs of the four *Torynorrhina flammea* beetles. (a) *T. f. violets*, (b) *T. f. chicheryi*, (c) *T. f. flammea* (juvenile) and (d) *T. f. flammea* (adult). The highly ordered multilayer structure can be seen for all four beetles. Scale bars: (a) 1 μm, (b-d) 2 μm.

can be linked to diffraction in these images as the specularly reflected light is far more intense than the diffracted light and is, therefore, dominant in secondary beam imaging scatterometry.

6.5 Manufacture and characterisation of *T. flammea* inspired synthetic systems

To understand the structural colour appearance of the *T. flammea* beetles, it was decided that a synthesised system should be made to see if the characteristic annulus of colour shown in the scatterograms (figure 6.8) could be recreated using the knowledge we had previously acquired. The green *T. f. chicheryi* beetle was chosen as a model for this analysis, mainly due to all the available light sources having a peak in intensity around 550 nm. To make the system with a high quality factor, it was decided that
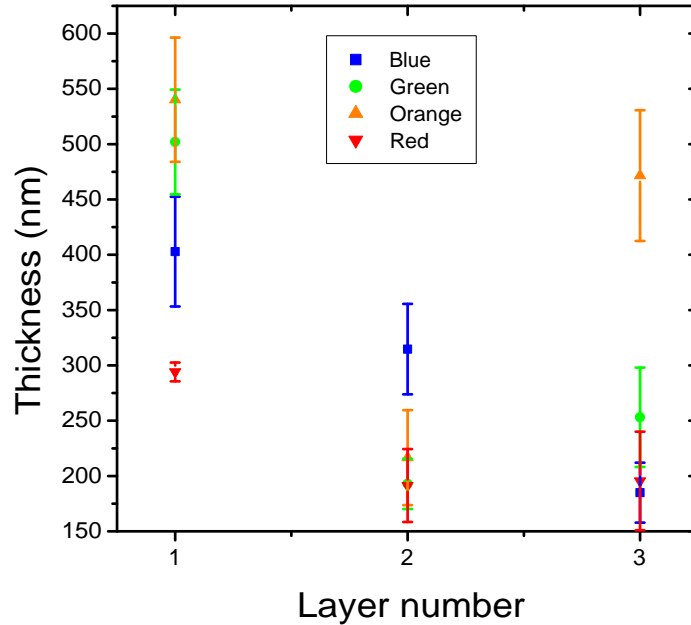
Figure 6.7: Dimensions of the first three layers from the surface for each of the *T. flammea* beetles. The measurements were taken from the TEM micrographs shown in figure 6.6.

the synthesised structure should be a quarter-wave stack so that both layers reflect the same wavelengths. The manufacture of the multilayer system was a two-step process. The first stage was to create a suitable multilayer. 17 layers of alternating silicon nitride (SiN_4) and silicon dioxide (SiO_2) were used, with refractive indices of 1.92 and 1.45 respectively. These materials were chosen as the system could easily be realised by chemical vapour deposition (CVD). The materials were deposited to thicknesses of $d_{SiN_4} = 78$ nm and $d_{SiO_2} = 103.4$ nm producing normal optical path lengths of $OPL_{SiN_4} = 149.76$ nm and $OPL_{SiO_2} = 149.93$ nm. The second step was to mill holes into the multilayer in the same quasi-hexagonal pattern exhibited by the *T. flammea* beetles and also an ordered hexagonal pattern for comparison. This was achieved using focussed ion beam (FIB) milling after sputtering the multilayers in 3 nm of gold (FIB milling was performed at the Georgia Institute of Technology by Ye Cai). The Gold was removed from the sample by bathing in potassium iodide (PI) for 10 minutes. This process left no damage to the structure, therefore no artefacts of this process would arise in optical interrogation. The patterns chosen to FIB mill the structure were all
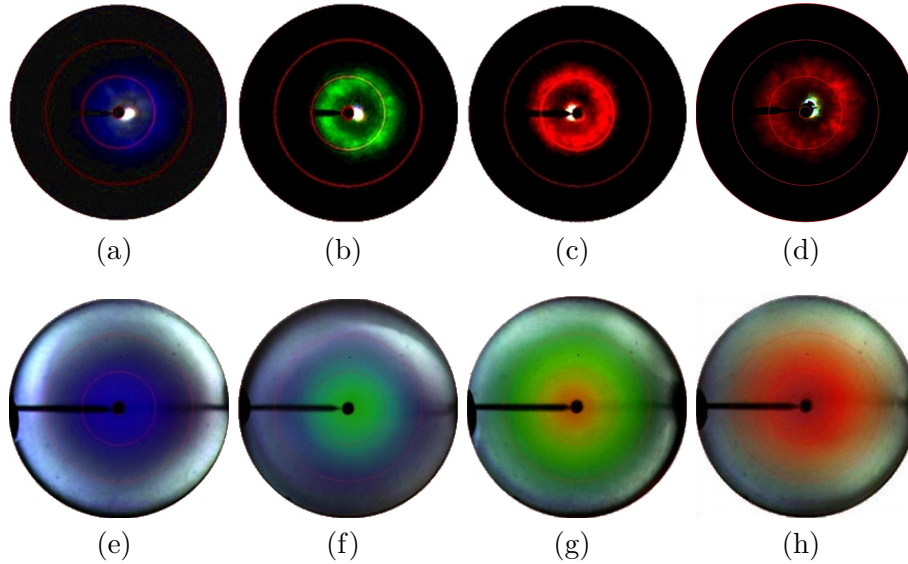
Figure 6.8: (a-d) Primary beam imaging scatterometry performed on *T. f. violets*, *T. f. chicheryi*, *T. f. flammea* (juvenile) and *T. f. flammea* (adult) respectively. A central white spot attributed to the zeroth order specular reflection from the beetle can be seen in each image. The colours produced by the multilayers all seem to be diffracted into an annulus 30° from the normal. (e-h) The corresponding secondary beam scatterometry showing the multilayer characteristics of each beetle structure. Here the iridescence of the structures can be seen as a drop in wavelength as the angle of incidence increases. Note in (e) how the low angle blue appearance becomes darker. This is due to the decrease in wavelength into the ultra violet, a colour not detected by ordinary optical CCDs or the human eye.
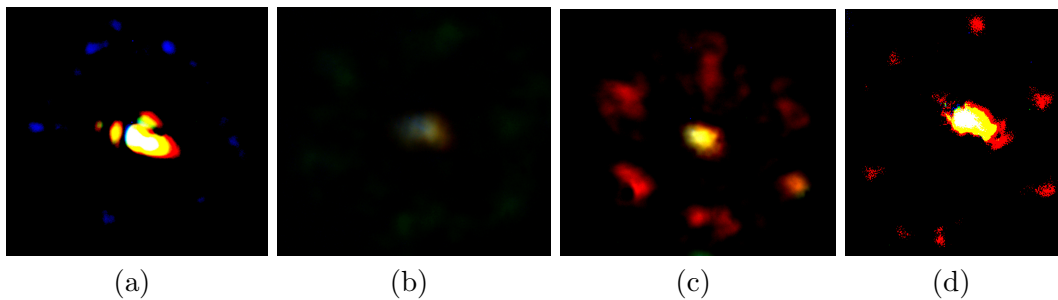
Figure 6.9: Micro-imaging scatterometry performed on each of the *Torynorrhina flammea* beetles, (a) *violets*, (b) *chicheryi*, (c) *flammea* (juvenile) and (d) *flammea* (adult). The images shown are taken using a 100x objective lens to ensure a small beam spot was achieved. The results show that the four beetles all have a close-range hexagonal order.

hexagonal in nature, with some having ordered patterns, and others having disordered patterns. The disorder of the hexagonal array was achieved by using MATLAB routines to perturb each lattice point from the ordered position by a pseudo-random x and y distance up to a pre-assigned maximum.

Initial synthesised systems shown in figure 6.10 included no disorder. They appeared to show the effect of the 2D array of rods when analysing the diffraction patterns obtained from imaging scatterometry but not the colour of the multilayer (figure 6.12). MSP performed on the samples (figure 6.11) show the effect of diffraction in both bright field and dark field. In bright field, where the light is incident and collected at near normal angles, it can be seen that a significant fraction of light is diffracted away from the normal. This effect is larger for the 1 μm pitch system because the diffracted angles will be larger according to the grating equation (equation 3.26), therefore the 2 μm pitch system will have diffracted modes reflected closer to the normal direction. Dark field MSP confirms with this data as the 1 μm pitch system has a higher intensity at high angles of incidence than the 2 μm pitch system, indicating that more light is diffracted by the sytstem with the 1 μm hexagonal lattice constant. The multilayer-only spectra shows little or no reflection in the dark field mode, as expected for a planar multilayer system.

Reflectance microscopy on the multilayer (figure 6.13) reveals the expected response with a reflection-band centred around 550 nm. The band-gap shifts towards the blue end of the spectrum as the angle is increased, which is a fundamental characteristic of a multilayer system. The imaging scatterometry agrees with this result as is clearly seen when we compare the reflection response (figure 6.13(c)) as a function of angle with the secondary beam scatterometry images (figure 6.13(b)). No discernible diffraction effects are manifested using this analysis, as the zeroth order diffracted spot (associated with specular reflection) is far more intense than the non-zero diffracted modes.

Narrow angle illumination, or primary beam imaging scatterometry on the ordered hexagonal lattices (pitch = 1 & 2 μm) demonstrate the fundamental characteristics of diffraction gratings (figure 6.12). The 1 μm pitch structure shows clearly the first order diffracted modes arising from the hexagonal array with a bright central white spot, indicating the zeroth order mode. The 2 μm pitch structure provides many more diffracted orders than the 1 μm pitch structure, as expected. When illuminating the structures with red laser light ($\lambda = 637nm$) as shown in figure 6.12, we can clearly see the six distinct diffracted orders separated by $60°$ thus making a hexagonal pattern around the white spot associated with the zeroth order mode. Considering that we know the illumination wavelength, the pitch of the hexagonal arrays can be calculated using equation 3.26. This yielded results of 802.9 nm and 1664.6 nm for the 1 and 2 μm pitch structures, respectively. In both cases the calculated pitches are less than the
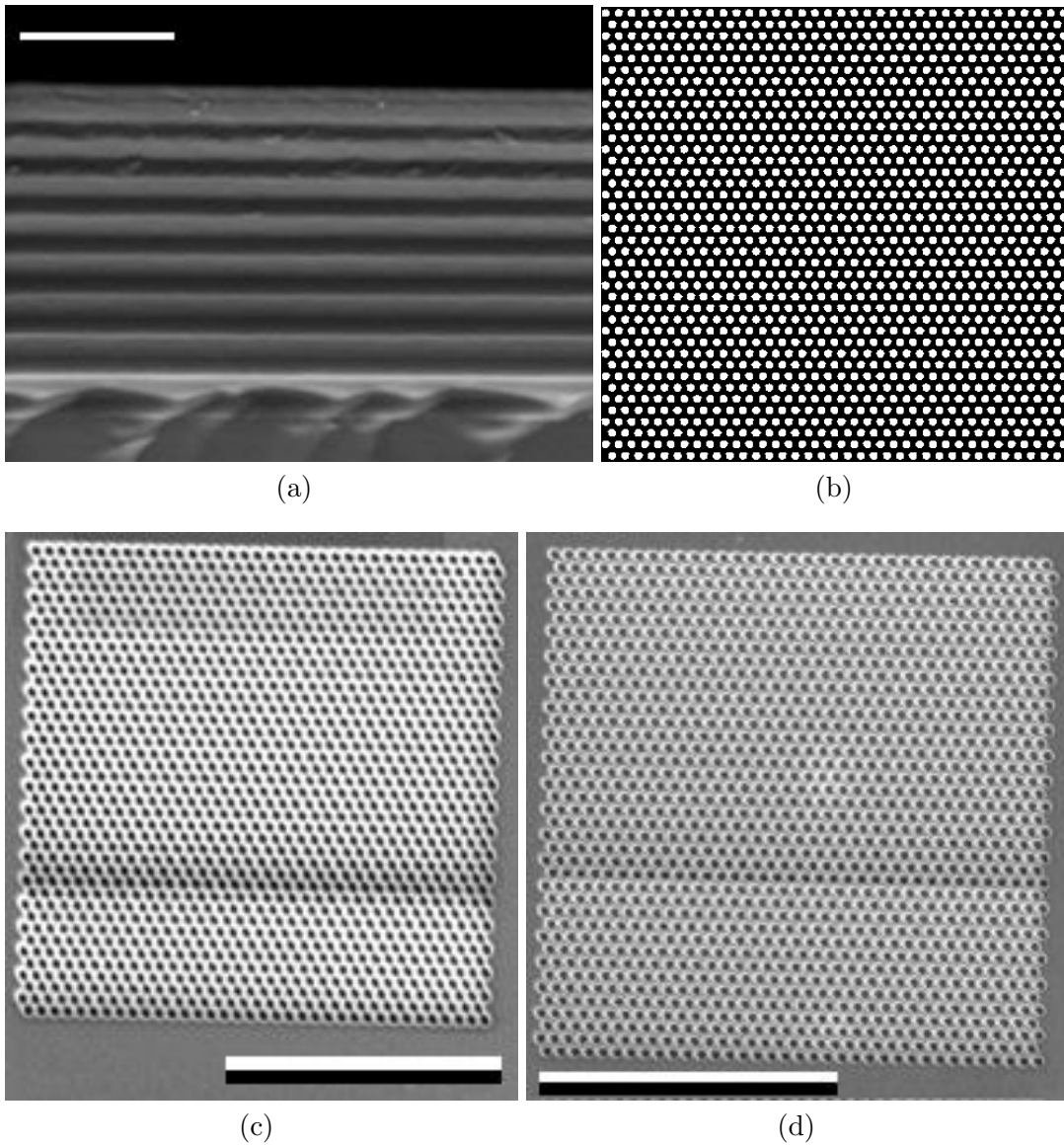
Figure 6.10: (a) The synthesised multilayer comprising 17 layers of alternating silicon nitride and silicon dioxide mounted on a glass slide substrate. (b) The image template used to FIB mill an ordered hexagonal array of rods into the multilayer. (c-d) The first synthesised samples made using the template shown in (b), they have hexagonal periodicities of 1 and 2 μm respectively.
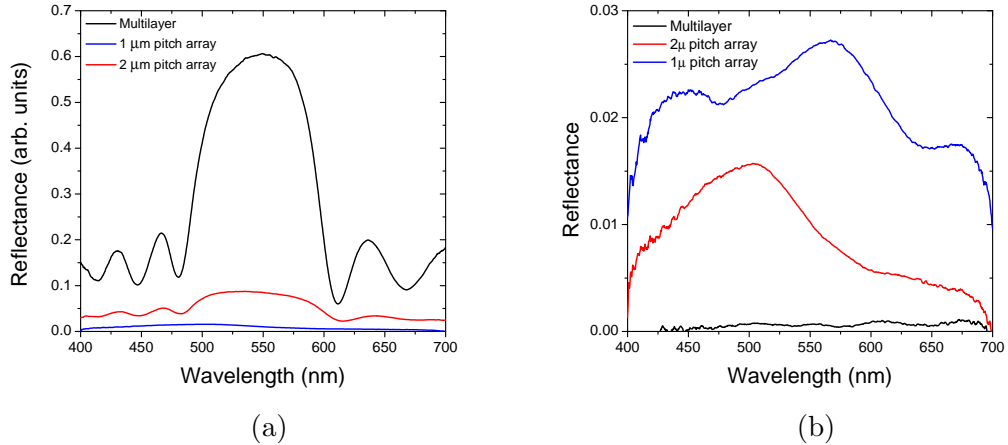
Figure 6.11: Micro-spectrophotometry (MSP) performed on the ordered, 1 μm and 2 μm synthesised systems. (a) Bright-field MSP showing the intensity reduction of the diffracting systems for normally incident and reflected illumination. (b) Dark-field MSP showing the increase in reflection of the diffracting systems for light reflected at high angles.

measured structures. The discrepancy in these results is attributed to the FIB milling process not having a perfect calibration, or less likely, the imaging scatterometer being misaligned.

The synthetic beetle distribution (SBD) sample was produced by taking a sub-surface focus (SSF) image of the beetle elytra (figure 6.14(a)). Sub-surface focussing is required as there are 2-3 surface layers covering the multilayer permeated with diffracting rods, therefore surface focus microscopy does not exhibit the required pattern. Once the SSF image was acquired, each scattering particle was highlighted (figure 6.14(b)) using image manipulation software. The original image was then removed, leaving a map of all the rod positions (figure 6.14(c)). Subsequently this image was then used to FIB-mill a pattern into the multilayer that directly mimics the natural *T. flammea* samples. A fast Fourier transform (FFT) of the pattern in figure 6.15(l) was performed to obtain an understanding of the scattering properties of the synthesised system. The FFT yields an annulus pattern surrounding a centralised bright spot, a result that agrees well with the optical scatterograms of the *T. flammea* natural systems (figure 6.8).

The disorder of the synthetic samples shown in figure 6.15 was characterised by taking the FWHM of the nearest neighbour distribution of the FIB milled particles (figure 6.16). The resulting FWHM values are 0 nm, 77 nm, 410 nm and 264 nm, respectively. The first three samples produced by the MATLAB/COMSOL code have

(a)　　　　　　　　　　　　　　　　(b)

(c)　　　　　　　　　　　　　　　　(d)
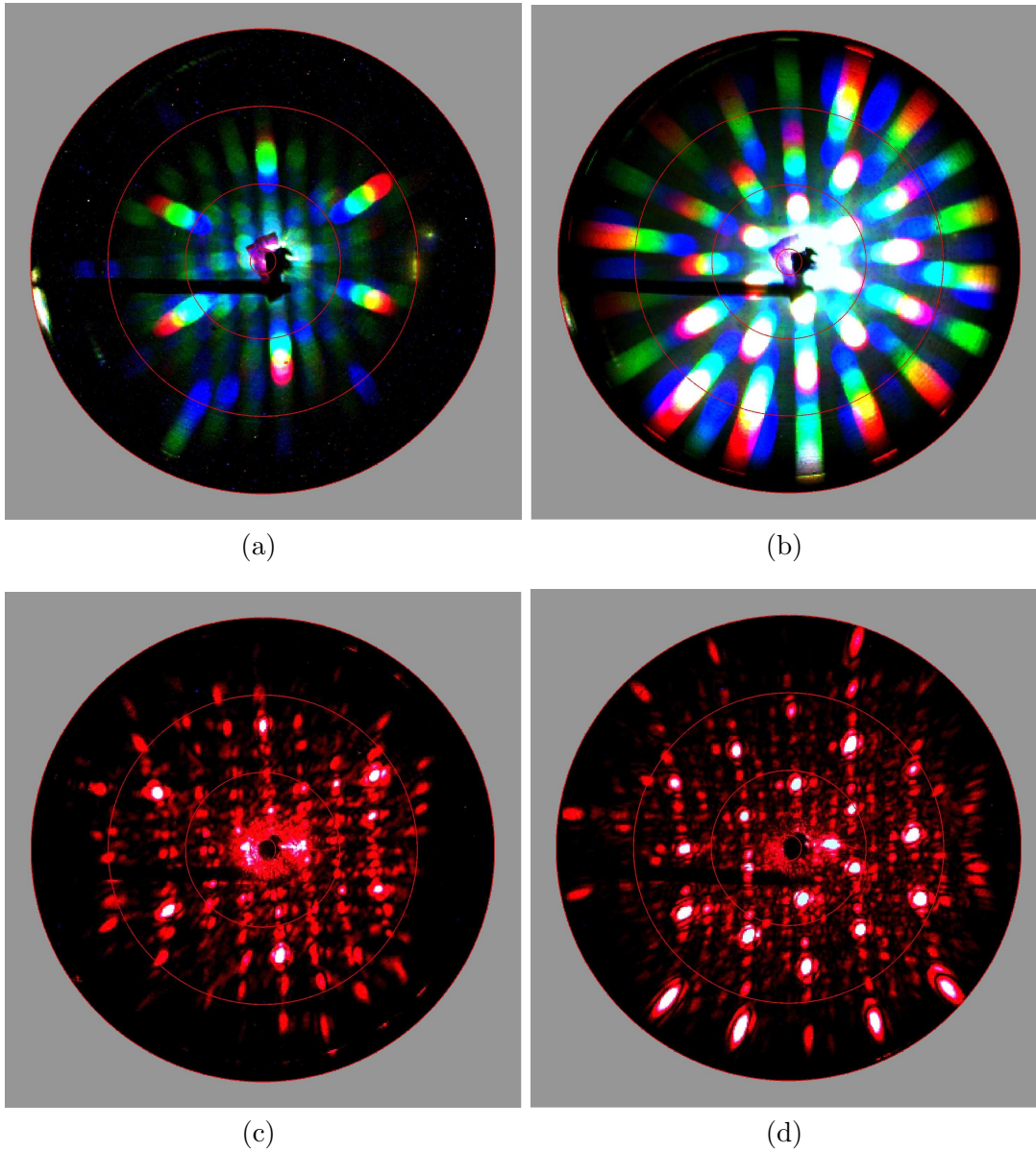
Figure 6.12: Primary-beam imaging scatterometry performed on the initial, ordered, synthesised systems with hexagonal rod-array lattice constants of (a) 1 μm and (b) 2 μm. As expected, there are many more diffracted modes exhibited by the 2 μm pitch structure. (c) and (d) show the corresponding primary beam scatterograms with 637 nm illumination. The purpose of using monochromatic light is to try and calculate the pitch of the structures using the grating equation (equation 3.26). The calculated pitches from this analysis were: (c) 802.9 nm and (d) 1664.6 nm.

(a)

(b)

(c)
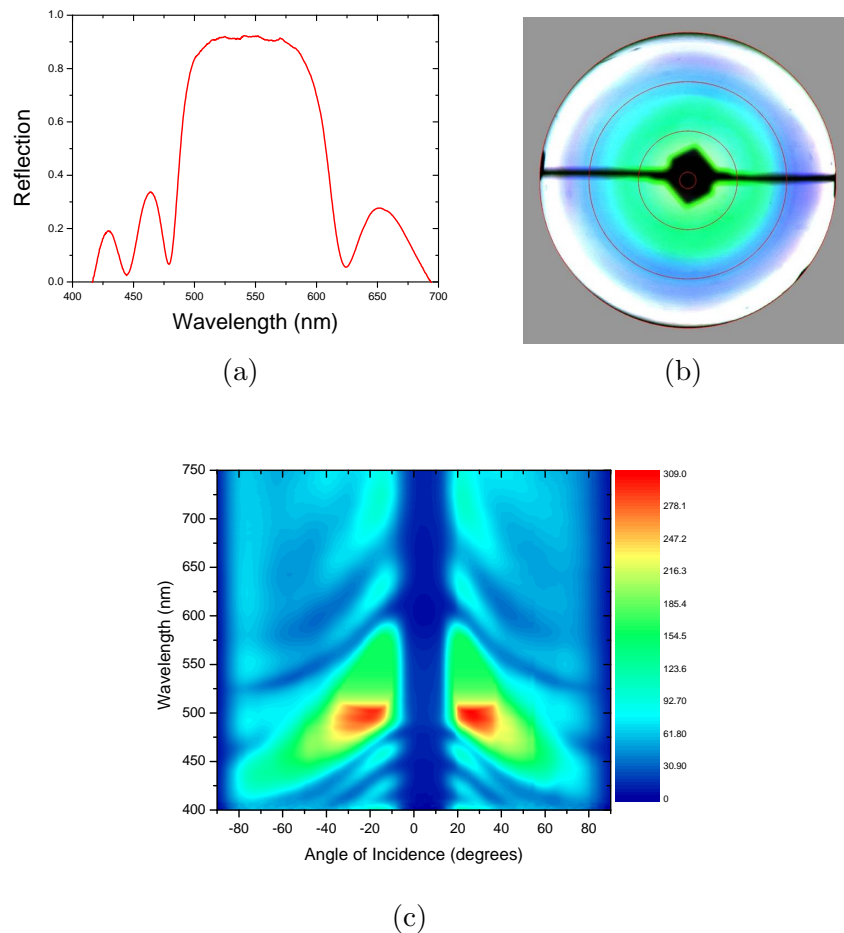
Figure 6.13: Optical characterisation of the synthesised multilayer replica. (a) Spectra obtained using a micro-spectrophotometer shows a characteristic response from a low-loss multilayer. The reflection-band is centred on 550 nm. (b) Secondary beam imaging scatterogram of the multilayer, showing the green colouration at normal incidence, the blue shift as the angle of incidence increases and the broadband reflection at high wavelengths (c) Angle-resolved spectra taken using the secondary-beam imaging scatterometer shown in (b). The spectra are taken using a 45° mirror in the imaging scatterometer experimental setup allowing spectra to be taken from any point of the scatterogram shown in figure 6.13(b). This graph shows the reflection-band decreasing in wavelength as the angle of incidence increases.
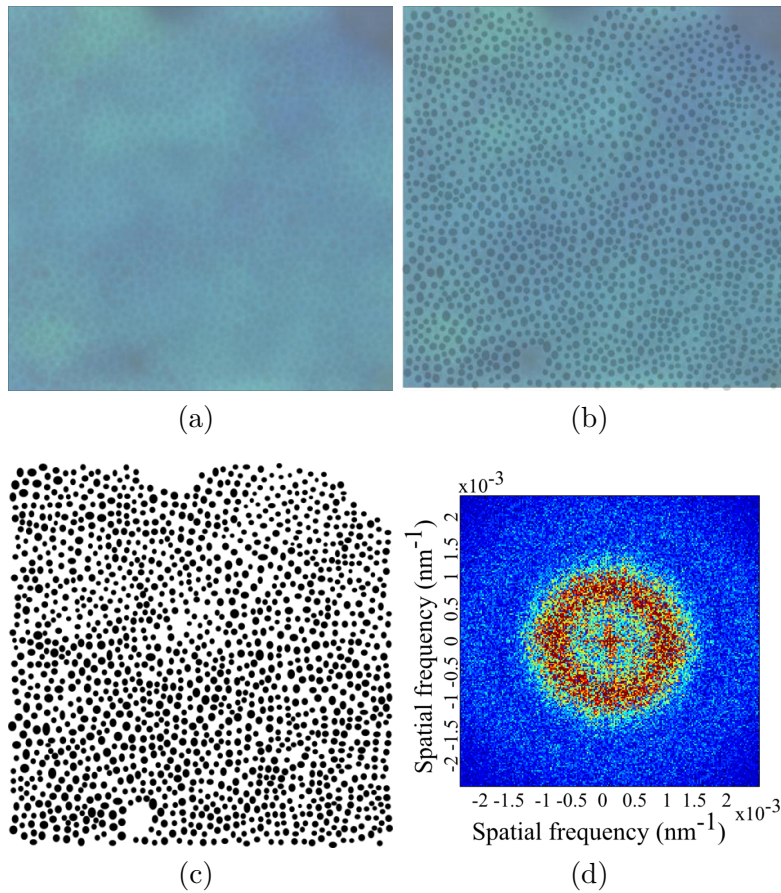
Figure 6.14: (a) A sub-surface focus image of *Torynorrhina flammea chicheryi* showing the arrangement of rods permeating the multilayer perpendicularly to the surface. (b) The same picture as (a) but with the rods individually highlighted. (c) The isolated rod distribution. (d) A fast Fourier transform of the distribution in (c) showing the annulus-like pattern, similar to the scatterograms of the beetles shown in figure 6.8.

a fixed particle diameter, however, the SBD sample has a varying hole diameter due to natural variation.

The scatterograms in figure 6.17 show that low levels of disorder in the 2D array of rods cause the characteristic hexagonal diffraction pattern to weaken in intensity and spread out in angle more isotropically, thus producing a more circlular pattern as opposed to 6 discrete diffraction spots. When the level of disorder is increased, the 6 discrete 1st order modes disappear, leaving a more isotropic, angle-independent colour. This is due to the random scattering events happening within the system that are caused by the increased level of disorder. Another effect can be seen as the level of disorder is increased, and that is that the colour of the multilayer starts to become

(a)   (b)   (c)   (d)

(e)   (f)   (g)   (h)

(i)   (j)   (k)   (l)
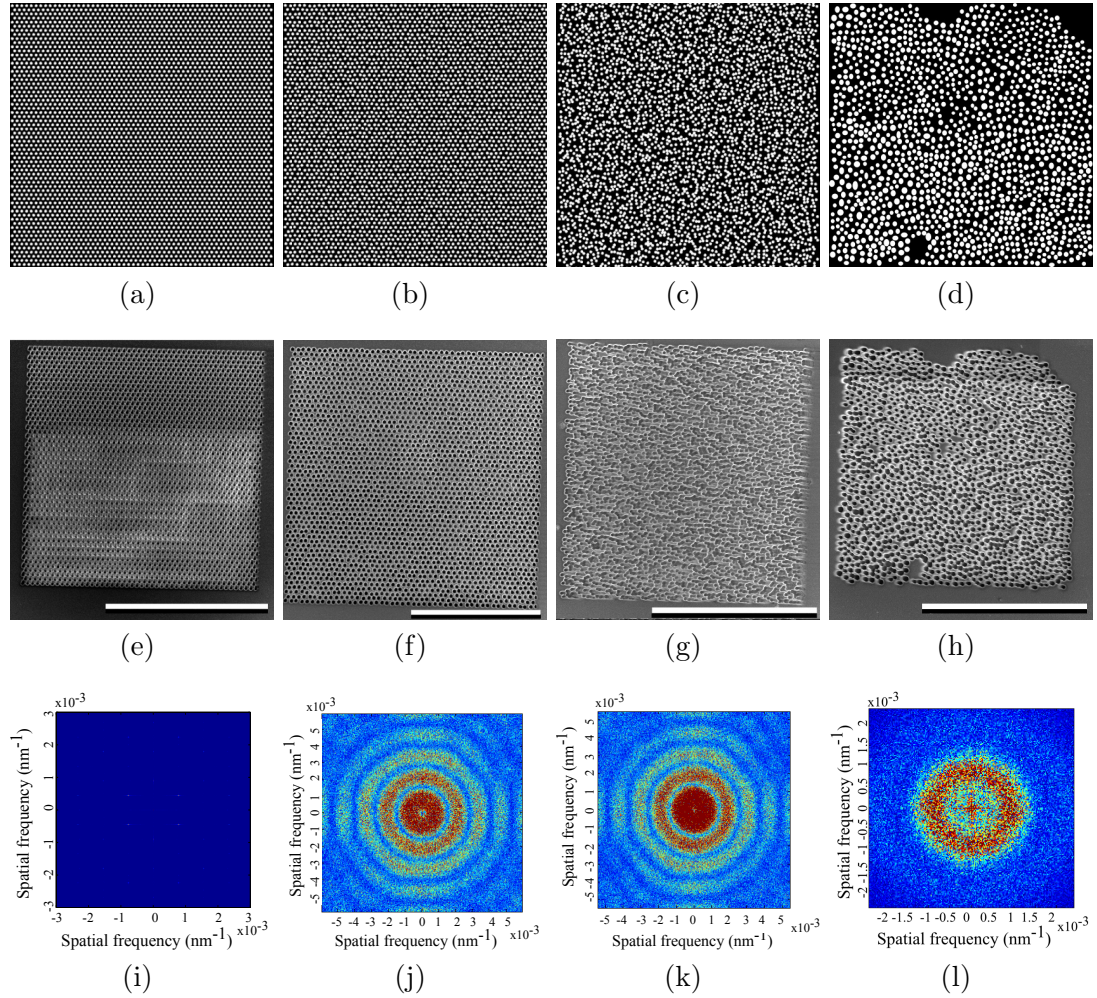
Figure 6.15: (a-d) The templates used for FIB milling the rod array out of the multilayer stack. The white areas are indicate to the FIB milling system where to mill. (e-h) The corresponding SEMs of the final synthetic structures. They show a normal view of the multilayers with the corresponding patterns in (a-d) FIB milled through the multilayer. (i-l) FFT images of the templates shown in (a-d). For the ordered structure we see the expected result of a hexagonal pattern that is orthoganol to the spatial image shown in (a). (j) and (k) both show concentric circles which is the expected result for a quasi-ordered hexagonal array of circular particles. Only the SBD structure shows the characteristic annulus seen in the primary beam scatterograms of the *T. flammea* beetles. It should also be noted that the SBD sample has varying hole diameters. Scale bars: (e) and (g): 40μm, (f) and (h) 30 μm.
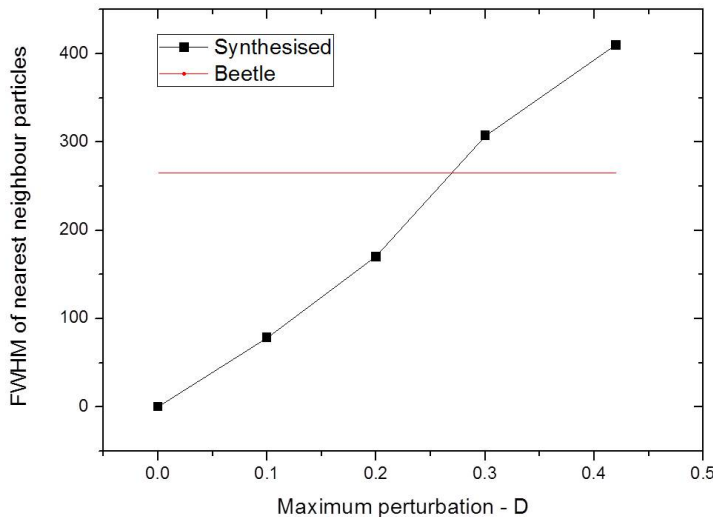
Figure 6.16: A graph showing the relation between the maximum perturbations of the particles in the hexagonal lattice and the FWHM of the nearest neighbour distributions. The values of D that give the most linear FWHM response were chosen for this project. These values are: 0, 0.1, 0.42 and the synthetic beetle distribution (red line). The corresponding FWHM values are 0 nm, 77 nm, 410 nm and 264 nm, respectively.

more apparent. This result suggests a reason why the natural *T. flammea* samples do not exhibit a rainbow like pattern consistent with ordered gratings, but rather just the colour produced by the multilayer. The sample based on the real distribution of the pillars in the beetle showed a similar result to the high-disorder synthetic system. This result was highly unexpected as the FFT image taken from the template used to make this structure (figure 6.15(l)) exhibits an annulus which is in agreement with the scatterograms produced by the natural *T. flammea* samples (figure 6.8).

This result disagrees with the original hypothesis that the array of permeating rods causes the colour of the multilayer to be diffracted into an annulus of colour around the specularly reflected white spot (figure 6.8). However, micro imaging scatterometry (MIS) performed on the natural *T. flammea* samples has shown that there is a close-range hexagonal order to the beetle samples (figure 6.9). This can be seen in the high magnification (100x objective lens) images as the 6 discrete hexagonal diffraction spots appear. The reason you only see the hexagonal diffraction pattern using the 100x objective lens is because this lens has the smallest spot size so the long-range disorder becomes less dominant. Another reason why the hypothesis is not completely incorrect is because the FFT of the image used to create the synthetic beetle distribution (SBD)

(a)　　　　　　(b)　　　　　　(c)　　　　　　(d)
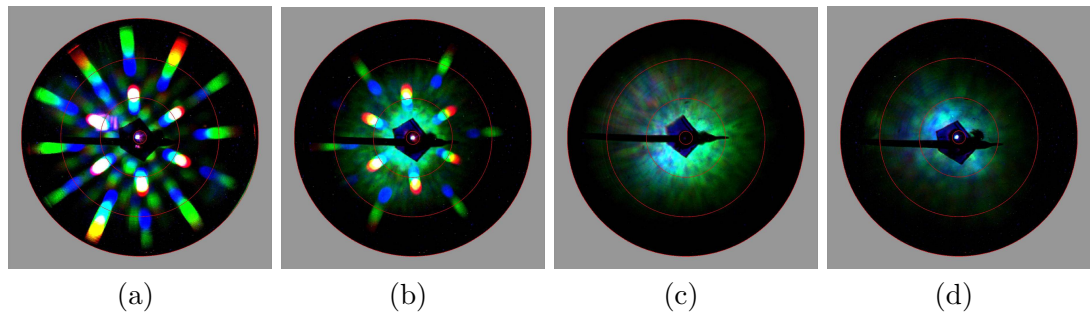
Figure 6.17:　　Imaging scatterometry performed on samples exhibiting four different levels of disorder. (a-d) show the scatterograms for the samples with FWHM values of nearest neighbour distances of: 0 nm, 77 nm, 410 nm and 264 nm (SBD), respectively. The characteristic hexagonal scattering pattern can be seen for the two most ordered structures but not the disordered structures. The SBD sample was predicted to show the annulus of colour that was observed in the *T. flammea* beetle scatterograms. However, a random scattering pattern of the colours reflected by the multilayer are exhibited.

sample shows an annulus much like the scatterograms of all four *T. flammea* beetles. Therefore it is uncertain as to why the annulus is not there. MIS on the SBD sample could shed some light on this inconsistency. Another reason for the discrepancy could be because the rods in the SBD sample are air holes, whereas in the natural samples they are solid rods.

An interesting feature of the primary beam imaging scatterogram of the ordered system (figure 6.17(a)) is the green, square-like pattern that appears at smaller angles than the 1st order diffrated modes. The smaller angle of diffraction indicates that the system producing this effect must be larger than the periodicity of the hexagonal array of holes. Analysis on the templates used to FIB mill the samples reveal that the green square feature is likely to be due to the way in which the MATLAB/COMSOL routines create the images. The hexagonal array is essentially two square arrays, with larger periodicity than the hexagonal array, offset by an angle of 60° (figure 6.19). This could explain the size and shape of the green square features observed in the scatterograms but further investigation would be required to be more certain.

Figure 6.18 shows the secondary beam imaging scatterometry images of the synthetic multilayer systems shown in figure 6.15. These images demonstrate the dominant nature of the multilayer structure over the diffracting structure for specularly reflected light as they display the same pattern as the multlilayer without the hexagonal array as shown in figure 6.13(b).

Figure 6.20 reveals that the dark field imaging scatterometry (DFIS) on the syn-
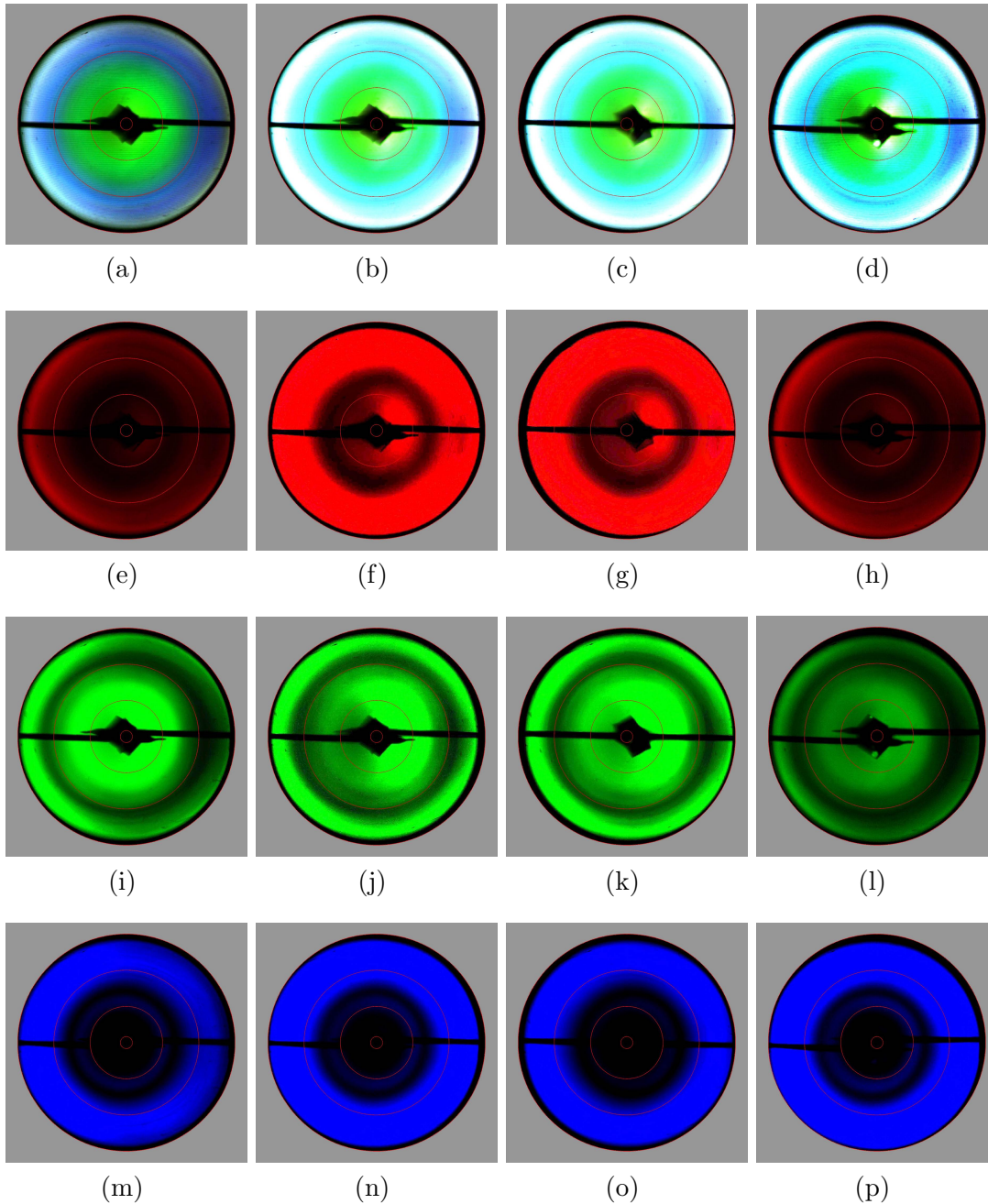
Figure 6.18:   Secondary beam imaging scatterometry performed on samples exhibiting four different levels of disorder. The columns show (from left to right) FWHM values of nearest neighbour distances of: 0 nm, 77 nm, 410 nm and 264 nm (SBD). The rows show (from top to bottom) secondary beam scatterometry with: broadband, 650 nm, 550 nm and 450 nm illumination.
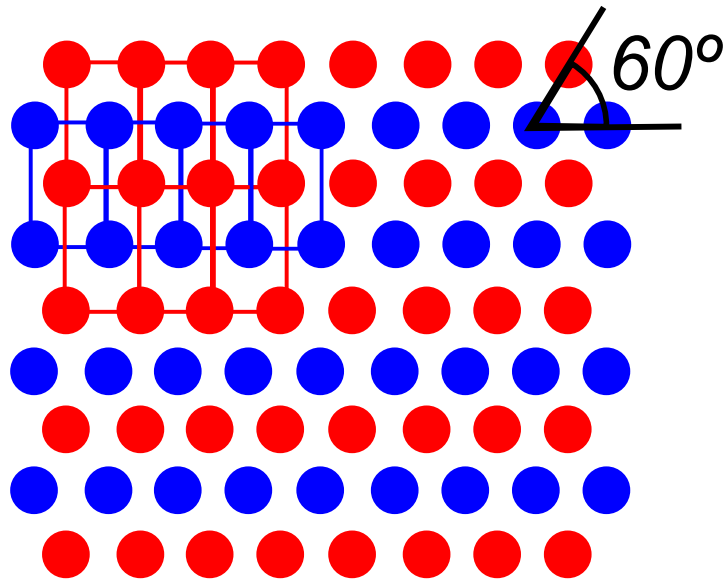
Figure 6.19: Schematic showing how the hexagonal arrays are produced. Starting with a rectangular array of rods, another rectangular array can be superimposed over the original array, but offset by 60°. Disorder was added by perturbing each particle from its lattice point by a pseudo-random fraction of the lattice constant.

thesised structures show a typical diffraction ring pattern for the ordered synthetic samples, broader rings for the low disorder sample and multilayer dominant results for the SBD and high disorder samples.

6.6 Computational modelling

6.6.1 Multilayers

Simple, infinite, multilayer, computational modelling of both the natural *T. flammea* beetles and the synthesised multilayer stacks were undertaken using TFCalc. Models of the beetle system were produced using the dimensions acquired from the TEM analysis. The materials used have refractive indices of $n = 1.68 + 0.1i$ and $n = 1.56$ for melanoprotein and chitin respectively [118]. Considering no difference between the dimensions of the dark layers and light layers in the TEMs, the layer thicknesses used are just half of the measured lattice constants (table 6.2). Figure 6.21 shows the results of this modelling compared with the experimental spectra obtained from the *T. flammea* beetles.

Table 6.3 shows the experimentally-obtained and calculated reflection maxima for each beetle. The peak reflected wavelenghts obtained via thin film modelling are con-
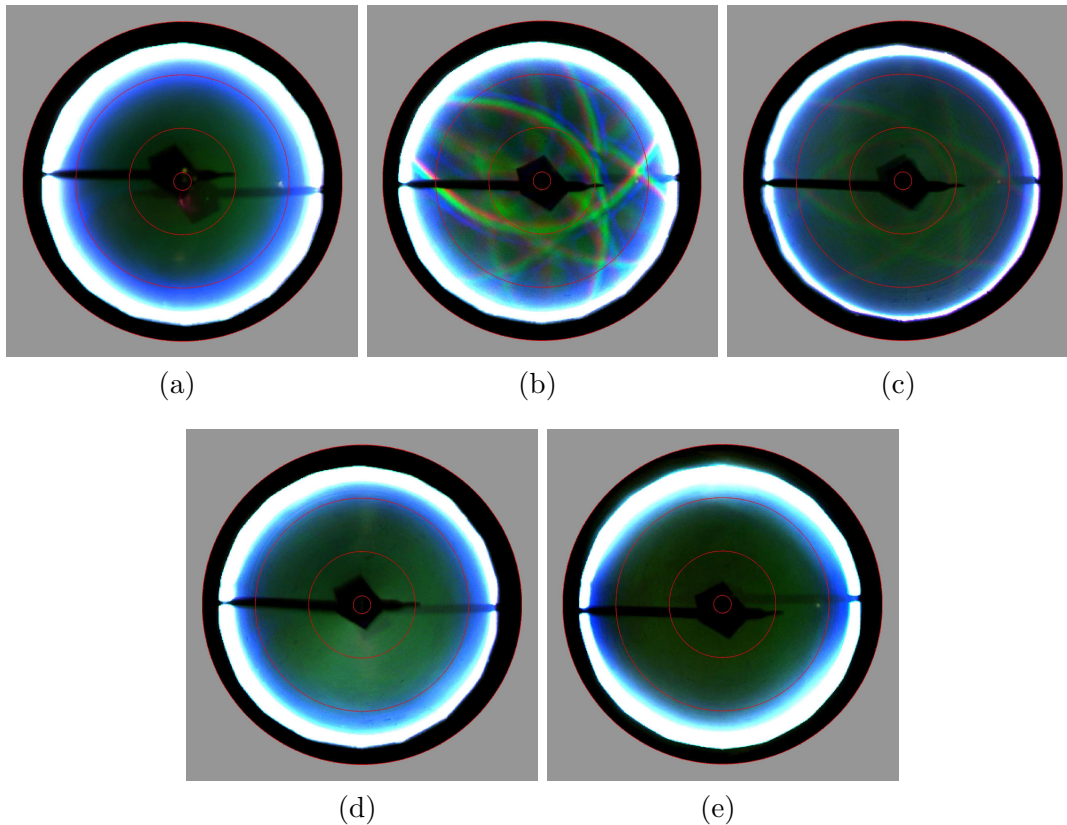
Figure 6.20: Dark field imaging scatterograms of the synthesised multilayers with hexagonal rod arrays with varying levels of disorder. (a) Dark field scatterogram of the multilayer withouth the FIB milled rod array. This reveals very low intensity refelction, an expected result for a non-scattering structure. (b) Dark field scatterogram of the completely ordered rod array within the multilayer. This image shows the expected rings of diffraction for a hexagonal array of particles. (c) Dark field scatterogram of the structure with the lowest non-zero level of disorder. This image still shows the rings of diffraction but they are far less intense due to the slight disorder level. (d) and (e) show the dark field scatterograms for the structure with the highest level of disorder from the MATLAB/COMSOL created patterns and the synthesised beetle structure, respectively. These both show no rings of diffraction as the level of disorder is too high. Instead, they both show a uniform pattern, similar to the multilayer-only dark field scatterogram.

Table 6.2: Physical dimensions of each beetle subspecies

Subspecies	Mean lattice constant (nm)	Mean layer thickness (nm)
T. f. violets	136.4	68.2
T. f. chicheryi	166.6	83.3
T. f. flammea (juvenile)	185.4	92.7
T. f. flammea (adult)	201.2	100.6
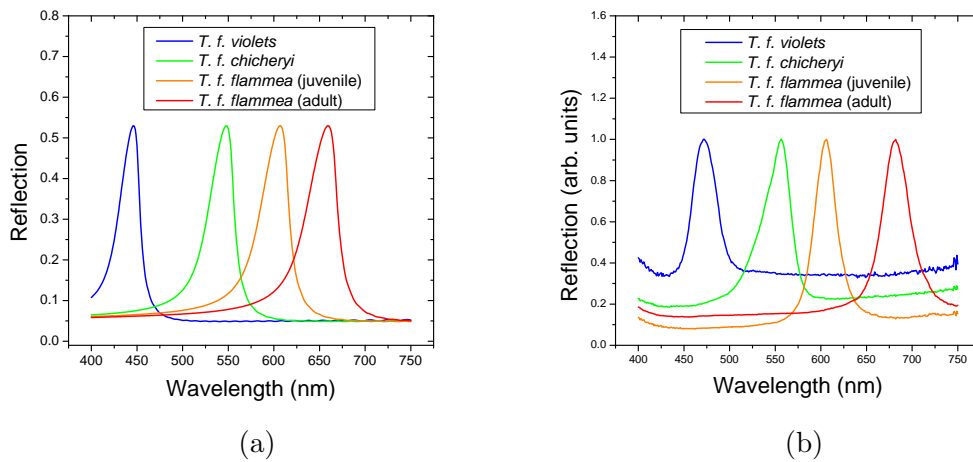
Figure 6.21: Optical spectra obtained by (a) thin film computational modelling and (b) optical bench experiment.

sistently lower than the experimentally-obtained values. The cause of this issue is most likely an artefact of the TEM preparation which involves infiltrating the systems with many different chemicals, some of which may cause shrinkage of the materials under interrogation.

6.6.2 Multilayers intersected with a 2D hexagonal array

Computational modelling of the perfectly ordered hybrid photonic crystal (figure 6.22), using FEM techniques, yields agreeable results with both experiment and also the Fresnel-based theory for the multilayer only model (figure 6.21(a)). It should be noted, however, that for the experimental spectra acquired using micro-spectrophotometry, light is collected for near-normal angles only and the FEM modelling data is integrated over the entire reflected hemisphere. The data is a close fit to the experimental results, however, there are still some unexplained features not present in the Fresnel-based theoretical data. It was considered likely that they were associated with inaccuracies within the model but subsequent models exhibiting a higher tetrahedral resolution did

Table 6.3: Comparison between experiment and modelling results of the maximally reflected wavelengths from the *Torynorrhina flammea* beetles

Subspecies	Experiment (nm)	Thin film modelling (nm)
T. f. violets	472	446
T. f. chicheryi	557	548
T. f. flammea (juvenile)	606	607
T. f. flammea (adult)	682	659

not yield any difference. These unexpected peaks and troughs could be due to allowed modes within the system, induced by the presence of the diffracting rods. Figure 6.22(c) shows a normal view of the far-field radiation pattern, obtained from the field calculations in the FEM model. This analysis reveals the characteristic 6 diffracted orders separated by 60 degrees for a hexagonal diffracting system. Six second order modes can also be seen. Figure 6.22(d) shows the far field radiation pattern as a function of theta, for twenty by twenty unit cells, and it can be seen that the first and second order modes are diffracted away from the normal at angles of approximately 30° and 60° respectively. This agrees with the results acquired from the grating equation (equation 3.26). This also agrees with experimentally acquired results for the ordered system using the imaging scatterometer (figure 6.17). This result confirms the hypothesis that the disordered hexagonal grating acts to diffract the colour of the multilayer.

To make a more complete picture using computational modelling, FEM modelling was undertaken using HFSS software. A 17-layer system comprising alternating layers of silicon nitride and silicon dioxide was modelled to replicate the synthetic structures that were analysed. The dimensions of the layers were chosen to replicate the synthetic system $d_{SiN_4} = 78$ nm and $d_{SiO_2} = 103.4$ nm.

The FEM modelling results show the characteristic band-gap attributed to a Bragg stack that was produced also by the thin film modelling shown in TFCalc (figure 6.21(a)). The two different methods, however, do not show an exact match. A minor reason for the discrepancy is attributed to the FEM technique being an approximation. The errors due to these approximations can be reduced by increasing the number of tetrahedra in the model, especially in the areas where high electric field amplitudes are expected. Increasing the number of tetrahedra has the major draw back of increasing processing time. The major cause of discrepancy is noticed when we look at the effect of the rod structure compared to the FEM model that comprises only a multilayer. The undulations in the spectra are not present in the multilayer only model, and only become apparent when the rods are added. Figure 6.23 shows the effect of changing the 2D hexagonal lattice constant. What we see is an increase in the undulations as

the lattice constant is decreased. The cause of this effect is in reality unknown but I speculate that it is due to the fact that the incident plane wave solver is not specifically designed to deal with diffraction and becomes increasingly unreliable as the diffraction edge of the modelled system is approached. This would explain why the undulations increase in amplitude as the hexagonal lattice constant is decreased.

6.6.3 Diffraction and disorder

Disordered systems can be fundamentally difficult to produce in a working computational model. The reason being that to eliminate any form of periodicity, one cannot use the master/slave boundaries that are usually employed to reduce processing time, as discussed in chapter 4. Therefore, one would have to produce a model as big as you would actually need to and considering current computer specifications, this would be an extremely expensive process. It is for these reasons that the computational modelling has been split into two parts, the ordered multilayer permeated by a hexagonal array (as shown in the last section) and simple Fast Fourier Transform (FFT) analysis of the 2D array of disordered rods, to see if the annulus pattern is reproducible. The FFT images (figure 6.15) were produced by using MATLAB routines on the images shown in figure 6.15(h).

Figure 6.15 shows the resulting FFT images gained from the patterns used as templates for FIB milling the arrays of pillars into the multilayers. As can be seen, the templates created using the MATLAB/COMSOL routines did not produce the expected annulus pattern. The FFT image instead yielded a filled-in circle, which represents a quasi-ordered hexagonal system. The reason for this could be the way in which the routine perturbs each particle from the hexagonal lattice by a pseudo-random distance with an upper limit defined by the variable D. However, the nature of this method will produce a disordered system at close range, and a level of order at long range. This differs from the real structure, as the *T. flammea* beetles exhibit close-range hexagonal order and long-range disorder. A MATLAB/COMSOL routine to fix this problem proved difficult to produce. This was the motivation needed to replicate the real structure by manually drawing the arrangement of rods by tracing over them using image manipulation software (figure 6.14). The results from this traced structure (figure 6.14) clearly show the expected annulus pattern exhibited in the FFT image.

6.7 Conclusion

The three sub species of *T. flammea* all exhibit a highly ordered multilayer that reflects a purer (smaller band-gap, higher Q-factor) colour for a natural system. When illumi-

(a)

(b)

(c)

(d)
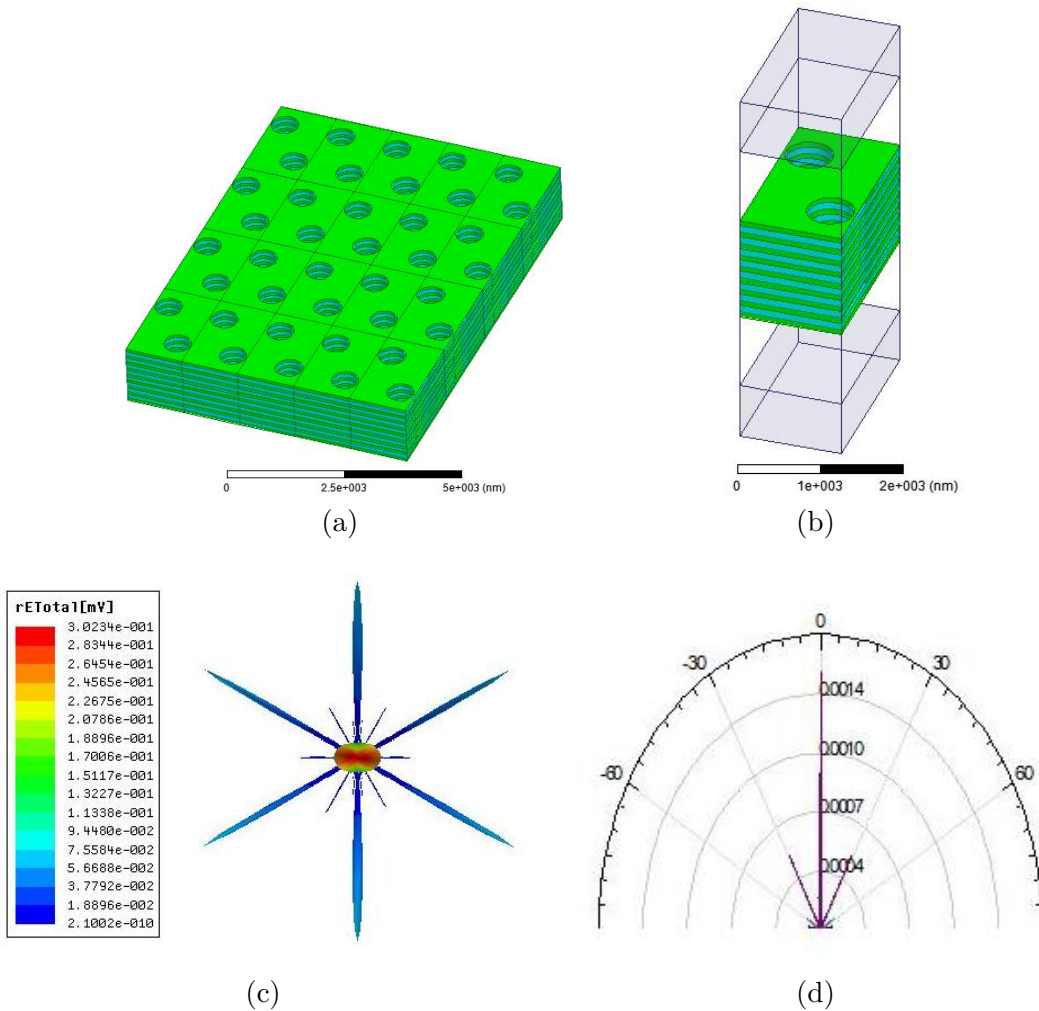
Figure 6.22: (a) A 4x5 unit cell section of the computational model created for FEM modelling of the synthesised structure. (b) A single unit cell surrounded by an air box on the top and bottom and also in the cylindrical holes. The boxes at the very top and very bottom represent the perfectly matched layers (PML's) used to prevent unwanted reflections from the edges of the air box. (c) The far field radiation pattern as a function of the ϕ angle. This clearly shows the hexagonal nature of the scattering pattern, agreeing with the ordered, synthesised scatterograms shown in figure 6.12 (d) The far field radiation pattern as a function of the θ angle from the surface normal for normally incident radiation. The angles of the first order diffracted modes agree well with the the result expected using equation 3.26.
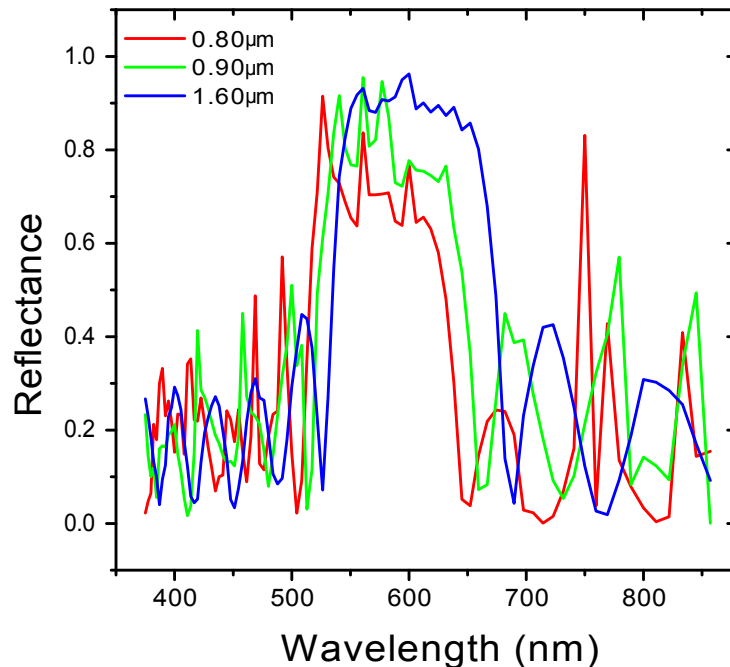
Figure 6.23: Optical spectra obtained by FEM modelling of the synthesised quarter-wave stack with a regular hexagonal array of permeating rods. For a lattice constant of 16 μm the spectra arees well with the experimental spectra (figure 6.13(a)). As the lattice constant of the hexagonal array decreases, the band-gap intensities decrease and there appears to be an increase in undulations within the spectra.

nated with normally incident broadband light, the vivid, reflected colours attributed to each beetle are diffracted into an annulus around a bright white spot in the normal direction. Analysis the structures of each beetle yielded a multilayer stack of up to 120 layers. Computational modelling provided supporting evidence that indicates the colour of each beetle is produced by the multilayer. The differences in the maximally reflected wavelength are attributed to proportional differences in the dimensions of the multilayer. The annulus pattern produced by primary beam scatterometry is believed to be caused by a quasi-ordered hexagonal array of rods which permeate the multilayer stack.

This hybrid 3D PhC was synthesised using dielectric materials on a glass substrate with means of fully understanding the system exhibited in the beetle elytra. The multilayer colour (band-gap centred on 550 nm) did not appear until a certain amount of disorder

was introduced into the system. Otherwise a typical hexagonal diffraction pattern was seen using primary beam scatterometry and the typical multilayer pattern was seen when using secondary beam imaging scatterometry. The synthesised multilayers that were produced from MATLAB/COMSOL routines did not produce the same annulus pattern that the _T. flammea_ beetles created, either experimentally in the scatterometer or theoretically in the FFT images. This is due to the chosen method to produce the templates with close range disorder and long range order, the opposite of the beetle structures. The synthesised structure that was created by tracing the structure seen in _T. flammea_ did produce the characteristic annulus pattern in the theoretical FFT images, but created a more random scattering pattern in the experimental scatterograms. The reason for this is unknown but we can speculate that that it could be because the rods are actually holes in the synthetically fabricated structure and are solid in the beetle's elytra. Further study would need to be performed to prove/disprove this hypothesis.

Evolutionary advantages of the colour appearances of the _T. flammea_ beetles are understood to be for sexual communication purposes. The beetles were acquired from tropical jungles of Thailand, therefore a bright colour appearance would be required for the beetles of opposite sex to be able to find each other in a dense, colourful environment. The reason for the unusual diffracted annulus of colour (shown in figure 6.8) is largely unknown but one hypothesis could be that the beetle needs the colour to appear brighter at angles visible by other beetles but not by predatory creatures such as birds. Recent unpublished data suggests that the rod array is present for the purpose of providing significantly improved structural integrity to the structure. Therefore, the annulus of colour, though interesting, may even be an artefact of the mechanical design of the structure.

Chapter 7

A detailed study of the butterfly *Parides sesostris*, utilising focussed ion beam nano-surgery

7.1 Introduction

In this chapter the most detailed analysis into the structure and colour of the green wing scales of *Parides sesostris* is presented. Macroscopic areas of the green wing patches were optically characterised followed by optical and structural characterisation of individual green wing scales. SEM cross-section micrographs were used to gain an understanding about the origins of the colour produced by the scales. Focussed ion beam (FIB) milling techniques were then employed to test the hypotheses by deconstructing the scale into its component pieces, which were then characterised individually. This investigation allowed us to deconvolve the function of the scale components so we could gain a much clearer understanding of how this complex system works. It should be noted that all SEM imaging and FIB milling was performed by Craig Cameron, Georgia Institute of Technology, Atlanta, GA, USA.

In the previous two chapters we looked at some interesting examples of multilayer structures and their optical character. Even though the structures were good examples of how diverse multilayers can be, comprehending the structural colouration was not too taxing. The structural analysis only required simple SEM and TEM cross-sections to fully understand the structure. However, not all species in nature provide us with such ease of analysis. In fact, sometimes it is necessary not only to obtain SEM cross-sections for structural analysis, but to deconstruct the structure into its component pieces for individual optical analysis. This can be rather a difficult task to achieve considering

the structures involved have dimensions comparable to the wavelength of visible light (hundreds of nanometres). Hence, such care, precision and above all, patience are required to achieve reliable results.

The species chosen for this investigation is *Parides sesostris*. The *P. sesostris* butterfly, also known as the emerald-patched cattleheart [1] has had quite a lot of attention in the field of natural photonics [1, 11, 22, 36, 45, 62, 63, 64, 122, 123] as it exhibits a triply-periodic, bi-continuous gyroid photonic poly-crystal [36, 124]. The butterfly presented here exhibits a multi-component light-scattering mechanism with the gyroid poly-crystal at the centre of each green wing scale. It is because of the amount of literature already available for *P. sesostris* and the complex, multi-component structure contained in the green wing scales, that *Parides sesostris* was chosen for demonstrating the precise deconstruction of intra-scalar components.

7.2 Optical characterisation of *P. sesostris*

The green wing patches of *P. sesostris*, when observed macroscopically, exhibit a largely angle-independent green colour (figure 7.1(a)). There is, however, a slight iridescence as the wing patches have a slight metallic appearance and a slight red-shift can be observed at high angles away from the surface normal. Different specimens have slightly different colours, with some samples exhibiting a bluish-green colour, some show a yellowish-green colour and the others lie somewhere inbetween. The green wing scales show a matt green colour on the top side (figure 7.1(c)), and a much more specular, shiny green colour on the bottom side of the scale (figure 7.1(d)). This would indicate that either; the green colour reflected from the top side is due to a green pigment, or there is a scattering mechanism present on the top side of the scale. If one looks closely at the top side of the scale, one can make out faint lines running down the length of the scale. This may be an indication of a diffraction grating which could produce the scattering required to reduce the angular dependence of the top side's colour appearance.

Initial optical characterisation was performed on individual whole wing scales and on sections of wing containing hundreds of scales. The whole wing scales were analysed using the reflection probe (figure 7.2). These spectra show a peak in wavelength of 545 ± 5 nm. The single scale reflection spectra were taken using micro-spectrophotmetry (MSP) techniques (figure 7.2). Spectra from the top and bottom sides of the scale show peaks in reflection at 525.8 ± 4.8 nm and 524.5 ± 6.3 nm respectively. This is a blue-shift from the whole wing patch of 20 nm. There appears to be no obvious reason why there would be a discrepancy between a macroscopic wing patch measurement and a microscopic single scale measurement. Therefore, the discrepancy is most likely due to the intra-species variation of different *P. sesostris* specimens. The top and bottom

(a)

(b)

(c)

(d)
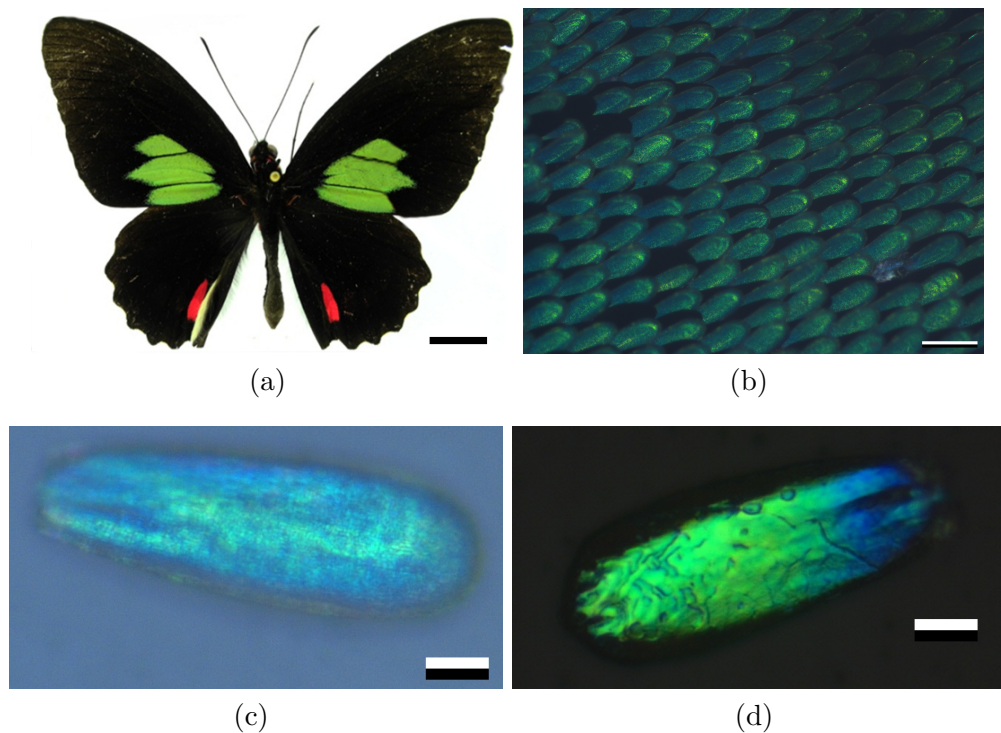
Figure 7.1: (a) *Parides sesostris* (a) The dorsal side of *P. sesostris* showing the green patch of scales which were investigated in this chapter. (b) A micrograph showing how the individual wing scales are aligned on the wing. There is strong directional order for the orientation. (c) A single scale as seen from the top showing a diffuse green colour. (d) A micrograph of a single green scale as seen from the underside. The same colour is reflected but this side has a much more shiny, metallic appeerence, indicating a flat, non-diffractive surface. Scale bars: (a) 1 cm, (b) 100 μm, (c) and (d) 20 μm. Image (a) courtesy of Craig G. Cameron, Georgia Institute for Technology.

sides of the scale produced similar peak reflected wavelengths, a result which disagrees with the hypothesis that there maybe green pigments on the top side. It seems intuitive that a coincidence of peak wavelengths would mean that both colours are produced by the same mechanism, but with the introduction of a scattering structure on the top side.

Imaging scatterometry was employed to gain a better understanding of the differences between the top and bottom of each scale. This way one can easily discern the levels of iridescence, and one can also gain clues of what kind of structures are responsible for the appearance of both sides of the scale.

Primary beam imaging scatterometry performed on the top side of the whole green wing scales (figure 7.3) reveals a largely isotropic green colour with a brighter streak

7. A detailed study of the butterfly *Parides sesostris*, utilising focussed ion beam nano-surgery
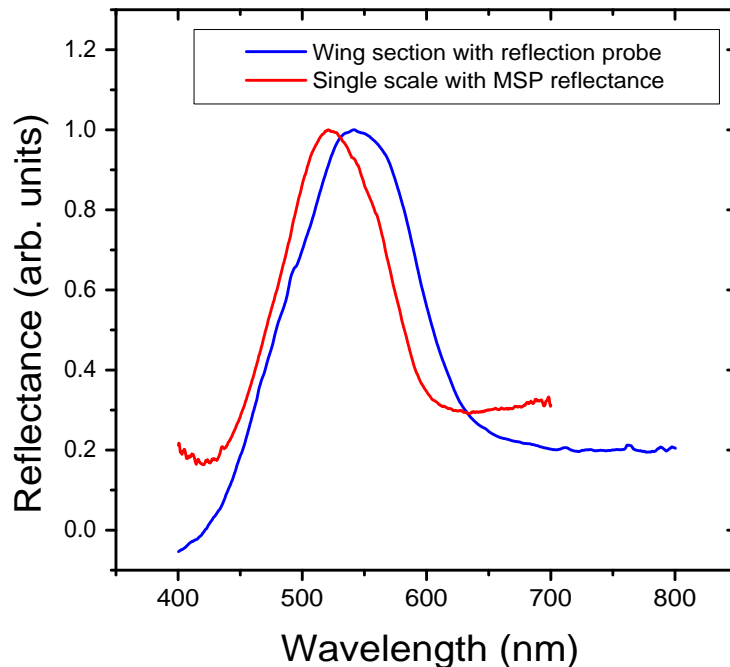
Figure 7.2: Reflection spectra from a macroscopic wing section using the reflection probe and a single scale using MSP techniques.

running perpendicular to the long axis of the scales. This indicates that the ridges seen in the micrographs (figure 7.1) do, in fact, have optical diffraction properties, though isolating the ridges would be necessary to say for certain. As previously stated, a diffraction grating would provide the necessary mechanism to cause the difference between the top and bottom of the scale. The membrane side of the scale provides a very different imaging scatterogram (as expected) as there is a highly specular response (figure 7.3(b)). This indicates a flat, smooth surface. The colour of the reflection is the same green as the ridge side but retains iridescent properties due to the lack of the diffracting ridges on the membrane side. An off-normal scatterogram of the membrane side confirms that the membrane side still provides a specular, mirror-like reflection.

Secondary beam imaging scatterometry was performed on both the top and bottom sides of the green wing scales (figures 7.3(c) & 7.3(d)) This interrogation reveals that the reflected colour of the ridge side is significantly angle-independent and the smooth bottom side exhibits iridescence as can be seen by the blue-shift in colour at high angles of incidence.

(a)

(b)

(c)

(d)
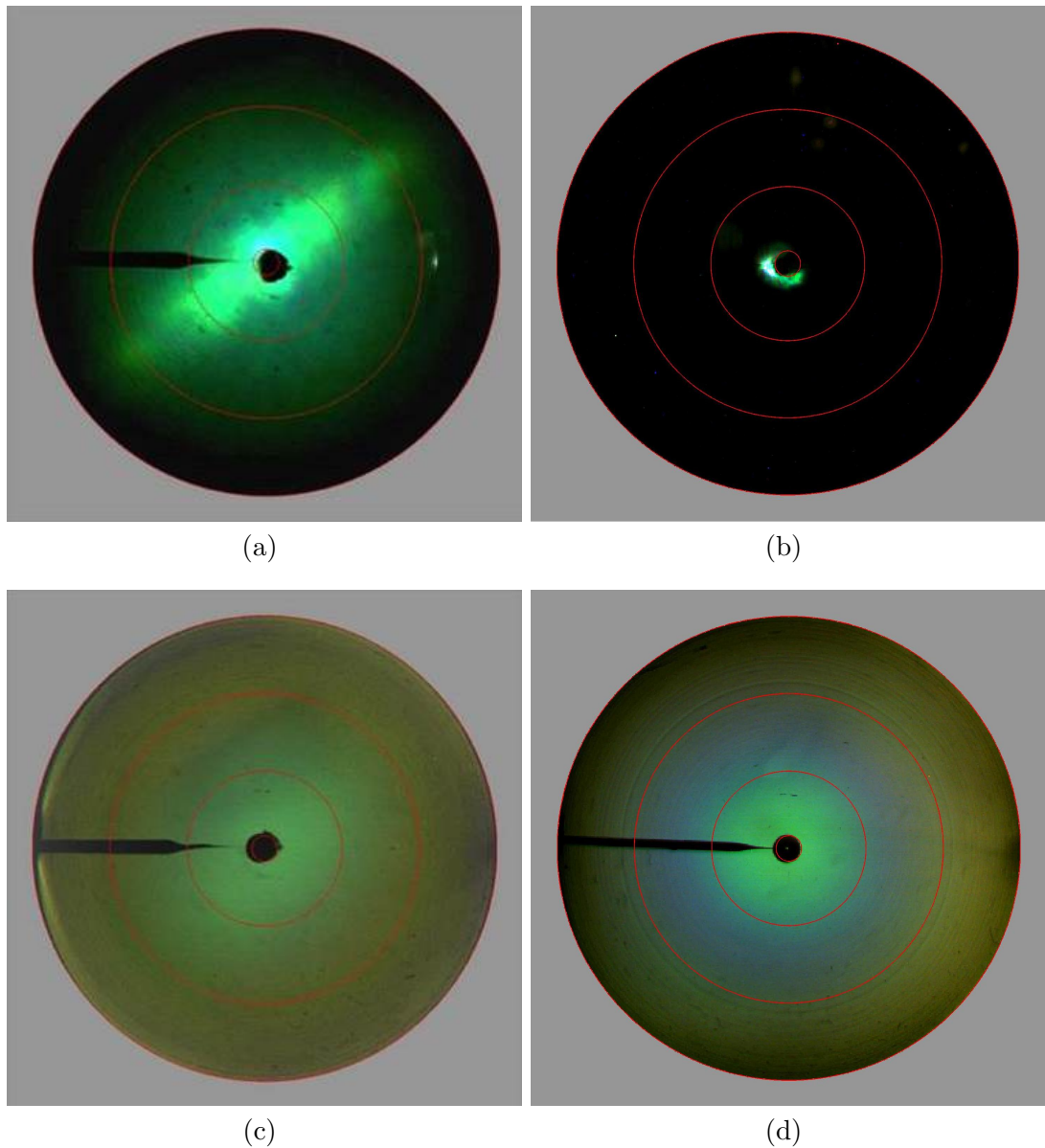
Figure 7.3: Imaging scatterograms from single green wing scales from *P. sesostris*. (a) Primary beam scatterometry of the ridge side of the scale, showing the diffuse nature of the green colouration. A bright streak is observed that is orientated parallel to the periodicity of the ridges present in the scales. (b) Primary beam scatterometry of the membrane side of the scale, showing the same green colour but only as a specularly reflected spot, indicating no diffracting or scattering structure is present on that side of the scale. (c) Secondary beam scatterometry of the ridge side of the scale showing how the colour does not change as the angle of incident light does. (d) Secondary beam scatterometry of the membrane side of the scale displaying the iridescent nature of the membrane side. This can be seen as a blue-shift in colour as the angle of incidence is increased.

7. A detailed study of the butterfly *Parides sesostris*, utilising focussed ion beam nano-surgery

The directional green streak present in the primary beam scatterogram of the top side of the green wing scales (figure 7.3(a)) and the strong order observed in the orientation of the scales on the wing (figure 7.1(b)) suggest that the directional green streak may be present, not only for an individual scale, but for the whole green wing patches. The literature has shown this to be true for other Lepidoptera [125]. To verify the hypothesis in this case, primary beam imaging scatterometry of a large wing patch (approximately 500 wing scales) was performed (figure 7.4). The results show that the directional green streak does persist. Taking into consideration that the female *P. sesostris* butterflies do not exhibit the green wing patches hints at a possible sexual communication function of the male green wing patches and the directional green streak observed. One other explanation for the macroscopic directional green streak is that it could just be an artefact of the colour diffusing mechanism that serves to suppress the iridescence in the scales.

The insignificant difference in reflection response between bright field and dark field secondary beam scatterometry performed on the top side of the scale (figure 7.5) demonstrates further evidence for the angle-independent nature of the scales as they sit on the wing membrane. The membrane side, however, shows a remarkably different response. As reported previously[1] the secondary beam bright field imaging scatterometry of the membrane side shows the same green colour as the top side at normal incidence, this colour blue-shifts with increasing angle from the normal. The dark field imaging scatterometry, however, shows a purple colour at normal incidence that, again, blue shifts with angle, but from reddish-blue, to green (figure 7.5(h)).

7.3   Structural characterisation of *P. sesostris*

It has been widely reported in the literature [1, 22, 63, 64] that the structure of the green wing scales of *P. sesostris* is found to comprise of three main sections, which are (from top to bottom) diffracting ridges, a triply-periodic, bi-continous gyroid poly-crystal and a smooth, thin film membrane layer on the bottom. The structural interrogation carried out here reveals that the diffracting ridges are 3.8 ± 0.4 μm thick, the gyroid is μm thick and the membrane is just 82.7 ± 21.7 nm thick. The small membrane thickness leads one to believe that its purpose is entirely for structural integrity, and not for optical purposes.

The ridge section appears to comprise a mono-grating (figure 7.6(a)), with a periodicity of 741.5 nm $\pm$ 14.4 nm. At normal incidence we find, using equation 3.26 that this grating will support a first order diffraction mode at optical wavelengths. This is further evidence, though not conclusive, that the ridge structure helps to diffuse, not only the reflected light but also the light that transmits through to the gyroid poly-
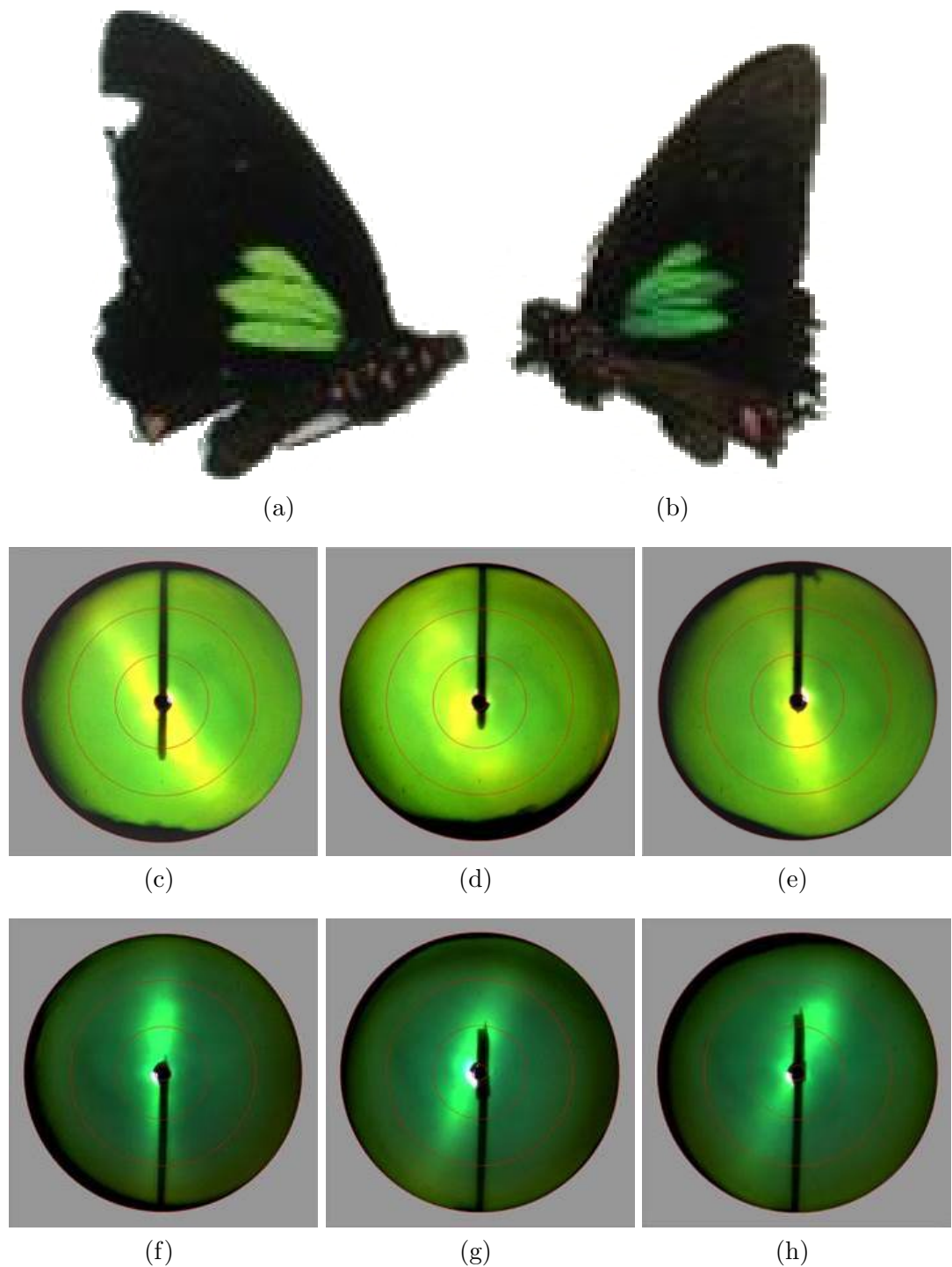
Figure 7.4: Two different *P. sesostris* specimens showing (a) yellowish-green and (b) bluish-green colourations, demonstrating the variances in colour within the species. Primary beam imaging scatterometry was performed on the three green wing patches shown in (a) and (b). A large beam spot was used to cover approximately 500 scales for each scatterogram. (c-e) Scatterograms of the green wing patches marked 1-3 in image (a) respectively. (f-h) Scatterograms of the green wing patches marked 1-3 in image (b) respectively. All of the scatterograms show that the bright streak associated with the diffracting ridges persists on a macroscopic scale.

7. A detailed study of the butterfly *Parides sesostris*, utilising focussed ion beam nano-surgery
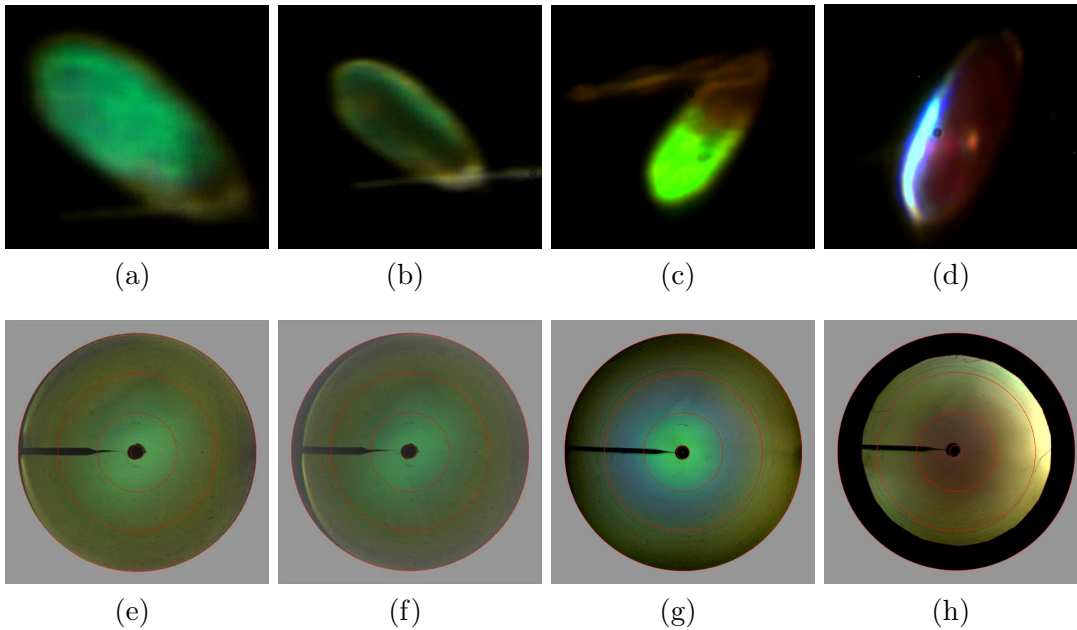
Figure 7.5: Photographs of the *P. sesostris* green wing scales showing (a) and (b) the top side in bright field and dark field respectively and (c) and (d) the membrane side in bright field and dark field respectively. Imaging scatterograms showing the top side with (e) full hemisphere illumination and (f) dark field illumination, the bottom side with (g) full hemisphere illumination and (h) dark field illumination.

crystal, where the band-gap wavelengths are reflected and will be diffracted again as the light passes back through the ridge section. This double-diffraction could explain the remarkable scattering efficiency seen in the primary beam scatterograms (figure 7.3(a)) but only in directions orthogonal to the ridges, hence the bright streak exhibited. The ridges cannot be the reason for the background, diffuse green colour seen. Increasing the magnification reveals a short pitch grating orthogonal to the ridges, effectively resulting in a bi-grating (figure 7.6(c)). Figure 7.6(d) reveals that the ridges are a protrusion of the long pitch grating, which is why the short pitch cannot be seen at lower magnification. The periodicity of the the smaller pitch is 228.3 ± 16.8 nm, a grating that will not diffract at optical wavelengths at normal incidence. It is, therefore, believed that the short pitch grating serves primarily as mechanical support for the protruding ridge structure.

The gyroid poly-crystal, as reported in the literature [64], has many different crystal domains at different angles. This configuration means that, when isolated, the gyroid poly-crystal domains will reflect different wavelengths depending on their orientation. Due to the tiny size of the crystal domains, there will be a pointillistic colour mixing

(a)

(b)

(c)

(d)

(e)
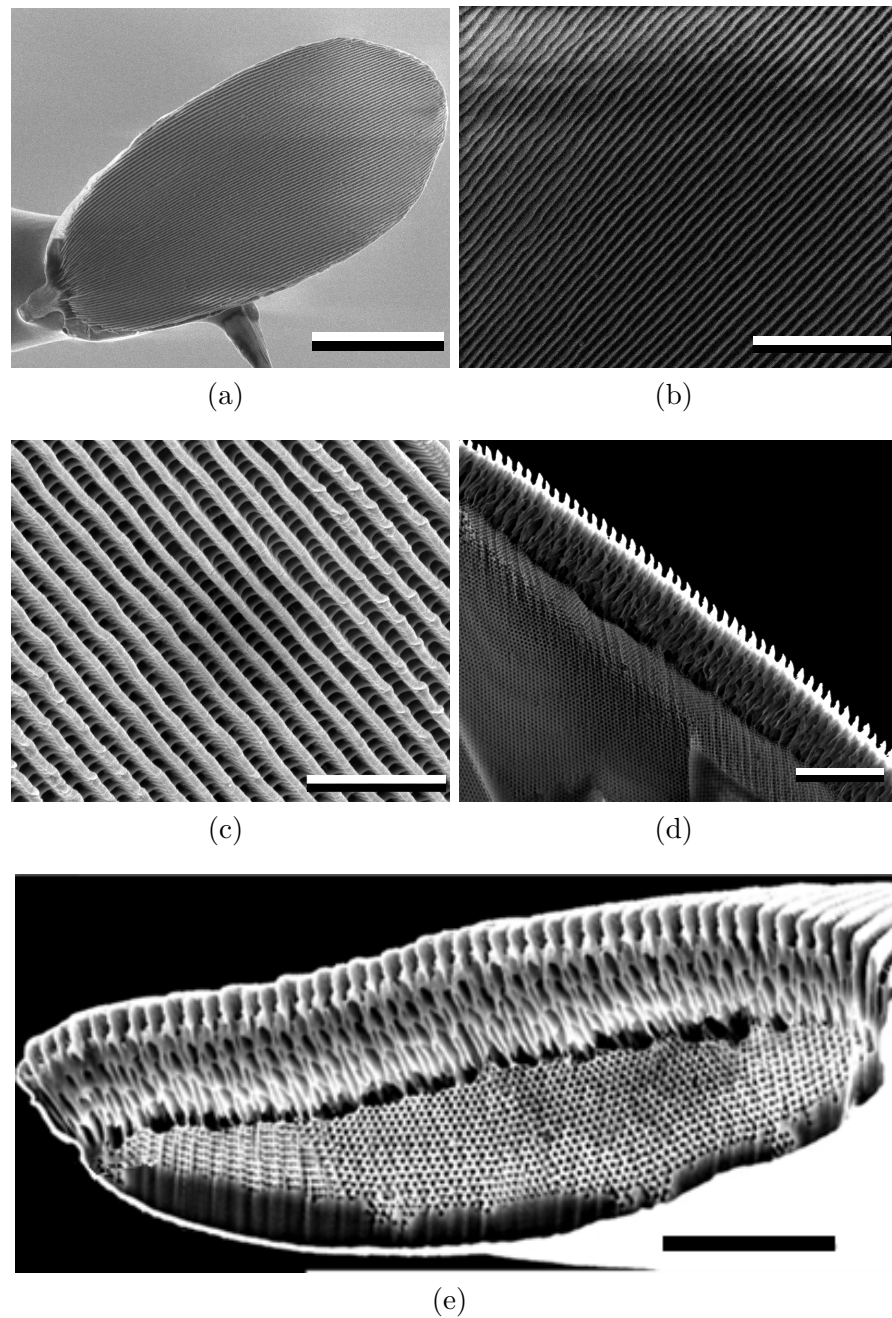
Figure 7.6: Electron micrographs of the ridge and tube section from the green wing scales of *P. sesostris*. (a) The ridge structure on the top side of the scale, showing that the ridges run longitudinally down the long axis of the scales. (b) A magnified image of the ridge structure, showing a highly ordered diffraction grating. (c) Magnifying even further shows the nano-tube array underneath the ridges. (d) A FIB cross-section through a single *P. sesostris* scale showing the nano-tube array and protruding ridges, sitting on top of the gyroid structure. (e) A cross-section through the entire scale revealing how all the component structures fit together. The ridges fit on top as a protuberance of the nano-tube array. This structure sits on top of the gyroid poly-crystal. The underside is then enveloped by the thin membrane layer. Scale bars: (a) 30 μm, (b) 10 μm, (c) 4 μm, (d) 5 μm, (e) 5 μm. SEM micrographs courtesy of Craig G. Cameron.

effect, resulting in a less iridescent, more angle-independent colour. This form of colour mixing has been reported in other Lepidopteran wing scales [126]. The combination of the pointilistic colour mixing from the poly-crystal and the diffraction from the ridges is believed to result in the remarkable angle-independence that is seen in figure 7.3(a).

7.4 Nano-surgery investigation

There have been a few attempts in the literature to deconvolve the effects of the scale components of butterfly wing scales [1, 22, 62, 127], but none as precise and rigourous as the investigation presented here. The work performed by Poladian et al. [62] showed the effect of removing the ridge structure from the green wing scales of *P. sesostris* by crudely using adhesive tape. The result was a blue colour emanating from the exposed photonic crystal juxtaposed by the characterisitic green colour emanating from the rest of the scale that remained intact. It was believed, then, that the photonic crystal reflected blue light into the fluorophore-rich ridge structure where the blue colour was absorbed and green light was emitted. This would result in the colour being even more angle-independent, due to the fact fluorophores scatter isotropically. The problem with that investigation was the method in which the ridges were removed. The ridge structure was separated using sticky-tape, an unreliable method that does not have a very high output of scales that are good enough to characterise optically. Another cause for concern in that investigation is the fact that the resulting ridge-removed scales are fixed to a strip of carbon tape. The carbon tape will change the optical properties of the membrane layer and, therefore, possibly the whole scale.

The FIB milling of individual, green wing scales presented here provided a variety of samples that were used to deconvolve the optical response of the whole green scales. Initial observations of a 'ridge only' green wing scale (the membrane and photonic crystal were FIB-milled away) indicate that the isolated ridges do not show much colour (figure 7.7(c)). They have a dark brown appearance, a colour which is most likely caused by melanin content of the constituent materials. This result is confirmed by reflection spectra (figure 7.7) where we see a relatively low-level broadband reflection from both sides of the isolated ridge region.

Figure 7.9 shows imaging scatterometry of the ridge and tube sections of the scale shown in figure 7.8. Primary beam imaging scatterometry with white light illumination reveals that the green colour of the photonic crystals does not originate from this region alone. Instead there is a conventional mono-grating diffraction pattern exhibited, namely a first-order mode either side of a specularly reflected white spot. This results confirms that the ridge/tube section of the scale diffracts the green colour emanating from the photonic crystal, thereby suppressing the iridesence. As the diffraction grating
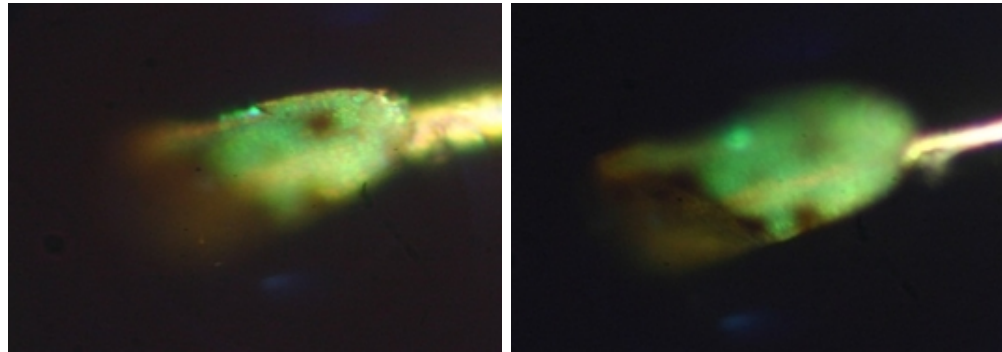
(a)   (b)
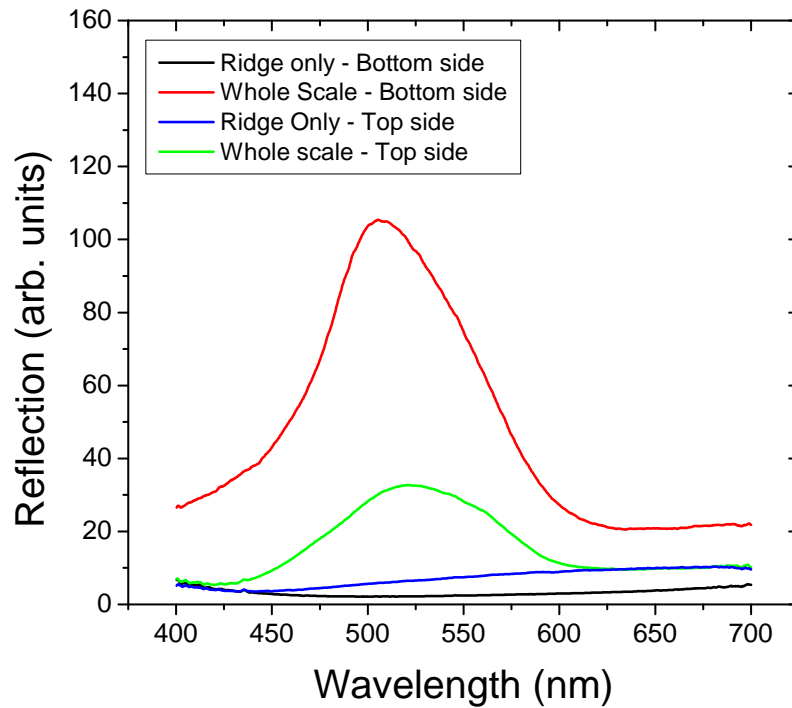
(c)

Figure 7.7:   Optical micrographs showing (a) the top and (b) the bottom side of a single *P. sesostris* scale with part of the photonic crystal and membrane removed. (c) Reflection spectra of a single scale using MSP tecniques. The areas investigated were, the intact region from both the top and bottom sides (the green and red lines, respectively), and the ridge only region from both the top and bottom sides (the blue and black lines, respectively).

(a)   (b)

(c)   (d)
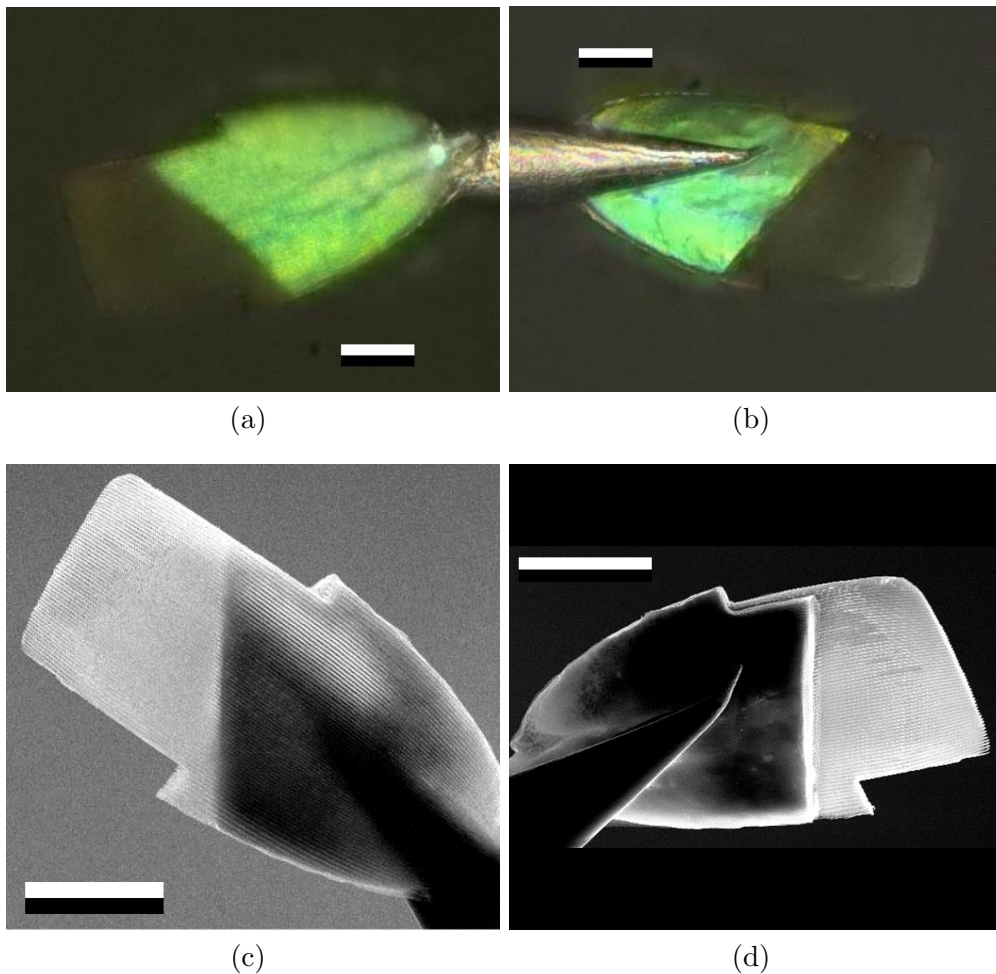
Figure 7.8:   (a) Optical micrograph of a ridge-side up green wing scale that has the gyroid and membrane removed on one half of the scale. (b) The same ridge-only scale as (a) but taken from the membrane side. (c) and (d) SEM micrographs taken from the ridge side and membrane side respectively. Optical and SEM micrographs courtesy of Craig G. Cameron.

formed by the ridges is on the very top of the scale, incident light will be diffracted into the gyroid poly-crystal section, as well as being diffracted again on reflection from the gyroid. This double diffraction process increases the efficiency of the iridesence suppression on the wing scales, giving a more angle-independent green colour appearance. It must be noted that the diffraction pattern on the ridge-only sample is not that of a bi-grating which is in good agreement with the original hypothesis that the small periodicity of the bigrating (228 nm) does not support optical diffraction at normal incidence. Other than the diffraction pattern exhibited by the ridge/tube only sample,

(a)   (b)
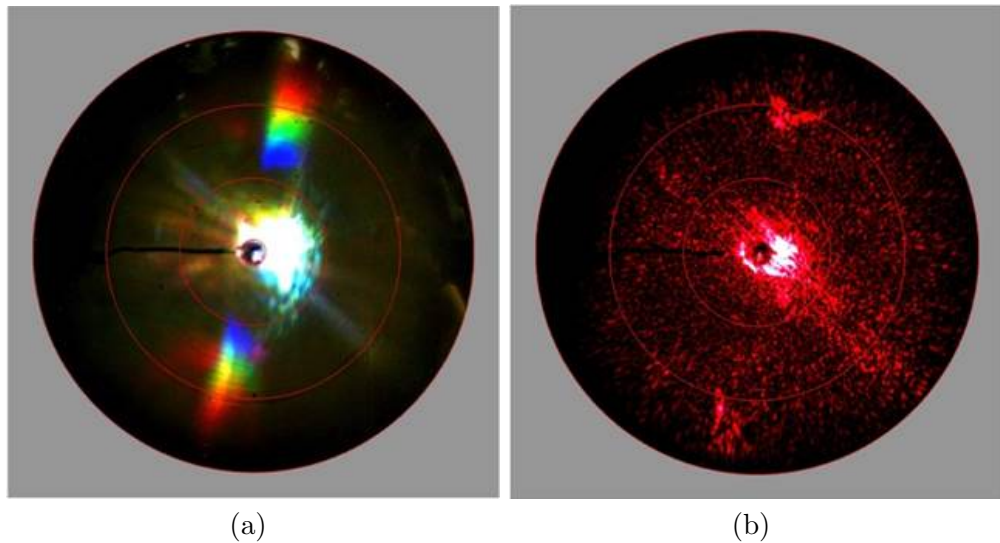
Figure 7.9: (a) Primary beam scatterometry of the ridge and tubes only. The whole scale green colour is not seen, suggesting that the green does not originate from this part of the scale. The characteristic mono-grating diffraction pattern is observed. A diffuse, near angle-independent brown colour is also observed. (b) is the same as (a) but with monochromatic 637 nm illumination provided by a laser diode. The purpose of only illuminating with 637 nm light is that a clearly defined angle of diffraction can be obtained and, therefore, used to measure the pitch of the grating using equation 3.26.

there is also an angle-independent, diffuse brown colour. Due to the non-iridescent nature of this colour, the origin is most likely to be the melanin content of the materials comprising the structure, agreeing with the result obtain from the isolated ridge spectra (figure 7.7). This cannot usually be seen from the whole scale as the colour from the photonic crystal is far brighter and, therefore, outshines the brown colour. The characteristic rainbow diffraction pattern is also not normally seen in the whole scale scatterograms, because the level of reflection is far lower for a grating than it is for a gyroid photonic crystal of the type found in the whole scale.

Figure 7.9(b) shows monochromatic, 637 nm illumination, primary beam imaging scatterometry on the isolated ridge and tube section of the scale. It can be seen that some of the red light has been scattered diffusely by the pigments in the material. The main features of the scatterogram though, are the central zeroth order reflection and the ± 1st order diffracted modes. The angle of these modes, the wavelength of the illumination and equation 3.26 tell us that the mono-grating causing the diffraction has a ridge periodicity of 739 nm. A result which is agrees with the measurement obtained from SEM analysis (741.5 nm ± 14.4 nm).

(a)

(b)

(c)

(d)
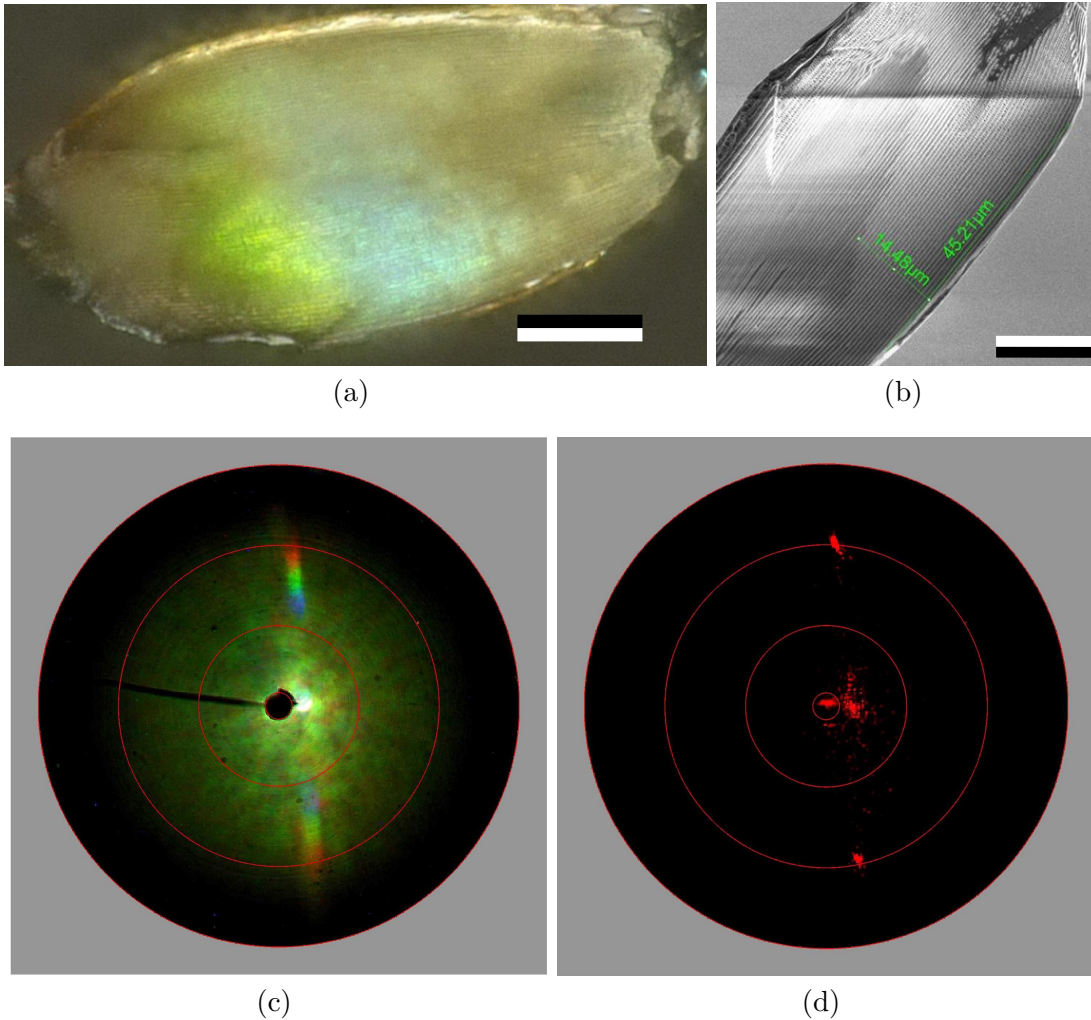
Figure 7.10:   (a) Optical micrograph of the green wing scale with the fins removed (via FIB-milling). (b) SEM image showng the region of the scale where the fins have been removed. Primary beam imaging scatterometry performed the green wing scales shown in (a) and (b) using (c) broadband illumination and (d) 637 nm laser light for the purpose of measuring the ridges using equation 3.26. The angles of the first order modes at 637 nm wavelength are 59 degrees either side of the normal. This yields a theoretical mono-grating periodicity of This result yields a value for the long periodicity of the nano-tube array of 743 nm. Scale bar: (a) 20 μm, (b) 15 μm. Optical and SEM micrographs courtesy of Craig G. Cameron.

7. A detailed study of the butterfly *Parides sesostris*, utilising focussed ion beam nano-surgery

The ridge section of the *P. sesostris* green butterfly scales consist of a nano-tube array with fins protruding from the larger periodicity to form a mono grating on the very top of each scale. The fins seem somewhat redundant as the nano-tube array is, at optical wavelengths, effectively just a mono-grating due to its small periodicity being too small for normally-incident diffraction. To test this hypotheses, just the fins were carefully removed from one scale, leaving the membrane, the gyroid poly-crystal and the nano-tube array in tact. The resulting structure can be seen in figure 7.10(a) where the blue region is found. This region is also marked on an SEM of the resulting structure seen in figure 7.10(b). Imaging scatterometry was then performed on the ridge side of the scale (7.10). This investigation reveals that the fins may play a bigger role in the overall colour production than initially thought. The reason for this is that the primary beam imaging scatterometry using broadband illumination shows a very different scattering pattern. The most striking difference is that the bright green streak, featured in figure 7.3(a), has been replaced with a mono-grating-like diffraction pattern. A first order diffraction mode can be seen either side of the specularly reflected, zeroth order white spot. It is difficult to say why the removal of the fins has produced the rainbow pattern instead of the brighter green streak. One theory is that the curvature at the top of the fins acts to reduce the amount of initial reflection because the array of fins can, therefore, be thought of as an effective index matching medium, just like the nipple arrays found on the compound eyes of some species of insect [8, 15, 64, 68, 87]. The advantage of this suggested mechanism is that less broadband light will be reflected from the ridges, therefore increasing the saturation, and therefore, the visibility of the green wing patches. Other than this diffraction pattern, the angle-independent green colour can still be seen to reflect from the gyroid poly-crystal and membrane section. Monochromatic, 637 nm illumination reveals a theoretical periodicty of 743 nm, this result agrees with the measured result from the SEMs and the result obtained from 637 nm laser diode illumination of the isolated ridge/tube imaging scatterometry.

Optical micrographs and reflection spectroscopy of the isolated gyroid poly-crystal (figure 7.11) reveal a significant blue-shift in colour from the whole green wing scales. The isolated gyroid region was mapped out using MSP techniques at a resolution of 1 μm x 1 μm. Figure 7.11(b) shows the peak reflected wavelength as a function of position on the scale. This analysis reveals that the isolated gyroid peak wavelength is a little over 480 nm, a result confirmed by fitting a Gaussian function to the average reflection spectra of the whole isolated gyroid region which yielded 483.6 nm as the peak wavelength.

The removal of the membrane area of the green wing scales shows a dramatic change in the overall colour exhibited. Figures 7.12 and 7.13 shows a scale that has had the membrane completely removed from one half of the scale via FIB milling. It should also
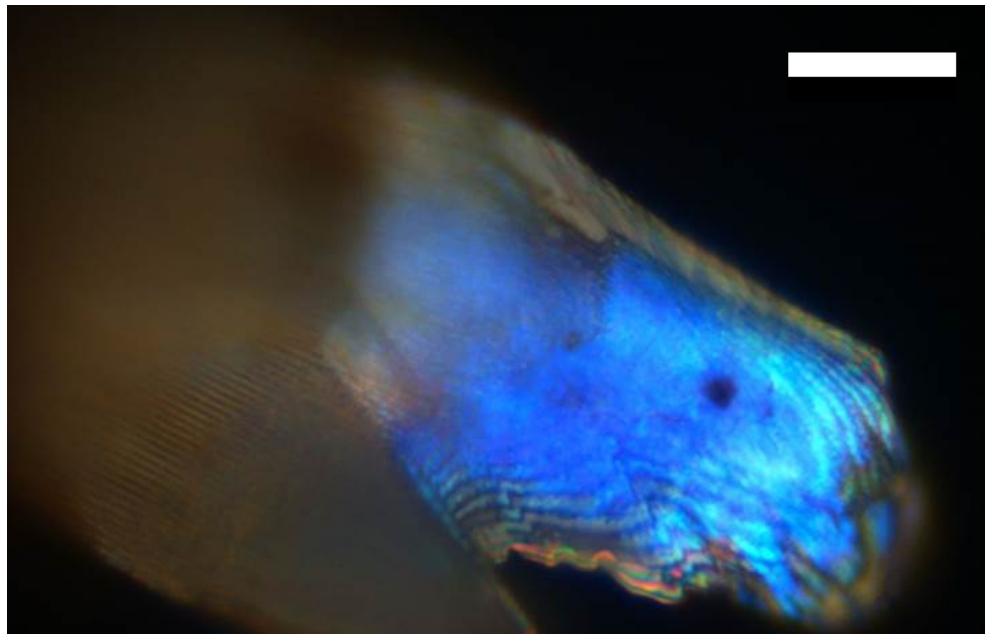
(a)
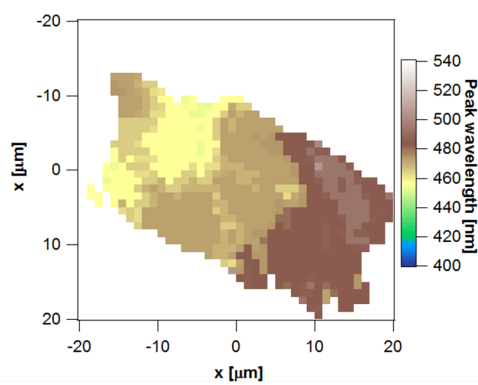
(b)
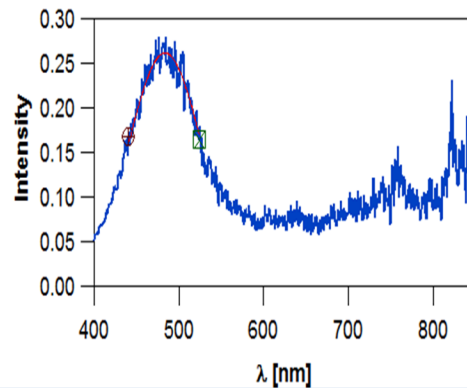
(c)

Figure 7.11: (a) Optical micrograph of the isolated gyroid poly-crystal from the *P. sesostris* green wing scales. The green colour from the whole scale was blue-shifted due to the removal of the ridge and membrane structure. (b) The peak wavelength from each pixel of the wing scale shown in (a) has been mapped out. This revels that gyroid poly crystal has a reflection peak just above 480 nm. (c) An average reflection spectra of the red area shown in (b). Gaussian fitting to this curve reveals a peak reflected wavelength of 483.6 nm. Scale bar: (a) 30 μm.

(a)

(b)

(c)

(d)
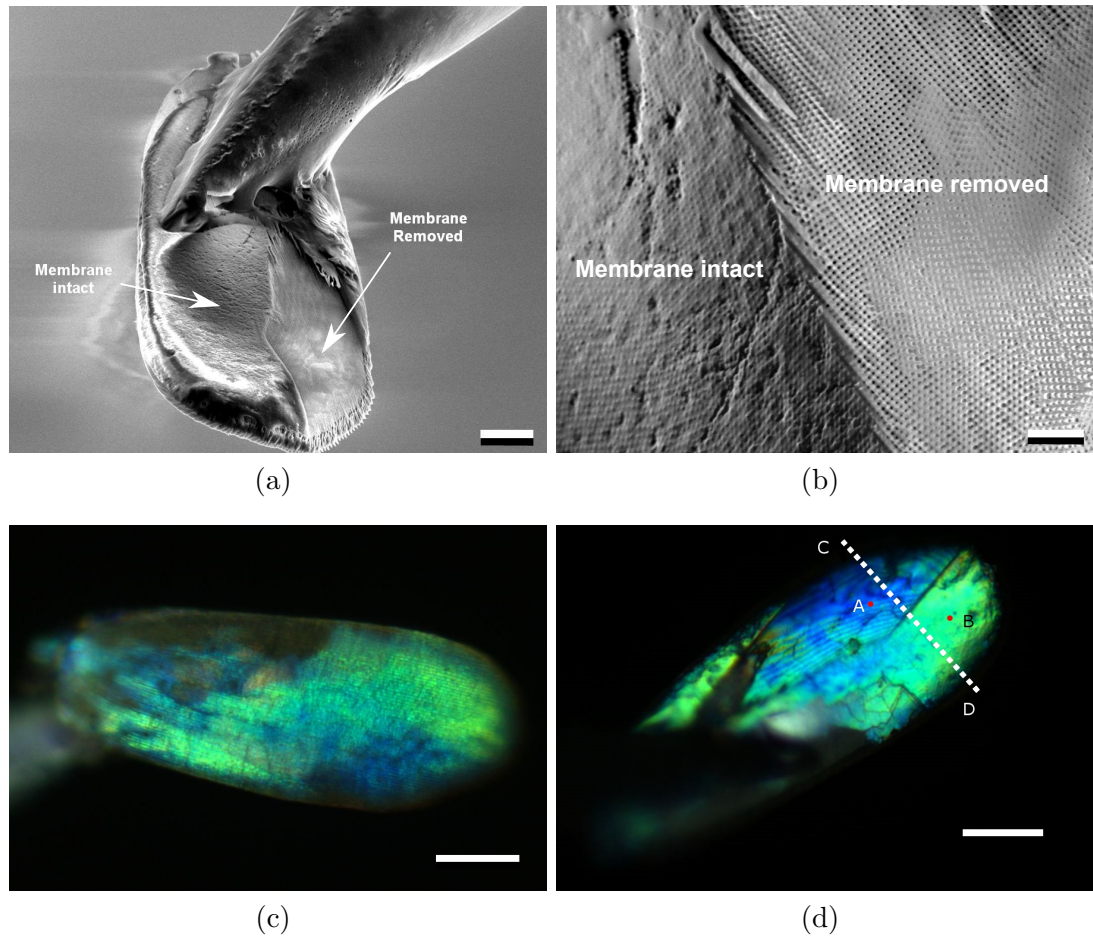
Figure 7.12: (a) SEM image showing the bottom side of the green wing scale, revealing the section where the membrane has been removed. (b) A magnified SEM of the interface between the milled and unmilled membrane regions. The gyroid poly-crystal can be seen in the membrane removed region. Optical micrographs of (c) the top side and (d) the bottom side of a single green wing scale with part of the membrane removed. A significant blue shift in colour can be seen on both sides of the scale, where the membrane has been removed. Scale bars: (a) 10 μm, (b) 2 μm (c) and (d) 20 μm. (SEM micrographs (a) and (b) courtesy of Craig G. Cameron).

7. A detailed study of the butterfly *Parides sesostris*, utilising focussed ion beam nano-surgery
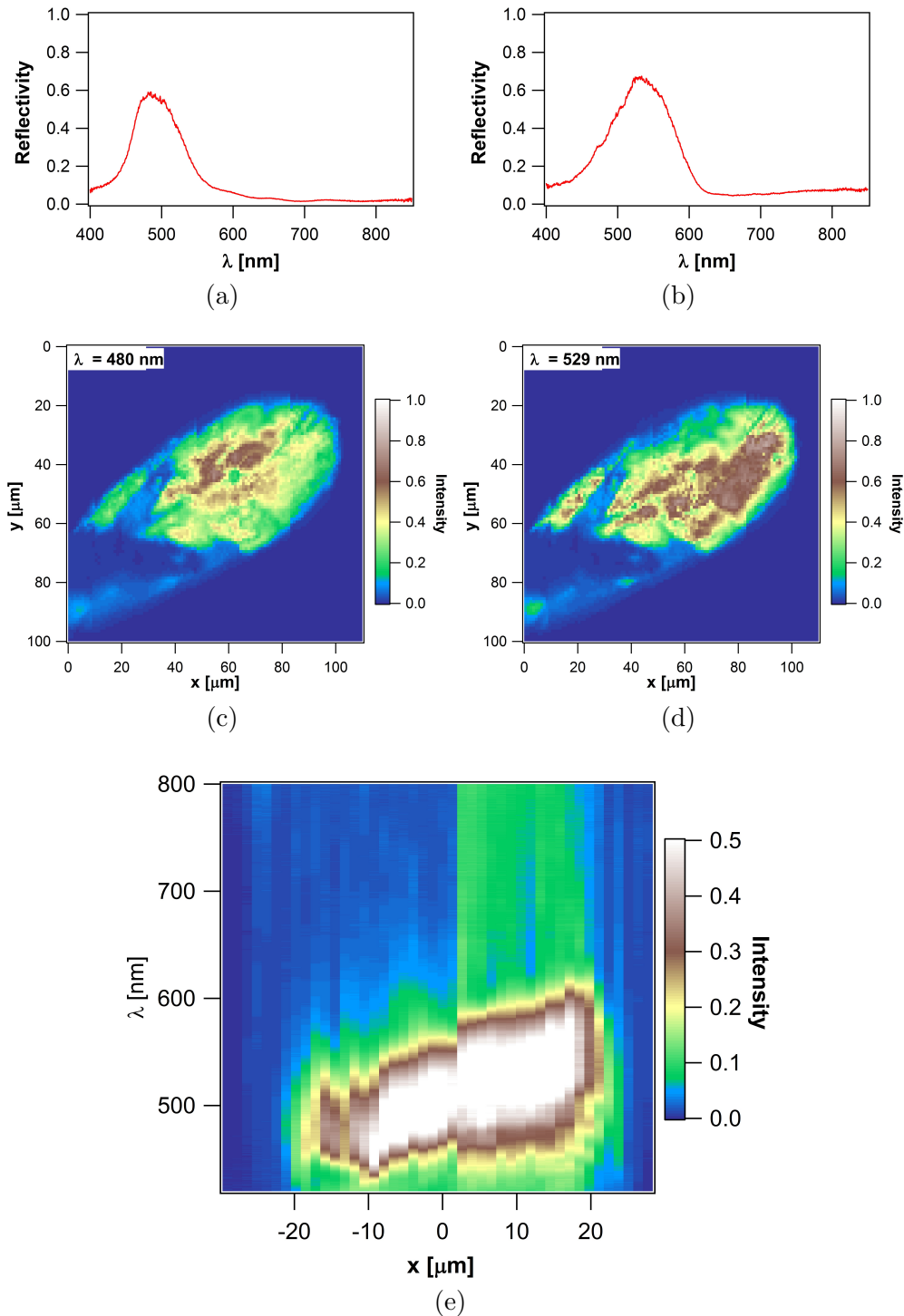
Figure 7.13: (a) and (b) show reflection spectra taken at the points A and B in figure 7.12(d), respectively, yielding peak wavelengths of 480 nm and 529 nm, respectively. Intensity maps of the scale at (c) 480 nm and (d) 529 nm, highlighting the change in colour between the two sections. (e) Reflection spectra as a function of distance between the points C and D in figure 7.12(d). A sharp blue-shift in the peak of the reflection band can be observed between the interface of the unmilled and milled sections of the scale.

be noted that some of the gyroid poly-crystal was also removed during this process. The scale exhibits a very blue colour appearance in reflection for the half of the scale that has had the membrane area removed via FIB-milling, and the characterisitc green colour persists for the half that is still intact. This suggests that the bottom of each scale plays a very important role in structural colour production.

To confirm the presence of fluorophores in the green wing scales, the wing patches were treated to 2 months of photo-bleaching using UV radiation. The prolonged exposure was used because otherwise the UV radiation would have to be more intense to achieve the same result in a shorter time, thereby risking damage to the scales due to the high intensity. The resulting photo-bleached wing patch, when observed with the eye, exhibited a remarkable blue-shift in colour from the untreated scales (figure 7.14). MSP reflection spectra were obtained, showing the new peak wavelength of the photo-bleached scales to be 463.4 nm, a blue-shift of about 80 nm. As shown earlier, the isolated gyroid structure has a peak wavelength of 480 nm, which was the expected result from the photo-bleaching treatment. The discrepancy could be due to the gyroid itself containing fluorophores. Another reason for the discrepancy becomes apparent when looking at the optical micrographs. They show that there may be some structural shrinkage of the scales. If the gyroid structure has decreased in size then it would exhibit a decreased value of peak reflected wavelength. Therefore, without structural analysis of the photo-bleached scales, few formal conclusions can be made from this process.

7.5   Computational modelling

To confirm the understanding of the triply periodic, bi-continous gyroid poly-crystal, and the membrane section of the green wing scales, computational models were required. Individual sections of *P. sesostris* were simulated using HFSS software [96] and TFCalc software [95].

7.5.1   Computational modelling of the bicontinous, triply periodic gyroid structure

To simulate the gyroid poly-crystal, HFSS software was used [96]. To produce a gyroid structure in HFSS, it has to be imported. The structure's surface was first mapped using K3DSurf software [128] using the equation for the surface of the gyroid minimal

7. A detailed study of the butterfly *Parides sesostris*, utilising focussed ion beam nano-surgery
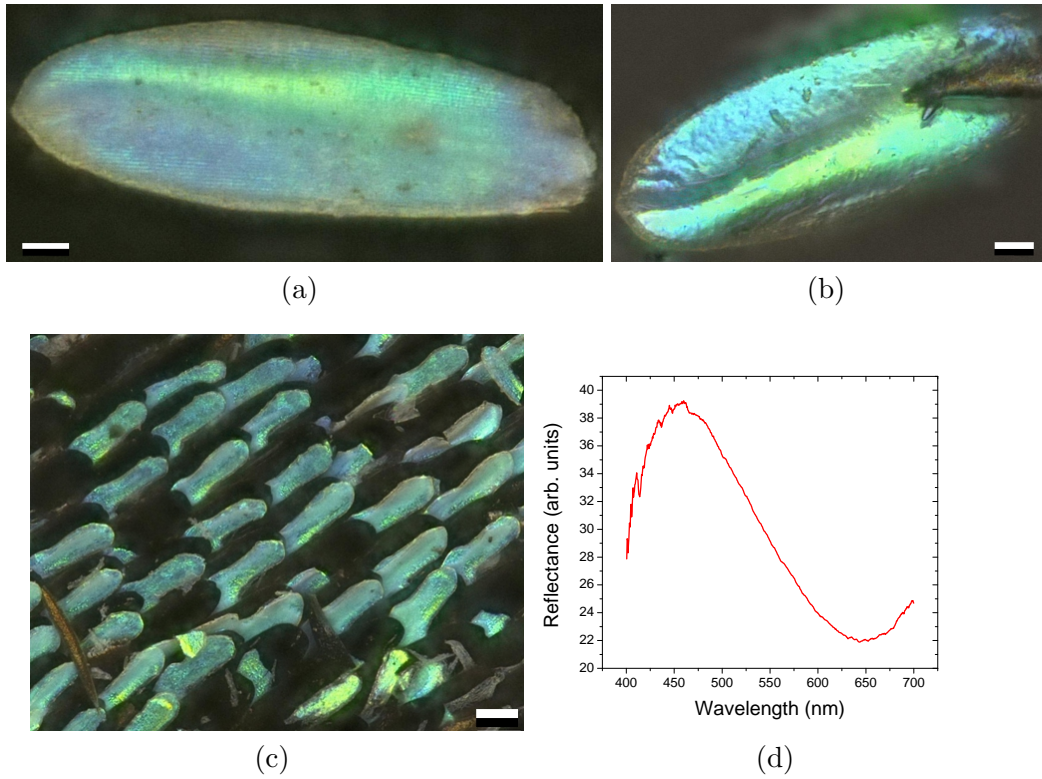
Figure 7.14: Optical micrographs of photo-bleached scales showing (a) a single scale top-side up and (b) a single scale bottom-side up. (c) shows a wing patch of photo-bleached scales. (d) Mean MSP reflection spectra from 30 different photo-bleached scales. The spectra reveals a peak wavelength of 463.4 nm, a blue-shift of approximately 80 nm when compared to the untreated scales. Scale bars: (a) and (b) 10 μm, (c) 40 μm. (Optical micrographs courtesy of Craig G. Cameron, optical spectra taken by Alfred J. Lethbridge).

surface, which is:

$$cos(2\pi x) \times sin(2\pi y) + cos(2\pi y) \times sin(2\pi z) + cos(2\pi z) \times sin(2\pi x) - t = 0, \quad (7.1)$$

where the value t defines the volume fractions of the continuous channels either side of the surface, using the restriction that the sum of the volume fractions of the two channels must equal one. The value $t = 0$ would define a gyroid that comprises 50% solid and 50% air of the total volume. The gyroid poly-crystal in *P. sesostris* has a chitin to total volume ratio of 0.4, and hence a value of $t = -0.3$ was required to achieve this. The gyroid surface could then be exported to Solid Works software [129]. Using Solid Works, the gyroid surface could be made into a solid by closing off and filling the

desired channel. The schematic for the minimal surface designed using K3DSurf and the solid gyroid unit cell created using Solid Works can be seen in figure 7.15. The single unit cell of solid gyroid was then exported to HFSS (figure 7.16(a)).

Four copies of the unit cell were stacked to form a 1x1x4 section of gyroid unit cells (figure 7.16(c)). Master and slave boundaries were applied on the x and y faces of the cubic unit cells, effectively making a structure that is 4 layers thick in the z direction and infinite in the x and y directions. The material chosen to model the gyroid was chitin, as was assumed in the literature [22, 64]. The refractive index was assumed to be $n = 1.56 + 0.06i$ [9]. The filling fraction was chosen to be 40% [63].This stucture was then analysed using the Floquet port solver as described in chapter 4.

The computational modelling confirms that the gyroid structure does exhibit a band gap at optical wavelengths as seen in figure 7.17. The band gap appears to be centred around approximately 410 nm. The experimental reflection obtained from the exposed gyroid poly-crystal (figure 7.11) gives a peak wavelength at 483.6 nm. This discrepancy is quite likely due to the presence of fluorophores within the chitin structure, which would shift the peak wavelength. Absorbance modelling of the structure reveals a family of absorbance peaks centred around 383.5 nm. Absorbance peaks are usually located at reflection band-edges (due to the high electric fields within the material at the band-edges), therefore, it is suggested that a family of reflection modes exist.

The gyroid was also modelled with the membrane underneath, to find out if the membrane and gyroid combined have a different structural colour effect (figure 7.18). As we can see there is no significant shift of the band gap wavelengths. However, there is notable increase in intensity and wavelength of the Fabry-Perot modes of the system. The significance of this, if any, is yet to be determined.

7.5.2   Membrane layer and ridge layer modelling

The membrane layer was modelled using TFCalc software [95]. It was modelled as a thin film consisting of chitin with a refractive index of $n = 1.56 + 0.06i$. The simulated thin film comprised of a thickness of 82.7 ± 21.7 nm, taken from the TEM analysis. This invesitigation reveals a low level of reflection throughout the optical regime (figure 7.19). The graph of reflection as a function of wavelength shows a peak intensity of 15.8%, occurring at 524 nm. A low reflection intensity is to be expected for a single layer system. This agrees with the original hypothesis that the membrane is not significant in the colour production of the scale. It appears that the membrane's sole function is to provide mechanical support to the bottom of the wing scales.
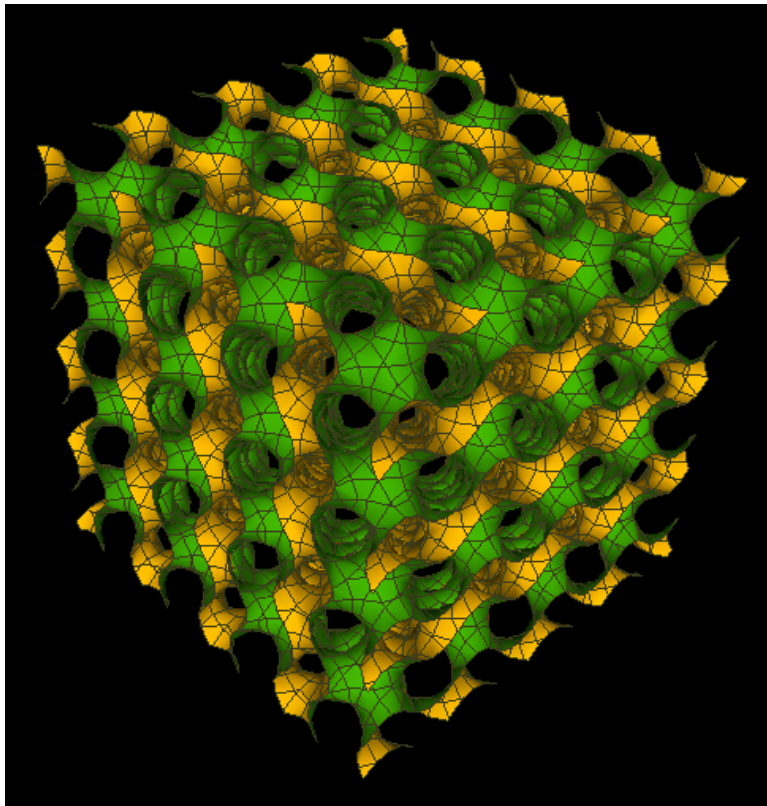
(a)
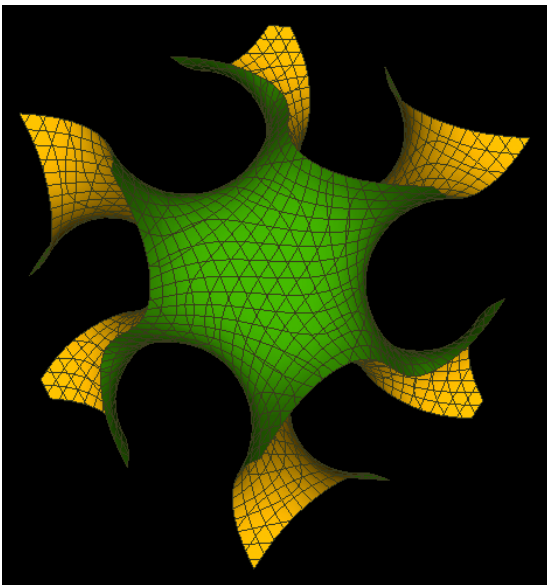
(b)
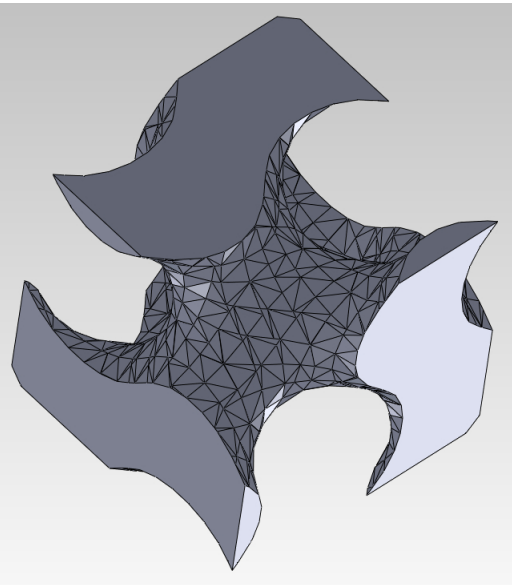
(c)

Figure 7.15: (a) A schematic of 4x4x4 unit cells of the gyroid minimal surface created using equation 7.1. (b) A single unit cell of the gyroid minimal surface, required as the first step to create the gyroid model in HFSS. (c) The second step of creating the gyroid unit cell is to import the minimal surface from (b) into Solid Works so that the channel that has a 40% filling fraction can be closed off and made into a solid object. The image in (c) shows the finished solid gyroid with 40% filling fraction of solid material.

(a)   (b)   (c)
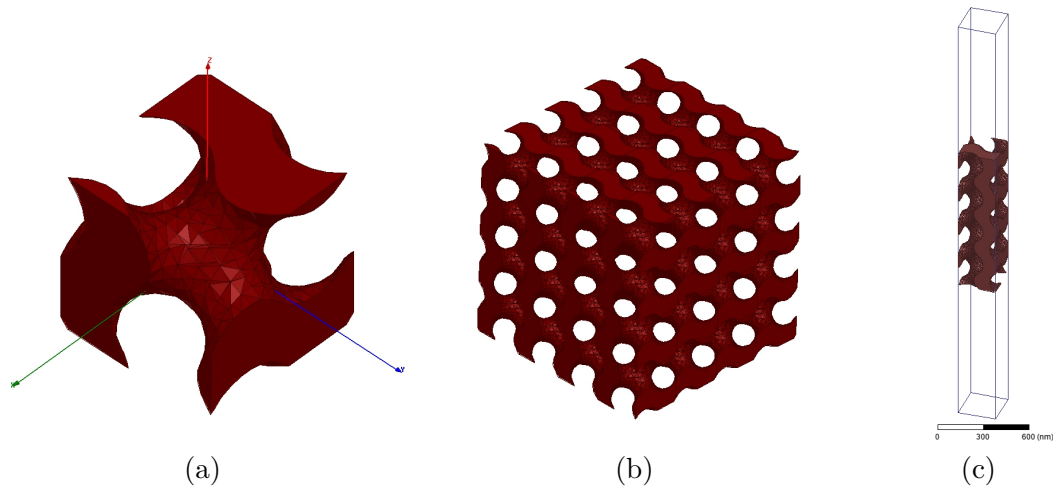
Figure 7.16: (a) A single unit cell of the gyroid structure. (b) A 4x4x4 section showing the full periodicity of the system. This total volume of the crystal comprises 40% chitin and 60 % air. (c) Schematic of the gyroid structure representing an infinite 'slab' of gyroid crystal that is four unit cells deep. This model was used for the simulations.

7.6 Conclusions

The whole wing scales have evolved to produce a largely angle-independent green colour in reflection. There is, however, a bright green diffraction streak present, revealed using imaging scatterometry, that is a directional colouration due to the diffracting ridges of the top layer of the structure. This green streak persists in the imaging scatterometry performed on a green wing patch, the resulting beam spot illuminates approximately 500 scales. This characteristic of the whole green wing patch is understood to offer an evolutionary advantage, if any, for sexual communication. The female of the species does not display the structurally coloured wing patches which indicates that sexual communication is the primary role of the male green wing patches, however, further study would be required to confirm this.

The ridge structure that causes the bright green streak in the imaging scatterometry does not appear to be the origin of the overall green colour of the scales. The primary beam scatterometry on the ridges-only sample has revealed that this structure is simply reduced to having the optical property of a mono-grating, agreeing with the hypothesis that it's function is scattering incident light and also light that is reflected from the rest of the structure. Reflection spectra confirm the low intensity, broadband colour from the isolated ridge region. Optical microscopy reveals a dark brown colour, suggesting also that there is probably a significant melanin content of the constituent materials.

7. A detailed study of the butterfly *Parides sesostris*, utilising focussed ion beam nano-surgery

(a) (b)
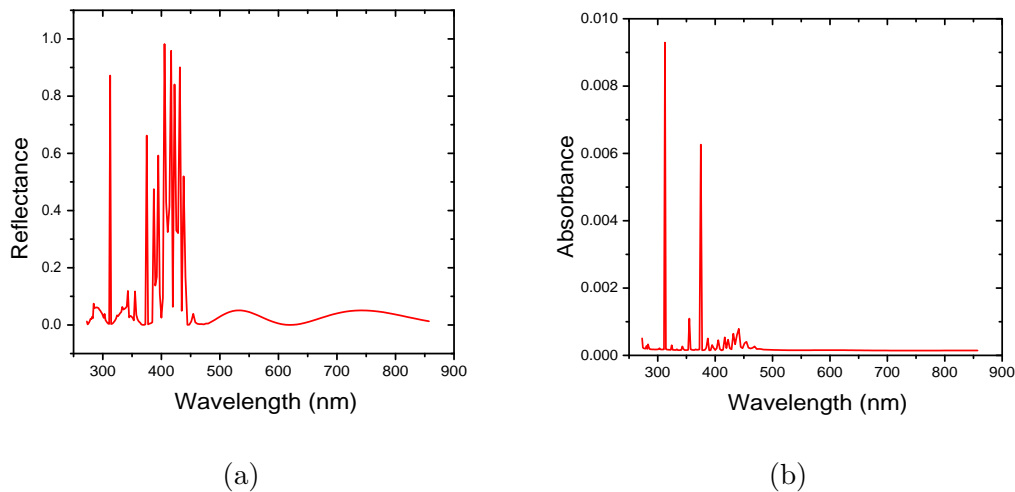
Figure 7.17: (a) Gyroid computational modelling reflection spectra as a function of wavelength. Here we see a band-gap between (approximately) 350 nm and 450 nm. The experimentally measured response from the exposed gyroid poly-crystal has a peak in reflected wavelength at approximately 480 nm, the difference is suspected to arise from fluorophores present throughout the gyroid crystal. (b) Absorbance spectra of the model shown in figure 7.16(c). Peaks in absorbance are usually located at the reflection band-edges. This indicates that a family of modes exisit for this system. The range of absorbance peaks is 312.5 nm to 454.5 nm with a midpoint of 383.5 nm, indicating an even lower peak reflected wavelength range.

The gyroid poly-crystal is found to reflect light of 483.6 nm in wavelength. This result was revealed after removing the membrane and the ridge structure from the sample. This value lies within the absorption curve found by Wilts et al. [1] and so it is speculated that the gyroid acts to reflect the excitation wavelengths of the fluorophores that are present in the ridge structure.

The membrane layer does not play a significant role with respect to structural colour, however, it does seem likely to be an area of the scale that contains a significant concentration of fluorophores. As the green colour of the scales blue shifts when the bottom of the scale (membrane and the lower part of the gyroid) is removed. When just the membrane is removed though, leaving the gyroid completely intact, there seems to be no shift in colour whatsoever. Whilst not intuitive when speculating how such structures could be formed, a graded distribution of absorbing material has been seen before in a paper by Mejdoubi et al. (2013) [130] reporting the structurally coloured blue wing scales of *Morpho rhetenor*. A graded distribution of fluorophores could be present in the *P. sesostris* green wing scales, though more work would need to be
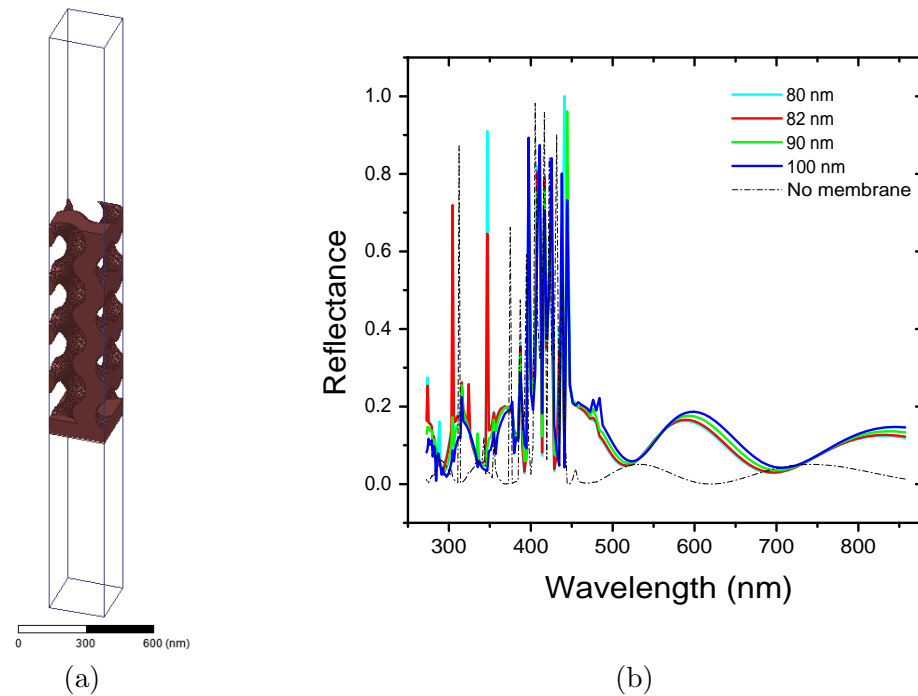
Figure 7.18: (a) A schematic of the model used to discern the effects of the membrane on the gyroid structure. (b) Theoretical reflection spectra from the model shown in (a), with a varying membrane thickness. The results show no significant change in the position of the photonic band-gap. However, the change that can be observed is an increase in the intensity and wavelength of the Fabry-Perot modes as the membrane thickness is increased.

undertaken to show this.

Whilst Wilts et al. [1] managed to confirm the presence of fluorophores, our own attempt to confirm this and to observe the effect of removing the fluorophores. The possible shrinkage of the gyroid poly-crystal during the photo-bleaching process means that few formal conclusions could be made.

It has been shown here that one can gain a much clearer understanding of a complex, multi-component structural colour system, by isolating the different elements in order to deconvolve their combined effects. In this study it was achieved using advanced FIB-milling and analysis techniques.

(a)

(b)
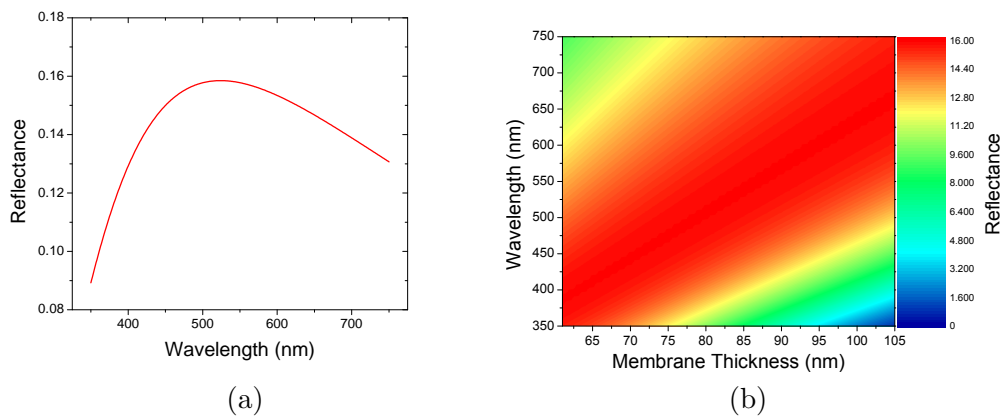
Figure 7.19: (a) The simulated spectra of the membrane layer, modelled as an 82.7 nm thin film of chitin $n = 1.56 + 0.06i$. A peak wavelength of 524 nm is observed. (b) A colour plot showing the effect of changing the thickness of the membrane. The range of values shown represent the mean value ± the standard deviation on the measurement of membrane thickness taken from TEM analysis.

Chapter 8

Fabrication and Characterisation of Bio-Templated Gyroid Structures from *Parides sesostris*

8.1 Introduction

As we learn more and more about how to tailor photonic devices for our purposes, it is important to also keep up manufacturing techniques. Considering the nano-scale of photonic crystals that interact with visible light, it can be extremely difficult to achieve a crystal of good quality and of useful size. This can be overcome to an extent by once again looking to nature, though not for inspiration in this case, but for direct bio-templating [131]. Bio-templating is becoming increasingly popular as it is far easier to acheive [50], especially in the case of 3D photonic crystals, where simple deposition techniques cannot be used.

The investigation reported in this chapter was performed to further the toolbox of photonic devices that can be produced for applications such as optical computing [3, 4, 5, 52, 132] and optical communications [133]. Biotemplated gyroid poly-crystals were produced using the gyroid structure found in the green wing scales of *Parides sesostris* as the template and surface sol-gel (SSG) treatment as the coating process. Firstly the scales were coated in an inorganic, high index materials with the intention of increasing the peak reflected wavelength of the whole scale. Then, the scales were pyrolised in order to remove the organic chitinous gyroid, leaving a purely inorganic, high refractive index structure. The optical interrogation was performed using the reflection probe for

wing patches and MSP techniques for the single scale characterisation.

For an investigation such as this, a suitable sample is needed. Such a sample should be easily infiltrated by liquid solutions and also a sample that is well known optically. *Parides sesostris* is a perfect specimen for this investigation as the triply-periodic, bicontinuous gyroid structure not only allows full liquid infiltration, but the structure would be incredibly difficult to replicate on the same scale, therefore this highlights the capabilities of the SSG coating process for replication purposes [48, 51, 105, 107, 120, 134, 135, 136, 137, 138, 139]. It should be noted that all SSG processing, SEM micrography and structural characterisation was performed by Jonathan P. Vernon, Georgia Institute of Technology, Atlanta, GA, USA.

8.2 Surface Sol-Gel coating of the *P. sesostris* green wing scales.

As reported in the last chapter, a macroscopic, reflection probe measurement on a *P. sesostris* green wing patch provides a peak in reflected wavelength of 545 ± 5 nm. It was also reported that there was a high variance of this value, due to the natural intra-species variation of the green colour in the wing patches and also a variation of colour across individual green wing patches. This led to the decision that the same areas on the same wing patches should be analysed. This meant characterising the wing patches in their natural state, then they were sent back to the USA to be coated with titania via SSG for a number of cycles then they were sent back to the UK to be optically analysed again. This process would be repeated on the same wing patch, coated with more and more layers of titania and tin-doped titania. This would ensure that any natural variation would not have an effect on the change in peak wavelength between samples. Two wing patches were chosen, one left in the natural state before the SSG cycles were applied, and the second had the surface dendritically amplified before the SSG process. Dendritic amplification refers to the atomic-branching of the structures surface, aiding the addition of further deposition [140]. Starting with a natural sample and a dendritically amplified sample should show clearly if the amplified surface improves the SSG coating process.

8.2.1 Optical characterisation of the titania-coated green wing scales.

Optical characterisation of the bio-templated samples was performed on both whole wing sections, and also on individual wing scales. Both were analysed to observe both the macroscopic and microscopic effects of the technique employed here. The whole wing sections were analysed using the reflection probe. Initially only the coated gyroid
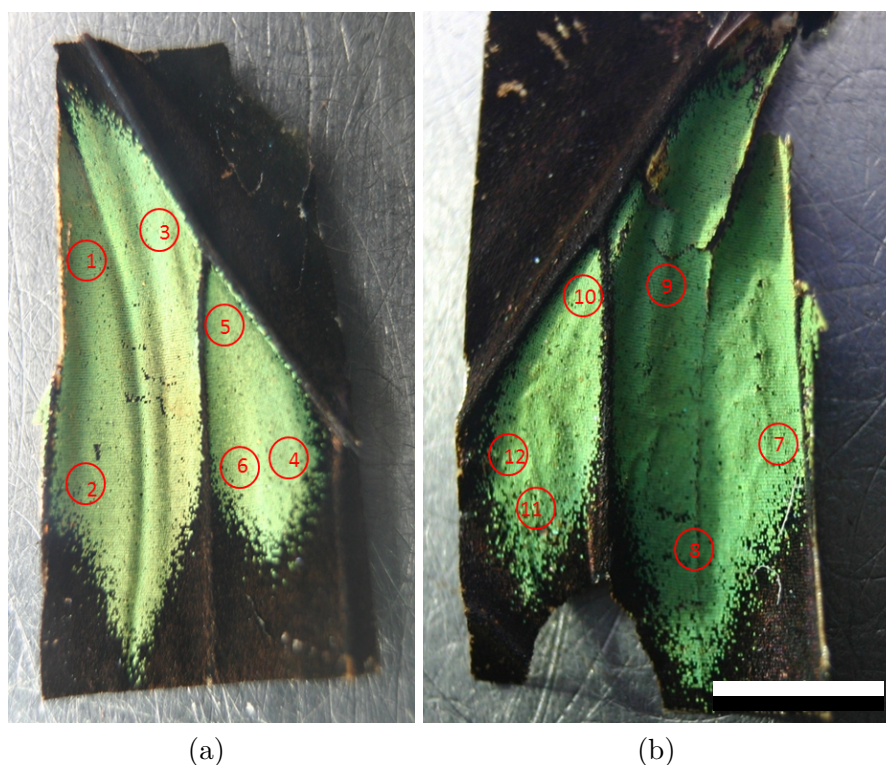
Figure 8.1: Photographs of two *P. sesostris* wings with (a) no treatment and (b) dendritic amplification treatment. The numbered regions correspond to the areas that were analysed by reflection microscopy and spectroscopy during the SSG treatment. Scale bar: 5 mm.

structures were analysed as the pyrolysis is an irreversible process.

Figure 8.1 shows the two wings that were used for this entire investigation (a) and (b) show the natural wing section and the dendritically amplified surface sample respectively. The numbers show the 12 areas that were used to optically characterise the sample at every stage of the invesigation. Specific areas were used because there is a significant amount of variation in peak wavelength across the samples, as shown in table 8.1. Areas 1-3 were coated with tin-doped titania, 4-6 were coated with titania, 7-9 were coated with tin-doped titania after dendritic amplification and areas 10-11 were coated with titania after amplification. Each area was analysed with the reflection probe 5 times resulting in 15 measurements for each treatment type, for each increment in layer number. The samples were analysed before any SSG cycles were applied, then 25 layers of each treatment were added incrementally, up to 150 layers.

Observations of the wing patches (figure 8.2) show that there is a consistent red-shift with an increasing number of SSG cycles for all treatment types. The most significant

Table 8.1: The peak reflected wavelengths of the 6 different regions of interest of the *P. sesostris* sample numbered in figure 8.1(a). Each peak reflected wavelength is a mean of 5 experimental measurements.

Area	Peak reflected wavelength (nm)	Standard Deviation (nm)
1	547.6	4.0
2	552.8	4.3
3	564.1	2.9
4	536.0	3.1
5	545.9	5.6
6	551.2	1.2

red-shift was seen with the tin-doped titania samples. The dendritic amplification of the sample actually appears to have had the opposite effect from that which was desired, as those samples exhibit a smaller red-shift. The titania samples both show less red shift than the tin-doped samples. Again the dendritic amplification has hindered the red-shift for the titania samples.

Figure 8.3 shows the reflection spectra obtained from the wing patches obtained using the reflection probe. A slight red-shift can be seen for all samples, this is made clearer by the insets, which show how the peak wavelength shifts when more cycles are added. The spectra agree with the visual observation that the tin-doped titania samples show a higher red shift than the titania samples.

When comparing the peak wavelength shifts for each sample set (figure 8.4), it is confirmed that not only the tin-doped titania samples exhibit a higher red-shift, but also that the dendritic amplification has not had the desired effect of promoting the SSG process. Instead it can be observed that the amplified samples are consistently lower in peak wavelength than the corresponding, non-amplified samples. Therefore, these samples were not analysed in any more detail. The peak wavelength graphs show a dip in peak wavelength for the dendritically amplified titania sample once the first 25 SSG cycles were applied, and then again for 150 layers. The amplified tin-doped titania sample also exhibits a drop in peak reflection after 150 cycles were applied. The reason for the dip is unknown.

At each stage of the SSG coating process, scales were scraped off the wing so that they could be analysed individually using MSP techniques. Both the ridge side and membrane side of the scale were analysed and compared. For each number of cycles, ten different scales were analysed for the membrane side and also ten different scales for the ridge side. The peak wavelength of each individual scale was found using Gaussian fitting. The mean was then taken for the 10 scales of each sample, for each side. Figure 8.5 shows optical micrographs of scales coated by 0, 50, 100 and 150 SSG cycles for both
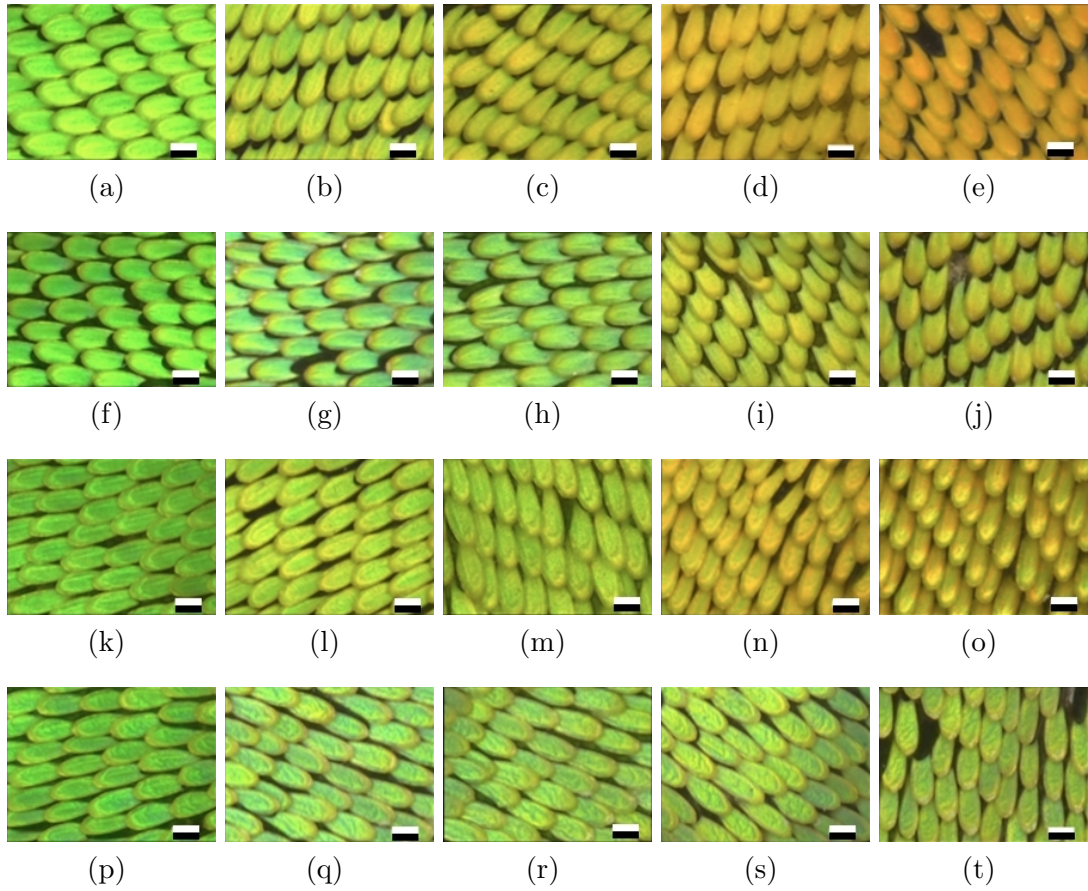
Figure 8.2: Optical micrographs of *P. sesostris* wing patches coated with (from left to right) 0, 25, 50, 75, 100 and 125 cycles of material using the SSG process. The specific SSG treatments were (a-e) *Sn*-doped TiO_2, (f-j) TiO_2, (k-o) dendritic amplification + *Sn*-doped TiO_2 and (p-t) dendritic amplification + TiO_2 Scale bars: (a-t) 50 μm. Images courtesy of Jonathan P. Vernon.

titania and tin-doped titania. The contrast in red-shift on the membrane side appears to be more exaggerated than for the ridge side (figure 8.2). The titania sample appears to show very little shift in colour when compared to the tin-doped samples. This result is expected as the refractive index for titania is much lower than it is for tin-doped titania. This means that the optical path length in the material will be smaller for the titania samples, resulting in the structure reflecting smaller wavelengths.

The MSP interrogation (figure 8.6) reveals the peak reflected wavelength shift on the single scale level is far more consistent than it is for the macroscopic measurements. This is especially true for the tin-doped titania samples. The sample coated with titania, however, does exhibit a dip in peak reflected wavelength on the membrane side at 50
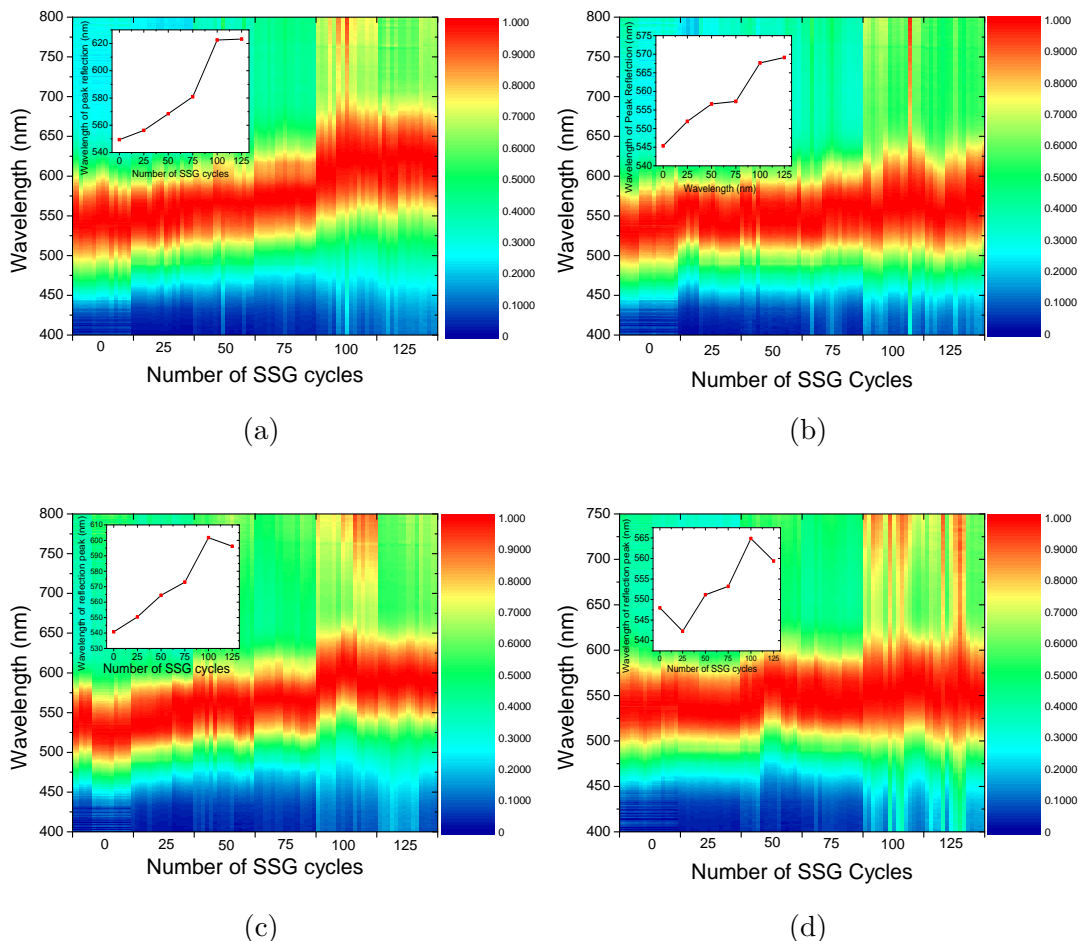
Figure 8.3: Reflection spectra showing a general red-shift of the maximally reflected wavelengths with an increasing number of SSG cycles. The four different SSG treatments applied were: (a) Sn-doped TiO_2, (b) TiO_2, (c) dendritically amplified Sn-doped TiO_2 and (d) dendritically amplified TiO_2. (a-d) insets: Number of SSG cycles vs. maximally reflected wavelength (nm).

cycles, then the peak continues to rise again until another dip at 125 cycles. These dips are non-intuitive, especially considering the care taken to avoid the effect of natural variation by taking an average of 10 different scales from the same wing patch. A possible reason for the observed variation is the possibility of errors in the SSG coating process such as errors in the temperature of the system or errors in the ratios of the solutions used.

(a)   (b)
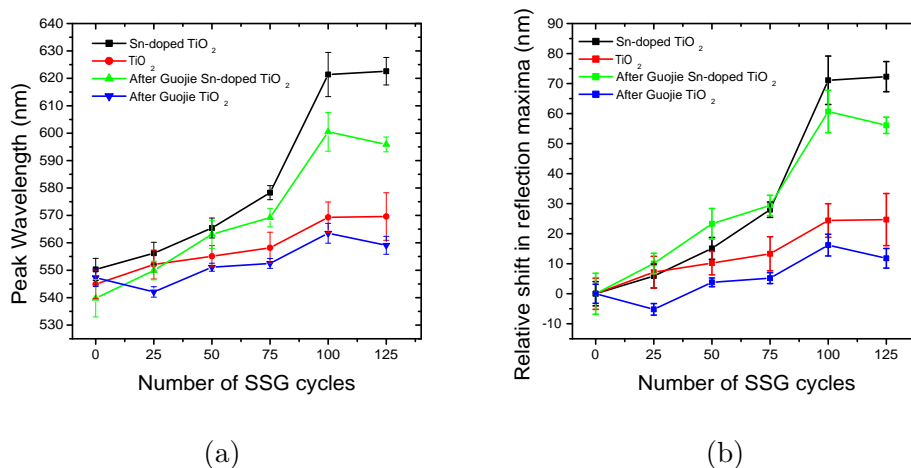
Figure 8.4: Macroscopic wing patches were analysed using the reflection probe to give graphs showing (a) the peak reflected wavelengths and (b) the relative shift in wavelength, with both graphs as a function of the number of SSG cycles applied. The error bars in both (a) and (b) indicate $\pm$ one standard deviation of each measurement.

(a)   (b)   (c)   (d)

(e)   (f)   (g)   (h)
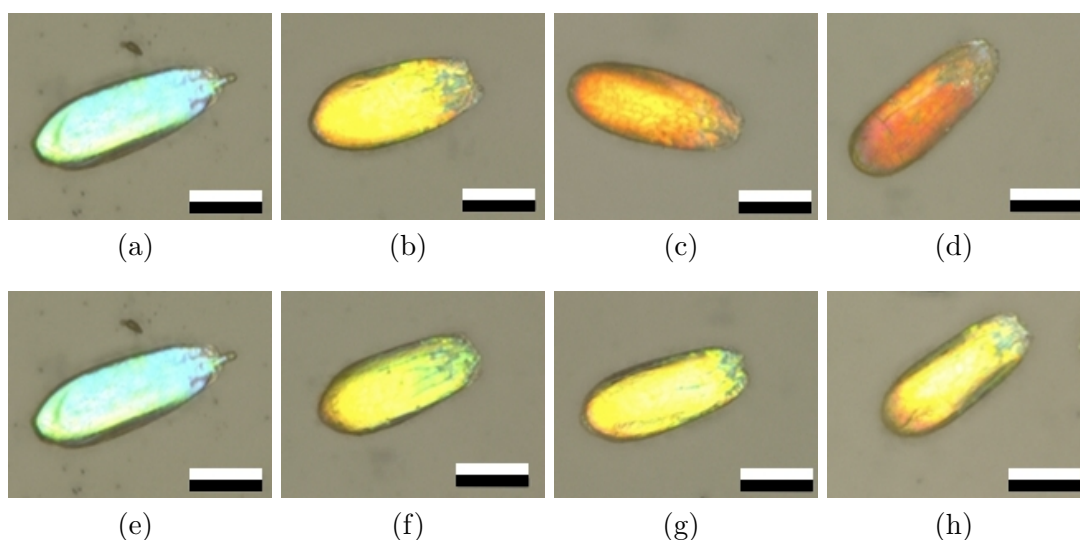
Figure 8.5: Optical micrographs of single *P. sesostris* scales. (a) & (e) show an untreated scale. (b-d) show scales scales coated with Sn-doped TiO_2 using 50, 100 and 150 SSG cycles respectively. (f-h) show scales scales coated with TiO_2 using 50, 100 and 150 SSG cycles respectively. The Sn-doped TiO_2 series shows a clear red-shift in colour as more SSG cycles are applied. The TiO_2 series also shows a red shift, however, the magnitude of the shift is far less. This result is expected as Sn-doped TiO_2 has a higher refractive index than TiO_2 exaggerating the colour shift. Scale bars: (a-h) 50 μm.

(a) (b)
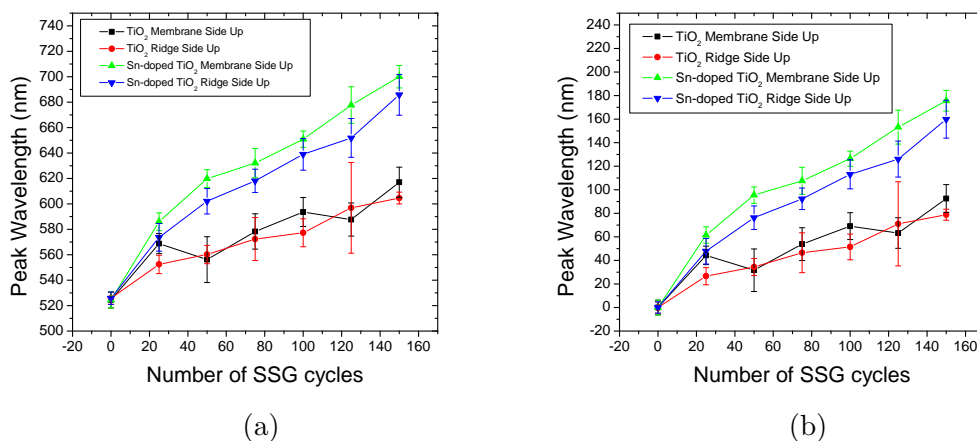
Figure 8.6: (a) Graph showing a general red-shift of peak wavelength when an increasing number of SSG cycles are applied to *P. sesostris* wing scales. The spectra were taken using MSP on single scales. 10 scales were analysed to obtain a mean value for each data point. The error bars indicate ± one standard deviation of each measurement. (b) The same graph as (a) as a relative shift in peak wavelength when increasing the number of SSG cycles applied. A shift of nearly 180 nm is observed for the membrane side of the *Sn*-doped TiO_2 scales after 150 SSG cycles were applied.

8.3 Pyrolysis, leading to completely inorganic, biotemplated gyroid polycrystals

Analysis of the coated samples revealed that the tin-doped titania samples exhibit the greatest shift in peak wavelength, therefore they were chosen to create inorganic replicas of the original green wing scales. To achieve this, the samples were pyrolised to a temperature of 450° for four hours. This results in the vapourisation of the organic material, leaving just the tin-doped titania structure (figure 8.7). It is expected that the tin-doped titania inorganic gyroid poly-crystal filaments will have hollow cores, due to the removal of the chitin within the shell of inorganic material.

8.3.1 Structural characterisation of the inorganic, biotemplated scales.

It has been shown that the pyrolised, inorganic templates exhibit a level of uniform shrinkage to the entire structure (figure 8.8). This shrinkage is likely to cause a blue-shift in colour of the reflected wavelength band. Observations (figure 8.9) of the exposed inorganic, gyroid poly-crystal reveal that the shrinkage has, in fact, caused the reflection bands of the scales to blue-shift quite considerably. The blue shift could also be attributed to the removal of the chitinous materials which contain the fluorophores
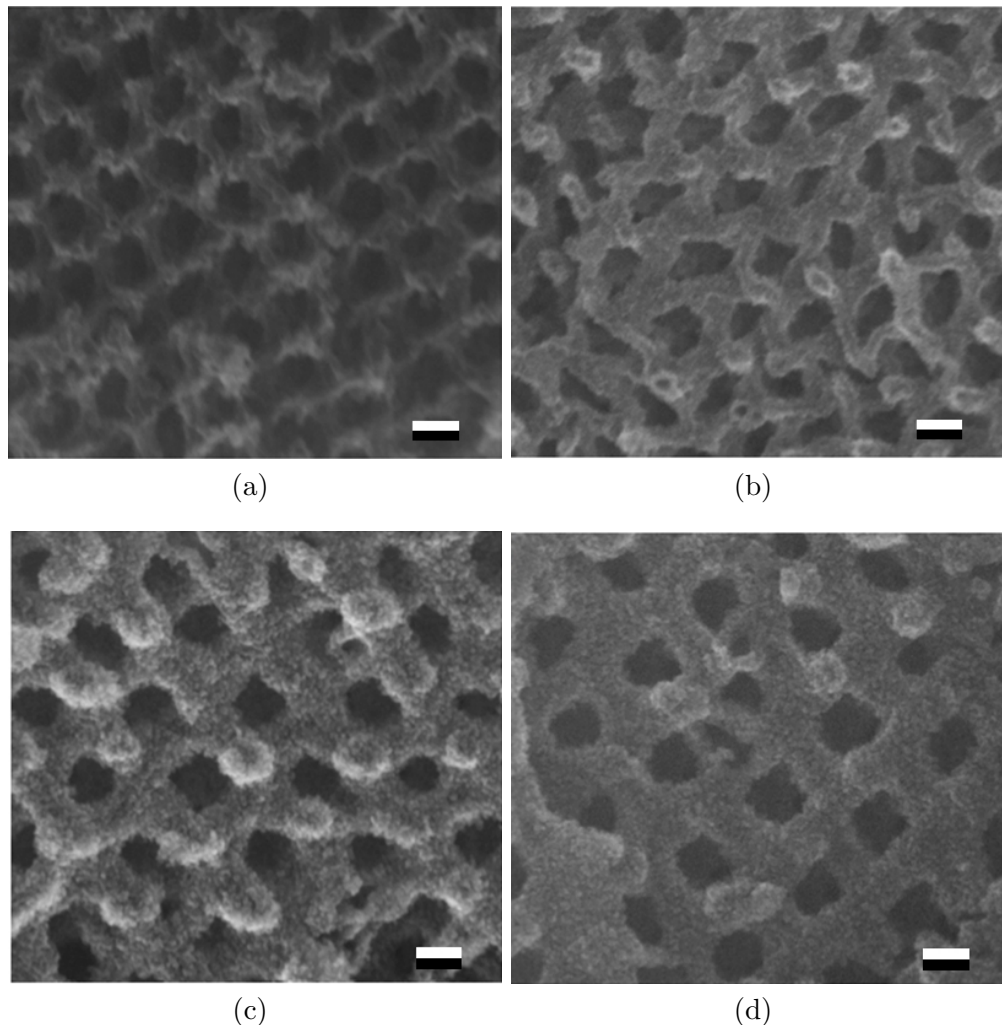
Figure 8.7: SEM images of the pyrolised tin-doped titania replicas of the *P. sesostris* green wing scales after (a) 25 SSG cycles, (b) 50 SSG cycles, (c) 75 SSG cycles and (d) 100 SSG cycles. Scale bars: (a-d) 100 nm. All SEM micrographs courtesy of Jonathan P. Vernon, The Georgia Institute for Technology.

necessary to produce the resultant green colour.

The whole coating and pyrolising process does not appear to produce exact inorganic replicas of the original *P. sesostris* gyroid poly-crystal, but because the chitin has to be vapourised by pyrolisis, a hollow core is produced, as expected. This is demonstrated quite clearly in the 100 SSG cycle titania sample shown in figure 8.7(d). This leads to a different character of the structural colour.

The pyrolisis process initially appeared to diminish the structural colour of the system because the ridge structure appeared to show very little or no colour. After FIB
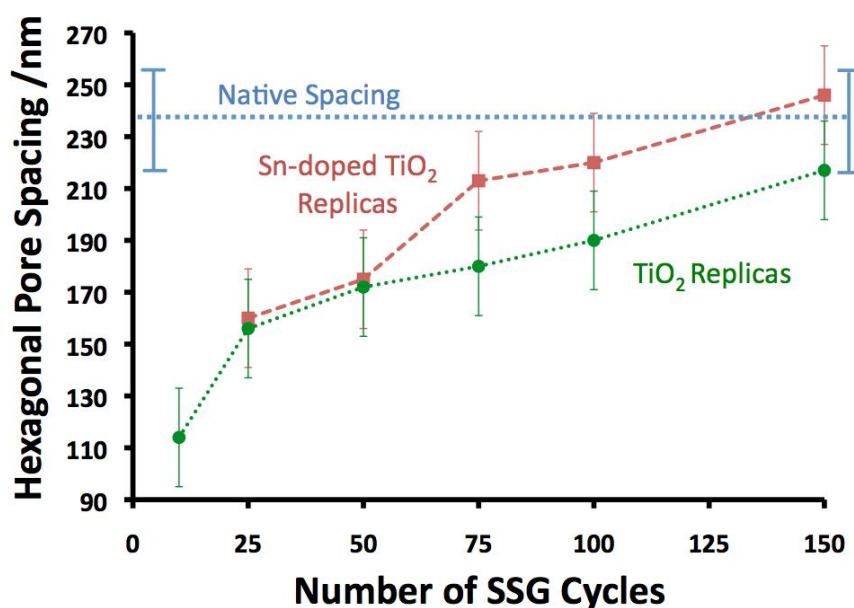
Figure 8.8: A graph showing the post-pyrolised hexagonal pore spacing of the gyroid structures with different numbers of applied SSG cycles (shown in figure 8.7). The pyrolised samples show a significant shrinkage due to the pyrolisis. The lattice constant is higher when more layers are applied. All data courtesy of Jonathan P. Vernon, The Georgia Institute for Technology.

milling, however, it was revealed that the gyroid poly-crystal still exhibits a bright structural colour. Therefore all the post-pyrolised samples were FIB-milled to expose the inorganic gyroid poly-crystal for the purpose of opticall analysis using MSP techniques. Optical micrographs of the post FIB-milled samples (figure 8.9) show that there is still structural colour present, as tin-doped titania without optical structuring is transluscent white in appearance. Three scales were FIB-milled, after being applied with 50, 100 and 150 SSG cycles. The colours observed in the micrographs are violet, cyan and green, repesctively. Figures 8.9(d)-8.9(f) show the corresponding maps of peak reflected wavelength as a function of position on the scale. The peak fitting program was created so that any areas that did not have a prominent peak (i.e the black backgroud in the micrographs or the broadband colour of the ridge section) show up as white pixels. These plots show that more SSG cycles result in a higher peak reflected wavelength. Figures 8.9(g)-8.9(i) show the average spectra for all the non-white pixels in the corresponding peak reflected wavelength maps. The peak reflected wavelength for each spectra was obtained using a Gaussian fitting routine. The results reveal peak wavelengths of 453.4 nm, 476.6 nm and 524.0 nm for the 50, 100 and 150 cycle samples, respectively. Figure 8.10 reveals the trend between number of SSG cy-
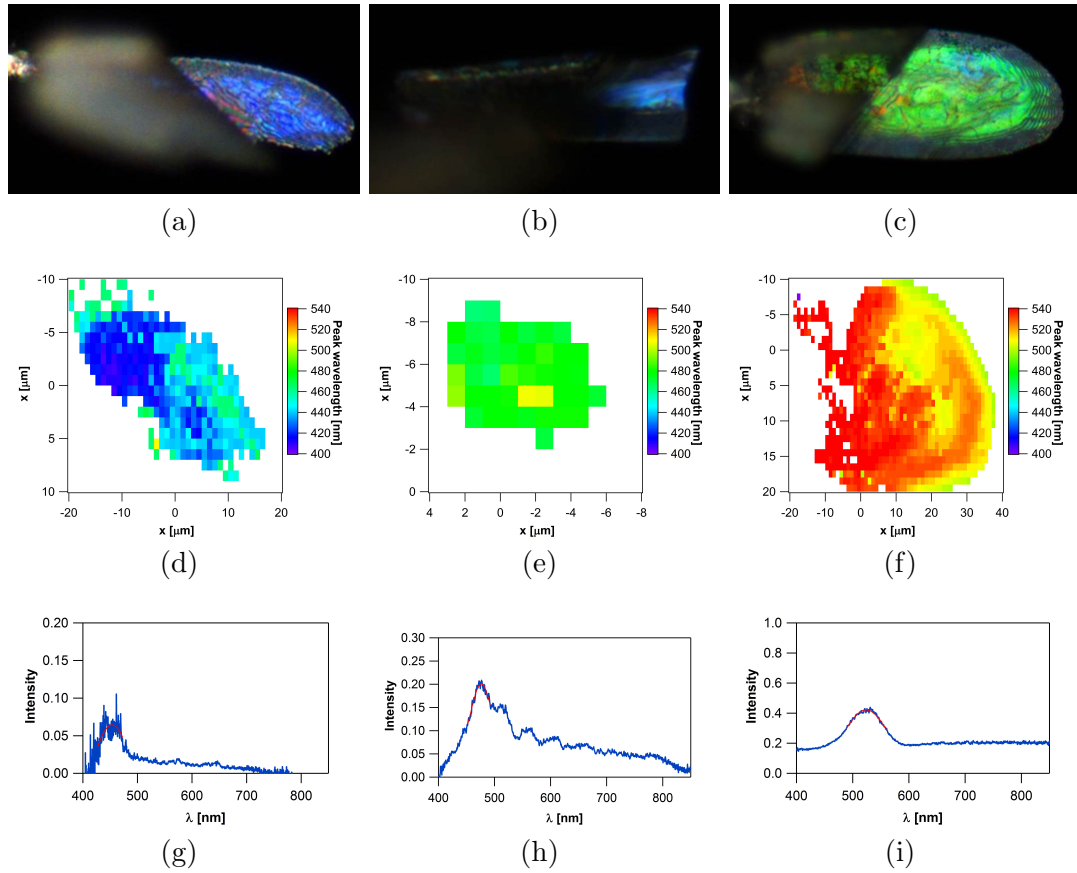
Figure 8.9: (a-c) Optical micrographs of three pyrolised, Sn-doped TiO_2 inorganic replicas of green wing scales treated with 50, 100 and 150 SSG cycles, respectively. The scales appear violet, cyan and green, respectively. (d-f) Graphs showing the peak reflected wavelength as a function of position on the scale for the three replicas shown in (a-c) respectively. A definite red shift in peak reflected wavelength can be seen for a larger number of SSG cycles. (g-i) The mean reflection spectra from the whole ridge-removed area of the scales shown in (a-c), respectively.

cles applied against the peak reflected wavelength for the post-pyrolised samples. It is near impossible to suggest that the trend is exponential or linear due to there only being three data points, but it can be inferred, at least, that the peak reflected wavelength is higher in value for the samples that were treated with more SSG cycles. The total shift in peak reflected wavelength between the 50 and 150 cycle samples is over 70 nm (figure 8.10(b)). This number is less than the 81.9 nm mean red-shift in peak wavelength from the unmilled 50 cycle sample to the unmilled 150 cycle sample, both un-pyrolysed and both treated with $SnTiO_2$ (figure 8.6). This value of peak reflected wavelength is a mean of the ridge side and membrane side values, 83.6 nm and 80.18,
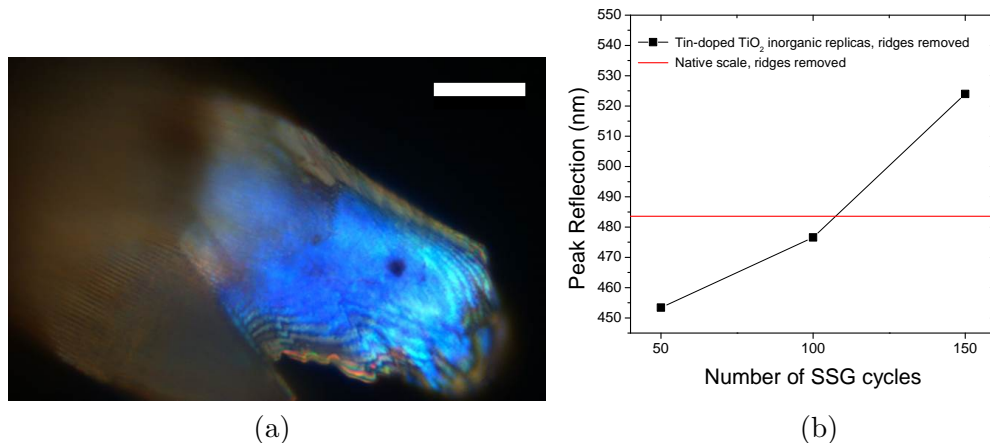
Figure 8.10: (a) Optical micrograph of the isolated gyroid poly-crystal of an untreated green wing scale that was optically analysed in chapter 7. (j) Peak wavelengths were taken from Gaussian fittings to the graphs in figure 8.9 as a function of number of SSG cycles. The fitting yields peak wavelengths of 453.4 nm, 476.6 nm and 523.98 nm, respectively. The red line shows the reflection maxima from the scale shown in (a), which we know to be 483.6 nm.

respectively. The ratios between the peak wavelength values at 150 and 50 SSG cycles for the pre-pyrolysis, membrane-side up measurement, the pre-pyrolysis, ridge-side up measurement and the post-pyrolysis, exposed gyroid measurement yield results of 1.13, 1.14 and 1.16, respectively. The two pre-pyrolysis ratios show consistent values, but the FIB-milled, pyrolised sample shows a larger value. This result can be explained by the fact that not only is there more high index material in the 150 cycle samples, but the pyrolysis causes shrinkage to a lesser extent to samples with a higher number of layers.

The red line in figure 8.10 shows the value of peak wavelength obtained, using MSP techniques, for the exposed gyroid-polycrystal of natural green wing scales of _P. sesostris_. Extrapolating from the graph reveals that to recover this value (483.4 nm) after pyrolisis you would need to apply 107 cycles of SSG using tin-doped titania.

8.4 Computational modelling

The finite element method of modelling was employed to strengthen our understanding of the coated _P. sesostris_ samples as layers of titanium dioxide and tin-doped titanium dioxide can easily be added using the HFSS software. Thin film computational modelling of the membrane and modelling of the diffracting ridge structure can be ignored
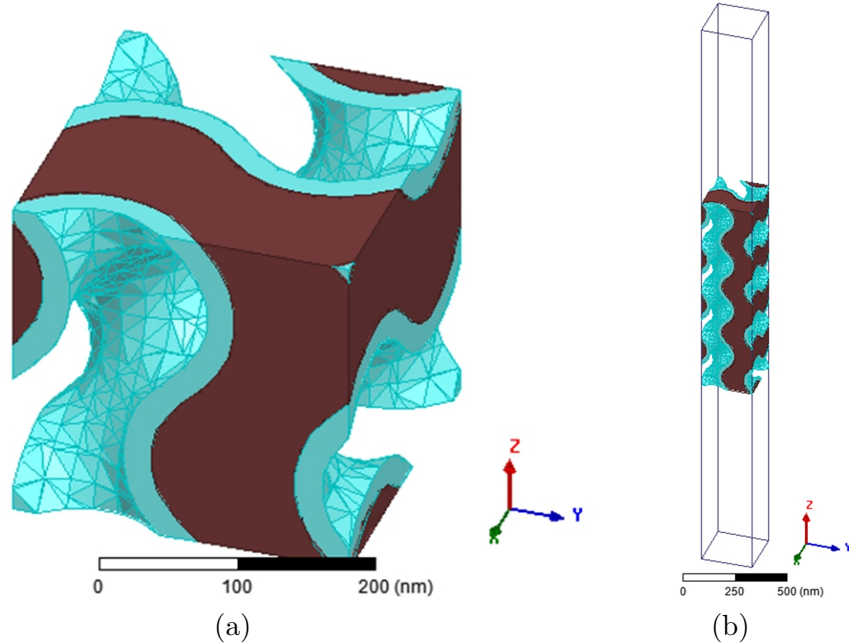
Figure 8.11: (a) A single unit cell of the simulated, coated gyroid photonic crystal. The brown material represents the natural chitinous gyroid and the cyan material represents the titania coating. (b) A schematic of the model used to compute the reflectance from the gyroid photonic crystal. The transparent box surrounding the crystal represents the air. This model is effectively infinitely repeated in the x and y directions.

as we know that these structures do not play an important role in colour production. We are only interested in the effect of coatings and pyrolysis of the gyroid structure. However, one drawback is that we can only model a single, semi-infinite crystal, as opposed to the poly-crystal found in the scales. The reason for this drawback is quite simply a matter of computing power and time. For a poly-crystal, one would need to produce a model that is the size of an entire scale, which is considered huge on an optical scale. The advantage of modelling a single crystal is that one only needs to make a single unit cell which can then be repeated to build up the semi-infinite slab. The model used for this investigation (shown in figure 8.11) used refractive index values of $n = 1.56 + 0.06i$ [9] for chitin and $n = 1.52 + 0.0606i$ for TiO_2 (taken from ellipsometry data performed by Jonathan P. Vernon, The Georgia Institute for Technology). The filling fraction of the chitin in the model was 40%, a value taken from the literature [22]. The lattice constant of the modelled gyroid was 260 nm, a figure obtained from SEM analysis of the gyroid structure by Jonathan P. Vernon, The Georgia Institute for Technology.
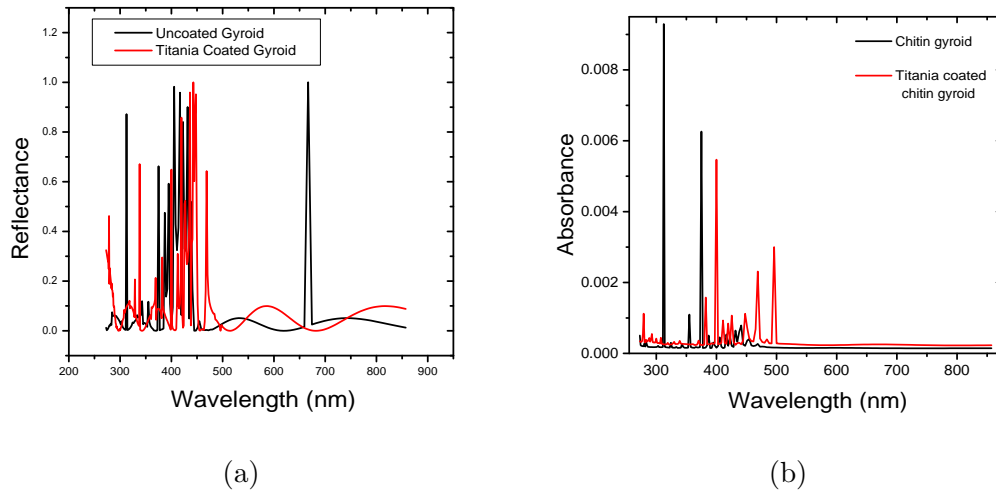
Figure 8.12: (a) Reflectance spectra and (b) absorbance spectra from the model shown in figure 8.11 and also from the model representing the uncoated, natural gyroid. A red-shift in the peak reflected wavelengths can be seen as the family of reflected modes have shifted further towards higher wavelength values, confirming the experimental results that were found and the original hypothesis that the addition of coatings would increase the optical dimensions of the structure and, hence, the reflection band wavelengths. The absorbance modelling confirms this result as the family of absorbance peaks also red-shifts upon application of the titania coating.

The FEM modelling shown in figure 8.12(a) confirms that the peak reflected wavelengths are red-shifted as high refractive index material is coated over the chitinous gyroid crystal. This can be seen more clearly in the absorption modelling calculated using: absorption = 1 - (reflection + transmission), shown in figure 8.12(b). The absorbance spectra of such a system should show maxima at the reflection band-edges, as this is where the electric fields are highest within the materials. The mono-crystalline gyroid model shows a family of peaks for both the coated and uncoated gyroids, probably due to the diffractive nature of the gyroid causing allowed modes within the reflection band-gap. The range of absorbance peaks for the uncoated gyroid model are 312.5 nm - 454.5 nm and for the coated gyroid the range is 382.2 nm - 495.9 nm. The midpoints of uncoated and coated ranges are 383.5 nm and 439.05 nm, respectively. This result confirms the original hypothesis that the coating procedure will cause a red-shift in the reflection band of the system.

8.5 Conclusions

The SSG process, resulting in a titania-coated, chitinous gyroid poly-crystal, has been shown to increase the maximally reflected wavelengths of the whole green wing scales. As more and more layers of titania or tin-doped titania are added, the peak reflected wavelengths red-shift significantly. This result was expected as the addition of high index material to the structure increases the optical path length, thereby making an effectively larger structure. In the case of the tin-doped titania, a shift in the peak reflected wavelength of 160.0 nm was seen on the ridge side of the scale, after 150 SSG cycles were applied. The value for the membrane side was even higher at 175.6 nm. This result confirms the tunability of this procedure. The tin-doped titania samples show the most dramatic red-shifts to the maximally reflected wavelengths, most likely due to the higher refractive index.

The dendritic amplification process was applied with the intention of aiding the SSG process and, therefore, an increased red-shift should have been observed. However, the dendritic amplification appears to have had the opposite effect, as the red-shifts observed were actually smaller for both the titania and tin-doped titania-coated samples.

It appears that the pyrolysed samples have decreased in physical size from the titania coated samples, and have, therefore, shown a considerable blue-shift in colour. The pyrolised scales still show the same positive trend between the number of SSG cycles and the peak reflected wavelength observed. It was discovered that in order to recover the original peak reflected wavelength of the natural *P. sesostris* exposed gyroid poly-crystal, then one would need to apply 107 SSG cycles using tin-doped titania. However, it appears that in order to recover the original lattice constant of the natural gyroid poly-crystal then approximately 134 SSG cycles would need to be applied (taken from figure 8.8). This discrepancy can be attributed to the high natural variance of the samples. Another reason for the discrepancy could be due to the fluorophore content of the natural sample (shown in the last chapter), that would not be present in the inorganic replica samples.

SEM micrographs of the pyrolysed inorganic replicas show that the basic gyroid structure has been retained. Some of the pyrolised samples even show quite clearly in the SEM micrographs that they exhibit a hollow core originating from the fact that the chitin has to be vapourised from the centre of the gyroid filaments in order to gain a fully inorganic tin-doped titania replicas.

FEM modelling of the uncoated and coated gyroid structures show that there is a noticeable red-shift present after the coating has been applied. This result confirms our understanding of how this optical system works.

A disadvantage to the bio templating method is the well noted variation in peak

wavelengths of different parts of the wing and also between different butterflies. Therefore reproducing the same crystal could be quite difficult. A way around this would be to make as many as you can and categorise the inorganic replicas into different peak reflected wavelength classes.

Chapter 9

Conclusions and future work

It has been shown in this thesis that there are many cases of structural colour in nature and three of those species were investigated in detail. It has also been shown that there are many ways of synthesising such structures, whether using industrial techniques such as chemical vapour deposition and spin coating, or by using biological samples as direct templates to produce the more complicated structures. Chapter 2 gives an overview of some species in nature that have already been studied and reported previously, thus demonstrating some of the diversity of species that exhibit structural colour, as well as the diversity of the structures themselves. It has been shown that many damselflies, butterflies, beetles exhibit iridescence and fruit and leaves from the floral species also. Chapter 3 gives a brief overview of the physics behind structural colour including examples of the different types of structures that are realised either in nature, or synthetically. A simple guide to show what happens when an electromagnetic wave is incident upon an interface between two optically different materials is presented, followed by the mathematics and physics needed to understand structures with many interfaces. Chapter 4 clearly explains how reflected electromagnetic waves are dependent on the incident radiation's angle of incidence and wavelength. It was then explained how these parameters can be measured using the different experimental techniques employed to carry out the research presented in this thesis. A diverse array of techniques were required to optically and structurally interrogate an array of different structurally coloured species.

9.1 Synthesising the structure of *M. nobilis*

The South American fruits of *M. nobilis* were reported to exhibit a multilayer structure that produced a greenish-blue iridescent colouration. The structure of the multilayer, however, was found to not be a simple one. The multilayers appeared to be comprised of

concentric tubes, producing a cylindrical multilayer system. The cylindrical multilayers, known as 'cells', were tessilated to form the epidermis of the fruit. The epidermis was found to be four layers of cells thick, supplying structural integrity to the fruit whilst not compromising the optical performance. The black colour of the seeds within the fruit is also believed to reduce reflection of light that is transmitted through the epidermis into the fruit. The result of this is maintaining the bright blue colour, because if the seeds were white then the transmitted light would be scattered back, causing a desaturation of the colour appearance. The selective advantage of the structure was speculated to deceive birds into thinking the fruit has sweet, nutritious flesh so that they will eat and disperse the seeds contained within. Such a fruit is known as a mimetic fruit.

The novel structure of the cylindrical multilayers provided inspiration to produce a synthetic system. The inspired system was a simplified version of just one of the cylindrical multilayers. The main difference here is that, due to the novel rolling technique used to make the synthetic system, it is not technically made of concentric cylindrical layers. but rather a spiral of layers. The synthetic fibres were manufactured from stretchable materials rolled around a glass fibre. Upon removal of the glass fibre, access to the stretchability is acquired and an experiment was performed to characterise the reflection spectra of the structure at different levels of strain. The expected result of the reflection bands decreasing in wavelength with increasing strain was acquired from this investigation. Optical microscopy and micro-spectrophotometry were used in conjunction to strengthen this conclusion. FDTD computational modelling of the system, performed by M. Kolle, showed good agreement with experimental data.

9.2 The striking iridescence of the *T. flammea* beetles

Four sub-species of the *T. flammea* beetles were investigated optically and structurally. It was shown that highly ordered multilayers produced a highly saturated colour in all four beetles. The four beetles exhibited blue, green, orange and red colour appearances and it was found that the lattice constants of the multilayers were directionally, positively proportional to the peak reflected wavlengths of the four beetles, respectively.

Scattering patterns acquired using imaging scatterometry have shown an unusual character. The normal-incidence primary beam scatterograms reveal a central, specularly refelcted white spot, surrounded by an annulus of colour produced by the multilayers. Structural interrogation and micro-imaging scatterometry reveal an array of rods that have a quasi-ordered hexagonal pattern that permeate the multilayer structure, producing a hybrid 3D photonic crystal. The quasi-ordered hexagonal array of rods is reported in this work to be the cause of the circular annulus of colour seen in the scatterograms.

To fully understand the rod structure and the resulting scattering pattern, the structure was fabricated synthetically. A simple ideal multilayer was produced using chemical vapour deposition. The array of rods was realised using FIB milling techniques, performed by Ye Cai, Georgia Institute of Technology. The rods in the synthesised structure were made of air and not a solid material like the natural structure. Imaging scatterometry performed on the synthesised hybrid photonic crystals did not produce the expected circular annulus of green, but rather, a highly scattered, bluish-green reflection. The bluish-green colour was produced from the multilayer. The discrepancy could arise due to the difference between the natural and synthetic systems as the rods were not made of a high refractive index solid material.

Computational modelling of the multilayer structure intersected with a perfectly ordered hexagonal array has shown that not only does the hybrid crystal reflect green wavelengths, but it also displays the expected scattering pattern for a hexagonal array of rods.

9.3   Nanosurgery of the green wing scales of *P. sesostris*

The structure of *P. sesostris* was examined in detail by deconstructing the green wing scales into one or more of the component pieces. These components were indentified to be, from the top of the scale down, a monograting of fins, a bigrating of nano-tubes, a triply-periodic bicontinuous gyroid poly-crystal and on the bottom, a thin membrane.

An optical interrogation was perfomed on scales that had different parts removed to deconvolve the optical effects of the whole scale. It was shown that the source of colour is the photonic crystal at the centre, the gyroid poly-crystal. This crystal reflects blue light into the ridge section which contains fluorophores that absorb blue wavelengths and emit green wavelengths. The purpose of the ridge structure appears to be to remove the angle-dependence of the gyroid crystal. The efficiency of the scattering is achieved due to incident light being scattered through to the gyroid which has many crystal domains, orientated in different directions, furthering the angle-independence. Reflected light from the gyroid is then scattered again by the ridge structure. Primary beam imaging scatterometry on the ridge structure was used to provide strong evidence of the scattering nature. Primary beam imaging scatterometry was also performed on the membrane side of the scale, this time demonstrating that, without the ridges, there is a specular nature of reflection. The purpose of the membrane appears largely for structural integrity or possibly as a vestige of growth morphology, as removing the membrane does not appear to change the colour of the scale. However, removing

layers of the gyroid poly-crystal close to the membrane leaves the system with a light blue colouration. Further FIB milling and microscopy has also shown that the colour emanating from the gyroid near the ridge section blue-shifts as the thickness of the gyroid decreases. This leads to the conclusion that the fluorophores are present within the chitin throughout the entire scale. Computational modelling of the membrane layer reveals that it only provides a small increase in reflection over the optical regime.

This nanosurgery investigation provided a method that allows a detailed investigation into a complex, multi-component structure that combines structural colour and pigment colour.

9.4 Using the green wing scales of *P. sesostris* as a bio-template to synthesise inorganic gyroid structures

The structure of the green wing scales of *P. sesostris* allows complete liquid infiltration into the air gaps, it is also a system that has been reported widely in the literature. It was for these reasons that the green wing scales were chosen for bio-templating, therefore producing an inorganic replica of the complicated gyroid photonic poly-crystal. This process involved coating the scales in a high refractive index material and then pyrolising the resultant structure with the aim of removing the organic materials, leaving an inorganic gyroid poly-crystal. Optical interrogation was performed before treatment, after the coating procedure, and also after the scales were pyrolised.

Optical interrogation of the coated scales reveals the expected response, namely an increase in peak reflected wavelength as more layers were added. The higher index materials were also shown to give a greater red-shift in peak reflected wavelength. Some of the scales had a treatment (dendritically amplification of the molecular structure of the surface of the chitin) applied before coating which dendritically amplified the surface of the chitin. This was performed to observe if the amplification process would aid the coating process, therefore further increasing the red-shift. It was found that this was not the case as the dendritically amplified samples actually exhibited a reduction in red-shift of the peak reflected wavelengths. It was found overall that the tin-doped titania coated samples exhibited the greatest red-shift in peak reflected wavelengths colour. Therefore, these samples were chosen for the pyrolisis stage of the investigation.

After pyrolisis the scales exhibited little colour. Removing the ridge structure, using FIB milling techniques, exposed the gyroid poly-crystal revealing that this part of the structure still exhibited a bright structural colouration. Four different samples had the ridge structure removed so that a comparison could be made. The samples were an untreated green wing scale, and then three scales that were coated, fired and FIB

milled. The last three scales were coated with 50, 100 and 150 layers of tin-doped titania. The optical interrogation reveals a reduction in peak reflected wavelengths from the post-coated scales. Structural interrogation reveals that the reduction in peak reflected wavelengths of the pyrolised scales was caused by a uniform shrinkage of the scale structures during pyrolisis. The scales still exhibited the same trend, the more layers added before pyrolisis meant a larger resulting peak reflected wavelength. Structural interrogation also reveals that more layers added before pyrolisis results in a lower level of shrinkage to the structure during pyrolisis.

This investigation demonstrated that an inorganic gyroid poly-crystal can be synthesised using a combination of SSG coating and pyrolisis. It has also been shown that the result inorganic replica can be tuned to reflect different wavelengths by varying the number of layers before the pyrolisis process.

9.5 Future work

9.5.1 Synthetic fibres inspired by *M. nobilis*

The synthetic fibres that were produced using the novel rolling technique were suggested to have an application in the form of stress-testing materials as an applied stress would change the colour appearance of the fibres. In order to test this idea further, enough fibres would have to be produced so that they could be embedded in a material to be tested or even to be woven together to produce a fabric. This fabric would then have stress applied to it calibrate the optical response to varying amounts of stress. This work would be performed with the aim of furthering textile technology such as dynamic colours and sport science.

9.5.2 Annular diffraction from the *T. flammea* beetles

The diffracted annulus of reflection that was found to be characteristic of three different beelte subspecies from the *T. flammea* species was the reason that a synthetic replica was produced. It was the aim to see if the synthesised structure would reproduce the annular diffraction pattern. Instead, the results revealed a random scattering that exhibited the colour of the multilayer. Future work is required to fully understand why this was the case. The main discrepancy between the synthesised and the natural beetle structure was that the array of permeating rods in the synthesised structure was made out of air and not a higher refractive index material. Therefore, the structure that was produced using the array found from the *T. flammea chicheryi* structure would need to be coated in a higher refractive index material for the purpose of filling in the holes.

The resultant structure would then be analysed again to see if the expected annular pattern appears.

The synthetic multilayer system permeated with an array of FIB-milled holes could be used to produce a liquid sensing photonic system. The infiltration of liquid into the holes would alter the optical characteristics of the structure. The optical differences could be utilised to calculate which liquids are present within the system.

9.5.3 Deconstructing the green wing scales of *P. sesotris*

The membrane area of the green wing scales of *P. sesostris* was not characterised in isolation as the membrane was too thin to remove from the bottom of the scales. Future work would need to be performed to develop a technique to achieve this isolation. Then, the membrane could be optically analysed to see what optical effects it actually offers as only unproven suggestions have been put forward so far. The membrane could then be analysed using fluorescence microscopy to confirm whether or not this part of the structure contains a significant concentration of fluorophores.

Other work that could be done on this area of reseach is the isolation, via FIB milling, of a single gyroid crystal. This would allow a more complete optical characterisation of the gyroid structure, as the whole scale exhibits a multi-crystalline structure which has the effect of diminishing the angular dependence of the overall structure. If a single crystalline domain was interrogated in isolation, then a firm grasp of the angular properties of the gyroid could be gained experimentally, as well as just theoretically using computational modelling.

The advanced FIB-milling techniques used in this thesis could be utilised to isolate a single crystal of the gyroid material for analysis via MSP reflection spectroscopy. This would then allow the a more complete understanding of the complex 3D system.

9.5.4 Surface sol-gel coating of the green wing scales of *P. sesostris*

The coated green wing scales of *P. sesostris* still contain organic chitin material, which is reported to contain a significant amount of fluorophores. Further study would have to be undertaken to gain a further understanding into the fluorpphore dependence of the overall colour appearance.

The inorganic replicas that were produced by coating and pyrolising the green wing scales of *P. sesostris* were only made out of two different materials. Further investigation could be made into the replicating process simply by choosing other suitable materials. This way, other ways of fine tuning the resultant peak reflected wavelengths from the pyrolised structures could be found.

Publications

Journal articles

- Jonathan P. Vernon, Nicholas Hobbs, Ye Cai, Alfred J. Lethbridge, Peter Vukusic, Dimitri D. Deheyn and Kenneth H. Sandhage, (2012) 3D photoluminescent lanthanide-doped barium titanate structures synthesized by coating and shape-preserving reaction of complex-shaped bioorganic templates, Journal of Materials Chemistry, **22**, 10435-10437[43].

- Mathias Kolle, Alfred J. Lethbridge, Moritz Kreysing, Jeremy J. Baumberg, Joanna Aizenberg and Peter Vukusic, (2013) Bio-inspired band-gap tunable elastic optical multilayer fibers, Advanced Materials, **25**, 22392245[44].

- Thomas J. Constant, Alastair P. Hibbins, Alfred J. Lethbridge, J. Roy Sambles, Edmund K. Stone and Pete Vukusic, (2013) Direct mapping of surface plasmon dispersion using imaging scatterometry, Applied Physics Letters, **102**, 251107(1-12)[89].

Journal articles in preparation

- Jonathan P. Vernon, Alfred J. Lethbridge, Craig G. Cameron, Ye Cai, Mathias Kolle, Joanna Aizenberg, Peter Vukusic and Kenneth H. Sandhage, (unpublished work) Layer-by-layer conformal coating and replication of butterfly photonic nano-architecures with higher index inorganic materials.

- Craig G. Cameron, Alfred J. Lethbridge, Jonathan P. Vernon, Russel Shimada, Dimitri Deheyn, Peter Vukusic and Kenneth H. Sandhage (unpublished work) Precision deconstruction of the butterfly wing scales of *Parides sesostris* via focussed ion beam nanosurgery.

- Silvia Vignolini, Alfred J. Lethbridge, Mathias Kolle, Ulli Steiner and Pete Vukusic, (unpublished work) Optics and morphology of the mimetic fruit *Margaritaria nobilis*.

Conference presentations

- Poster presentation: A. J. Lethbridge, Structural colouration of an iridescent seed, PECS-IX - Ninth International Conference on Photonic and Electromagnetic Crystal Structures, Granada, Spain, 26-30 September 2010.

- Poster presentation: A. J. Lethbridge, BIOOPTICS 1st annual review, Harvard University, Cambridge MA, USA, November 2010.

- Poster presentation: A. J. Lethbridge, Geometry of Interfaces, Primošten, Croatia, October 2011

- Poster presentation: A. J. Lethbridge, The physical origin of strikingly different colour appearances in four subspecies of *Torynorrhina flammea* beetles, BIOOPTICS 2nd annual review, Georgia Institute of Technology, Atlanta, GA, USA, November 2011.

Research visits

- Stavenga Laboratories, Zernike Institute for Advanced Materials, University of Groningen, Groningen, The Netherlands, October 2010.

- Aizenberg Laboratories, Laboratory for Integrated Science and Engineering, Harvard University, Cambridge MA, USA, October 18th - November 4th 2011.

References

[1] WILTS, B.D., MICHIELSEN, K., DE RAEDT, H., AND STAVENGA, D.G. Iridescence and spectral filtering of the gyroid-type photonic crystals in Parides sesostris wing scales. *Interface Focus*, **2**, 681 (2011). xii, 5, 21, 57, 124, 128, 132, 146, 147

[2] YASUMOTO, K. *Electromagnetic Theory and Applications for Photonic Crystals.* CRC Press (2005). 1

[3] BRAUN, P.V. AND WILTZIUS, P. Electrochemically grown photonic crystals. *Nature*, **402**, 603 (1999). 1, 149

[4] LIN, S. Experimental Demonstration of Guiding and Bending of Electromagnetic Waves in a Photonic Crystal. *Science*, **282**, 274 (1998). 1, 149

[5] JOANNOPOULOS, J.D. Self-assembly lights up. *Nature*, **414**, 257 (2001). 1, 149

[6] DEBORD, J.D. AND LYON, L.A. Thermoresponsive Photonic Crystals. *The Journal of Physical Chemistry B*, **104**, 6327 (2000). 1

[7] DARWIN, C. *Origin of Species By Means of Natural Selection, or the Preservation of Favoured Races in the Struggle for Life.* John Murray Publishers, London (1859). 5

[8] PARKER, A.R. 515 million years of structural colour. *Journal of Optics A: Pure and Applied Optics*, **2**, R (2000). 5, 72, 137

[9] VUKUSIC, P., SAMBLES, J.R., LAWRENCE, C.R., AND WOOTTON, R.J. Quantified interference and diffraction in single ¡i¿Morpho¡/i¿ butterfly scales. *Proceedings of the Royal Society B: Biological Sciences*, **266**, 1403 (1999). 5, 13, 14, 15, 16, 143, 161

[10] NIXON, M., A.G. ORR, AND VUKUSIC, P. Subtle design changes control the difference in colour reflection from the dorsal and ventral wing-membrane surfaces

References

of the damselfly Matronoides cyaneipennis. *Optics Express*, **21**, 1479 (2013). 5, 7, 8, 9

[11] VUKUSIC, P. AND SAMBLES, J. Shedding light on butterfly wings. *Proceedings of SPIE*, **4438**, 85 (2001). 5, 101, 124

[12] LIU, F., YIN, H., DONG, B., QING, Y., ZHAO, L., MEYER, S., LIU, X., AND CHEN, B. Inconspicuous structural coloration in the elytra of beetles ¡i¿Chlorophila obscuripennis¡/i¿ (Coleoptera). *Physical Review E*, **77**, 1 (2008). 5, 96, 98

[13] STAVENGA, D.G., LEERTOUWER, H.L., PIRIH, P., AND WEHLING, M.F. Imaging scatterometry of butterfly wing scales. *Optics express*, **17**, 193 (2009). 5, 52, 57, 58

[14] SEAGO, A.E., BRADY, P., VIGNERON, J.P., AND SCHULTZ, T.D. Gold bugs and beyond: a review of iridescence and structural colour mechanisms in beetles (Coleoptera). *Journal of the Royal Society, Interface / the Royal Society*, **6 Suppl 2**, S165 (2009). 5

[15] XIE, G., ZHANG, G., LIN, F., ZHANG, J., LIU, Z., AND MU, S. The fabrication of subwavelength anti-reflective nanostructures using a bio-template. *Nanotechnology*, **19**, 1 (2008). 5, 137

[16] MICHIELSEN, K., DE RAEDT, H., AND STAVENGA, D.G. Reflectivity of the gyroid biophotonic crystals in the ventral wing scales of the Green Hairstreak butterfly, ¡i¿Callophrys rubi¡/i¿. *Journal of the Royal Society, Interface / the Royal Society*, **7**, 765 (2010). 5

[17] STEINBRECHT, R.A., MOHREN, W., PULKER, H.K., AND SCHNEIDER, D. Cuticular interference reflectors in the golden pupae of Danaine butterflies. *Proceedings of the Royal Society of London. Series B, Biological Sciences*, **226**, 367 (1985). 5, 72, 93

[18] GLOVER, B.J. AND WHITNEY, H.M. Structural colour and iridescence in plants: the poorly studied relations of pigment colour. *Annals of botany*, **105**, 505 (2010). 5, 6, 29, 72, 96

[19] WILTS, B.D., PIRIH, P., ARIKAWA, K., AND STAVENGA, D.G. Shiny wing scales cause spec(tac)ular camouflage of the angled sunbeam butterfly, Curetis acuta. *Biological Journal of the Linnean Society*, **109**, 279 (2013). 5

[20] SPINNER, M., KOVALEV, A., GORB, S.N., AND WESTHOFF, G. Snake velvet black: Hierarchical micro- and nanostructure enhances dark colouration in Bitis rhinoceros. *Scientific reports*, **3**, 1 (2013). 5

[21] YOSHIOKA, S. AND KINOSHITA, S. Polarization-sensitive color mixing in the wing of the Madagascan sunset moth. *Optics Express*, **15**, 2691 (2007). 5, 6

[22] MICHIELSEN, K. AND STAVENGA, D.G. Iridescence and spectral filtering of the gyroid-type photonic crystals in Parides sesostris wing scales. *Journal of the Royal Society, Interface / the Royal Society*, **5**, 85 (2008). 5, 20, 124, 128, 132, 143, 161

[23] STAVENGA, D.G., GIRALDO, M.a., AND HOENDERS, B.J. Reflectance and transmittance of light scattering scales stacked on the wings of pierid butterflies. *Optics express*, **14**, 4880 (2006). 5

[24] SWEENEY, A., JIGGINS, C., AND JOHNSEN, S. Polarized light as a butterfly mating signal. *Nature*, **423**, 31 (2003). 5, 96

[25] FITZPATRICK, S. Colour schemes for birds : structural coloration and signals of quality in feathers. *Ann. Zool. Fennici.*, **35**, 67 (1998). 5

[26] VUKUSIC, P., WOOTTON, R.J., AND SAMBLES, J.R. Remarkable iridescence in the hindwings of the damselfly Neurobasis chinensis chinensis (Linnaeus) (Zygoptera: Calopterygidae). *Proceedings of the Royal Society B: Biological Sciences*, **271**, 595 (2004). 5

[27] SIMONIS, P., BAY, A., WELCH, V.L., COLOMER, J.F., AND VIGNERON, J.P. Cylindrical Bragg mirrors on leg segments of the male Bolivian blueleg tarantula Pamphobeteus antinous (Theraphosidae). *Optics express*, **21**, 6979 (2013). 5

[28] GRAHAM, R.M., LEE, D.W., AND NORSTOG, K. Physical and ultrastructural basis of blue leaf iridescence in two neotropical ferns. *American Journal of Botany*, **80**, 198 (1993). 5, 29, 72

[29] LUKE, S.M., HALLAM, B.T., AND VUKUSIC, P. Structural optimization for broadband scattering in several ultra-thin white beetle scales. *Applied Optics*, **49**, 4246 (2010). 5, 25, 26, 27, 28, 64

[30] WILTS, B.D., MICHIELSEN, K., DE RAEDT, H., AND STAVENGA, D.G. Hemispherical Brillouin zone imaging of a diamond-type biological photonic crystal. *Journal of the Royal Society, Interface / the Royal Society*, **9**, 1609 (2012). 5

References

[31] VIGNERON, J., KERTÉSZ, K., VÉRTESY, Z., RASSART, M., LOUSSE, V., BÁLINT, Z., AND BIRÓ, L. Correlated diffraction and fluorescence in the backscattering iridescence of the male butterfly Troides magellanus (Papilionidae). *Physical Review E*, **78**, 021903 (2008). 5, 6

[32] DEPARIS, O., RASSART, M., VANDENBEM, C., WELCH, V., VIGNERON, J.P., AND LUCAS, S. Structurally tuned iridescent surfaces inspired by nature. *New Journal of Physics*, **10**, 013032 (2008). 5

[33] DE STEFANO, L., MADDALENA, P., MORETTI, L., REA, I., RENDINA, I., DE TOMMASI, E., MOCELLA, V., AND DE STEFANO, M. Nano-biosilica from marine diatoms: A brand new material for photonic applications. *Superlattices and Microstructures*, **46**, 84 (2009). 5, 6

[34] VUKUSIC, P. AND HOOPER, I. Directionally Controlled Fluorescence Emission in Butterflies. *Science*, **310**, 2005 (2005). 5

[35] VUKUSIC, P., HALLAM, B., AND NOYES, J. Brilliant Whiteness in Ultrathin Beetle Scales. *Science*, **315**, 348 (2007). 5, 25

[36] SCHRÖDER-TURK, G.E., WICKHAM, S., AVERDUNK, H., BRINK, F., FITZ GERALD, J.D., POLADIAN, L., LARGE, M.C.J., AND HYDE, S.T. The chiral structure of porous chitin within the wing-scales of Callophrys rubi. *Journal of structural biology*, **174**, 290 (2011). 5, 124

[37] PARKER, A.R. Colour of in Burgess on Shale in the animals and the effect light evolution Cambrian. *Proceedings of the Royal Society of London. Series B, Biological Sciences*, **265**, 967 (1998). 5, 13

[38] BERTHIER, S., CHARRON, E., AND BOULENGUEZ, J. Morphological structure and optical properties of the wings of Morphidae. *Insect Science*, **13**, 145 (2006). 5, 101

[39] DOUGHERTY, R.C., STRAIN, H.H., SVEC, W.A., UPHAUS, R.A., AND KATZ, J.J. Structure, properties and distribution of chlorophyll c. *Journal of the American Chemical Society*, **92**, 2826 (1970). 6

[40] BERTHIER, S. *Iridescences: The Physical Colors of Insects*. Springer Science + Business Media, LLC, New York (2007). 6

[41] PARKER, A.R. AND MARTINI, N. Structural colour in animalssimple to complex optics. *Optics & Laser Technology*, **38**, 315 (2006). 6

[42] PULSIFER, D.P. AND LAKHTAKIA, A. Background and survey of bioreplication techniques. *Bioinspiration & Biomimetics*, **6** (2011). 6, 72

[43] VERNON, J.P., HOBBS, N., CAI, Y., LETHBRIDGE, A., VUKUSIC, P., DE-HEYN, D., AND SANDHAGE, K. 3D Photoluminescent Lanthanide-doped Barium Titanate Structures Synthesized by Coating and Shape-preserving Reaction of Complex-shaped Bioorganic Templates. *Journal of Materials Chemistry*, pages 10435–10437 (2012). 6, 171

[44] KOLLE, M., LETHBRIDGE, A., KREYSING, M., BAUMBERG, J.J., AIZENBERG, J., AND VUKUSIC, P. Bio-Inspired Band-Gap Tunable Elastic Optical Multilayer Fibers. *Advanced Materials* (2013). 6, 171

[45] LARGE, M., WICKHAM, S., HAYES, J., AND POLADIAN, L. Insights from nature: Optical biomimetics. *Physica B: Condensed Matter*, **394**, 229 (2007). 6, 29, 72, 124

[46] POTYRAILO, RADISLAV, A., GHIRADELLA, H., VERTIATCHIKH, ALEXEI DOV-IDENKO, KATHARINE COURNOYER, J.R., AND OLSON, E. Morpho butterfly wing scales demonstrate highly selective vapour response. *Nature Photonics*, **1**, 123 (2007). 6

[47] PRIS, A.D., UTTURKAR, Y., SURMAN, C., MORRIS, W.G., VERT, A., ZA-LYUBOVSKIY, S., DENG, T., GHIRADELLA, H.T., AND POTYRAILO, R.A. Towards high-speed imaging of infrared photons with bio-inspired nanoarchitectures. *Nature Photonics*, **6**, 195 (2012). 6

[48] CHATTOPADHYAY, S., HUANG, Y., JEN, Y., GANGULY, A., CHEN, K., AND CHEN, L. Anti-reflecting and photonic nanostructures. *Materials Science and Engineering: R: Reports*, **69**, 1 (2010). 6, 72, 150

[49] TSAI, M.A., HAN, H.W., TSAI, Y.L., TSENG, P.C., YU, P., KUO, H.C., SHEN, C.H., SHIEH, J.M., AND LIN, S.H. Embedded biomimetic nanostructures for enhanced optical absorption in thin-film solar cells. *Optics express*, **19**, A757 (2011). 6, 72

[50] XIE, G., ZHANG, G., LIN, F., ZHANG, J., LIU, Z., AND MU, S. The fabrication of subwavelength anti-reflective nanostructures using a bio-template. *Nanotechnology*, **19**, 1 (2008). 6, 72, 149

[51] VUKUSIC, P. Natural photonics. *Physics Wo*, pages 35–39 (2004). 6, 150

References

[52] HUANG, J., WANG, X., AND WANG, Z.L. Controlled replication of butterfly wings for achieving tunable photonic properties. *Nano letters*, **6**, 2325 (2006). 6, 72, 149

[53] INTONTI, F., VIGNOLINI, S., TURCK, V., COLOCCI, M., BETTOTTI, P., PAVESI, L., SCHWEIZER, S.L., WEHRSPOHN, R., AND WIERSMA, D. Rewritable photonic circuits. *Applied Physics Letters*, **89**, 1 (2006). 6

[54] NOYES, J.A., VUKUSIC, P., AND HOOPER, I.R. Experimental method for reliably establishing the refractive index of buprestid beetle exocuticle. *Optics Express*, **15**, 4351 (2007). 7, 10, 11, 96, 98

[55] PARKER, A.R., MCKENZIE, D.R., AND LARGE, M.C.J. Multilayer reflectors in animals using green and gold beetles as contrasting examples. *The Journal of Experimental Biology*, **201**, 1307 (1998). 10

[56] HINTON, H.E. AND GIBBS, D.F. Diffraction gratings in phalacrid beetles. *Nature*, **221**, 953 (1969). 13

[57] BERTHIER, S., CHARRON, E., AND DA SILVA, A. Determination of the cuticle index of the scales of the iridescent butterfly Morpho menelaus. *Optics Communications*, **228**, 349 (2003). 15

[58] TRZECIAK, T.M. AND VUKUSIC, P. Photonic crystal fiber in the polychaete worm Pherusa sp. *Physical Review E*, **80**, 1 (2009). 16, 17, 18, 19

[59] YOSHIOKA, S. AND KINOSHITA, S. Effect of Macroscopic Structure in Iridescent Color of the Peacock Feathers. *Forma*, **19**, 169 (2002). 17

[60] KIENTZ, B., VUKUSIC, P., LUKE, S., AND ROSENFELD, E. Iridescence of a marine bacterium and classification of prokaryotic structural colors. *Applied and environmental microbiology*, **78**, 2092 (2012). 18

[61] MORRIS, R.B. Iridescence from diffraction structures in the wing scales of Callophrys rubi, the Green Hairstreak. *Journal of Entomology Series A, General Entomology*, **49**, 149 (1975). 20

[62] POLADIAN, L., WICKHAM, S., LEE, K., AND LARGE, M.C.J. Iridescence from photonic crystals and its suppression in butterfly scales. *Journal of the Royal Society, Interface / the Royal Society*, **6 Suppl 2**, S233 (2009). 20, 124, 132

[63] POUYA, C. AND VUKUSIC, P. Electromagnetic characterization of millimetre-scale replicas of the gyroid photonic crystal found in the butterfly Parides sesostris. *Interface Focus*, **2**, 645 (2012). 20, 21, 124, 128, 143

[64] Vukusic, P. and Sambles, J.R. Photonic structures in biology. *Nature*, **424**, 852 (2003). 21, 72, 124, 128, 130, 137, 143

[65] Pouya, C., Stavenga, D.G., and Vukusic, P. Discovery of ordered and quasi-ordered photonic crystal structures in the scales of the beetle Eupholus magnificus. *Optics express*, **19**, 11355 (2011). 22, 23, 24, 25, 57

[66] Luke, S.M., Vukusic, P., and Hallam, B. Measuring and modelling optical scattering and the colour quality of white pierid butterfly scales. *Optics Express*, **17**, 14729 (2009). 26, 29, 30, 31

[67] Vigneron, J., Rassart, M., Vértesy, Z., Kertész, K., Sarrazin, M., Biró, L., Ertz, D., and Lousse, V. Optical structure and function of the white filamentary hair covering the edelweiss bracts. *Physical Review E*, **71**, 1 (2005). 28

[68] Thomas, K.R., Kolle, M., Whitney, H.M., Glover, B.J., and Steiner, U. Function of blue iridescence in tropical understorey plants. *Journal of the Royal Society, Interface / the Royal Society*, **7**, 1699 (2010). 29, 30, 72, 137

[69] Jones, C.M., Mes, P., and Myers, J.R. Characterization and Inheritance of the Anthocyanin fruit (Aft) Tomato. *Journal of Heredity*, **94**, 449 (2003). 29, 71

[70] Wheelwright, N.T. and Janson, C.H. Colors of Fruit Displays of Bird-Dispersed Plants in Two Tropical Forests. *The American Naturalist*, **126**, 777 (1985). 29, 71

[71] Vignolini, S., Moyroud, E., Glover, B.J., and Steiner, U. Analysing photonic structures in plants. *Journal of The Royal Society Interface*, **10**, 1 (2013). 29, 71, 72

[72] Lee, D.W., Taylor, G.T., and Irvine, A.K. Structural Fruit Coloration in Delarbrea michieana (Araliaceae). *International Journal of Plant Sciences*, **161**, 297 (2000). 29, 72, 80, 90

[73] Vignolini, S., Rudall, P.J., Rowland, A.V., Reed, A., Moyroud, E., Faden, R.B., Baumberg, J.J., Glover, B.J., and Steiner, U. Pointillist structural color in Pollia fruit. *Proceedings of the National Acadamy of Science*, **109**, 15712 (2012). 31, 72, 80, 93

[74] Ward, A.J. and Pendry, J.B. Refraction and geometry in Maxwell's equations. *Journal of Modern Optics*, **43**, 773 (1996). 33

References

[75] JOANNOPOULOS, J.D., JOHNSON, S.G., WINN, J.N., AND MEADE, R.D. *Photonic Crystals, Molding the Flow of Light.* Princeton University Press, Princeton and Oxford, second edition (2008). 33, 46, 95, 96, 100

[76] SASTRY, G.P. The generalised Brewster condition from the extinction theorem. *European Journal of Physics*, **8**, 124 (1987). 36

[77] HECHT, E. *Optics.* Addison-Wesley, third edition (1998). 38, 49

[78] KITTEL, C. *Introduction to Solid State Physics.* John Wiley & Sons, New Caledonia, 8th edition (2005). 40

[79] YABLONOVITCH, E. Photonic Crystals. *Journal of Modern Optics*, **41**, 12 (2007). 40

[80] BINGSHE, X., PEIDE, H., LIPING, W., JIAN, L., XUGUANG, L., MINGWEI, C., AND ICHINOSE, H. Optical properties in 2D photonic crystal structure using fullerene and azafullerene thin films. *Optics Communications*, **250**, 120 (2005). 40

[81] OUELLETTE, J. Seeing the future in photonic crystals. *The Industrial Physicist*, **2002**, 14 (2001). 40

[82] LAND, M.F. The physics and biology of animal reflectors. *Progress in Biophysics and Molecular Biology*, **24**, 77 (1972). 42

[83] ANDERSSON, S., HYDE, S.T., LARSSON, K., AND LIDIN, S. Minimal surfaces and structures: from inorganic and metal crystals to cell membranes and biopolymers. *Chemical Reviews*, **88**, 221 (1988). 44

[84] AKAHANE, Y., ASANO, T., SONG, B.S., AND NODA, S. High-Q photonic nanocavity in a two-dimensional photonic crystal. *Nature*, **425**, 944 (2003). 48, 96

[85] SIEVENPIPER, D.F., SICKMILLER, M.E., AND YABLONOVITCH, E. 3D Wire Mesh Photonic Crystals. *Physical review letters*, **76**, 2480 (1996). 48

[86] NICODEMUS, F.E., RICHMOND, J.C., HSIA, J., GINSBERG, I.W., AND LIMPERIS, T. *Geometrical Considerations and Nomenclature for Reflectance.* October. U. S. Government printing office, Washington, D. C. (1977). 52

[87] VUKUSIC, P. AND STAVENGA, D.G. Physical methods for investigating structural colours in biological systems. *Journal of the Royal Society, Interface / the Royal Society*, **6 Suppl 2**, S133 (2009). vii, 52, 137

[88] MathWorks. MATLAB and Statistics Toolbox Release 2012a (2012). 58, 64

[89] Constant, T.J., Hibbins, A.P., Lethbridge, A.J., Sambles, J.R., Stone, E.K., and Vukusic, P. Direct Mapping of Surface Plasmon Dispersion using Imaging Scatterometry. *Applied Physics Letters*, **102**, 251107 (2013). 59, 171

[90] Zeiss, C. Axiovision 4.8.2.0 (2006). 61

[91] Spurr A. R. A low-viscosity epoxy resin embedding medium for electron microscopy. *J. Ultrastruct. Res.*, **26**, 1 (1969). 64

[92] Vukusic, P., Sambles, J.R., and Lawrence, C.R. Structurally assisted blackness in butterfly scales. *Proceedings of the Royal Society B: Biological Sciences*, **271**, S237 (2004). 64, 96

[93] Burger, W. and Burge, M.J. *Principles of Digital Image Processing: Core Algorithms.* Springer (2009). 64

[94] Duhamel, P. and Vetterli, M. Fast Fourier transforms : a tutorial review and a state of the art. *Signal Processing*, **19**, 259 (1990). 64

[95] TFCalc (1995). 66, 141, 143

[96] HFSS V.12, Ansoft Corporation, W. HFSS (????). xii, 66, 141

[97] Oskooi, A.F., Roundy, D., Ibanescu, M., Bermel, P., Joannopoulos, J., and Johnson, S.G. Meep: A flexible free-software package for electromagnetic simulations by the FDTD method. *Computer Physics Communications*, **181**, 687 (2010). 66, 90

[98] Cazetta, E., Zumstein, L.S., Melo-Júnior, T.a., and Galetti, M. Frugivory on Margaritaria nobilis L.f. (Euphorbiaceae): poor investment and mimetism. *Revista Brasileira de Botânica*, **31**, 303 (2008). 71, 72, 73

[99] Gautier-Hion, A., Duplantier, J.M., Quris, R., Feer, F., Sourd, S., Decoux, J.P., Dubost, G., Emmons, L., Erard, C., Hecketsweiler, P., Moungazi, A., Roussilhon, C., and Thiollay, J. Oecologia. *Oecologia*, **65**, 324 (1985). 71

[100] Julliot, C. Fruit choice by red howler monkeys (Alouatta seniculus) in a tropical rain forest. *American Journal of Primatology*, **40**, 261 (1996). 71

[101] Mcdiarmid, R.W., Ricklefs, R.E., and Foster, M.S. Dispersal of Stemmadenia donnell-smithii (Apocynaceae) by Birds. *Biotropica: The Journal of Tropical Biology and Conservation*, **9**, 9 (1977). 71

References

[102] Murray, D.R. *Seed Dispersal.* Academic Press (1987). 71

[103] Markaris, P., Linvingston, G.E., and Fellers, C.R. Quantitative aspects of strawberry pigment degradation. *Journal of Food Science*, **22**, 117 (1957). 71

[104] Parker, A.R. and Townley, H.E. Biomimetics of photonic nanostructures. *Nature nanotechnology*, **2**, 347 (2007). 72

[105] Saison, T., Peroz, C., Chauveau, V., Berthier, S., Sondergard, E., and Arribart, H. Replication of butterfly wing and natural lotus leaf structures by nanoimprint on silica solgel films. *Bioinspiration & Biomimetics*, **3** (2008). 72, 150

[106] Parker, A.R. A vision for natural photonics. *Philosophical transactions Series A Mathematical physical and engineering sciences*, **362**, 2709 (2004). 72

[107] Xu, J. and Guo, Z. Biomimetic Photonic Materials with Tunable Structural Colors. *Journal of Colloid and Interface Science*, **In Press** (2013). 72, 150

[108] Rudall, P.J. Jodrell Laboratory, Royal Botanic Gardens (2011). 73

[109] Woolley, J.T. Refractive index of soybean leaf cell walls. *Plant physiology*, **55**, 172 (1975). 80

[110] Kolle, M., Zheng, B., Gibbons, N., Baumberg, J.J., and Steiner, U. Stretch-tuneable dielectric mirrors and optical microcavities. *Optics Express*, **18**, 4356 (2010). 83

[111] Kolle, M., Lethbridge, A., Kreysing, M., Baumberg, J.J., Aizenberg, J., and Vukusic, P. Bio-Inspired Band-Gap Tunable Elastic Optical Multilayer Fibers. *Advanced Materials*, pages 1–7 (2013). ix, 88

[112] Tong, L., Hu, L., Zhang, J., Qiu, J., Yang, Q., Lou, J., Shen, Y., He, J., and Ye, Z. Photonic nanowires directly drawn from bulk glasses. *Optics Express*, **14**, 82 (2006). 94

[113] Tong, L., Gattass, R.R., Ashcom, J.B., He, S., Lou, J., Shen, M., Maxwell, I., and Mazur, E. Subwavelength-diameter silica wires for low-loss optical wave guiding. *Nature*, **426**, 816 (2003). 94

[114] Tong, L. and Mazur, E. Glass nanofibers for micro- and nano-scale photonic devices. *Journal of Non-Crystalline Solids*, **354**, 1240 (2008). 94

[115] YOSHIOKA, S. AND KINOSHITA, S. Direct determination of the refractive index of natural multilayer systems. *Physical Review E*, **83**, 051917 (2011). 98

[116] AKAHANE, Y., ASANO, T., SONG, B.S., AND NODA, S. Fine-tuned high-Q photonic-crystal nanocavity. *Optics express*, **13**, 1202 (2005). 96

[117] ARMANI, D.K., KIPPENBERG, T.J., SPILLANE, S.M., AND VAHALA, K.J. Ultra-high-Q toroid microcavity on a chip. *Nature*, **421**, 925 (2003). 96

[118] LIU, F., DONG, B., ZHAO, F., HU, X., LIU, X., AND ZI, J. Ultranegative angular dispersion of diffraction in quasiordered biophotonic structures. *Optics Express*, **19**, 7750 (2011). 96, 99, 115

[119] JEWELL, S.A., VUKUSIC, P., AND ROBERTS, N.W. Circularly polarised colour reflection from helicoidal structures in the beetle Plusiotis boucardi. *New Journal of Physics*, **9**, 1 (2007). 96, 98

[120] GALUSHA, J.W., RICHEY, L.R., JORGENSEN, M.R., GARDNER, J.S., AND BARTL, M.H. Study of natural photonic crystals in beetle scales and their conversion into inorganic structures via a solgel bio-templating route. *Journal of Materials Chemistry*, **20**, 1277 (2010). 96, 98, 150

[121] GALUSHA, J.W., RICHEY, L.R., GARDNER, J.S., CHA, J.N., AND BARTL, M.H. Discovery of a diamond-based photonic crystal structure in beetle scales. *Physical Review E*, **77**, 050904 (2008). 96, 98

[122] VUKUSIC, P., KELLY, R., AND HOOPER, I. A biological sub-micron thickness optical broadband reflector characterized using both light and microwaves. *Journal of the Royal Society, Interface*, **6**, S193 (2009). 124

[123] PRUM, R.O., QUINN, T., AND TORRES, R.H. Anatomically diverse butterfly scales all produce structural colours by coherent scattering. *Journal of Experimental Biology*, **209**, 748 (2006). 124

[124] SCHOEN, A. Infinite Periodic Minimal Surfaces without Self-Intersections. Technical report, NASA (1970). 124

[125] GIRALDO, M.A., YOSHIOKA, S., AND STAVENGA, D.G. Far field scattering pattern of differently structured butterfly scales. *Journal of comparative physiology. A, Neuroethology, sensory, neural, and behavioral physiology*, **194**, 201 (2008). 128

References

[126] VUKUSIC, P., SAMBLES, J.R., AND LAWRENCE, C.R. Colour mixing in wing scales of a butterfly. *Nature*, **404**, 457 (2000). 132

[127] WANG, H., ZHOU, W., AND LI, E. Focused Ion Beam Nano-Precision Machining for Analyzing Photonic Structures in Butterfly. *Key Engineering Materials*, **447-448**, 174 (2010). 132

[128] TAHA, A. K3DSurf (????). 141

[129] SYSTEMS, D. Solid Works (2011). 142

[130] MEJDOUBI, A., ANDRAUD, C., BERTHIER, S., LAFAIT, J., BOULENGUEZ, J., AND RICHALOT, E. Finite element modeling of the radiative properties of Morpho butterfly wing scales. *Physical Review E*, **87**, 022705 (2013). 146

[131] JAKŠIĆ, Z., PANTELIĆ, D., SARAJLIĆ, M., SAVIĆ-ŠEVIĆ, S., MATOVIĆ, J., JELENKOVIĆ, B., VASILJEVIĆ-RADOVIĆ, D., ĆURČIĆ, S., VUKOVIĆ, S., PAVLOVIĆ, V., BUHA, J., LAČKOVIĆ, V., LABUDOVIĆ-BOROVIĆ, M., AND ĆURČIĆ, B. Butterfly scales as bionic templates for complex ordered nanophotonic materials: A pathway to biomimetic plasmonics. *Optical Materials* (2013). 149

[132] YEH, C. *Applied Photonics*. Academic Press Inc., San Diego (1994). 149

[133] TAUBES, G. Photonic Crystal Made to Work at an Optical Wavelength. *Science*, **278**, 1709 (1997). 149

[134] WANG, G., FANG, Y., KIM, P., HAYEK, A., WEATHERSPOON, M.R., PERRY, J.W., SANDHAGE, K.H., MARDER, S.R., AND JONES, S.C. Layer-By-Layer Dendritic Growth of Hyperbranched Thin Films for Surface Sol-Gel Syntheses of Conformal, Functional, Nanocrystalline Oxide Coatings on Complex 3D (Bio)silica Templates. *Advanced Functional Materials*, **19**, 2768 (2009). 150

[135] HSUEH, H.Y., CHEN, H.Y., SHE, M.S., CHEN, C.K., HO, R.M., GWO, S., HASEGAWA, H., AND THOMAS, E.L. Inorganic Gyroid with Exceptionally Low Refractive Index from Block Copolymer Templating. *Nano letters*, pages 4994–5000 (2010). 150

[136] GALUSHA, J.W., JORGENSEN, M.R., AND BARTL, M.H. Diamond-structured titania photonic-bandgap crystals from biological templates. *Advanced materials (Deerfield Beach, Fla.)*, **22**, 107 (2010). 150

[137] Yao, B., Shi, H., Wu, Y., and Zhang, L. Photoluminescence of transparent mesoporous titania gel-monolith. *Journal of Materials Science Letters*, **20**, 767 (2001). 150

[138] Mille, C., Tyrode, E.C., and Corkery, R.W. Inorganic chiral 3-D photonic crystals with bicontinuous gyroid structure replicated from butterfly wing scales. *Chemical communications (Cambridge, England)*, **47**, 9873 (2011). 150

[139] Link, S. and El-sayed, M.A. Spectral Properties and Relaxation Dynamics of Surface Plasmon Electronic Oscillations in Gold and Silver Nanodots and Nanorods. *Journal of Physical Chemistry B*, **103**, 8410 (1999). 150

[140] Weatherspoon, M.R., Dickerson, M.B., Wang, G., Cai, Y., Shian, S., Jones, S.C., Marder, S.R., and Sandhage, K.H. Thin, conformal, and continuous SnO2 coatings on three-dimensional biosilica templates through hydroxy-group amplification and layer-by-layer alkoxide deposition. *Angewandte Chemie (International ed. in English)*, **46**, 5724 (2007). 150